The Hierarchy of Rogue Wave Solutions in Nonlinear Systems

David J. Kedziora

A thesis submitted for the degree of
Doctor of Philosophy
The Australian National University

September 2014

Declaration

All of the research reported in this thesis is my own original work except where otherwise acknowledged.

My participation in publications undertaken as part of my PhD studies is described as follows:

- *Major contributor to the 'rogue triplets' paper [1]. Provided numerical investigation and editorial support.*
- *Primary contributor to the 'circular clusters' [2], 'degenerate breather' [3], 'triangular cascades' [4], 'phase shift' [5], 'rogue hierarchy' [6] and 'cnoidal background' [7] papers. Writer of all sections. Nail Akhmediev and Adrian Ankiewicz provided background knowledge and editorial support.*
- *Minor contributor to the collaborative 'resonance model' [8] and the 'derivative model' [9] papers. Writer of the supplementary Lax pair sections. Provided background knowledge and editorial support.*

I hereby acknowledge that the use of original material from collaborative papers is limited to citation within this thesis, so as to avoid conflicts of interest. I neither intend to infringe upon nor claim ownership of the rights allowing the main authors to use the relevant content as they see fit.

I also declare that all publications included in this work [2–7], complete with original journal format and linguistic style, are reprinted with the permission of all co-authors and copyright holders.

David J. Kedziora

Adrian Ankiewicz

Nail Akhmediev
September 2014

To Victos, the Sentinel and the Hedron.
And to those closest to me who understand.

Acknowledgements

The existence of this thesis and the research it encapsulates would not have been possible without the support of numerous people. For that reason, I thank my PhD supervisors, Prof. Nail Akhmediev and Dr. Adrian Ankiewicz, for providing both the necessary background information and investigative oversight to explore the fascinating concept of rogue waves. Nail should be particularly commended on his insightful holistic view of the field, always informing me of curious new problems to tackle, while the technical expertise of Adrian has proved greatly invaluable, bolstering our results with scientific rigour. Moreover, both have always been friendly and readily approachable. Indeed, I am torn between what I appreciate the most; their words of great wisdom or their words of great humour! Certainly, this paragraph cannot sufficiently detail the ways in which they have aided both my study and this thesis, but I can strongly claim that my continuing development as a physicist is largely to their credit.

I next extend my gratitude to all the members and friends of the Optical Sciences Group in the Research School of Physics and Engineering, especially within the years ranging from 2011 to 2014, for enriching our tea breaks with both relaxing conversation and lively debates. Special mention must go to the 'heart' of the group, Dr. Natasha Devine, who has contributed towards a very welcoming work environment. She has always been the one who organises the birthday gifts, cakes and celebrations. So my appreciation of her generosity can only ever be understated. Similar thanks must also go to my office mate, Amdad Chowdury, who has frequently shared in the thrills of our scientific discoveries. Surely, this long journey could not have been half as rewarding without an ally bearing his level of passion for the topic.

Beyond this, I am indebted to all of my friends, near and far, and my ever-growing family. I pay my respects to Marcel de Vriend, for graciously allowing me to invade his home during my frequent visits to Sydney, and also to my in-laws, Douglas and Alison McKemmish, for helping me settle in Canberra. Of course, some of my greatest regards then go to my parents. I would not be at this stage of study without years of prior education and nurture, courtesy of both my mother, Lucyna, and father, Andrew. This dissertation is thus a testament to their unconditional and continuing support. So too do I appreciate my sister, Joanna, for the close bond we share and the cheer she has provided me throughout these years. Again, a simple paragraph cannot do justice to the ways in which my extended family have helped me over the past several years, so this is just the smallest token of heartfelt thanks.

Finally, to my dearest wife, Laura, this is as much your thesis in spirit as it is mine. Except I did the research. And the writing up. And the pretty pictures. But you still shared in the adventure, 3.5 years in the making, and that is what ultimately matters. I could try listing everything you have done for me as a separate chapter, but it might overshadow the content of this dissertation. So I will just say thanks and finish here; both of us knowing that, in the end, words cannot convey.

David J. Kedziora
September 2014

Abstract

Oceanic freak waves, optical spikes and extreme events in numerous contexts can arguably be modelled by modulationally unstable solutions within nonlinear systems. In particular, the fundamental nonlinear Schrödinger equation (NLSE) hosts a high-amplitude spatiotemporally localised solution on a plane-wave background, called the Peregrine breather, which is generally considered to be the base-case prototype of a rogue wave. Nonetheless, until very recently, little was known about what to expect when observing or engineering entire clusters of extreme events. Accordingly, this thesis aims to elucidate this matter by investigating complicated structures formed from collections of Peregrine breathers. Many novel NLSE solutions are discovered, all systematically classifiable by their geometry.

The methodology employed here is based on the well-established concept of Darboux transformations, by which individual component solutions of an integrable system are nonlinearly superimposed to form a compound wavefunction. It is primarily implemented in a numerical manner within this study, operating on periodically modulating NLSE solutions called breathers. Rogue wave structures can only be extracted at the end of this process, when a limit of zero modulation frequency is applied to all components. Consequently, a requirement for breather asymmetry ensures that a multi-rogue wavefunction must be formed from a triangular number of individual Peregrine breathers (e.g. $1, 3, 6, 10, ...$), whether fused or separated. Furthermore, the arrangements of these are restricted by a maximum phase-shift allowable along an evolution trajectory through the relevant wave field.

Ultimately, all fundamental high-order rogue wave solutions can be constructed via polynomial relations between origin-translating component shifts and squared modulation frequency ratios. They are simultaneously categorisable by both these mathematical existence conditions and the corresponding visual symmetries, appearing spatiotemporally as triangular cascades, pentagrams, heptagrams, and so on. These parametric relations do not conflict with each other, meaning that any arbitrary NLSE rogue wave solution can be considered a hybridisation of this elementary set. Moreover, this hierarchy of structures is significantly general, with complicated arrangements persisting even on a cnoidal background.

Contents

Introduction

Rogue waves are unusually large and seemingly spontaneous disturbances within a medium. They are best known to the public in an oceanic context, infamously capable of causing significant damage to seafaring vessels. However, most abstractly, they can fundamentally be considered as localised and unexpectedly significant deviations from a regular or quiescent state. This generalisation has thus inspired a truly interdisciplinary movement over the last couple of decades, drawing parallels between all sorts of extreme events and all manners of emergent behaviour. Ideas have cross-pollinated between a diverse array of fields, ranging from fluid dynamics [10, 11] and optics [12–14] to condensed matter [15, 16], plasma theory [17, 18] and even finance [19]. In essence, there is a quest within the scientific community to understand the physics behind rogue wave evolution, so that the phenomenon may be both predicted within nature and engineered in the laboratory.

Given that the discipline is still young and continuously evolving, it follows that there are ongoing debates about applicability, relevance and even definition itself [20]. This chapter thus aims to provide a general but non-exhaustive overview of rogue wave science in its current state. Accordingly, the oceanic origins of the phenomenon are described in Sec. 1.1, while Sec. 1.2 discusses the transfer of ideas into the optical domain. The need to develop theories for compound rogue waves is then motivated in Sec. 1.3, which leads into an overview of this thesis in Sec. 1.4.

1.1 From Deep Ocean to a Wave Tank

The concept of rogue waves initially originated in a hydrodynamic context. Unlike tsunamis, the destructive influence of which solely appears at coastal regions due to a wave shoaling process, rogue waves tend to occur in regions of great fluid depth. This has traditionally limited observers to those unlucky enough to be affected by the event, which means that the phenomenon of 'freak' waves has largely been considered a maritime legend for centuries. Indeed, it is debated whether giant breakers depicted in various historical artworks, exemplified by Fig. 1.1a, can be considered as the first documented rogue waves [21, 22, 24]. All the same, it was not until New Year's Day, 1995, that an occurrence was finally unambiguously confirmed with a measuring instrument at an offshore platform [25]. Despite the existence of earlier studies [26, 27], this Draupner wave can loosely be considered as the inception of sustained oceanographic research into the topic. Since then, technological improve-

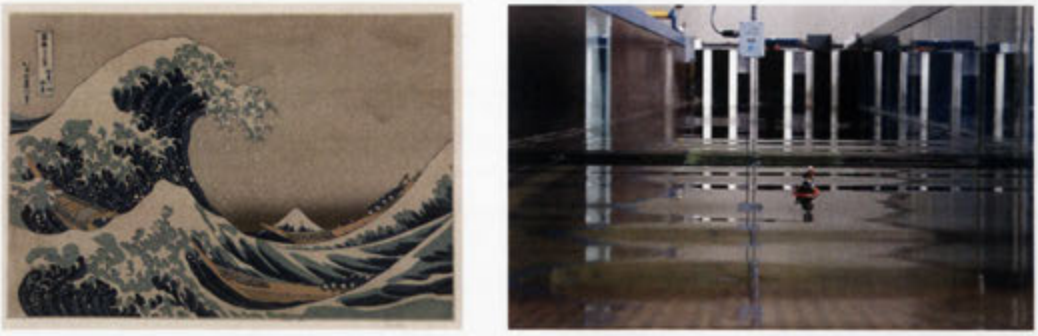

(a) (b)

Figure 1.1: Examples of rogue waves in an oceanic context. (a) Katsushika Hokusai's *The Great Wave off Kanagawa* (c. 1829-32); a depiction of a possible freak wave [21, 22]. (b) A 'super rogue wave' engineered in a wave tank, on the verge of colliding with a lego pirate [23].

ments and a refining of focus have listed many more incidents [28], with preliminary satellite data indicating that rogue waves may be far more common than expected [29].

It is also in the discipline of fluid dynamics that rogue waves are perhaps most stringently classified. Specifically, if significant wave height (SWH) is defined as the mean vertical trough-to-crest distance for the largest third of waves in a recorded time series, then an individual wave is considered rogue if it possesses a height more than twice this value [20, 30, 31]. Consequently, there is no amplitude restriction for a freak wave. One metre in height could be considered sufficiently rogue if the background sea is calm enough. However, this functional definition is not without controversy. It is based on a threshold for outliers within a 'normal' Rayleigh distribution, which already assumes prior knowledge of rogue wave statistics. In contrast, heavy-tail distributions may be more appropriate depending on the actual physics behind freak wave generation [32, 33].

Fundamentally, oceanic rogue waves cannot be strictly categorised without a deeper understanding of their evolution dynamics. Some argue that freak waves frequently arise as triplets, in what is known as the 'three sisters' phenomenon [28, 34], while others claim that shallow-water coastal events should also be considered as rogue waves [35, 36]. The ongoing debate of what is legitimate in the field may ultimately depend on whether the physics is shared or even similar between different high-amplitude incidents. Unsurprisingly, various mechanisms have been suggested for rogue wave generation, each with its own core principle. Broadly put, they are encapsulated by:

Standard Linear Theory	–	A wave formed from the linear superposition of two others can only have their amplitude sum as its maximum, at points of constructive interference. Nonetheless, with proper phase alignment of all spectral components in a wave field, crests and troughs of extreme amplitude could possibly arise, if with extreme rarity. This purist form of conjecture is no longer commonly favoured, with most modern 'linear' theories invoking novel concepts to bias Gaussian statistics [37, 38]. Certainly, as amplitudes increase, the concept of linearity worsens as an approximation of realistic wave dynamics.
Focussing by external factors	–	Wave components with different directions can potentially compress wave trains or align phases to produce rogue wave focal points. Diffraction due to coastal geometries and certain current-based effects are candidates for this process [22, 39].
Energy from external sources	–	Introducing energy into a wave field generally increases the chance of greater heights arising. Storms, winds and thermal convection could contribute to this scenario [40, 41].
Nonlinear Theory	–	New frequencies can only be generated within a wave spectrum once nonlinear effects are taken into account. In this case, interactions between wave components in the background sea could naturally give rise to large amplitudes, without any significant external input [42, 43].

While no consensus yet exists, there is a strong preference within the research community towards the importance of nonlinearities in rogue wave evolution. For instance, the shallow-water 1D Korteweg-de Vries (KdV) and 2D Kadomtsev-Petviashvili (KP) equations have been proposed as models for coastal events [35, 44]. More importantly, from the perspective of this thesis, deep-water waves happen to be well described by the nonlinear Schrödinger equation (NLSE) [45, 46]. This is particularly significant as the NLSE is applicable in numerous fields and has been studied with various methods. It is also well known that the system hosts a unique spatiotemporally localised solution, referred to as either a Peregrine breather or a Peregrine soliton [47]. Whether this theoretical structure truly depicts natural freak wave behaviour in the ocean is under debate, but the prototype function certainly adheres to all the relevant definitional criteria [48, 49]. Based on these ideas, in 2011, a small-scale rogue wave was created in a water tank for the first time [11]. A snapshot of a subsequent experiment is shown in Fig. 1.1b.

1.2 A Bright Light in an Optical Fibre

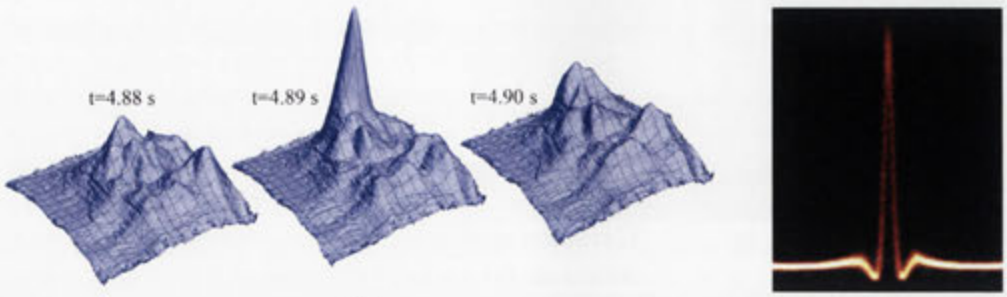

(a) (b)

Figure 1.2: Examples of rogue waves in an optical context. (a) Transient appearance of a bright spot in a laser beam profile during a filamentation experiment involving xenon [50]. (b) Temporal profile of an optical Peregrine breather generated in a standard telecommunications fibre [51].

Although the concept of rogue waves originated in oceanography, the ripples of interest it generated in the field of optics were no less substantial. It has long been known that, given certain assumptions, the evolution of light in an optical waveguide can be described by the NLSE. The analogy between waves in optical fibre and on deep-water surfaces has thus been equally clear, leading to an unusual transmission of ideas between distinct disciplines. One such example of an adapted notion is the concept of solitons, defined in the simplest instance as localised pulses that propagate without losing shape. They were first scrutinised in Scotland's Union Canal as 'waves of translation' in the early 19th century [52, 53], but it was not until 1973 that their existence was proposed within the optical domain [54]. Fortunately, in the case of rogue wave theory, the dissemination has been significantly faster.

In 2007, a report was published on the evolution of a pulse train in an optical fibre [12]. Although the experiment was primarily about exploring supercontinuum generation, a consequence of spectral broadening, analysis of the resulting radiation indicated the existence of short-lived intensity spikes with large amplification. While such events could be averaged out in the presence of a chaotic background, they nonetheless occurred often enough to be reminiscent of a long-tailed probability distribution. In effect, this marked the first reported observation of optical rogue waves. Since then, the stochastic generation of these extreme events has been further investigated from various angles, including laser beam filamentation [55] and turbulence [56]. An example of a transient intensity flare arising in one such experiment is shown in Fig. 1.2a.

To date, no consensus truly exists for the definition of a rogue wave in an optical context. Certainly, the field is less than a decade old, but there are other differences with respect to hydrodynamics that rationalise this fact. For instance, amplitudes are not restricted by aspects such as wave breaking [57]. A rogue wave in fibre

could potentially be orders of magnitude more intense than accompanying pulses, provided both that there is enough background energy to focus into the peak and that the damage threshold of the material is not surpassed [58]. Nonetheless, there are simultaneously fewer 'nuisance parameters' involved in modelling the evolution of light within a waveguide, so the mechanism for generating these extreme events is conversely less controversial. Indeed, it is usually very complicated to suppress or isolate the peripheral effects of currents, coastal geometries and meteorological events in general ocean surface waves, whereas the materials and engineered physics of common optical fibres are, theoretically at least, well defined.

Consequently, this thesis adopts the assumption that rogue waves are produced by the phenomenon of 'modulational instability', whereby an event is capable of growing and shrinking in a manner of 'breathing' via the interplay of dispersion and nonlinear focussing [59]. These effects arise from the interaction between electromagnetic radiation and certain waveguide materials, allowing for an infinitesimal perturbation to develop into a short-lived spatiotemporally localised crest with high intensity. Specifically, the simplest wavefunction of this type is the aforementioned Peregrine breather [47], exemplified in profile form within Fig. 1.2b, which has a remarkably simple analytic form. Thus, although this NLSE solution was originally developed with a hydrodynamic perspective in 1983, it was within an optical fibre in 2010 that a rogue wave was deterministically generated for the first time [13].

1.3 The Quest for the Rogue Hierarchy

With scientific research entering a new decade, rogue waves had been controllably generated in both a wave tank [11] and an optical fibre [13] via the application of nonlinear theory. Unsurprisingly, the scientific community would still debate the relevance of the Peregrine breather with respect to extreme events in nature, but the proof of principle regarding the generation of waves with 'rogue features' had inspired a new surge of research enthusiasm. Accordingly, similar phenomena have been theorised and occasionally reproduced within numerous fields, primarily due to the universality of the NLSE. Analogues have been investigated for Bose-Einstein condensates (BECs) [15], superfluids [60], laboratory plasmas [17], the atmosphere [61], and so on. Even crises within the realm of finance have been associated with the theory of freak waves [19].

However, until very recently, most studies targeted the dynamics of a single rogue wave event. Even the oceanic three sisters phenomenon is typically considered to be several oscillations localised under the envelope of a solitary wave packet [62]. Yet noise and chaos exist in numerous domains, capable of converting modulationally unstable perturbations into a multitude of extreme amplitude spikes [63]. This is frequently observed in various optical processes [12, 64]. As for the ocean, it is such an intrinsically complex system that it too could hypothetically harbour multiple rogue waves in spatial and temporal proximity to each other, with only one solitary incident ever being experienced and reported. Certainly, particular types of chaotic

environment increase the frequency of freak wave formation [65] and, in turn, the possibility of such an agglomerate occurrence. Hence it is of substantial interest to investigate where and when potentially catastrophic extreme events [58, 66] could appear, if physically interdependent.

Of course, prediction is but one side of the topic. It is inevitable that, with greater understanding, matters of engineering will also arise. Potential applications for constructed arrays of rogue waves range from the practical, such as the control of supercontinuum generation with extra finesse [67], to the highly speculative, such as the distribution of hydrodynamic effects to damage naval convoys [68]. But whatever the eventual implementation may be, dealing with multiple rogue waves opens up many new questions. For instance:

- Is it even possible to superimpose multiple rogue waves?
- If so, are certain spatiotemporal arrangements restricted?
- Can the remaining wavefunctions then be sensibly classified in some hierarchical manner?
- If so, do variations in a background modify the chosen categories?
- Likewise, how general is the hypothetical scheme with respect to deviations from the normal NLSE?

These problems are all addressed by the research presented in this thesis, so that the answers will be available once experimental methodology catches up with theory. They are not trivial matters either, with mathematical limit issues and 'axial translation' peculiarities once stymying progress beyond the most standard of superimposed solutions [69, 70]. It is only through the fusion of analytic and numerical techniques that a better understanding of complicated multi-rogue structures has now been achieved. Consequently, this dissertation describes the development of novel NLSE rogue wave solutions that possess remarkable geometries, the intrinsic nature of which is remarkably robust. Using appropriate procedures, these various patterns of extreme events should be reproducible within wave tanks, optical fibres and other relevant domains.

Naturally, as with most frontier fields, rogue wave theory has continued to evolve alongside the investigation conducted for this thesis. Notably, the importance of spatiotemporally localised NLSE solutions has occasionally led to independent verification of the results in this thesis [71, 72]. Moreover, much of the research included here has already been adopted in numerous theoretical investigations within the physics community [73–75], with experiments also beginning to support the relevant findings [76, 77]. In essence, it is likely that the next few years will determine the utility of the established rogue wave hierarchy, potentially expanding scientific focus beyond individual extreme events towards an aggregate perspective.

1.4 Thesis Overview

The research in this dissertation is presented in a 'thesis by publication' format. Each core chapter contains a journal article that effectively details a step in the development of NLSE multi-rogue wave solutions and the scheme by which they are categorised. Overarchingly, Chapters 2, 4 and 6 reveal new classes of spatiotemporally localised structure, while Chapters 3 and 5 discuss their features. Chapters 7 and 8 then investigate the generality of the classification hierarchy. This entire work is performed computationally, although a mix of both symbolic and numerical calculations is deployed throughout. In greater detail, the narrative of this study is organised in the following way.

Chapter 2 serves as an introduction to the topic, with a particular focus on the first spatiotemporally 'fissioned' type of compound rogue wave discovered, known as a circular cluster [2]. To contextualise this result, many vital concepts are introduced that are ubiquitous within this thesis. These include the NLSE in optical notation, the solution-generating Darboux scheme and the set of 'first-order' breathers used in the construction of high-order solutions. In particular, the latter component wavefunctions consist of both the Akhmediev breather (AB) and the Kuznetsov-Ma (KM) 'soliton', as well as the fundamental Peregrine breather that arises in the 'rogue wave limit'. With this established, the chapter then discusses the novel idea of incorporating spatiotemporally perturbating 'axial shifts' within the Darboux scheme, contrasting previously-known 'fused' rogue wave solutions with the aforementioned circular clusters.

Chapter 3 returns to a more generalised investigation of (axially-aligned) second-order breathers, with particular focus on the so-called degenerate and rogue wave limits [3]. This research presents exact expressions for various NLSE solutions, including wavefunctions formed from two ABs, two KM solitons or one of each breather type interacting together, as well as similar structures where a zero modulation-frequency limit has been applied to one of the breathers alone. Most significantly, the limit case of two breathers becoming identical is explored, with an inherently required asymmetry having profound effects on the composition of a compound rogue wave.

Chapter 4 extends the known set of multi-rogue wave solutions by revealing the existence of triangular rogue wave cascades [4]. Accordingly, the parametric constraint for the production of the solution is presented. Unlike with the case of circular clusters, a complicated relationship must be established between both axial shifts and the modulation frequencies of component breathers. However, the 'circularity' and 'triangularity' of a fissioned high-order rogue wave can be tuned independently of each other, allowing hybrid 'claw-like' NLSE solutions to be derived. These are displayed and discussed.

Chapter 5 elaborates on the phase features of high-order rogue waves, exploring their impact on a thus-far ignored carrier wave [5]. Specifically, evolution trajectories through amplitude surges and troughs are examined in the complex plane, identifying various types of homoclinic orbit that correspond with multiples of a 2π phase

shift. This is done for both fused and fissioned structures. Subsequently, the use of phase information to produce a better understanding of rogue wave 'anatomy' is discussed, particularly in situations of near-maximal spatiotemporal compression and general chaotic domains.

Chapter 6 presents the core result of this thesis; a systematic way to generate elementary NLSE solutions of any order that are spatiotemporally localised, all categorisable within one fundamental rogue wave hierarchy [6]. Consequently, polynomial relations involving both component modulation frequencies and axial shifts of variable 'order' are established as existence conditions for different arrangements of fused and separated Peregrine breathers. The generated wavefunctions are displayed up to sixth order, characterised by a rotational symmetry associated with each parametric constraint. Structural features are then extrapolated for NLSE solutions of extreme order, synthesising knowledge from the previous chapters. Again, geometric qualities of these compound rogue waves can still be tuned independently of each other, allowing for a concept of hybridisation that is exemplified within the article.

Chapter 7 examines whether the newly developed rogue wave hierarchy still exists when the plane wave background is replaced by a cnoidal wave field [7]. The Darboux scheme is thus modified appropriately, with numerical propagation partially adopted. Subsequently, the relation between traditional solitons and breathers is clarified via smooth transformations of the background, with rogue waves shown to exist for all cases where energy is sufficiently mobile. Cnoidal parameter space is further explored, revealing the existence of unintuitive 'diffuse' rogue waves. In any case, the rogue wave hierarchy is ultimately shown to be substantially general with respect to the background.

Chapter 8 then briefly discusses possible future directions for multi-rogue wave research, from the perspective of its universality among nonlinear systems. This is inspired by the fact that, without discarding the basic tenets of NLSE modulational instability, it is possible to extend the equation via discretisation, coupling or the inclusion of higher-order nonlinearities and related terms. It is consequently suggested, with strong evidence, that the rogue wave hierarchy is not unique to the standard NLSE.

Final conclusions are drawn in Chapter 9.

Chapter 2

Circular Rogue Wave Clusters

Prologue

In early 2011, it seemed that many of the surprises presented by rogue waves were already accounted for. Nonlinearity-based explanations for their existence were favoured by the scientific community, grounded in the rationale that the nonlinear Schrödinger equation (NLSE) was a reasonably accurate first-order description of wave evolution in both deep-water surfaces [45] and optical waveguides [78]. Particularly appealing was the concept of modulational (a.k.a. Benjamin-Feir) instability [79, 80], by which a small perturbation in a regular waveform could grow to substantial amplitudes. Indeed, decades worth of mathematical research had discovered a class of NLSE solutions that encapsulated this phenomenon, called 'breathers' [59, 81, 82]. Most significantly, this set of structures possessed a special limit case, now named the Peregine breather [47]. It not only possessed a significantly higher peak than its surrounding plane-wave background, but was even spatiotemporally localised. In effect, it "came out of nowhere", formed an amplitude spike and then "disappeared without a trace" [48]. Accordingly, the Peregrine breather soon became known as a prototypical representation of freak waves, eventually being replicated in both a wave tank [11] and in optical fibre [13].

However, initial interest into extreme events formed from the interactions of multiple rogue waves was limited. This was despite many of the same methods that generated the Peregrine breather [78, 83, 84] being perfectly well equipped to investigate higher-order nonlinear superpositions of the structure. Certainly, 'fused' rogue waves of various orders had already been explored [69, 70], where individual components were all centred at a common origin. Nonetheless, discarding that constraint of geometric coincidence was generally ignored within the community. This may have been due to a linear-based mentality, whereby separating the two components that combine into a composite second-order rogue wave was assumed to result in no more than two distinct formations arising out of the plane-wave background.

Surprisingly, seminal investigations soon overturned expectations [85, 86]. One of them [1] forms the inception of the research within this thesis, employing a method of NLSE solution generation called the Darboux scheme. This well-established recursive procedure [84, 87] works here by algebraically combining n unique 'first-order components', each essentially representing an individual breather, into a wavefunction of order n. However, what was new at this stage was the inclusion of 'axial

shift' parameters, allowing each component to be centred at a different origin. Subsequently, a numerical application of the modified scheme was synthesised with an analytical investigation to confirm that a 'fissioned' second-order rogue wave was actually comprised of three distinct Peregrine breathers, rather than the presumed two. This structure is now known as a rogue triplet [1].

Certainly, once the importance of spatiotemporal perturbations was realised, it was not difficult for various procedures to begin fissioning compound structures [88]. However, the particular implementation of the Darboux scheme in this thesis had one major strength. Specifically, given a natural choice of scaling, the NLSE happened to arrange the three individual peaks of the rogue triplet in a spatiotemporally circular fashion. The question then arose; did this same geometry extend to higher-order structures?

This chapter, as a published manuscript [2], answers that question in the affirmative. Specifically, it presents and discusses the effects of using the Darboux scheme to shift one component of a multi-rogue wave relative to all others. It is also an appropriate publication for this thesis to begin with, as it introduces numerous concepts that will be referred to in later chapters. These include:

- The NLSE in optical notation.
- The Darboux transformation procedure, by which wavefunctions of order n are constructed from a background 'seeding solution'.
- Akhmediev breathers (ABs) and Kuznetsov-Ma (KM) 'solitons', as first-order solutions arising from modulational instability.
- The Peregrine 'soliton', as the prototype for a first-order rogue wave.
- The rogue triplet, along with an exact expression for its wavefunction.
- High-order 'fused' rogue waves.

Most importantly, from the perspective of the field, this paper presents novel high-order rogue wave solutions that appear as circular clusters of individual Peregrine breathers. They are an unintuitive consequence of limit theory and can only be contained within a finite portion of the spatiotemporal domain if the shift of the perturbed component is both carefully chosen and infinitesimal.

PHYSICAL REVIEW E **84**, 056611 (2011)

Circular rogue wave clusters

David J. Kedziora,* Adrian Ankiewicz, and Nail Akhmediev
Optical Sciences Group, Research School of Physics and Engineering, The Australian National University, Canberra ACT 0200, Australia

(Received 28 July 2011; published 28 November 2011)

Using the Darboux transformation technique and numerical simulations, we study the hierarchy of rational solutions of the nonlinear Schrödinger equation that can be considered as higher order rogue waves in this model. This analysis reveals the existence of rogue wave clusters with a high level of symmetry in the (x,t) plane. These structures arise naturally when the shifts in the Darboux scheme are taken to be eigenvalue dependent. We have found single-shell structures where a central higher order rogue wave is surrounded by a ring of first order peaks on the (x,t) plane.

DOI: 10.1103/PhysRevE.84.056611 PACS number(s): 05.45.Yv, 47.20.Ky, 42.65.−k

I. INTRODUCTION

The notion of rogue waves first appeared in studies of deep ocean waves [1–3] and gradually moved to other fields of physics such as optics [4], capillary waves [5], superfluidity [6], Bose-Einstein condensates (BECs) [7], etc. There are various approaches in these studies, starting from linear wave analysis [8], which can explain some of the phenomena that involve high amplitudes. However, the most comprehensive approach is based on nonlinear physics [1].

In particular, deep ocean waves, as described by the nonlinear Schrödinger equation (NLSE) [1], have specific solutions which are localized in both space and time. Such localization is exemplified by the Peregrine soliton, which has been studied both theoretically [9,10] and experimentally [11,12]. There is now growing interest in identifying higher order rational solutions [13–19], which are also doubly localized. Recent publications by Matveev's group significantly developed the technique of obtaining multirogue wave solutions and presented explicit forms for these higher order structures [15,17–20]. However, the complexity of these solutions does not allow for easy manipulation, despite being provided in analytical form. Even plotting them does not reveal all the intricate features of the solutions. We estimate that a large amount of work still has to be done in the analysis of multirogue wave solutions.

To derive expressions for compound rogue waves and visualize them, there are currently two main procedures in favor: a method based on Wronskian determinants developed by Matveev's group [15,17–20], which has seen success in reaching the sixth order solution analytically [21], and the Darboux method [22–24], which we employ in this investigation. Most attempts thus far have assumed the free parameters in the solution to be zeros. In this case, all components of the higher order structure are aligned perfectly at one point and the field has a single high maximum. However, here, we deviate from this assumption. This has already been done to a limited extent and has produced the "rogue triplet" solution [15,20,25]. In this work, we extend this investigation to higher order solutions using both symbolic computation and numerics, and present surprising clustered structures reminiscent of an atom with a shell of electrons. Perfect geometrical patterns obtained here clearly demonstrate that the world of NLSE solutions is significantly richer than we thought before.

We begin by writing the NLSE in the dimensionless form,

$$i\frac{\partial\psi}{\partial x}+\frac{1}{2}\frac{\partial^2\psi}{\partial t^2}+|\psi|^2\psi=0. \tag{1}$$

The wave function $|\psi(x,t)|$ in Eq. (1) commonly describes the wave envelope. In fiber optic applications [11], the variable x is the distance along the fiber, while t is the retarded time in the frame moving with the pulse group velocity. On the other hand, in water wave applications [12], x is the dimensionless time, while t is the distance in the frame moving with the group velocity. This difference is related to conventions and traditions in each field, rather than to any particular physical meaning. A simple linear transformation with the variable involving the group velocity allows us to change the equation and variables from one form to another. Generally speaking, the linear relation between the two variables in this transformation may be one of the essential points for understanding the unusual results of our work; namely, the high level of symmetry in the (x,t) plane.

There is a class of first order solutions to Eq. (1) that can be described by a complex eigenvalue l with imaginary part $\mathrm{Im}(l)$. This whole class has been previously presented [26]. If $0<\mathrm{Im}(l)<1$, the solutions are periodic in t and localized in x. They are presently known as Akhmediev breathers (ABs) [27–30]. An example is shown in Fig. 1(a). If $\mathrm{Im}(l)>1$, the solution is localized in t and periodic in x. The solution is known as a Ma soliton. It is shown in Fig. 1(b). In the limit of $l\to i$, the period in both x and t goes to infinity and a solution involving rational terms arises. This first order wave function is known as the Peregrine soliton [9]. Due to localization both in space and time we can also call it a "wave that appears from nowhere and disappears without a trace" (WANDT) [13].

First order solutions are the simplest amidst NLSE solutions. Among more complicated known examples we can mention multisoliton solutions [23]. Via similar processes to the construction of this class, we can generate a nonlinear superposition of multi-AB solutions. This can be done in various ways, such as by following Wronskian methodology [17,18]. In this work, we employ an alternative procedure that uses Darboux transformations [31]. This allows for the nonlinear superposition of n ABs, each centered at an arbitrary coordinate (x_j,t_j) and each with a different eigenvalue l_j,

*djk105@rsphysse.anu.edu.au

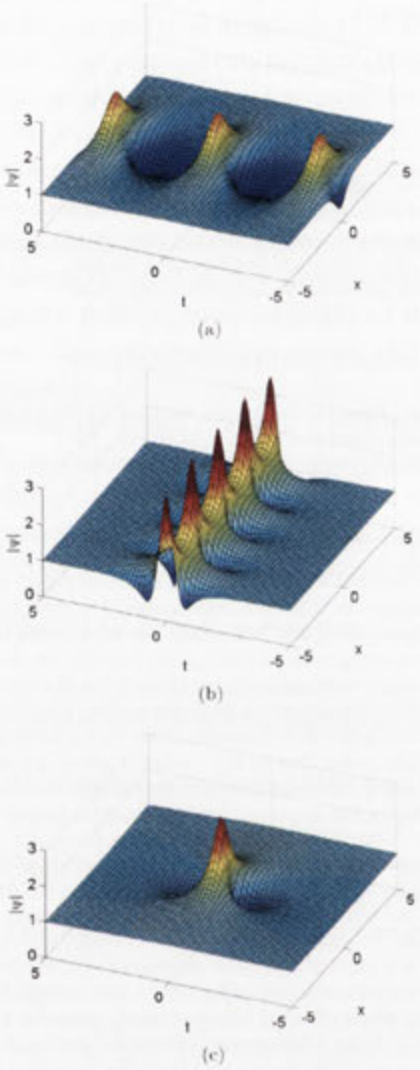

FIG. 1. (Color online) Various types of NLSE solution with l as eigenvalue. (a) Akhmediev breather with $l = 0.65i$. (b) Ma soliton with $l = 1.35i$. (c) Peregrine soliton with $l = i$ (or $\kappa = 0$).

where $j = 1, \ldots, n$. Frequencies of modulation are expressed through the eigenvalues as $\kappa_j = 2\sqrt{1 + l_j^2}$. For AB solutions, these are real.

II. LOW ORDER ANALYTIC SOLUTIONS

The Darboux method [31] allows us to present exact solutions of any order explicitly. The process is described in the Appendix and elaborated elsewhere [24,32]. However, generally the method does not allow two AB components to share the same eigenvalue, otherwise degenerate solutions arise. In these situations, numerical simulations can also experience difficulties. One of the ways to overcome such obstacles is by defining the n eigenvalues in the form $\kappa_j = j\kappa$ $(j = 1,2,\ldots,n)$ and taking the limit $\kappa \to 0$ afterwards. The sequence of calculations has previously been described in detail [32,33] and will not be repeated here. The rational solution of order n in general form, depending on x and t, can be written as

$$\psi_n(x,t) = \left[(-1)^n + \frac{G_n + i\,H_n}{D_n}\right] e^{it}, \tag{2}$$

where G_n, H_n, and D_n are all real polynomials of x and t.

A nontrivial observation is that higher order rational solutions are nonlinear combinations of the elementary component in Fig. 1(c). Their relative locations are uniquely defined by the shifts x_j and t_j, which effectively serve as coordinates of origin for each component. Depending on these parameters, we can have a variety of solutions of the same order n. A further nontrivial fact is that these shifts are eigenvalue dependent and need to be considered as functions of κ:

$$\begin{aligned} x_j &= \sum_{m=1}^{\infty} \kappa^{2(m-1)} X_{jm} \\ &= X_{j1} + X_{j2}\kappa^2 + X_{j3}\kappa^4 + \cdots, \\ t_j &= \sum_{m=1}^{\infty} \kappa^{2(m-1)} T_{jm} \\ &= T_{j1} + T_{j2}\kappa^2 + T_{j3}\kappa^4 + \cdots, \end{aligned} \tag{3}$$

where $1 \leqslant j \leqslant n$. The conceptual subtlety here is that, although the terms with nonzero orders of κ in Eq. (3) vanish in the $\kappa \to 0$ limit, analysis and numerics prove that their coefficients X and T have a crucial effect in defining the structure of higher order solutions.

In the first order case, $n = 1$, only X_{11} and T_{11} have any effect on the structure of the wave function in the $\kappa \to 0$ limit. So, for this $(n = 1)$ solution (Peregrine soliton), we have

$$\begin{aligned} G_1 &= 4, \\ H_1 &= 8(x - X_{11}), \\ D_1 &= 1 + 4(x - X_{11})^2 + 4(t - T_{11})^2. \end{aligned} \tag{4}$$

All higher order terms in Eq. (3) can be ignored. These two constants describe a simple translation of the solution in Fig. 1(c) relative to the origin. On the other hand, simple analytic study shows that the second order rational solution must have $X_{11} = X_{21}$ and $T_{11} = T_{21}$. Otherwise $\psi_2 \to \psi_0 = e^{it}$ in the limit $\kappa \to 0$. Thus because such a requirement only involves a global shift of origin for all components, we can set $X_{j1} = T_{j1} = 0$ without loss of generality. Analytically, applying the $\kappa \to 0$ limit now produces the general second order $(n = 2)$ solution, described by

$$\begin{aligned} G_2 &= -\tfrac{1}{8}(5x^2 + t^2)(x^2 + t^2) - \tfrac{3}{16}(3x^2 + t^2) \\ &\quad + xx_d + tt_d + \tfrac{3}{128}, \\ H_2 &= -\frac{1}{4}x(x^2 + t^2)^2 - \frac{1}{8}x(x^2 - 3t^2) + \frac{15}{64}x \\ &\quad + \left(x^2 - t^2 - \frac{1}{4}\right)x_d + 2xtt_d, \end{aligned}$$

$$D_2 = \frac{1}{24}(x^2+t^2)^3 + \frac{1}{32}(3x^2-t^2)^2 + \frac{3}{128}(11x^2+3t^2) + \frac{3}{512} - \left(\frac{1}{3}x^3 - xt^2 + \frac{3}{4}x - \frac{2}{3}x_d\right)x_d - \left(x^2t - \frac{1}{3}t^3 + \frac{1}{4}t - \frac{2}{3}t_d\right)t_d, \quad (5)$$

where second order relative shifts are defined by the κ^2 coefficients of $x_1 - x_2$ and $t_1 - t_2$. Specifically

$$x_d = X_{12} - X_{22}, \qquad t_d = T_{12} - T_{22}. \quad (6)$$

When the relative shifts (x_d and t_d) between the components are zero, the resulting solution is an already known [13,33] second order rational solution with a single high maximum at the origin, shown in Fig. 2(a). When x_d and t_d are not zero, the second order peak breaks apart and, for sufficiently large second order shifts, forms a set of three first order rational solutions, the centers of which form an equilateral triangle. This solution is shown in Fig. 2(b). We have studied this form in detail [25] and can express the radius of the triangle's circumcircle in terms of x_d and t_d:

$$R \approx 2^{2/3}\left(x_d^2 + t_d^2\right)^{1/6}. \quad (7)$$

For the sake of comparison, we can relate the parameters γ and β found via the Wronskian methodology [18] with those of the current formalism by $\gamma = 2^5 x_d$ and $\beta = -2^5 t_d$.

As mentioned, analytically deriving general expressions for higher order rational solutions using the Darboux method is tedious, either by hand or with a computer. The Wronskian method appears to have had greater success generating these solutions [18,21]. However, incorporating the relative shift parameters this way is still difficult and has not been done.

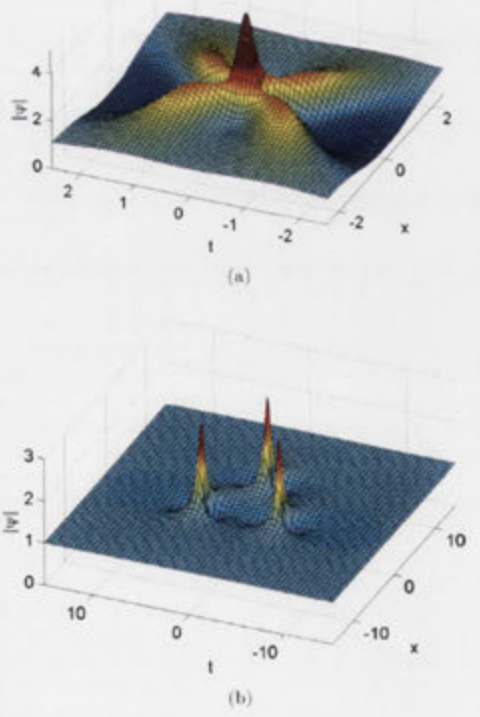

FIG. 2. (Color online) (a) Second order rational solution with zero shifts: $x_d = 0$ and $t_d = 0$. (b) Second order "rogue wave triplet" appears when $x_d = 5^2$ and $t_d = 0$.

III. HIGHER ORDER NUMERICAL RESULTS

Being a set of algebraic equations, the Darboux method can easily be converted into a numerical recursion procedure for any finite order n with eigenvalues and shifts as free adjustable parameters. It allows higher order rational solutions to be visualized in the $\kappa \to 0$ limit without presenting the cumbersome analytic expressions. Algebraic transformations can be done with high numerical accuracy to make the results indistinguishable from the rational solution. In fact, writing down the exact solutions would require many journal pages [18,21] and cannot be considered as a convenient way of presenting them.

In Fig. 3, we present higher order rational solutions, each with a single maximum at the origin, for $n = 3,4,5,6$. Analytical expressions for some of them have been presented earlier [14,21]. The maximum height of an order n rational solution is $2n + 1$ and the structure also has $n(n+1)/2 - 1$ local maxima on each side of the $x = 0$ line. Starting from large negative x, an observer of its evolution would witness a row of n small peaks, then a row of $n - 1$ larger peaks, then $n - 2$ peaks, etc., before the central high amplitude solitary wave appears. The process is then symmetrically reversed in x so that, at large x, the wave "disappears without a trace." Thus, as noted before [21], the number of local maxima for an order n WANDT is $n(n+1) - 1$. For example, from Fig. 3(b) ($n = 4$), we see that successive rows have four, three, two, one, two, three, and finally four peaks.

Naturally, applying shifts changes the profiles. As was analytically evident with orders $n = 1$ and 2, it is also clear from numerics that only one coefficient per AB component from Eq. (3) has any effect on a higher order solution in the $\kappa \to 0$ limit; namely X_{jn} or T_{jn}, where j is the component number and n is the order of the solution. Here, we limit ourselves to shifting only one of the components; specifically, we apply the x shift in Eq. (3) to the first ($\kappa_1 = \kappa$) component alone. In this case, the $n = 3$ structure is solely determined by the $X_{13}\kappa^4$ term, the $n = 4$ structure by $X_{14}\kappa^6$, and so on. In each case, the coefficients of lower order κ terms must be the same between all components, otherwise $\psi_n \to \psi_{n-2}$ in the $\kappa \to 0$ limit. As for the coefficients of higher order κ terms, they are irrelevant.

The resulting wave functions for orders $n = 3,4,5,6$ are shown in Fig. 4. Remarkably, all higher order solutions display a ring structure. We observe rings with five peaks in Fig. 4(a), seven peaks in Fig. 4(b), etc. All peaks within the ring are first order rational solutions, i.e., Peregrine solitons. Naturally, each individual first order rational solution is always oriented in the

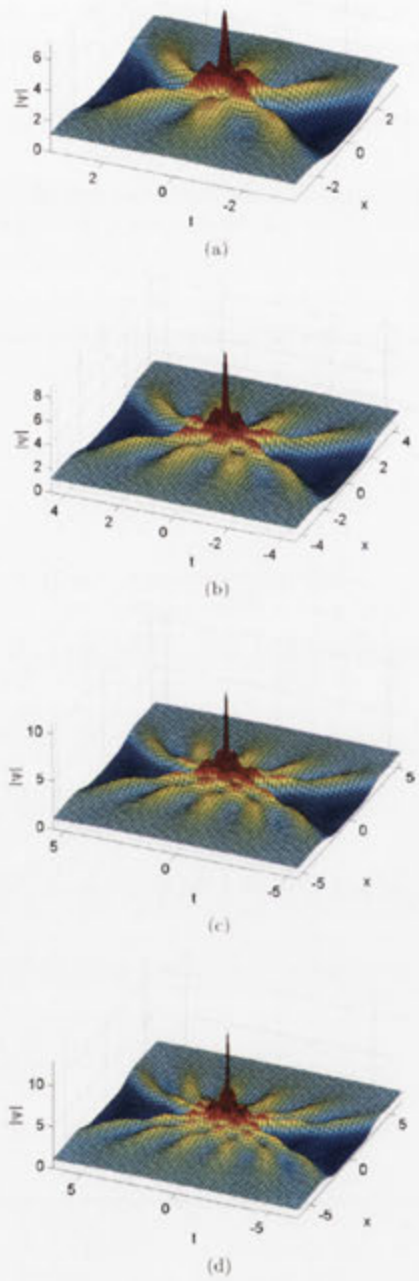

FIG. 3. (Color online) Higher order rational solutions with zero shifts, i.e., with its elementary components located at the origin. (a) The case of order $n = 3$. (b) $n = 4$. (c) $n = 5$. (d) $n = 6$.

same direction. Generally, the outer shell of an order n rational solution is composed of $2n - 1$ first order rational solutions. Evidently, the second order rogue wave triplet shown in Fig. 2(b) is the first in a series of higher order "shell" structures.

Another remarkable feature of these solutions is the presence of the central peak in each of them. Moreover, the central peak becomes more complicated with increasing n. When $n = 2$, the central peak is absent. When $n = 3$, the central peak is the same as the others, i.e., a first order rational solution. When $n = 4$, the central peak is more complicated. In fact, it is the $n = 2$ solution with zero shifts, i.e., the one shown in Fig. 2(a). All higher order solutions similarly display a central structure, which in each case is the order $n - 2$ rational solution with zero shifts. For example, the fifth order rational solution in Fig. 4(c) has a third order WANDT remaining in the middle of the structure. Likewise, after applying a shift proportional to κ^{10}, the sixth order rational solution shown in Fig. 4(d) has a fourth order rational solution in the middle. Generally, any sufficiently large shift moves $2n - 1$ first order rational solutions to its outer circular shell, leaving in the middle a WANDT of order $n - 2$.

Based on numerical evidence, we conjecture that the radius of the shell in the (x,t) plane for higher order structures follows a similar relation to Eq. (7), viz.

$$R \propto \left(X_{1n}^2 + T_{1n}^2\right)^{1/[2(2n-1)]}. \tag{8}$$

However, confirmation of a proportionality constant will require analytic expressions for the higher order wave functions. Furthermore, as the number of component shifts x_j that we can take to be nonzero is increased with n, additional relative shifts may split the central structure and create more shells.

IV. DISCUSSION: ROGUE WAVE "ATOMS"

Comparing our results with those of Matveev's group [15,17–20], published recently, our main achievements are as follows:

(1) We have found the relation between the shift parameters of the Darboux transformation scheme and the free parameters of the multirogue wave solutions that control their structure. These relations are important and far from being trivial.

(2) We have revealed the highly symmetric structure of multirogue wave solutions in the (x,t) plane. This is also a highly nontrivial result, as plotting the solutions does not reveal the symmetry immediately [15,17–20].

(3) We have found that, when we change their free parameters, the multirogue wave solutions split into substructures.

One way to interpret the wave functions in Fig. 4 is as atomic structures in the (x,t) plane with a "nucleus" and "electrons." Presently, this analogy is nothing other than visual. First, atoms are located in real space rather than in the (x,t) plane, unlike rogue waves of the NLSE. Second, real atoms with several shells are significantly more complicated. Thus this analogy still needs careful consideration, which may show that there is no real basis for it. Nevertheless, we cannot reject this attractive idea from the very beginning.

In order to see more similarities beyond the visual one, we note that, in a real atom, the first subshell s can have two electrons and each subsequent subshell has four more electrons than the previous subshell. Thus subshells p,d,f,g can have maxima of 6,10,14,18 electrons, respectively. So the nth full shell has $2 + 6 + \cdots + (4n - 2) = 2n^2$ electrons. Likewise, an order n rogue wave for even n has an increasing number of electrons in the shells. If the core of the rogue wave

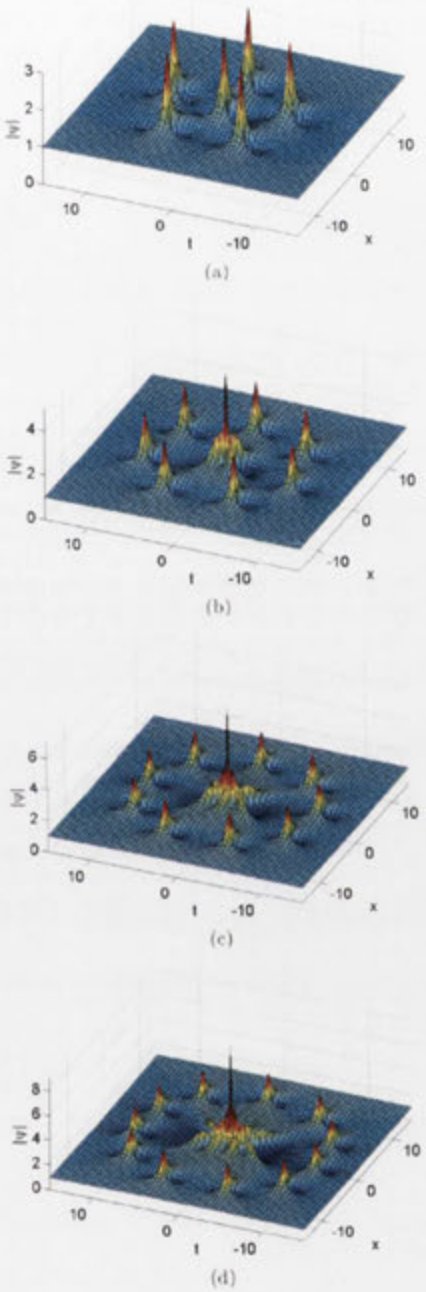

FIG. 4. (Color online) Higher order WANDTs with only the first component shifted. All $X_{1k} = 0$ unless specified. (a) Order 3 with $X_{13} = 5^4$. (b) Order 4 with $X_{14} = 5^6$. (c) Order 5 with $X_{15} = 5^8$. (d) Order 6 with $X_{16} = 5^{10}$.

cluster were to be expanded into several rings, it would be evident that the series in this case is $3 + 7 + \cdots + (2n - 1)$ with the total number of electrons being $n(n + 1)/2$. Similarly, for odd n the sum is $1 + 5 + \cdots + (2n - 1) = n(n + 1)/2$. Furthermore, the nature of this electron series is likely related to the denominator of the polynomial expression for the nth rogue wave, which is of order $n(n + 1)$ [14].

Curiously, there may also be some link with the nuclear shell model in that, if nuclear levels are labeled as $n = 1,2,3,\ldots$, then the number of states in level n is also $n(n + 1)$. Thus the analogies may actually be more profound than at first consideration. Further study may explain why the NLSE rogue wave cluster arranges itself in a regular fashion reminiscent of atomic shell theory.

With regard to experiment, a major application of these results might be found in optics or with deep water waves. Indeed, the simplest of these structures, namely the Peregrine soliton, has been recently observed in each of these cases [11,12]. These experiments clearly demonstrated that rogue wave solutions do exist and, moreover, the governing equation for these waves is indeed the NLSE. Using more complicated initial conditions in the corresponding experiments may lead to the observation of higher order structures described in the present work. Such experiments would confirm to what extent we can use the NLSE as a model for these waves. There is already no doubt that rogue wave triplets could be observed with ease as they essentially consist of three separated Peregrine solitons. For structures of higher order, such observations are more difficult but certainly worthy of trial. Taking into account that the new solutions are highly nontrivial, experiments will require significant effort to upgrade the capability of both controlled rogue wave production and detection. Nonetheless, we suggest that a progressive experimental program could feasibly generate circular rogue wave clusters within the next few years.

In some physical applications, e.g., optical self-focusing, both variables are spatial. In such a case, the whole geometric structure appears in two-dimensional space. On the other hand, in problems related to wave propagation, the time and space variables are related through the group velocity and can be swapped. Thus we can see these solutions either in a (t,t) or (x,x) plane. Perhaps this is a clearer way of understanding the beauty of the geometric structure of these formations.

In conclusion, we have studied families of higher order rational solutions of the NLSE with free real parameters. We have shown that these parameters are responsible for the "diffusion" of the central peak of the solution into clusters with a high level of symmetry. The clusters are arranged in circular shells, similar to the structure of electron shells in atoms.

ACKNOWLEDGMENTS

The authors acknowledge the support of the Australian Research Council (Discovery Project No. DP110102068). N.A. and A.A. acknowledge the support from the Volkswagen Stiftung. N.A. acknowledges support from the Alexander von Humboldt Foundation.

APPENDIX: THE DARBOUX METHOD

The NLSE arises from the compatibility of the following linear equations:

$$\frac{\partial R}{\partial t} = lJR + UR, \quad \frac{\partial R}{\partial x} = l^2 JR + lUR + \frac{1}{2}VR, \quad \text{(A1)}$$

with matrices

$$U = \begin{pmatrix} 0 & i\psi^* \\ i\psi & 0 \end{pmatrix}, \quad V = \begin{pmatrix} -i|\psi|^2 & \frac{\partial \psi^*}{\partial t} \\ -\frac{\partial \psi}{\partial t} & i|\psi|^2 \end{pmatrix},$$

$$J = \begin{pmatrix} i & 0 \\ 0 & -i \end{pmatrix}, \quad R = \begin{pmatrix} r \\ s \end{pmatrix}, \tag{A2}$$

and l as a complex eigenvalue.

Choosing a seeding solution of

$$\psi_0 = e^{ix} \tag{A3}$$

and restricting l to being purely imaginary, the system in Eq. (A1) is compatible with $\psi = \psi_0$ when $r = r_{1j}$ and $s = s_{1j}$, defined as

$$r_{1j} = 2ie^{-ix/2}\sin(A_{jr} + iA_{ji}),$$
$$s_{1j} = 2e^{ix/2}\cos(B_{jr} + iB_{ji}). \tag{A4}$$

The subscripts r and i refer to real and imaginary parts, respectively. The functions A and B are then given by

$$A_{jr} = \frac{1}{2}\left[\arccos\left(\frac{\kappa_j}{2}\right) + (t - t_j)\kappa_j - \frac{\pi}{2}\right],$$
$$B_{jr} = \frac{1}{2}\left[-\arccos\left(\frac{\kappa_j}{2}\right) + (t - t_j)\kappa_j - \frac{\pi}{2}\right],$$
$$A_{ji} = B_{ji} = \frac{1}{2}\left[(x - x_j)\kappa_j\sqrt{1 - \frac{\kappa_j^2}{4}}\right], \tag{A5}$$

where $\kappa_j = 2\sqrt{1 + l_j^2}$. The j subscript indicates that eigenvalue l_j and coordinate shifts (x_j, t_j) are free parameters. For example, $j = 4$ refers to the fourth set of eigenvalue and shift parameters.

A first order solution to the system in Eq. (A1) incorporates only one chosen set of free parameters and its corresponding r and s equations from Eq. (A4), denoted by $j = 1$. The first order wave function is thus expressed as

$$\psi_1 = \psi_0 + \frac{2(l_1^* - l_1)s_{11}r_{11}^*}{|r_{11}|^2 + |s_{11}|^2}. \tag{A6}$$

An order $n > 1$ solution requires higher order versions of the expressions for r and s. These are recursively generated [24,32] by

$$\begin{aligned} r_{np} = {} & [(l_{n-1}^* - l_{n-1})s_{n-1,1}^* r_{n-1,1}s_{n-1,p+1} \\ & + (l_{p+n-1} - l_{n-1})|r_{n-1,1}|^2 r_{n-1,p+1} \\ & + (l_{p+n-1} - l_{n-1}^*)|s_{n-1,1}|^2 r_{n-1,p+1}] \\ & /(|r_{n-1,1}|^2 + |s_{n-1,1}|^2), \\ s_{np} = {} & [(l_{n-1}^* - l_{n-1})s_{n-1,1}r_{n-1,1}^* r_{n-1,p+1} \\ & + (l_{p+n-1} - l_{n-1})|s_{n-1,1}|^2 s_{n-1,p+1} \\ & + (l_{p+n-1} - l_{n-1}^*)|r_{n-1,1}|^2 s_{n-1,p+1}] \\ & /(|r_{n-1,1}|^2 + |s_{n-1,1}|^2). \end{aligned} \tag{A7}$$

The p subscript in Eq. (A7) is used purely for enumeration and does not necessarily refer to a particular set of parameters. For example, the second order function r_{21} involves the first order sets r_{11}, s_{11}, r_{12}, and s_{12}. Similarly, the third order function r_{31} involves the second order functions r_{21}, s_{21}, r_{22}, and s_{22}, which, in turn, are based on r_{11}, s_{11}, r_{12}, s_{12}, r_{13}, and s_{13} at the lowest order of recursion. This way, Eq. (A7) allows n sets of free parameters to be incorporated into an order n solution. The diagram in Fig. 2.2 of the *Solitons* book [32] can be of use in representing this sequence of calculations. Then, the order n NLSE solution is generated through recursion by

$$\psi_n = \psi_{n-1} + \frac{2(l_n^* - l_n)s_{n1}r_{n1}^*}{|r_{n1}|^2 + |s_{n1}|^2}. \tag{A8}$$

In this work we are mainly interested in the specific case of the $\kappa_j \to 0$ limit. Then all unequal κ_j are expressed in terms of a common variable such as κ. The numerator and denominator from every iteration of Eq. (A8) is then Taylor expanded in terms of κ and only the lowest order is retained. This results in "rational" solutions, such as Eqs. (4) and (5).

[1] A. R. Osborne, *Nonlinear Ocean Waves And The Inverse Scattering Transform* (Academic Press, New York, 2010).
[2] E. Pelinovsky and C. Kharif, *Extreme Ocean Waves* (Springer, Berlin, Heidelberg, 2008).
[3] C. Garrett and J. Gemmrich, Phys. Today **62**(6), 62 (2009).
[4] D. R. Solli, C. Ropers, P. Koonath, and B. Jalali, Nature (London) **450**, 1054 (2007).
[5] M. Shats, H. Punzmann, and H. Xia, Phys. Rev. Lett. **104**, 104503 (2010).
[6] V. B. Efimov, A. N. Ganshin, G. Kolmakov, P. McClintock, and L. Mezhov-Deglin, Eur. Phys. J. Spec. Top. **185**, 181 (2010).
[7] Y. V. Bludov, V. V. Konotop, and N. Akhmediev, Phys. Rev. A **80**, 033610 (2009).
[8] F. T. Arecchi, U. Bortolozzo, A. Montina, and S. Residori, Phys. Rev. Lett. **106**, 153901 (2011).
[9] D. Peregrine, J. Aust. Math. Soc. Series B **25**, 16 (1983).
[10] V. Shrira and V. Geogjaev, J. Eng. Math. **67**, 11 (2010).
[11] B. Kibler, J. Fatome, C. Finot, G. Millot, F. Dias, G. Genty, N. Akhmediev, and J. M. Dudley, Nat. Phys. **6**, 790 (2010).
[12] A. Chabchoub, N. P. Hoffmann, and N. Akhmediev, Phys. Rev. Lett. **106**, 204502 (2011).
[13] N. Akhmediev, A. Ankiewicz, and M. Taki, Phys. Lett. A **373**, 675 (2009).
[14] N. Akhmediev, A. Ankiewicz, and J. M. Soto-Crespo, Phys. Rev. E **80**, 026601 (2009).
[15] P. Dubard, P. Gaillard, C. Klein, and V. Matveev, Eur. Phys. J. Spec. Top. **185**, 247 (2010).
[16] A. Ankiewicz, P. Clarkson, and N. Akhmediev, J. Phys. A **43**, 122002 (2010).
[17] P. Gaillard, preprint: halshs-00536287, version 1 - 15 Nov. 2010.
[18] P. Gaillard, preprint: hal-00573955, version 2 - 7 Apr. 2011.
[19] P. Gaillard, J. Phys. A **44**, 435204 (2011).
[20] P. Dubard and V. B. Matveev, Nat. Hazards Earth Syst. Sci. **11**, 667 (2011).

[21] P. Gaillard, preprint: hal-00589556, version 1 - 29 Apr. 2011.

[22] V. B. Matveev and M. Salle, *Darboux Transformations and Solitons* (Springer-Verlag, Berlin, Heidelberg, 1991).

[23] N. Akhmediev and N. V. Mitskevich, IEEE J. Quantum Electron. **27**, 849 (1991).

[24] N. Akhmediev, J. M. Soto-Crespo, and A. Ankiewicz, Phys. Lett. A **373**, 2137 (2009).

[25] A. Ankiewicz, D. J. Kedziora, and N. Akhmediev, Phys. Lett. A **375**, 2782 (2011).

[26] N. Akhmediev, V. M. Eleonskii, and N. E. Kulagin, Teor. Math. Fiz. (USSR) **72**, 183 (1987) [Theor. Math. Phys. **72**, 809 (1988)].

[27] K. B. Dysthe and K. Trulsen, Phys. Scr. **T82**, 48 (1999).

[28] I. Ten and H. Tomita, Reports of RIAM Symposium No. 17SP1-2, Chikushi Campus, Kyushu University, Kasuga, Fukuoka, Japan, March 10–11, 2006.

[29] D. Clamond, M. Francius, J. Grue, and C. Kharif, Eur. J. Mech. B **25**, 536 (2006).

[30] V. V. Voronovich, V. I. Shrira, and G. Thomas, J. Fluid Mech. **604**, 263 (2008).

[31] N. Akhmediev, V. I. Korneev, and N. V. Mitskevich, Zh. Eksp. Teor. Fiz. **94**, 159 (1988) [Sov. Phys. JETP **67**, 89 (1988)].

[32] N. Akhmediev and A. Ankiewicz, *Solitons: Nonlinear Pulses and Beams*, Optical and Quantum Electronics Vol. 5 (Chapman & Hall, London, 1997), Chaps. 3 and 4.

[33] N. Akhmediev, V. M. Eleonskii, and N. E. Kulagin, Zh. Eksp. Teor. Fiz. **89**, 1542 (1985) [Sov. Phys. JETP **62**, 894 (1985)].

Epilogue

Unlike the case of rogue triplets [1], a structure that had been identified several times before in both serendipitous [65] and intentional [85] manner, the discovery of circular clusters presented in this work [2] genuinely seems to have no precedent in the literature. This is in a sense unusual, as both the solution-generating procedure in this thesis and the alternative 'Wronskian' method [88] are, at their core, based on Darboux transformation theory [84]. It is then arguable that the advantages of either one must arise specifically from how spatiotemporal perturbations are applied to a compound rogue wave.

Certainly, in this study, component functions are treated as representations of the components themselves, with the relevant 'tuning' parameters considered physically as translations in space and time. It was thus inevitable that one component would be 'shifted' in isolation to all others, resulting in the discovery of circular clusters. Presumably, this physics-based perspective is lost in the mix when dealing with abstract mathematical parameters obfuscated by Wronskian matrices. However, in retrospect, it appears that the perturbations in the Wronskian implementation have their own mathematical elegance. For instance, so-called 'triangular rogue wave cascades' were a simple result of this alternative method [86], seemingly so trivial that they were only mentioned in passing. In contrast, discovering them via the Darboux scheme in this thesis proved far more complicated. They are presented and discussed in Chapter 4.

In any case, the revelation of these structures appears to have had lasting impact in the field, contributing to a surge of interest in identifying numerous multi-rogue wave structures [71, 72, 89, 90]. The clusters are frequently cited as solutions that appear not just for the NLSE but also in other nonlinear systems [73, 91, 92], even though the spatiotemporal arrays are generally somewhat distorted in these cases. This ubiquity is in itself interesting and is touched on in Chapter 8. Indeed, to date, not much is known as to why their geometry is so perfectly circular for the particular scaling of the NLSE adopted in this thesis [93]. They are valid solutions mathematically, but it is unclear why the epicentres of modulational instability are physically arranged in such a manner. This peculiar rotational symmetry arises even when examining the first-order Peregrine breather more closely. For instance, it is possible to define the momentum of a wave [94] as

$$P = \frac{1}{2i}\int\left(\psi^*\frac{\partial\psi}{\partial t} - \psi\frac{\partial\psi^*}{\partial t}\right)dt \tag{2.1}$$

in optical convention, with ψ as a solution of the NLSE. In fact, this P is a conserved quantity for the nonlinear equation. It follows then that $\delta P = (\partial P/\partial t)\,\delta t$ can very loosely be considered as the momentum present in a small portion of the wave with width δt. Shaded contours of this localised momentum are shown in Fig. 2.1a, indicating how the energy in the wave is drawn into the peak of the Peregrine breather at the origin, before the flow symmetrically reverses itself for $x > 0$. Sequential derivatives of δP with respect to the evolution variable further describe the dynamics

of the rogue wave to an ever finer degree. Remarkably, as displayed in the rest of Fig. 2.1, rotational symmetries are readily apparent in the contour plots. While these patterns only become more complicated for multi-rogue waves, this basic result hints that a concerted study of NLSE energetics may be required to fully comprehend the arrangements of circular rogue wave clusters.

There are also other interesting leads to follow from here. Indeed, the prediction made about the existence of multi-ring clusters would eventually be proved true by both the research within this thesis [6] and an independent investigation [72], as is further discussed in Chapter 6. These structures can be considered as multi-shell extensions of the 'atom' analogy, although caution should still be applied when drawing links. Granted, there are good reasons to seek connections between particle and wave phenomena, particularly as the field of photonics was conceived in such a manner [95], but the dimensional issues of the NLSE have not yet been accounted for. On the other hand, with traditional solitons frequently favoured as particle models [96, 97], rogue waves may yet have a relation to solitonic collisions. This speculation is expanded upon in Chapter 7.

Theory aside, the applications for circular rogue wave clusters appear promising. With both fused rogue waves [23, 98] and a fissioned triplet [77] recently created inside a water tank, there is no reason to doubt the generation of higher-order waveforms in the near future.

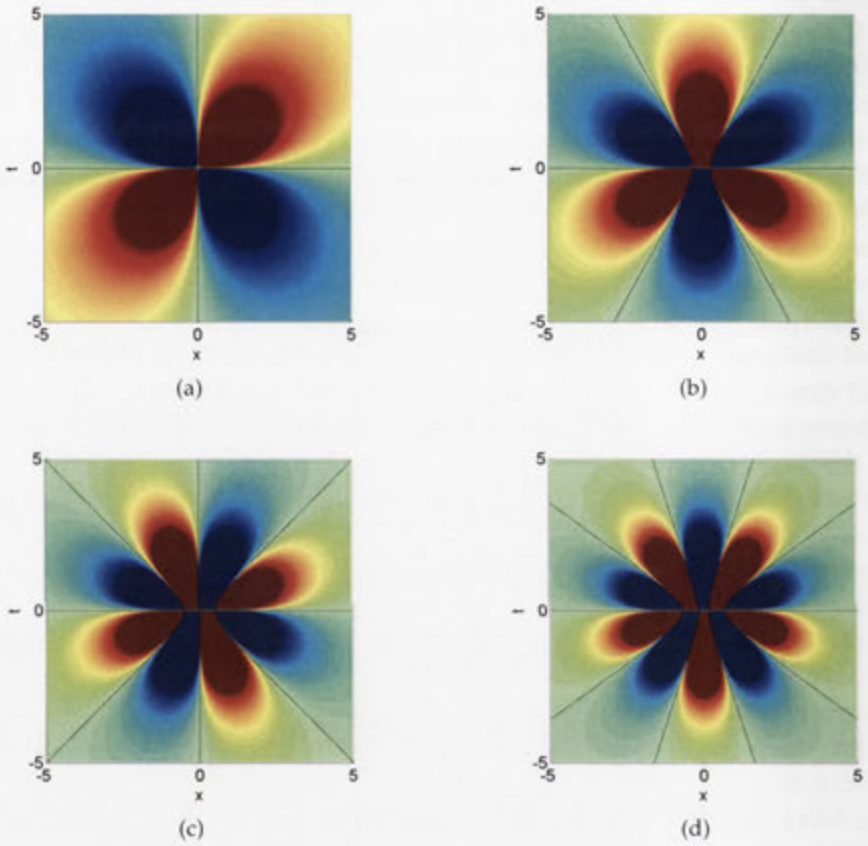

Figure 2.1: Contour plots of 'localised' momentum and relevant evolution-variable derivatives with regard to a first-order rogue wave solution (i.e. Fig. 1c in the paper [2]). Red colours denote positive values (an upward direction) and blue colours denote negative values (a downward direction). Colour bars are omitted as the spectrum is proportional to $\partial P/\partial t$ and the relevant x derivatives, irrespective of the δt value. Black lines mark zero contours. (a) Localised momentum, δP. (b) Localised force, $\delta F = \delta P_x$. (c) Localised 'yank', δP_{xx}. (d) Localised 'tug', δP_{xxx}.

Chapter 3

Second-order NLSE Breather Solutions in the Degenerate and Rogue Wave Limits

Prologue

The discovery of circular rogue wave clusters [2], as detailed in Chapter 2, revealed that the evolution dynamics of high-order spatiotemporally localised NLSE solutions were much richer than previously expected. However, the novel structures were still but the result of a numerically automated procedure, viz. the Darboux scheme [84]. Little was yet understood about why Peregrine breathers arranged themselves in such a way. In particular, naive reasoning still suggested that a rogue wave of order n should have been constructed from n individual first-order structures, rather than the $n(n+1)/2$ Peregrine breathers that inductive logic showed was actually the case. Certainly, with regard to traditional multi-soliton wavefunctions of order n [87], it is relatively simple to identify the influence of n individual solitons.

Ultimately, the key to resolving this seeming paradox rests with the fact that the Darboux scheme technically superimposes breathers of general type, as opposed to Peregrine breathers specifically. This difference turns out to be crucial, as the 'zero modulation-frequency' rogue wave limit is only ever applied at the very end following the nonlinear superposition process. Indeed, every spatiotemporally localised structure in the circular clusters paper [2] is but one complicated incident of modulational instability that has been mathematically extracted from an even more intricate wavetrain of crests and troughs. So, while a solitary AB or KM soliton does indeed leave behind a single rogue wave peak when its periodic modulation stretches out to the limit, interaction with a secondary breather in the same domain changes the rules.

This apparent asymmetry between components is yet another consequence of Darboux transformation theory, in that no two individual components can have the same shape-determining eigenvalue or corresponding modulation frequency. It is as true for breathers as it is for solitons [99, 100]. This inequality must hold all the way down to the rogue wave limit, even as both frequencies approach a value of zero, otherwise the compound solution becomes effectively undefined. All the same, it is still of physical interest to examine what actually occurs on the verge of eigenvalue

equality, known as the degenerate limit. No true understanding of high-order NLSE rogue wave structures can be attained without first comprehending the intricacies of the breather solutions from which they are extracted.

This chapter, as a published manuscript [3], explicitly catalogues all axially-aligned second-order breathers of the NLSE. They are derived via the Darboux method and, in contrast to most of the numerical results in this thesis, their limits are applied analytically. This set of solutions includes:

- The general two-breather wavefunction, which allows for various frequency ratios between components.
- The hybrid two-breather wavefunction, where isolated application of the rogue wave limit transforms one component into a Peregrine breather.
- The limit case of degeneracy, where modulation frequencies for two components are effectively identical.
- The fused and fissioned second-order rogue waves that remain when the rogue wave limit is applied to the degenerate case.

Subsequently, the most significant conclusion to be drawn from this paper is that the NLSE does not permit two identical first-order modulation crests to exist together in isolation of any other plane-wave perturbation. Accordingly, the symmetry required of degeneracy is compensated for by one excess peak being drawn into the fusion of a triplet [1]. However, this is parametrically a very unstable situation and, even in the case of breathers, anything more than a select infinitesimal shift will repel the breathers so that they move away, eventually becoming infinitely far apart in the spatiotemporal domain.

PHYSICAL REVIEW E **85**, 066601 (2012)

Second-order nonlinear Schrödinger equation breather solutions in the degenerate and rogue wave limits

David J. Kedziora,* Adrian Ankiewicz, and Nail Akhmediev
Optical Sciences Group, Research School of Physics and Engineering, The Australian National University, Canberra ACT 0200, Australia
(Received 17 January 2012; published 4 June 2012)

We present an explicit analytic form for the two-breather solution of the nonlinear Schrödinger equation with imaginary eigenvalues. It describes various nonlinear combinations of Akhmediev breathers and Kuznetsov-Ma solitons. The degenerate case, when the two eigenvalues coincide, is quite involved. The standard inverse scattering technique does not generally provide an answer to this scenario. We show here that the solution can still be found as a special limit of the general second-order expression and appears as a mixture of polynomials with trigonometric and hyperbolic functions. A further restriction of this particular case, where the two eigenvalues are equal to i, produces the second-order rogue wave with two free parameters considered as differential shifts. The illustrations reveal a precarious dependence of wave profile on the degenerate eigenvalues and differential shifts. Thus we establish a hierarchy of second-order solutions, revealing the interrelated nature of the general case, the rogue wave, and the degenerate breathers.

DOI: 10.1103/PhysRevE.85.066601 PACS number(s): 05.45.Yv, 47.20.Ky, 42.65.−k

I. INTRODUCTION

Breather solutions of certain nonlinear equations are presently well accepted as potential prototypes for the notorious rogue waves in the ocean [1–9] and other fields of physics [10–12]. Breathers develop due to the instability of small amplitude perturbations that may grow in size to disastrous proportions. As the perturbations are usually chaotic and may contain many frequencies in their spectra, an important issue is our ability to construct higher-order solutions that grow as a nonlinear superposition of several lowest-order breathers [13,14]. Numerically, such solutions can be constructed with ease, and this has been done in a number of previous publications [14,15]. Analytic expressions for these solutions are another matter. They are usually cumbersome and admit many forms. Finding the simplest one is always a challenge.

In this work, we provide the two-breather solution of the nonlinear Schrödinger equation (NLSE) in explicit form. The solution has two eigenvalues as variable parameters of the breathers, thus allowing for a variety of particular cases. Of special interest is the case when the two eigenvalues coincide. The answer provided by the standard inverse scattering technique then becomes undefined. Nevertheless, the solution still does exist but requires special methods to reveal it. This procedure is analogous to the method employed with two-soliton solutions [16,17] where the degenerate case also requires a special approach. These techniques are highly nontrivial, but the final results are usually simpler than we may expect. They appear as a mixture of polynomials with trigonometric and hyperbolic functions.

The general solution with one, two, or more eigenvalues can be obtained using a variety of techniques including Darboux transformations [18]. This is the methodology that we use in this work. Having an explicit analytic solution has the advantage that we can also consider all particular cases analytically, including the rational solutions that have been studied in a number of recent works [19–24]. These include higher-order rogue waves [19,20] and their varied forms [21–27]. In our present approach, rational solutions are just one of the limiting cases of the two-breather solution. A superposition of breathers that create a rogue wave can also be considered [14]. Thus our approach here is quite general. It provides a comprehensive understanding of second-order NLSE breather solutions and their hierarchical nature.

The NLSE can be written in dimensionless form as

$$i\frac{\partial\psi}{\partial x}+\frac{1}{2}\frac{\partial^2\psi}{\partial t^2}+|\psi|^2\psi=0. \tag{1}$$

The wave function $|\psi(x,t)|$ in Eq. (1) commonly describes the wave envelope. In fiber optic applications [12], the variable x is the distance along the fiber while t is the retarded time in the frame moving with the pulse group velocity. On the other hand, in water wave applications [9], x is the dimensionless time while t is the distance in the frame moving with the group velocity. Such a difference is more related to traditions in each field rather than to any particular physical meaning. Simple linear transformation between the variables involving the group velocity allows us to change the equation and variables from one form to another.

There is a class of first-order solutions to Eq. (1), pertaining to modulation instability [28], that can be described by a complex eigenvalue l [29]. The real part of the eigenvalue represents the angle that the one-dimensionally localized solutions form with the x axis, and the imaginary part characterizes the frequency of periodic modulation. A variety of different forms for this solution has been given in several publications by different authors [14,30–33]. The case of complex eigenvalues is rather involved and numerical results [15] may be easier to comprehend than analytic solutions. In this work, we restrict our analysis to purely imaginary eigenvalues, thus allowing us to present and analyze the second-order solutions in a relatively simple way.

The general form of the first-order breather solution [34] is

$$\psi=\left[\frac{\kappa^2\cosh\delta(x-x_1)+2i\kappa\nu\sinh\delta(x-x_1)}{2[\cosh\delta(x-x_1)-\nu\cos\kappa(t-t_1)]}-1\right]e^{it}, \tag{2}$$

*djk105@rsphysse.anu.edu.au

where $\nu = \mathrm{Im}(l)$, $\kappa = 2\sqrt{1+l^2}$, and both x_1 and t_1 serve as coordinate shifts from the origin. The dependent variable $\delta = \kappa\nu$ in this expression is the growth rate of modulation instability; this is the process occurring as the plane wave evolves from a small periodic perturbation at $x = -\infty$.

When $0 < \nu < 1$ and κ is real, the solution is a t-periodic wave function that is localized in x, currently known as an Akhmediev breather (AB) [2,6,7]. This solution has been illustrated earlier in Fig. 1(a) of Ref. [27]. On the other hand, when $\nu > 1$ and κ is imaginary, the trigonometric (dependent on t) and hyperbolic (dependent on x) functions in Eq. (2) convert to their analogues via the relations

$$\sinh(z) = -i\sin(iz) \quad \text{and} \quad \cosh(z) = \cos(iz). \tag{3}$$

Taking into account these transformations, we obtain a soliton solution in the following form:

$$\psi = \left[\frac{-p^2\cos\Omega(x-x_1) - 2ip\nu\sin\Omega(x-x_1)}{2[\cos\Omega(x-x_1) - \nu\cosh p(t-t_1)]} - 1\right]e^{ix}, \tag{4}$$

where $\kappa = ip$, $p = 2\sqrt{\nu^2-1}$, and $\delta = i\Omega$, $\Omega = p\nu$. This is a soliton on a background, localized in t and periodic in x. It is known as a Kuznetsov [35] or Ma [36] (KM) soliton and has previously been presented in Fig. 1(b) of Ref. [27].

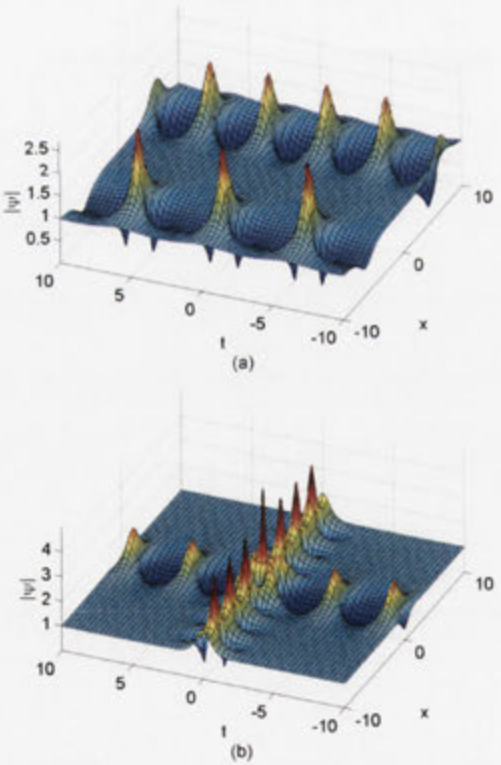

FIG. 1. (Color online) Various forms of second-order NLSE solution with different eigenvalues l_j. (a) Nonlinear superposition of two ABs with $l_1 = 0.65i$ and $l_2 = 0.85i$. Finite shifts are $x_1 = 5$ and $x_2 = -5$. (b) An AB with $l_1 = 0.65i$ crossing a KM soliton with $l_2 = 1.35i$.

Equations (2) and (4) represent an AB and a KM soliton, respectively, with the frequency parameters κ and Ω being real values in each case. One is the analytic continuation of the other when the parameter ν passes through the point 1. Each solution can be written in the general form below with real G_n, H_n, and D_n [see Eq. (5)]. In what follows, we take this fact into account and assume, in several equations below, that coefficients may take real or imaginary values, thus avoiding the need to explicitly present several real-coefficient versions of the same solution. When loaded into modern software such as MATLAB, the assumption of complex coefficients allows these equations to be computed correctly without the need for further specifications.

In the nontrivial limit, when $\nu \to 1$ or $\kappa \to 0$, the above expressions become undefined. However, this problem can be resolved using l'Hôpital's rule. Then, the period of either solution goes to infinity and the resulting wave function is the Peregrine soliton localized in both x and t. It was shown earlier in Fig. 1(c) of Ref. [27]. This solution is also known as a first-order rogue wave. Using the general form

$$\psi_n(x,t) = \left[(-1)^n + \frac{G_n + i\,H_n}{D_n}\right]e^{ix} \tag{5}$$

to represent a NLSE solution of order n, this rational solution has the values for G_1, H_1, and D_1 given by

$$\begin{aligned} &G_1 = 4, \quad H_1 = 8(x-x_1), \\ &D_1 = 1 + 4(x-x_1)^2 + 4(t-t_1)^2. \end{aligned} \tag{6}$$

NLSE breather solutions take the above simple forms only when the real part of the eigenvalues is zero. The general case of complex eigenvalues is significantly more complicated, but the method and low-order analytic results have previously been presented (see the appendix of Ref. [14]).

II. TWO-BREATHER SOLUTION IN GENERAL FORM

Various methods exist for generating higher-order NLSE solutions that exist on a background plane wave. We employ the recursive Darboux method [13,18], which nonlinearly superimposes distinct components of AB or KM soliton form. Each first-order component j in the higher-order solution is described by the (imaginary) eigenvalue l_j, the modulation frequency $\kappa_j = 2\sqrt{1+l_j^2}$, and a shifted point of origin (x_j, t_j). A detailed step-by-step description of this technique has been presented previously (see the appendix of Ref. [27]). For convenience, we define $x_{sj} = x - x_j$ and $t_{sj} = t - t_j$ as shifted variables.

With these parameters, we find that the general solution can be written in the same form as Eq. (5), but with the values for G_2, H_2, and D_2 given by

$$\begin{aligned} G_2 = -\left(\kappa_1^2 - \kappa_2^2\right)\Bigg(&\frac{\kappa_1^2\delta_2}{\kappa_2}\cosh(\delta_1 x_{s1})\cos(\kappa_2 t_{s2}) \\ &- \frac{\kappa_2^2\delta_1}{\kappa_1}\cosh(\delta_2 x_{s2})\cos(\kappa_1 t_{s1}) \\ &- \left(\kappa_1^2 - \kappa_2^2\right)\cosh(\delta_1 x_{s1})\cosh(\delta_2 x_{s2})\Bigg). \end{aligned}$$

$$
\begin{aligned}
H_2 = -2\left(\kappa_1^2-\kappa_2^2\right)\Bigg(&\frac{\delta_1\delta_2}{\kappa_2}\sinh(\delta_1 x_{s1})\cos(\kappa_2 t_{s2})\\
&-\frac{\delta_1\delta_2}{\kappa_1}\sinh(\delta_2 x_{s2})\cos(\kappa_1 t_{s1})\\
&-\delta_1\sinh(\delta_1 x_{s1})\cosh(\delta_2 x_{s2})\\
&+\delta_2\sinh(\delta_2 x_{s2})\cosh(\delta_1 x_{s1})\Bigg),\\
D_2 = 2\left(\kappa_1^2+\kappa_2^2\right)&\frac{\delta_1\delta_2}{\kappa_1\kappa_2}\cos(\kappa_1 t_{s1})\cos(\kappa_2 t_{s2})\\
&+4\delta_1\delta_2\Big(\sin(\kappa_1 t_{s1})\sin(\kappa_2 t_{s2})\\
&+\sinh(\delta_1 x_{s1})\sinh(\delta_2 x_{s2})\Big)\\
&-\left(2\kappa_1^2-\kappa_1^2\kappa_2^2+2\kappa_2^2\right)\cosh(\delta_1 x_{s1})\cosh(\delta_2 x_{s2})\\
&-2\left(\kappa_1^2-\kappa_2^2\right)\Bigg(\frac{\delta_1}{\kappa_1}\cos(\kappa_1 t_{s1})\cosh(\delta_2 x_{s2})\\
&-\frac{\delta_2}{\kappa_2}\cos(\kappa_2 t_{s2})\cosh(\delta_1 x_{s1})\Bigg),
\end{aligned}
\tag{7}
$$

where the instability growth rate for each component is $\delta_j = \kappa_j\sqrt{4-\kappa_j^2}/2$. A special case of this solution, where the two frequencies of modulation are harmonics of each other, has been given previously in Ref. [34]. We stress here that the two frequencies are independent parameters of the solution. Moreover, this present solution includes both ABs and KM solitons in any combination. To have an explicit real-parameter form for the cases when one or two values of $\nu_j = \mathrm{Im}(l_j)$ are greater than 1 (or the corresponding κ_j values are imaginary), we can again apply the relations in Eq. (3) to Eq. (7).

Thus, within the set of solutions with purely imaginary eigenvalues, Eqs. (5) and (7) are capable of describing a variety of possible second-order cases. For example, the case of one AB developing with a time delay after another is shown in Fig. 1(a), where both have different modulation frequencies. Alternatively, the intersection of an AB with a KM soliton is shown in Fig. 1(b). These two examples demonstrate that our second-order solution is a versatile tool for modeling the nonlinear superposition of two arbitrary ABs, KM solitons, or their combinations. This idea has previously been explored with the concept of rogue waves being formed from colliding ABs [14]. Despite the fact that our present solution is a particular case of complex eigenvalues, it is presented here in a simple explicit analytic form. Two more examples are shown in Fig. 2. These are combinations of two ABs located at the same position in x and t, but with different frequencies.

Generally, second-order solutions of the NLSE do not admit two equal eigenvalues, otherwise the analytic expressions become undefined. Our present solution given by Eqs. (5) and (7) is not an exception. Moreover, none of the eigenvalues in the above expressions can be equal to i. It can easily be seen that in these cases, G_2, H_2, and D_2 are zero, and the analytic expression has to be further modified in order to be presented in explicit form.

These problems are complicated but can be surmounted by applying analytic limits. As demonstrated for the first-order solution in Sec. I, taking the limit $l_j \to i$ is the key to accessing important rational rogue wave solutions. In order to avoid the case of equal eigenvalues, we can, as in previous work [27], choose to set $\kappa_j = j\kappa$ and then apply the $\kappa \to 0$ limit. This trick effectively extends the period of the wave function shown in Fig. 2(a) to infinity, leaving behind only the central second-order rogue wave peak. This technique ensures that the component eigenvalues are distinct all the way to the $l_j = i$ limit.

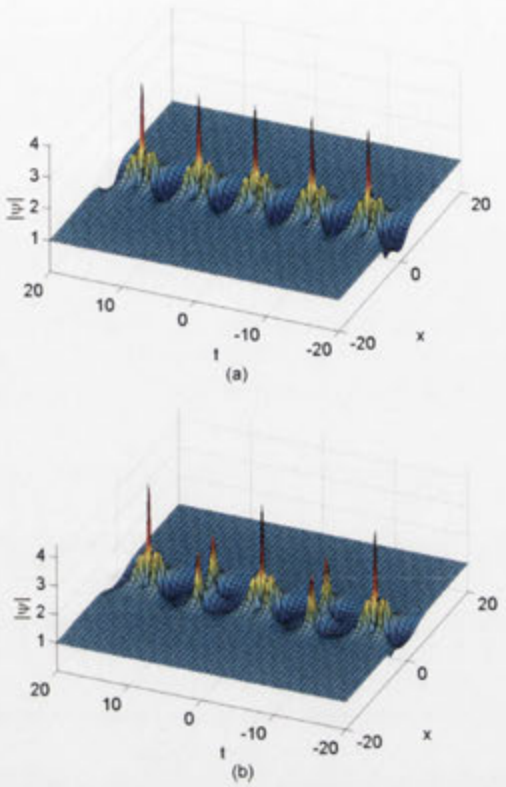

FIG. 2. (Color online) Nonlinear superposition of two ABs with two different modulation frequencies κ_j. (a) The frequency ratio is 2 : 1 with $\kappa_1 = 0.8$ and $\kappa_2 = 1.6$. (b) The frequency ratio is 3 : 2 with $\kappa_1 = 0.8$ and $\kappa_2 = 1.2$.

Notably, this technique for finding the rational limit works for any ratio of κ_j that is not one-to-one. As acknowledged in our previous work [26], a second-order rogue wave is generally built from three first-order Peregrine solitons. Therefore, enforcing a default 2 : 1 ratio with $\kappa_2 = 2\kappa_1$ allows us to obtain a solution where two component ABs form first-order triplets that merge into second-order peaks, provided that they share the same origin. This case is shown in Fig. 2(a). In contrast, a 3 : 2 ratio with $\kappa_2 = 1.5\kappa_1$, shown in Fig. 2(b), forms a series of triplets, which are merged together, alternating with distinct doublets. Similar structures repeating along the x axis appear in the KM soliton regime, although we caution that the integer ratios in this situation must be applied to $\delta_1 : \delta_2$ (or $\Omega_1 : \Omega_2$ in the real-parameter form), not $\kappa_1 : \kappa_2$. As Eq. (4) shows, this is because a KM soliton is periodic in x with a frequency of

$\Omega = -i\delta$ rather than κ. Nevertheless, in either case, the $\kappa \to 0$ limit isolates the single centrally located second-order rogue wave.

To see this merging of the triplet in greater detail, we present another particular case generated from the general two-breather solution in Eq. (7). This is the nonlinear superposition of an AB or a KM soliton with a Peregrine soliton and can be generated if we take the infinite period limit of one component independently of the other. Specifically, if $\kappa_1 \neq 0$ and $\kappa_2 \to 0$, then Eq. (7) reduces to a semirational expression (i.e., a mixture of polynomials with both trigonometric and hyperbolic functions in x and t):

$$\begin{aligned} G_2 &= \frac{\kappa_1}{8}\big(\kappa_1\big(\kappa_1^2\big(4x_{s2}^2 + 4t_{s2}^2 + 1\big) - 8\big)\cosh(\delta_1 x_{s1}) \\ &\quad + 8\delta_1 \cos(\kappa_1 t_{s1})\big), \\ H_2 &= \frac{\kappa_1}{4}\big(8x_{s2}\big(\delta_1 \cos(\kappa_1 t_{s1}) - \kappa_1 \cosh(\delta_1 x_{s1})\big) \\ &\quad + \delta_1\kappa_1\big(4x_{s2}^2 + 4t_{s2}^2 + 1\big)\sinh(\delta_1 x_{s1})\big), \\ D_2 &= -\frac{1}{4\kappa_1}\big(\delta_1\big(\kappa_1^2\big(4x_{s2}^2 + 4t_{s2}^2 + 1\big) - 16\big)\cos(\kappa_1 t_{s1}) \\ &\quad + \kappa_1\big\{\big(\kappa_1^2\big(4x_{s2}^2 + 4t_{s2}^2 - 3\big) + 16\big)\cosh(\delta_1 x_{s1}) \\ &\quad - 16\delta_1[x_{s2}\sinh(\delta_1 x_{s1}) + t_{s2}\sin(\kappa_1 t_{s1})]\big\}\big). \end{aligned} \tag{8}$$

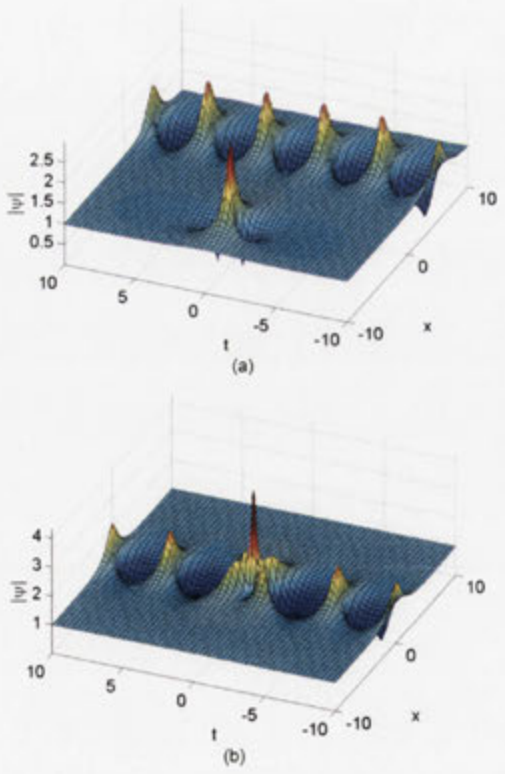

FIG. 3. (Color online) Nonlinear superposition of an AB ($l_1 = 0.65i$) with a Peregrine soliton ($l_2 = i$). (a) Shifts are $x_1 = 5$ and $x_2 = -5$. (b) Shifts are zero.

When the two components in this formula are well separated, the resulting solution appears as a Peregrine soliton and an AB (or a KM soliton), shown in Fig. 3(a). However, when these two components are nonlinearly overlaid, they appear as a first-order AB with a central second-order rogue wave peak, shown in Fig. 3(b). Three first-order peaks have effectively merged into a second-order peak. If we further apply the $\kappa_1 \to 0$ limit, we obtain the equation for a second-order rogue wave given below [see Eq. (10)]. This hybrid solution in Eq. (8) is thus one way to bridge the gap between a general second-order solution and an isolated rogue wave.

III. EQUAL-EIGENVALUE DEGENERATE SECOND-ORDER BREATHER

The general two-breather solution in Eq. (7) becomes undefined when the two eigenvalues l_1 and l_2 coincide. Despite this mathematical fact, numerical results similar to those in Fig. 2 show that, when the ratio of AB frequencies approaches 1 : 1, the solution appears as two almost parallel lines of periodically located peaks curving in at the origin to produce a second-order rogue wave in the center. In accordance with this observation, we set $x_1 = x_2 = t_1 = t_2 = 0$ and analytically apply the $\kappa_2 \to \kappa_1$ limit to Eq. (7). This can be done using a special form of l'Hôpital's rule. Specifically, we set $\kappa_1 = \kappa$ and $\kappa_2 = \kappa + \epsilon$, then Taylor expand both the numerator and denominator of $(G_2 + iH_2)/D_2$ in terms of ϵ. As all higher-order terms become zero at the $\epsilon \to 0$ limit, only the coefficients of the lowest-order terms in ϵ form the new numerator and denominator in the limiting solution.

This process results in the degenerate equal eigenvalue solution still given by Eq. (5), but now with real G_2, H_2, and D_2 given (again by mixtures of polynomials with trigonometric and hyperbolic functions in x and t) by

$$\begin{aligned} G_2 &= -\frac{2\kappa}{\delta}(\cosh(\delta x)((\delta^2 + \kappa^2)\cos(\kappa t) + \delta^2\kappa t\sin(\kappa t) \\ &\quad - 2\delta\kappa\cosh(\delta x)) + \cos(\kappa t)\sinh(\delta x)(2\delta^2 - \kappa^2)\delta x), \\ H_2 &= -\frac{1}{2\delta\kappa}(8\delta x(2\delta^2 - \kappa^2)[\delta\cos(\kappa t)\cosh(\delta x) - \kappa] \\ &\quad + 8\delta^3\sinh(\delta x)[\cos(\kappa t) + \kappa t\sin(\kappa t)] \\ &\quad + (\kappa^4 - 4\delta^2)\kappa\sinh(2\delta x)), \\ D_2 &= -\frac{1}{4\delta^2\kappa^2}(\kappa^4(\delta^2 + \kappa^2) + 8\delta^2\kappa^2(\delta^2 t^2 + \kappa^2 x^2) \\ &\quad + 32\delta^4 x^2(\delta^2 - \kappa^2) + 4[\kappa^4\cosh(2\delta x) - \delta^4\cos(2\kappa t)] \\ &\quad - 16\delta^2\kappa x(2\delta^2 - \kappa^2)\cos(\kappa t)\sinh(\delta x) \\ &\quad - 4\delta\kappa^2[4\delta^2 t\sin(\kappa t) + \kappa^3\cos(\kappa t)]\cosh(\delta x)), \end{aligned} \tag{9}$$

where the lack of subscripts on κ and δ variables indicates that the two constituent components have equal parameters.

When using a real κ value, Eq. (9) represents two coincident ABs with equal eigenvalues, illustrated with the contour plot in Fig. 4(a). If κ is, instead, purely imaginary, then δ becomes imaginary and, as with Eq. (4), the trigonometric and hyperbolic functions swap via the relations in Eq. (3). In this case, localization in the x axis and periodicity in the t axis is replaced with localization in the t axis and periodicity in the x axis. The solution represents two coincident KM solitons with equal eigenvalues. It is illustrated in Fig. 4(b). In either situation, the

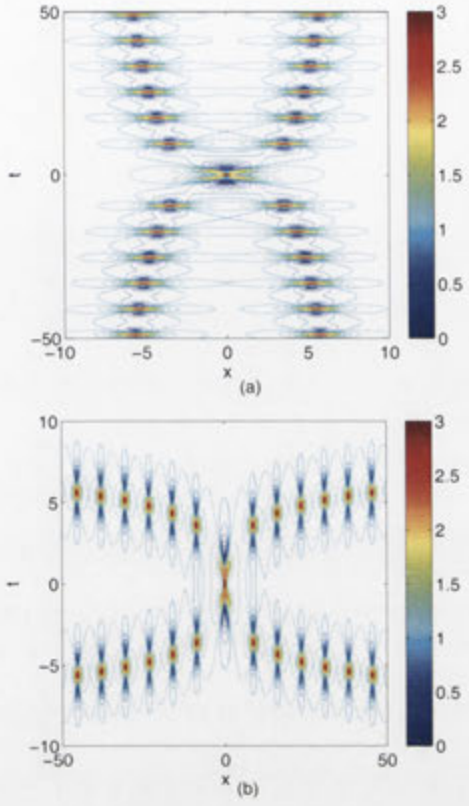

FIG. 4. (Color online) Contour plots of the two-breather solution $|\psi|$ in the equal eigenvalue limit. One axis in each plot is exaggerated in order to emphasise the curvature of the wave trains. The upper color bar limit does not signify the maximum amplitude. (a) Two ABs with equal $\kappa = 0.8$. (b) Two KM solitons with equal $\kappa = 0.8i$.

wave profile consists of two lines of peaks hinged upon one second-order rogue wave. This degenerate solution resembles the ordinary two-soliton degenerate solution presented in Fig. 3.15 of Ref. [37]. However, the difference is that the solution in Eq. (9) contains periodic structures that appear due to the presence of the background plane wave.

An interesting feature of the two solutions presented in Fig. 4 is that the location of the peaks almost coincide when one is rotated by 90° around the origin and overlaid on the other, even though the orientation of the substructures are kept unchanged (i.e., the pairs of troughs for each peak always line up along the t axis). This happens only when the coefficients of the NLSE are chosen to be those that we show in Eq. (1). In fact, most of the variation between peak alignment is due to the frequency of the periodic structures in an AB and a KM soliton being κ and $\Omega = -i\delta$, respectively. Thus the NLSE in this form has a remarkable symmetry, as has already been noted in our previous work [27].

Having the degenerate form of the two-breather solution in Eq. (9), we can use it to find the already familiar limit $\kappa \to 0$. This stretches the period of the wave train out to infinity, leaving at the center a single second-order rogue wave. The

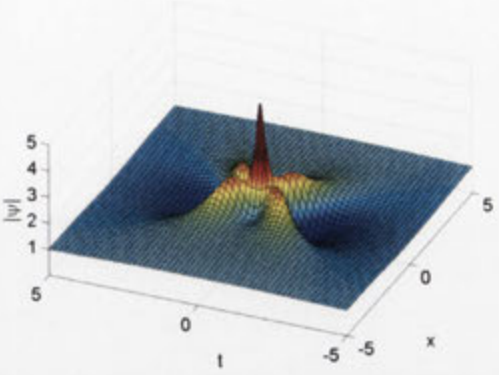

FIG. 5. (Color online) Second-order rogue wave given by Eq. (10).

resulting analytic expression is

$$
\begin{aligned}
G_2 &= \frac{1}{96}(80x^4 + 96x^2t^2 + 16t^4 + 72x^2 + 24t^2 - 3),\\
H_2 &= \frac{1}{48}x(16x^4 + 32x^2t^2 + 16t^4 + 8x^2 - 24t^2 - 15),\\
D_2 &= -\frac{1}{1152}(64x^6 + 192x^4t^2 + 192x^2t^4 + 64t^6 + 432x^4\\
&\quad -288x^2t^2 + 48t^4 + 396x^2 + 108t^2 + 9),
\end{aligned}
\tag{10}
$$

which gives the wave function shown in Fig. 5. Thus we have fully established the hierarchy of unshifted second-order breather solutions, ranging from the general case to the rogue wave via degenerate breathers.

IV. DIFFERENTIAL SHIFTS

Now the question is how to incorporate the shifted coordinates $x_{sj} = x - x_j$ and $t_{sj} = t - t_j$ into the equal eigenvalue limit. This is another highly nontrivial point in obtaining the limiting solutions and, as shown previously [27], the shifts need special consideration when eigenvalue limits are applied. Returning to the ϵ Taylor expansion process that turns Eq. (7) into Eq. (9), we realize that shifts cannot be arbitrary values independent of any other parameter. When $x_j \neq 0$ and $t_j \neq 0$ are treated as arbitrary, the lowest-order terms of G_2 and H_2, after Taylor expansion, are of order ϵ^1. However, the lowest-order term in D_2 is $48^2[\cos[\kappa(t_2 - t_1)] - \cosh[\delta(x_2 - x_1)]]\epsilon^0$. This means that $(G_2 + iH_2)/D_2 = 0$ in the limit unless $t_1 = t_2$ and $x_1 = x_2$. This difficulty was also present when considering rogue wave clusters [27] and the only solution to this problem was to have shifts dependent on the limiting parameter. Specifically, we have to define $x_j = X_j\epsilon$ and $t_j = T_j\epsilon$. This definition changes the result of the ϵ expansion process, such that G_2, H_2, and D_2 have lowest-order terms of equal order in ϵ, thus avoiding a zero or infinite expression for $\epsilon \to 0$.

We caution that, as ϵ is defined to be proportional to κ in the Taylor expansion process, ABs and KM solitons have a real and imaginary value for ϵ, respectively. As x_j and t_j are always real-valued, pertaining to a shift of component origin in real space and time, then the nature of X_j and T_j consequently depends on ϵ. Specifically, these parameters are restricted to

being real for ABs and imaginary for KM solitons, otherwise singular solutions result.

When these definitions are taken into account, the degenerate equal eigenvalue limit becomes

$$\begin{aligned}
G_2 = &-\frac{\kappa}{2\delta}[((8\delta^2+\kappa^4)\cos(\kappa t)+4\delta^2\kappa(t+\kappa T_d)\sin(\kappa t)\\
&-8\delta\kappa\cosh(\delta x))\cosh(\delta x)\\
&+4\delta[\delta^2(2x+\kappa X_d)-\kappa^2 x]\cos(\kappa t)\sinh(\delta x)],\\
H_2 = &-\frac{1}{2\delta\kappa}(8\delta[\kappa^2 x-\delta^2(2x+\kappa X_d)]\\
&\times[\kappa-\delta\cos(\kappa t)\cosh(\delta x)]+\kappa(\kappa^4-4\delta^2)\sinh(2\delta x)\\
&+8\delta^3[\cos(\kappa t)+\kappa(t+\kappa T_d)\sin(\kappa t)]\sinh(\delta x)),\\
D_2 = &-\frac{1}{4\delta^2\kappa^2}(\kappa^6+2\delta^2\kappa^2(\kappa^2(1+4x^2)-2)\\
&+8\delta^6(2x+\kappa X_d)^2+4\delta^4(1+2\kappa^2[(t+\kappa T_d)^2\\
&-2x(2x+\kappa X_d)]-\cos(2\kappa t))\\
&+\kappa[(4\delta^2+\kappa^4)\kappa\cosh(2\delta x)\\
&-16\delta^3\kappa(t+\kappa T_d)\cosh(\delta x)\sin(\kappa t)\\
&+4\delta\cos(\kappa t)(4\delta[\kappa^2 x-\delta^2(2x+\kappa X_d)]\sinh(\delta x)\\
&-\kappa^4\cosh(\delta x))]),
\end{aligned}\tag{11}$$

where we define the differential shifts as $X_d = X_1 - X_2$ and $T_d = T_1 - T_2$. Again we stress that the differential shifts have imaginary values in the KM soliton regime, although naturally $|X_d|$ and $|T_d|$ always represent the magnitude of the differential shifts. To avoid confusion, we will henceforth examine degenerate ABs, although the conclusions drawn have close analogues in the KM soliton case.

The first feature revealed by Eq. (11) is that a differential shift T_d along the t axis of the degenerate two-breather solution, shown in Fig. 4, does not change the overall structure of the wave profile. Two first-order ABs remain symmetrically arrayed and held in close proximity with a single intersection. However, the nature of this point of intersection depends on the value of the differential shift. It may change if the two breather components with equal eigenvalues are shifted relative to each other, at which point the perfect peak alignment in the middle of the intersection disappears. This case is shown in Fig. 6(a). The intersection more closely resembles the rogue wave triplet [26] than a second-order rogue wave with a single peak. However, periodicity of the solution suggests that the latter arrangement can be restored at specific values of T_d and its multiples. Indeed, Fig. 6(b) shows that the high peak appears again at a nonzero value of differential shift T_d.

The differential shift X_d has a different effect on the solution with equal eigenvalues. As shown in Fig. 7(a), the intersection point starts to disappear when X_d takes nonzero values. For a sufficiently large shift, the two first-order components are separated and the intersection disappears completely. This case is shown in Fig. 7(b). However, the interaction between the two breathers is still surprisingly strong. As a result, the two components are organized in an interleaving zigzag structure. Such an asymmetric arrangement appears to be a direct consequence of the $\epsilon \to 0$ limit. Indeed, taking the limit with κ_2 set as $\kappa - \epsilon$ instead of $\kappa + \epsilon$ is likely to flip the zigzag structure. However, we reiterate that the absolute shifts $x_j = X_j\epsilon$ and $t_j = T_j\epsilon$ are still technically zero in this limit, irrespective of the X_j and T_j values, and this may be vital in explaining why the two breathers do not repel each other to the infinity horizon of the (x,t) plane.

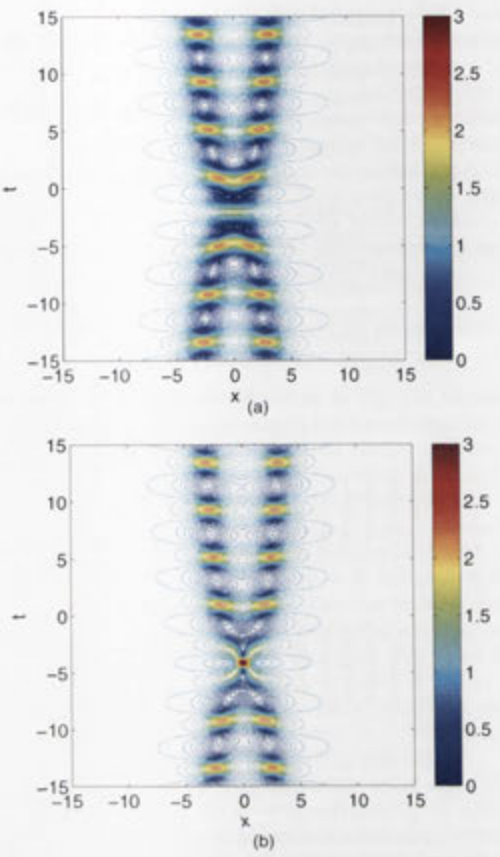

FIG. 6. (Color online) Contour plots of the two-breather solution $|\psi|$ in the degenerate limit, with $l = 0.65i$ and a nonzero differential shift T_d between the two components. The upper color bar limit does not signify the maximum amplitude. (a) $T_d = 0.9\kappa$. (b) $T_d = 1.8\kappa$.

Linking this result to already known solutions, the $l \to i$ ($\kappa \to 0$) limit of Eq. (11), with any value of the differential shift applied, is expected to produce a rogue wave triplet [26]. However, as κ approaches zero and the period of the breathers becomes infinite, keeping the values of X_d and T_d constant is not sufficient to prevent the components from repelling each other to infinity. Instead, we define $X_d = x_d\kappa$ and $T_d = t_d\kappa$, which alternatively allows the difference between absolute shifts to be written in full as $x_1 - x_2 = x_d\kappa\epsilon$ and $t_1 - t_2 = t_d\kappa\epsilon$. Fixed values of x_d and t_d keep the circumradius of the rogue wave triplet constant, even when it is the only structure left at the origin of the (x,t) plane in the $\kappa \to 0$ limit. An example of this process with two KM solitons is shown in Fig. 8. Furthermore, unlike X_d and T_d, the values of x_d and t_d are always real, even in the KM soliton regime, as $\kappa\epsilon$ is always real. In any case, the second-order breather solution with equal eigenvalues can be considered as an intermediate

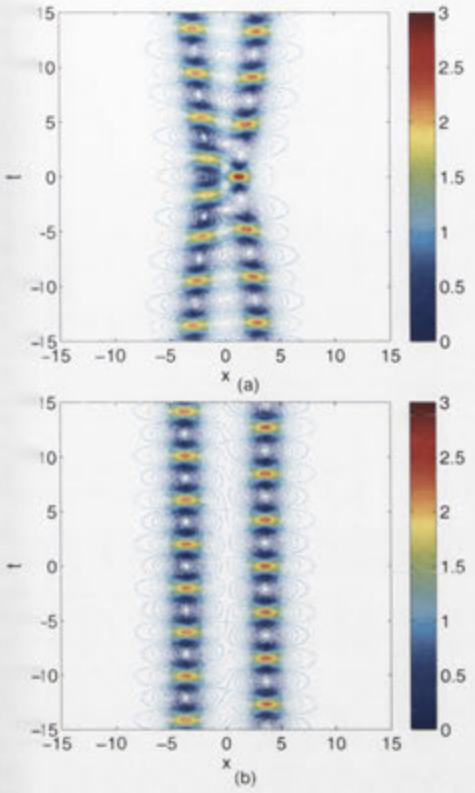

FIG. 7. (Color online) Contour plots of the two-breather solution $|\psi|$ in the degenerate limit, with $l = 0.65i$ and a nonzero differential shift X_d between the components. The upper color bar limit does not signify the maximum amplitude. (a) $X_d = 1.8\kappa$. (b) $X_d = 18\kappa$.

link between pure rogue waves and the general second-order breather solutions given by Eq. (7).

Direct analytic application of the $\kappa \to 0$ limit to Eq. (11) generates the following solution

$$
\begin{aligned}
G_2 &= \frac{1}{96}(80x^4 + 96x^2t^2 + 16t^4 + 72x^2 - 192xx_d \\
&\quad + 24t^2 - 192tt_d - 3), \\
H_2 &= \frac{1}{48}(16x^5 + 32x^3t^2 + 16xt^4 + 8x^3 - 96x^2x_d \\
&\quad - 24xt^2 + 96x_dt^2 - 192xtt_d - 15x + 24x_d), \\
D_2 &= -\frac{1}{1152}(64x^6 + 192x^4t^2 + 192x^2t^4 + 64t^6 \\
&\quad + 432x^4 - 768x^3x_d - 288x^2t^2 + 2304xx_dt^2 \\
&\quad - 2304x^2tt_d + 48t^4 + 768t^3t_d + 396x^2 - 1728xx_d \\
&\quad + 2304x_d^2 + 108t^2 - 576tt_d + 2304t_d^2 + 9). \qquad (12)
\end{aligned}
$$

This is the same solution for the shifted second-order rogue wave given previously [22–24,27], although x_d and t_d here have a different scaling factor of 2/3. This minor difference is due to the rogue wave limit in this work being taken with a different frequency ratio between components. Indeed, had $\kappa_1 : \kappa_2$ been, for example, 1 : 3 rather than 1 : 2 in the previous derivation [27], x_d and t_d would have been scaled differently yet again. Nonetheless, as ϵ is of order κ, the process described in this work still supports the claim that a second-order rogue wave requires shifts proportional to κ^2 in order to be transformed into a triplet of finite circumradius in the $\kappa \to 0$ limit [27].

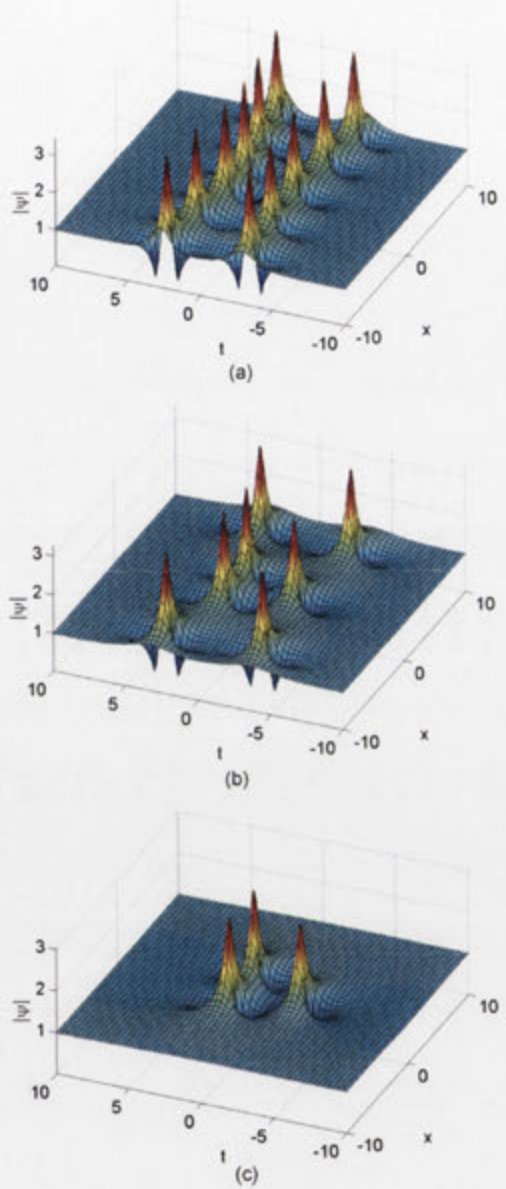

FIG. 8. (Color online) Two KM solitons with equal eigenvalues, given by Eq. (11). The differential shift is $T_d = 3\kappa$ ($t_d = 3$) in all three cases. The two equal eigenvalues are (a) $l = 1.2i$. (b) $l = 1.1i$. (c) $l \approx i$. The period of the two breathers approaches infinity when the eigenvalues tend to i.

V. CONCLUSION

In summary, our main results are as follows.

i) We have found a general analytic expression for the two-breather solution of the NLSE with two independent imaginary eigenvalues. This solution describes nonlinearly superimposed ABs or KM solitons as well as their combinations.

ii) We have found the nontrivial degenerate solution in the limit of equal eigenvalues. Where simple substitution leads to an undefined expression, special application of l'Hôpital's rule allows the solution to be presented in explicit form. We illustrated this solution with two cases where the component breathers are either ABs or KM solitons. The analysis shows that in each case, these degenerate solutions consist of two near-parallel lines almost periodic in structure, with only one point of intersection.

iii) We introduced two free parameters, differential shifts between components, that modify the structure of the degenerate solution. We studied the wave profile at the point of intersection and how it is influenced by these parameters. In particular, the profile varies between the single-peak second-order rogue wave and the three-peak rogue wave triplet, depending solely on the value of the differential shifts.

iv) We have found that the rogue wave limit of infinite period, when the two equal eigenvalues are equal to i, generates the familiar second-order rogue wave with two free parameters; differential shifts along the t and x axes.

Ultimately, we have established how these wave functions are all related in a hierarchy of second-order breather solutions. This concept has previously been obtuse, at best. The degenerate solutions are in effect a missing link between arbitrary superpositions and rogue waves. This understanding is particularly significant as analytic expressions for higher orders become vastly more complex, even for simple rogue wave limits [23]. Second order is potentially the final regime where the hierarchy of all structures can be efficiently described. Even so, multibreather solutions that appear in a chaotic wave field can still be studied in a similar way as presented. The analysis here gives a good qualitative description of the higher-order structures expected to be generated. Numerics demonstrate, as shown in Fig. 9 with a fifth-order rogue wave produced in the intersection of five KM solitons, that this is potentially a way to produce very high amplitude waves from much smaller structures, without resorting to ideal rogue waves with infinite period.

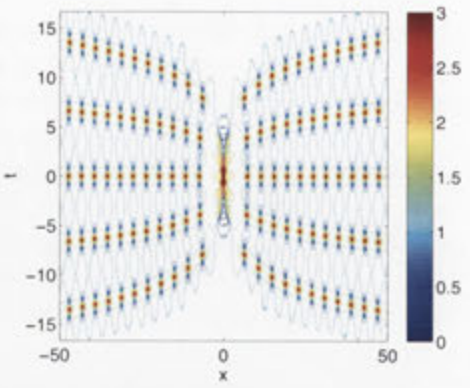

FIG. 9. (Color online) Numerical contour plot of the five-breather solution $|\psi|$ near the equal eigenvalue limit, with $l \approx 1.2i$ for all KM solitons. One axis is exaggerated to emphasize the curvature of the wave trains. The upper color bar limit does not signify the maximum amplitude.

One of the important applications of our results is related to the description of the higher-order modulation instability of constant amplitude waves [38]. Varying two independent frequencies within the instability band may create significantly more complicated controllable periodic structures as a result of modulation instability [39]. We have already mentioned higher amplitude peaks within each period of modulation, but the amplitude profile within each period may also vary and can be tailored by adjusting the modulation depth and delay between the two frequency components. These experiments can be conducted either with water waves or in optics. Thus our explicit solutions may significantly enrich the family of pulse sequences and wave shapes that can be generated in fiber and water tanks, respectively. The seminal experiments have already been completed [9,12] and we expect further progress in this exciting area of research.

ACKNOWLEDGMENTS

The authors acknowledge the support of the Australian Research Council (Discovery Project No. DP110102068). N.A. and A.A. acknowledge support from the Volkswagen Stiftung.

[1] D. Peregrine, J. Austral. Math. Soc. Ser. B **25**, 16 (1983).

[2] K. B. Dysthe and K. Trulsen, Phys. Scr., T **82**, 48 (1999).

[3] A. R. Osborne, *Nonlinear Ocean Waves and the Inverse Scattering Transform* (Elsevier, Amsterdam, 2010).

[4] E. Pelinovsky and C. Kharif, *Extreme Ocean Waves* (Springer, Berlin, 2008).

[5] V. V. Voronovich, V. I. Shrira, and G. Thomas, J. Fluid Mech. **604**, 263 (2008).

[6] V. Shrira and V. Geogjaev, J. Eng. Math. **67**, 11 (2010).

[7] I. Ten and H. Tomita, Reports of RIAM Symposium, Kasuga, Fukuoka, Japan, 2006, Report No. 17SP1-2.

[8] C. Garrett and J. Gemmrich, Phys. Today **62**(6), 62 (2009).

[9] A. Chabchoub, N. P. Hoffmann, and N. Akhmediev, Phys. Rev. Lett. **106**, 204502 (2011).

[10] V. B. Efimov, A. N. Ganshin, G. Kolmakov, P. McClintock, and L. Mezhov-Deglin, Eur. Phys. J. Spec. Top. **185**, 181 (2010).

[11] M. Shats, H. Punzmann, and H. Xia, Phys. Rev. Lett. **104**, 104503 (2010).

[12] B. Kibler, J. Fatome, C. Finot, G. Millot, F. Dias, G. Genty, N. Akhmediev, and J. M. Dudley, Nature Phys. **6**, 790 (2010).
[13] N. Akhmediev, V. I. Korneev, and N. V. Mitskewich, Zh. Experimentalnoii i Teoreticheskoii Fiziki (USSR) **94**, 159 (1988) [Sov. Phys. JETP, **67**, 89 (1988)].
[14] N. Akhmediev, J. M. Soto-Crespo, and A. Ankiewicz, Phys. Lett. A **373**, 2137 (2009).
[15] N. Akhmediev, J. M. Soto-Crespo, and A. Ankiewicz, Phys. Rev. A **80**, 043818 (2009).
[16] N. Akhmediev and A. Ankiewicz, Opt. Commun. **100**, 186 (1993).
[17] L. Gagnon and N. Stevenart, Opt. Lett. **19**, 619 (1994).
[18] V. B. Matveev and M. Salle, *Darboux Transformations and Solitons* (Springer-Verlag, Berlin, 1991).
[19] N. Akhmediev, A. Ankiewicz, and M. Taki, Phys. Lett. A **373**, 675 (2009).
[20] N. Akhmediev, A. Ankiewicz, and J. M. Soto-Crespo, Phys. Rev. E **80**, 026601 (2009).
[21] P. Dubard, P. Gaillard, C. Klein, and V. Matveev, Eur. Phys. J. Spec. Top. **185**, 247 (2010).
[22] P. Gaillard, Institut National des Sciences Mathématiques et de Leurs Interactions, Report No. halshs-00536287, 2010 (unpublished).
[23] P. Gaillard, Institut de Mathématiques de Bourgogne, Report No. hal-00573955, 2011 (unpublished).
[24] P. Gaillard, J. Phys. A: Math. Theor. **44**, 435204 (2011).
[25] P. Dubard and V. B. Matveev, Natural Hazards and Earth System Sciences **11**, 667 (2011).
[26] A. Ankiewicz, D. J. Kedziora, and N. Akhmediev, Phys. Lett. A **375**, 2782 (2011).
[27] D. J. Kedziora, A. Ankiewicz, and N. Akhmediev, Phys. Rev. E **84**, 056611 (2011).
[28] N. Akhmediev and V. I. Korneev, Teoreticheskaya i Matematicheskaya Fizika (USSR) **69**, 189 (1986) [Theor. Math. Phys. **69** 1089 (1986)].
[29] N. Akhmediev, V. M. Eleonskii, and N. E. Kulagin, Theoreticheskaya i Mathematicheskaya Fizika (USSR) **72**, 183 (1987) [Theoretical and mathematical physics **72**, 809 (1987)].
[30] M. Tajiri and Y. Watanabe, Phys. Rev. E **57**, 3510 (1998).
[31] Q.-Han Park and H. J. Shin, Phys. Rev. Lett. **82**, 4432 (1999).
[32] S. L. Lu Li, Zhonghao Li and G. Zhou, Opt. Commun. **234**, 169 (2004).
[33] V. Zakharov and A. Gelash, arXiv:1109.0620v2 (2011).
[34] N. Akhmediev, V. M. Eleonskii, and N. E. Kulagin, Zh. Eksperimentalnoii i Teoreticheskoii Fiziki **89**, 1542 (1985) [Sov. Phys. JETP **62**, 894 (1985)].
[35] E. A. Kuznetsov, Dokl. Akad. Nauk SSSR **236**, 575 (1977) [Sov. Phys. Dokl. **22**, 507 (1977)].
[36] Y.-C. Ma, Stud. Appl. Math. **60**, 43 (1979).
[37] N. Akhmediev and A. Ankiewicz, *Solitons: Nonlinear Pulses and Beams*, Vol. 5 of *Optical and Quantum Electronics* (Chapman & Hall, London, 1997), Chap. 3–4.
[38] S. Wabnitz and N. Akhmediev, Opt. Commun. **283**, 1152 (2010).
[39] M. Erkintalo, K. Hammani, B. Kibler, C. Finot, N. Akhmediev, J. M. Dudley, and G. Genty, Phys. Rev. Lett. **107**, 253901 (2011).

Epilogue

As a publication dedicated to generalised two-breather solutions in exact analytical form [3], the contents of this chapter have had an impact beyond rogue wave theory, with the solutions used in the topic of similarity transforms to higher-dimensional equations [74, 75]. However, at this stage, it is worth addressing several terminological oddities. It is evident that, while the main text in this thesis seeks to maintain a consistent convention for both breathers and solitons, the incorporated journal articles often mix labels. For instance, certain solutions on a plane-wave background are frequently called Peregrine or Kuznetsov-Ma 'solitons'. This ambiguity of nomenclature also goes the other way in the literature, with high-order zero-background beating solitons occasionally referred to as 'breathers' [93, 101]. Naturally, while this dissertation attempts to demarcate breathers from solitons based on the type of background they are built on, this terminological confusion is not simply due to tradition. There is actually a deep physical relation between the two solution types, elaborated in Chapter 7.

Even without knowing this link, the wavetrains pertaining to both breathers and solitons still discernibly behave in similar fashion. This follows from examination of the expression for a general first-order soliton given by

$$\psi_1(x,t) = -2ib_1 \mathrm{sech}(2b_1\,(t_{s1} + 2a_1 x_{s1}))\, e^{-2i\left(a_1 t_{s1} + \left(a_1^2 - b_1^2\right) x_{s1}\right)}, \tag{3.1}$$

where the fully-complex eigenvalue is $\lambda_1 = a_1 + ib_1$ and the shifted origin is denoted by both $x_{s1} = x - x_1$ and $t_{s1} = t - t_1$. It is clear from the equation that, even without a velocity imparted by a_1, a soliton oscillates in phase with regular eigenvalue-dependent frequency. This is analogous to the modulating envelope of a breather. Consequently, the appearance of aligned second-order solutions becomes a matter of interference patterns. For example, Fig. 3.1a displays the nonlinear superposition of two unshifted $a_j = 0$ solitons, derived via numerical implementation of the Darboux scheme with a seeding solution of $\psi_0 = 0$. Each collision peak in the surface plot corresponds to a point of constructive phase interference, with alignment enforced at $x = 0$. The crests directly adjacent to the centre actually have a value of $-\psi(0,0)$ at those points, but the negative sign is ignored by the modulus operation.

For comparison, two superimposed ABs with the same choice of frequency values are shown in Fig. 3.1b. This structure can be interpreted in two ways. The first is as in the paper [3], according to which the 5 : 3 ratio results in eight Peregrine breather peaks needing to be distributed per repetitive cycle. Three fuse into a second-order rogue wave, while the other five are arranged to maximise symmetry. In this case, that means there are two doublets and a singlet between each adjacent second-order collision. On the other hand, the second interpretation is as in the case of the beating solitons. Analogously to Fig. 3.1a, there should effectively be five points of constructive modulational interference at the same locations, albeit along t instead of x. Sure enough, there are, but the summative effect of the plane wave must now be taken into account. For the central and the outermost displayed peaks, all amplitudes construc-

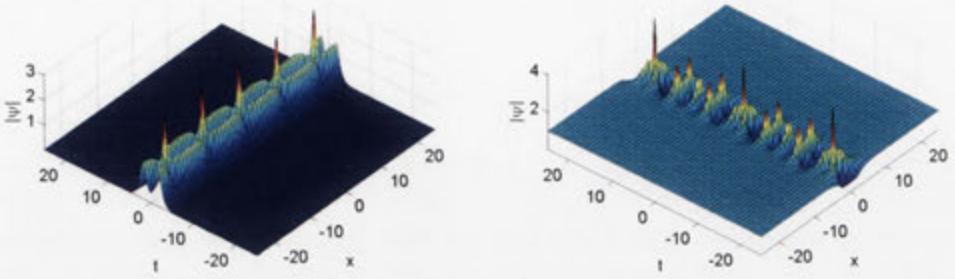

(a) (b)

Figure 3.1: Beating second-order NLSE solutions. (a) Two aligned solitons, with phase frequencies $2b_1^2 = 0.9$ and $2b_2^2 = 1.5$. (b) Two aligned breathers, with modulation frequencies $\kappa_1 = 0.9$ and $\kappa_2 = 1.5$.

tively interfere to produce second-order peaks. In contrast, the intermediate nodes feature maximum destructive interference between the background and the aligned modulations, leaving behind rogue singlets for the particular wavefunction depicted. The remaining doublets then correspond to the 'craters' in Fig. 3.1a.

This close correlation between traditional solitons and breathers is what motivated research into the degenerate case in the first place. For the solitonic case [99, 100], attempting to enforce eigenvalue equality via limit theory is equivalent to reducing the beating frequency of the wavefunction in Fig. 3.1a, extending the spatiotemporal distance between peaks until there is but one collision between two seemingly parallel solitons (as shown in Fig. 7d of the cnoidal paper [7]). By this logic, it follows that a degenerate breather would resemble the same shape. The only significant difference here is that the endless wavetrains are now composed of doublets.

Ultimately, the relevance of this discussion to the topic of multi-rogue waves is as follows. No two breathers can have exactly the same periodicity as this would be physically equivalent to a beating frequency of zero, essentially corresponding to linear superposition. This is of course not possible, as the nonlinearity in the NLSE precludes ψ and 2ψ from simultaneously being nontrivial solutions. So one breather will always have at least one more (or one less) modulation crest in its wavetrain than another. In effect, each component attempts to differ from every other breather in the smallest number of modulation peaks possible, as befits the degenerate limit, but without actually being identical to any other. However, the degenerate limit of two aligned breathers must still induce some symmetry, and this is achieved by fusing any excess wavetrain crests into an interaction between the two. In this second-order case, one breather donates one modulation crest and a second donates two towards this analogy of constructive interference, so that the remaining

wavetrains are perfectly equal and symmetric. This asymmetry also carries over to higher-order fusions, such that while one breather contributes one 'quantum' and a second contributes two, a third contributes three, a fourth contributes four, and so on, ordered by their relative pre-limit modulation frequencies. This is why a rogue wave, in the absence of the rest of the breather wavetrains, consists of a triangular number (i.e. $1, 3, 6, 10, ...$) of Peregrine breathers [2].

Incidentally, arguments based on breather asymmetry are but one of several ways to justify this sequence. They are physically inspired, but not necessarily the easiest to express. In contrast, this series can also be mathematically attained via an algebraic exploration of polynomials within the exact functional form of fused rogue wave solutions [69] and is elaborated in a publication on rogue triplets [1]. Moreover, there is yet an even simpler conceptual justification that can be discussed, but this requires a better understanding of how rogue waves are related to solitons and is deferred until Chapter 7.

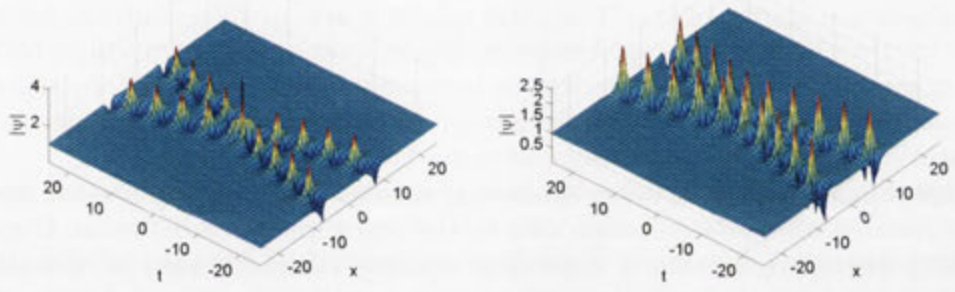

(a) (b)

Figure 3.2: Colliding breathers with equal (real parts of) modulation frequency. Eigenvalues are $\lambda_1 = 0.1 + 0.8i$ and $\lambda_2 = -0.1 + 0.8i$ (a) Unshifted. (b) First component breather is shifted by $t_1 = \pi/\kappa_1$.

This work also strongly suggests that a rogue doublet, at least in quasi-rational form [69], cannot exist. The localised description of energetics introduced in the epilogue of Chapter 2 somewhat justifies this, as it is difficult to imagine energy flow reversing between two Peregrine breathers without any external influence, such as an additional rogue wave. Some physical feature seems required to flip the outward direction of localised wave momentum inwards. Nonetheless, this concept can be further explored by examining the first-order component functions of a breather (i.e. Eq. A4 of clusters paper [2]). Accordingly, maximal constructive interference at the origin can be converted to maximal destructive interference by simply applying a π/κ_j phase shift to one of the components indexed by j. This can convert a breather collision, as shown in Fig. 3.2a, into a seeming reflection of wavetrains, as depicted in Fig. 3.2b. The technique is actually the basis of deriving so-called quasi-Akhmediev

breathers [102] with the Darboux scheme. However, it is both analytically and numerically clear that the destructively interfering version of the degenerate case is not so simply envisaged as the solution in Fig. 3.2b. It effectively involves two wavetrains, equal in the quantity of modulational peaks they each host. They are maximally repelled to spatiotemporal infinities and cannot be depicted in a finitely bounded domain. Taking a rogue wave limit of this structure is indeed possible and would leave behind a rogue doublet, as one element in the homogeneous chain, but this would do nothing to counteract the effect of destructive interference that repelled the individual Peregrine breathers infinitely apart in the first place.

Chapter 4

Triangular Rogue Wave Cascades

Prologue

The detour into the theory of degenerate breathers [3], as detailed in Chapter 3, explained the composition of compounded extreme events to some extent. However, many intriguing mysteries remained following the discovery of circular rogue wave clusters [2]. For instance, considering that the modulation wavetrains of breathers are always linearly arranged [103], it still seemed counterintuitive that these compound structures could possess a ring-shaped geometry. These kinds of issues helped spark a growing interest in multi-rogue wave study. Indeed, initial investigations into other related nonlinear systems were beginning to show that these cluster shapes were not restrictively dependent on the physics of the NLSE [73]. It would become clear that higher-order terms and other perturbations did not preclude their existence [91, 92].

More curiously, there were suggestions that these circular clusters were not the only possible arrangements of NLSE rogue wave solutions [86]. Research carried out for the paper in Chapter 2 had already hinted at the existence of multi-ring wavefunctions, while an alternative method had recently indicated that the circular geometry itself could be perturbed [71]. Yet none of these structures could be consistently confirmed with the Darboux scheme parameter choices employed thus far in the thesis. Progress here was stymied until an unintuitive concept was considered, inspired by the variations between both the degenerate and the rogue wave limit [3]; different orders of infinitesimal shifts have different structural effects.

Clarification of this idea requires the following train of thought. Rogue wave solutions of the NLSE are generated from breathers, as made explicit in Chapter 3. Achieving this requires a non-degenerate modulation frequency ratio to be established between components, with a common factor κ. Thus, when the rogue wave limit $\kappa \to 0$ is applied, all breathers are still distinct. Now, given this definition, a rogue wave of order n transforms into a ringed structure when any number of components are shifted by a value proportional to $\kappa^{2(n-1)}$. A larger exponent results in shifts that are too small to induce any fission in the $\kappa \to 0$ limit, while a smaller exponent has typically been associated with infinite spatiotemporal 'ring expansion' for the same frequency values [2]. However, numerical application of the Darboux scheme soon indicated that triangularly arrayed structures of finite circumradius could be isolated from a composite breather and kept stable for decreasing κ values (as shown in Fig. 1 of the hierarchy paper [6]), provided that the ratio of

modulation frequencies was finely tuned with respect to component shifts. Moreover, unlike the case of circular clusters, these new solutions required each and every component breather to be shifted with respect to all others by a value proportional to κ^2, regardless of composite solution order.

This chapter, as a published manuscript [4], explicitly details the parametric constraints required to produce triangular rogue wave 'cascades'. These novel solutions of the NLSE are unique fundamental high-order structures, in that they are solely comprised of first-order Peregrine breathers. They are also more complicated to produce arbitrarily than circular clusters, as the second-order manifestations of both forms are identical and higher-order cascades have more stringent requirements. All the same, it is of great importance that the existence conditions for each form are effectively independent. As a consequence of this, it is possible to controllably fission a rogue wave of order n into either a ringed structure or a triangular array, or 'hybridise' both features. Unique 'claw-like' structures exemplify unusual arrangements of Peregrine breathers from this mixing process, thus usefully serving to further expand the set of known multi-rogue wave NLSE solutions.

PHYSICAL REVIEW E **86**, 056602 (2012)

Triangular rogue wave cascades

David J. Kedziora,* Adrian Ankiewicz, and Nail Akhmediev
Optical Sciences Group, Research School of Physics and Engineering, The Australian National University, Canberra ACT 0200, Australia
(Received 20 June 2012; published 8 November 2012)

By numerically applying the recursive Darboux transformation technique, we study high-order rational solutions of the nonlinear Schrödinger equation that appear spatiotemporally as triangular arrays of Peregrine solitons. These can be considered as rogue wave cascades and complement previously discovered circular cluster forms. In this analysis, we reveal a general parametric restriction for their existence and investigate the interplay between cascade and cluster forms. As a result, we demonstrate how to generate many more hybrid rogue wave solutions, including semicircular clusters that resemble claws.

DOI: 10.1103/PhysRevE.86.056602 PACS number(s): 05.45.Yv, 47.20.Ky, 42.65.−k

I. INTRODUCTION

An unfortunate fact of life is that extreme events have a tendency to arrive in bunches. This concept is reflected in the well-known proverb "bad things come in threes" and its equivalent, "misfortunes never come singly." Indeed, where one occurrence may be labeled a minor disaster, successive incidents can compound a situation into a complete catastrophe. Furthermore, each event is normally unexpected and always appears "from nowhere." So, given the notorious unpredictability of extreme events, due consideration must be given to any scientific approach that explains how these incidents arise.

Archetypically, the serial nature of rogue waves is exemplified by the oceanic "three sisters" phenomenon, where three large waves appear as successive events. This is no longer merely legend but is now actively discussed in the literature [1–4]. Furthermore, many natural disasters potentially modelled as rogue waves show a repetitive or correlated nature. Hence, the issue naturally arises whether groups of extreme events can be described mathematically and whether they are arranged in a specific pattern. Of course, these are generally complicated questions to answer. Nevertheless, if we start with a certain simple model, such as one involving deep ocean wave evolution, we can write a partial differential equation that describes rogue wave phenomena in the lowest approximation. With this, we can give fundamental solutions that portray a group of distinct rogue waves as sequences of extreme events.

In particular, this approach can be applied to the nonlinear Schrödinger equation (NLSE) [5–7]. This is a well-justified model for deep ocean waves [8–10] as well as many other phenomena in physics [11–14]. The basic Peregrine soliton, a spatiotemporally localized solution of the NLSE, has been considered as a prototype of a first-order rogue wave. It has been studied both theoretically [15,16] and experimentally [17,18]. Furthermore, despite being a rough approximation of reality, the NLSE accurately describes physical rogue waves of relatively high order [19].

From this model, it is apparent that second-order rogue waves may appear as a single event [20] or as triplets [21] in space and time. Remarkably, there are no solutions that describe rogue waves appearing as doublets. This fact alone tells us that only certain patterns of rogue waves represent legitimate solutions to the NLSE [22]. This interesting observation poses the general question of what patterns are possible when we deal with extreme events of even higher order. Clearly, if we try to explain rogue waves based on linear theory [23–25], the concept of interference should allow any imaginable configuration, including a double peak. However, taking into account the rarity of a single high peak wave, two of them occurring in conjunction would be exceptionally improbable within the constraints of linear theory.

Thus, we utilize nonlinear analysis [8], which has been fruitful in describing not only single events but even higher-order solutions [6,22,26,27]. This approach recently led to the discovery of sophisticated circular "atomlike" structures [28], as well as higher-order triangular patterns [29] as an alternative arrangement. Each of these cases is nontrivial and requires special techniques for investigation, such as Wronskian methodology [26,27,30], Schur polynomials [29], or Darboux transformations [31–33]. Even so, the rapid increase of complexity with respect to solution order means that the analytic forms of these rogue wave arrangements become unwieldy beyond the case of a simple rogue wave triplet [21]. It is becoming clear that none of the techniques mentioned above can provide a complete understanding of all the structures that may exist in higher orders.

Nonetheless, in the present work, we have made a further step forward and found a systematic way to generate rogue wave patterns in the form of triangular arrays. Although glimpsed as a special case by Ohta and Yang [29], these structures not only complement previously discovered circular cluster forms [28] but can even be "hybridized" with them to produce new solutions of the NLSE, acting almost like primary elements of a structural basis set. To show this, we use the Darboux transformation method [31–33], which was specifically designed for constructing higher-order solutions of a certain class. The main difficulty here is to find the parameters that control the pattern. Unlike eigenvalues from the inverse scattering transform, these parameters do not automatically arise from standard techniques. They are buried deep within the methodology. Although implicitly related to translations along the spatiotemporal axes, they are not simple and describe the structure as a whole rather than the positioning of individual peaks. Thus, they have to be carefully detailed in the theory to be associated with a certain pattern.

*djk105@rsphysse.anu.edu.au

Here, we show how triangularly arrayed cascade solutions appear in our scheme and prescribe the way they can be generated numerically for any order. The first time these complicated structures become pertinent is at third order, which already offers several patterns, in contrast to the simple triplet at second order. This is because the latter solution can be considered as either a triangular or circular array, while the distinction between the two forms must be made clear in the third-order case. By additionally hybridizing the circular cluster and triangular cascade forms, we can find new legitimate solutions of the NLSE, such as a "claw" structure. Thus, our work opens up another range of possible structures to encounter in nature or to produce in experimental works.

II. THE THEORY

We, first, establish the key concepts from the Darboux process [31], modified here to operate on the NLSE. In dimensionless form, the target equation is written as

$$i\frac{\partial\psi}{\partial x}+\frac{1}{2}\frac{\partial^2\psi}{\partial t^2}+|\psi|^2\psi=0, \tag{1}$$

where the wave function $|\psi(x,t)|$ in Eq. (1) commonly describes the wave envelope. Variables x and t have different physical meanings, depending on traditions in each field. For example, in fiber optic applications [17], the variable x is the distance along the fiber while t is the retarded time in the frame moving with the pulse group velocity. On the other hand, in water wave applications [18,34], x is the dimensionless time while t is the distance in the frame moving with the group velocity. Nevertheless, this difference is largely unimportant, as simple linear transformation involving the group velocity allows us to change the equation and variables from one form to another. However, the choice of scaling factors in front of each term in Eq. (1) is unusually prescient; it is because of this particular choice that rogue wave clusters are spatiotemporally circular [28] and, likewise, the cascades we present below are essentially equilateral.

Applied to the NLSE, the Darboux method allows complicated solutions to be generated as nonlinear superpositions of lower-order forms. This procedure is well established in the literature and detailed specifics can be found elsewhere [28,33]. As a conceptual summary, the process creates n independent first-order components, the basic structure of which is uniformly determined by a zeroth-order seeding solution, and these are recursively combined into an order-n wave function. For example, a zero-background seeding input, $\psi_0=0$, generates simple solitons as individual first-order components, which then can be combined into multisolitonic structures [32].

More relevant to this work is the case when a plane wave, $\psi_0=e^{ix}$, is used as the seeding solution. The resulting first-order "building blocks" produced by the Darboux method are breather solutions, each with an identifying number j and three unique parameters. Two are simply regarded as shifts from a common origin along the x and t axes, which we label as x_j and t_j, respectively. The third is the eigenvalue l_j, which controls the shape of the first-order component. As the real part of l_j only affects the angle a solution makes with respect to the x and t axes, it can be omitted without loss of generality. However, the imaginary part is important for tuning the modulation period of the breather solution, as well as deciding to which axis the wave train is parallel.

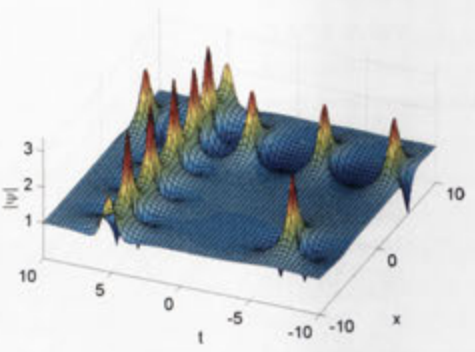

FIG. 1. (Color online) A third-order NLSE solution. Component 1 is an AB (aligned with the t axis) with parameters $l_1=0.8i$, $x_1=5$, and $t_1=0$. Component 2 is a Peregrine soliton with $l_2\approx i$ located at $x_2=-5$ and $t_2=-5$. Component 3 is a KM soliton (aligned with the x axis) with parameters $l_3=1.2i$, $x_3=0$, and $t_3=5$.

For purely imaginary l_j, we can define the modulation frequency of a component as $\kappa_j=2\sqrt{1+l_j^2}$. In the case when $0<\mathrm{Im}(l_j)<1$ (κ_j is real), the solution is an Akhmediev breather (AB), which is localized in x but periodic in t. When $\mathrm{Im}(l_j)>1$ (κ_j is imaginary), the component is a Kuznetsov-Ma(KM) soliton, which is localized in t but periodic in x. In the limit of $l_j\to i$ ($\kappa_j\to 0$), the period of each solution goes to infinity and, in the first-order scenario, a solitary peak remains. This quasirational solution is named the Peregrine soliton and has gained traction as a prototypical rogue wave. The three structures have been individually displayed previously [28]. In contrast, Fig. 1 here shows the result of the Darboux process for a third-order superposition involving a Peregrine soliton, an AB and a KM soliton, all in a single solution. For long periods, both the AB and KM soliton can be treated as chains of Peregrine soliton peaks. Indeed, in this limit ($\kappa_j\to 0$ for all j), every well-separated peak appears identical to a Peregrine soliton [17]. Thus, we shall henceforth refer to these as "rogue wave quanta" for convenience.

For the most part, higher-order multibreather solutions of the NLSE are intuitive and easy to comprehend. Although the recursive Darboux method is highly involved, the nonlinear superpositions of individual components are relatively recognizable, as in Fig. 1. However, there are a couple of exceptions to this rule. One is in the limit of two component eigenvalues becoming equal, called the degenerate case, and has been previously investigated in detail [35]. The other is the aforementioned higher-order rogue wave limit, when all component eigenvalues approach i. If x_j and t_j have been left alone, all components are located at the same origin, and the overall wave function appears as a complicated but solitary peak, exemplified by Fig. 2(a). The analytic expression for this solution of eighth order can be written in explicit form [36]. To give an idea of its complexity, we only mention here that it occupies 60 printed pages. When the shift parameters enter

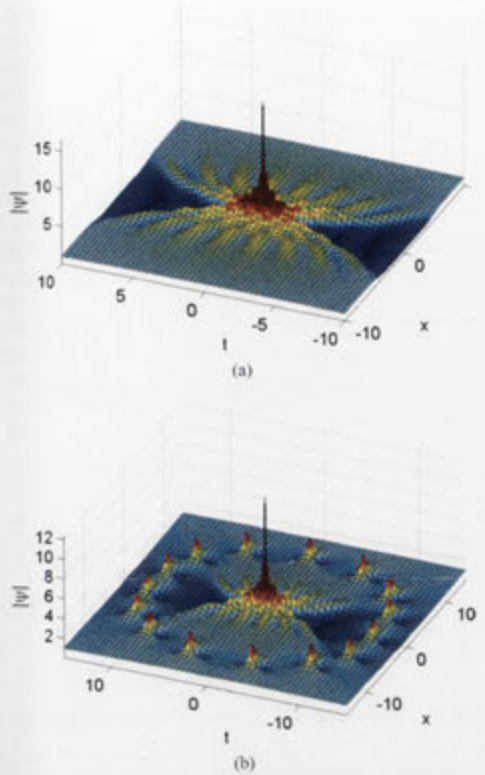

FIG. 2. (Color online) Eighth-order rogue waves. (a) Unshifted, with all components located at origin. The maximum amplitude is 17, as expected [22]. (b) Shifted, with $X_{18} = 5^{14}$.

into play, as in Fig. 2(b), the solution becomes significantly more lengthy.

To avoid unnecessary complications, we henceforth assume component modulation frequencies are ordered by index and are multiples of a common parameter; specifically that $\kappa_j = k_j\kappa$ and $k_1 < k_2 < \cdots < k_n$. If we further assume, without loss of generality, that all components are ABs before the $\kappa \to 0$ rogue wave limit, then it is known that component j donates j quanta to the resulting structure, such that an order n rogue wave can be considered to consist of $n(n+1)/2$ quanta [28]. For example, the eighth-order rogue wave in Fig. 2(a) is constructed from eight components but, in reality, it is a fusion of 36 quanta. This is a particularly deep property of NLSE breather solutions, as it indicates that two identical components cannot exist in the same domain without enforcing some asymmetry, essentially by way of contributing unequal numbers of rogue wave quanta to the total solution [35]. The simplest consequence of this property is that no rogue doublet has yet been identified.

Optimally, the way to show the existence of these quanta is to spatiotemporally separate components with the use of the shift parameters x_j and t_j, but this is a nontrivial task. In the $\kappa \to 0$ limit, any nonzero difference in shift between components is sufficient to repel them from each other to the infinity horizon of the (x,t) plane. However, if component shifts are made dependent on eigenvalue before the $\kappa \to 0$ limit is applied, according to the relation

$$x_j = \sum_{m=1}^{\infty} \kappa^{2(m-1)} X_{jm} = X_{j1} + X_{j2}\kappa^2 + X_{j3}\kappa^4 + \cdots,$$
$$t_j = \sum_{m=1}^{\infty} \kappa^{2(m-1)} T_{jm} = T_{j1} + T_{j2}\kappa^2 + T_{j3}\kappa^4 + \cdots, \tag{2}$$

where X_{jm} and T_{jm} are "shift expansion" coefficients that are independent of κ, then it is possible to generate new structures by carefully selecting which coefficients to make nonzero. This is a fundamentally difficult concept to understand due to the intricacies of limit theory; all total shifts are technically zero for $\kappa \to 0$, provided that $X_{j1} = T_{j1} = 0$, but the coefficients still survive by a unique form of dissemination into the solution. The result is that, by changing X_{12} (or T_{12}) alone, a second-order rogue wave becomes a rogue triplet with three quanta pulled apart [21]. Furthermore, for an order n rogue wave, X_{1n} pulls out a ring of $2n-1$ quanta, leaving behind a central rogue wave of order $n-2$. This is demonstrated by an unshifted eighth-order rogue wave in Fig. 2(a) becoming a circular rogue wave cluster in Fig. 2(b), with 15 peaks arrayed in a ring. Thus, for convenience, we henceforth refer to X_{jn} (or T_{jn}) as a shift of order n.

In previous work [28], only one component was shifted with respect to the others, which meant the structures were relatively easy to predict. With this restriction, an order n circular cluster forms only if X_{jn} or T_{jn} is nonzero. A higher-order shift does nothing to perturb a rogue wave, while a lower-order shift strips the ring entirely, leaving behind a rogue wave of order $n-2$. We now extend the investigation to include manipulations of several components at the same time.

General solutions of up to order 2 are analytically attainable with symbolic software, but those of higher order become computationally intractable and cumbersome to express. Instead, we numerically employ the Darboux method as a recursive algorithm. Although technically we can present exact rogue wave solutions explicitly, in reality these solutions are much too oversized to be printed in journal pages. On the other hand, the shifts can be defined as functions of κ such that, if the structure of a certain wave function remains unchanged as κ becomes arbitrarily small, the numerical solution can be considered to approximate a rogue wave with the shifts as free parameters of the solution. This is an efficient way of revealing the new higher-order rogue wave structures.

We emphasize here that all the results presented in the next section use the exact same method as in previous work [28]. The new physics lies instead in an updated appreciation of Eq. (2). Prior thought assumed that each component shift was equivalent to one additional degree of freedom in the rogue wave limit. Correspondingly, an order n wave function only depended on X_{jn} (and T_{jn}) to transform into a nontrivial circular cluster structure, while all other terms in the shift expansion were considered unimportant due to complicated cancellations in the mathematics of the Darboux procedure. It is now understood, guided by numerics, that each shift order relates to its own degree of freedom in the rogue wave limit, and the structures presented in the following section differ intrinsically from circular clusters.

III. THE GENERAL PRESCRIPTION FOR CASCADE SOLUTIONS

With component shifts defined as in Eq. (2), first-order rogue waves are easy to understand. They are represented by a single Peregrine soliton that can be translated anywhere in the (x,t) plane using our parameters X_{11} and T_{11}. Second-order rogue waves also appear to be fully understood; the first-order shifts X_{j1} and T_{j1} translate the global structure, provided they are the same across the components, while the second-order shifts X_{j2} and T_{j2} break the structure apart into a triplet [21].

Complications start with the third-order rogue waves. These have three pertinent orders of shift, namely X_{j1}, X_{j2}, and X_{j3}, as well as three components to move around. First-order shifts remain important only as translation variables for the global structure, and the third-order shifts appear to only separate a circular ring of five quanta from the main structure. As for the second-order shifts, they appear irrelevant when applied to one component alone [28] and, in most cases, equally unimportant when applied to multiple components. In the $\kappa \to 0$ limit, nonzero X_{j2} and T_{j2} values generally appear to expel five quanta to the infinity boundary of the (x,t) plane.

However, there is a nontrivial exception to the rule for these second-order shifts. Certain combinations of values can in fact arrange the solution into a stable structure with finite circumradius, where all six quanta are visible in the domain. For simplicity, we work only with shifts along the x axis and assume $X_{12} < X_{22} < X_{32}$, although the following results are easily generalized. If the three components are equally and sufficiently "spaced apart," such that $|X_{12} - X_{22}| = |X_{32} - X_{22}| \gg 0$, and the frequency ratio adheres to the rule $\kappa_1 : \kappa_2 : \kappa_3 = k_1 : \sqrt{(k_1^2 + k_3^2)/2} : k_3$, the third-order rogue wave becomes arrayed in triangular fashion, as seen in Fig. 3(a). The six constituent quanta are well separated and the distances between the adjacent peaks are the same. We call this a rogue wave cascade as, in this typical arrangement, an observer would witness an increasing number of rogue waves over time, beginning with one solitary peak and ending with n Peregrine solitons for an order n structure. Of course, "cascade" is merely a convenient label. As we show later in Sec. IV, this structure can be freely rotated. This means that the progression of incidents can occur in reverse or even that the most dangerous time to experience this event may be midway between the first and last quanta observed.

With regard to structural control, varying the value of "differential shifts" tunes the spacing between the peaks. Knowing that a value of zero for all these second-order shifts results in a typical third-order rogue wave, structurally similar to Fig. 2(a) with one central high-amplitude peak, it is evident that small differential shifts will result in transitional wave functions, such as in Fig. 3(b). The triangular array is still evident in this case, but the quanta are deforming from perfect Peregrine solitons as they nonlinearly interact and merge. However, it is clear from the numerics that shifts alone do not control the interpeak spacing. As the difference between k_1 and k_3 increases, the cascade becomes more spatiotemporally compressed. Likewise, the cascade expands in the domain as the frequencies become more similar in value. The reason for this is likely to be that an AB with higher frequency contains more peaks within a set length than a lower-frequency AB. Even though the rogue wave limit leaves behind only a small number of peaks, depending on component number, the proportions of the frequency ratio are still reflected in the spatiotemporal length of a cascade edge.

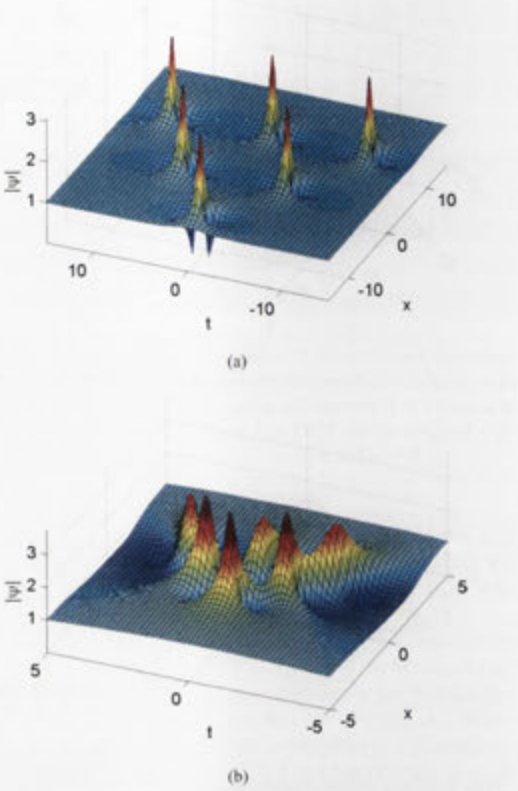

FIG. 3. (Color online) Third-order rogue wave cascades. Component frequencies κ_1, κ_2, and κ_3 have a ratio of $1 : \sqrt{2} : \sqrt{3}$. (a) Three components involving six rogue wave quanta are well separated: the shifts are $X_{12} = -25$, $X_{22} = 0$, and $X_{32} = 25$. (b) The three components are overlapping: the shifts are $X_{12} = -0.25$, $X_{22} = 0$, and $X_{32} = 0.25$.

Remarkably, the differences $|X_{12} - X_{22}|$ and $|X_{32} - X_{22}|$ do not have to be one to one for a rogue wave cascade to arise, despite the regularity in interpeak spacing. If d_j denotes the second-order differential shift between the components j and $j+1$, then it is possible to generalize the frequency ratio required for such a structure as

$$\kappa_1 : \kappa_2 : \kappa_3 = k_1 : \sqrt{\frac{d_2 k_1^2 + d_1 k_3^2}{d_1 + d_2}} : k_3. \tag{3}$$

For a rogue wave cascade to exist, there must be a perfect balance between shift parameters and the frequency ratio. Thus, for example, the set of parameters $X_{12} = -300$, $X_{22} = 0$, $X_{32} = 500$, and $\kappa_1 : \kappa_2 : \kappa_3 = 3 : \sqrt{15} : 5$ produces a rogue wave cascade in the $\kappa \to 0$ limit, appearing no different from Fig. 3(a) except in spatiotemporal size. But any deviation from

this prescription results in a structural transition from cascade to cluster, which is instantaneous in the $\kappa \to 0$ limit. As previously recognized [28], maintaining nonzero second-order shifts in this case forces a cluster ring to expand to the infinity horizon of the x and t axis, leaving behind one central Peregrine soliton. Therefore each rogue wave cascade is a specific case in parameter space and is highly unstable to general perturbation.

As mentioned by Ohta and Yang [29], higher-order cascades are also possible. For the Darboux method, this requires nothing more than a minor extension of the third-order prescription in Eq. (3). For simplicity, we continue to work only with x shifts and the ordering $X_{12} < X_{22} < \cdots < X_{n2}$, noting that the results can be generalized to include t shifts and rewritten for unorthodox orderings. Recalling that d_j is the second-order differential shift between components j and $j+1$, a rogue wave cascade is always produced in the $\kappa \to 0$ limit, provided that

$$\kappa_j : \kappa_{j+1} : \kappa_{j+2} = k_j : k_{j+1} : \sqrt{\frac{(d_j + d_{j+1})k_{j+1}^2 - d_{j+1}k_j^2}{d_j}}, \tag{4}$$

for all j ranging from 1 to $n-2$. This is the exact same ratio as given for the third-order case, only expressed in terms of the first two component frequencies. This recursive relation also indicates that the structural stability of a rogue wave cascade depends only on how the frequency and position of a component relates to its nearest neighbors. Provided this constraint holds, cascades are generated instead of clusters, such as the fifth-order example in Fig. 4(a) and the seventh-order example in Fig. 4(b). Curiously, the sides of the triangular arrays hint at some degree of curvature.

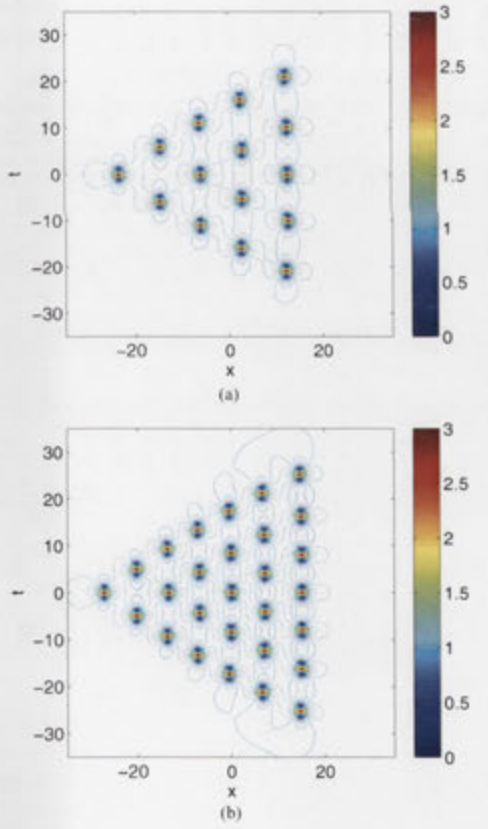

FIG. 4. (Color online) Higher-order rogue wave cascades generated recursively with Eq. (4). (a) Cascade of order 5 with $X_{j2} = 25j^2$ and $\kappa_1 : \kappa_2 = 1 : \sqrt{3}$. (b) Cascade of order 7 with $X_{j2} = 25(j-4)$ and $\kappa_1 : \kappa_2 = 1 : \sqrt{2}$.

IV. CASCADE PERTURBATIONS AND "CLAWLIKE" STRUCTURES

So far we have established that, modified in isolation, shifts of order n generate circular clusters and second-order shifts are responsible for cascade solutions, provided a perfect balance is achieved with component frequency ratios. This is consistent with a second-order rogue wave, as a rogue triplet can be considered as both a cluster and cascade simultaneously. However, new third-order rogue wave structures, previously unreported in the literature, can be produced by manipulating shifts of second and third order simultaneously. For example, beginning with the cascade in Fig. 3(a), adding a third-order

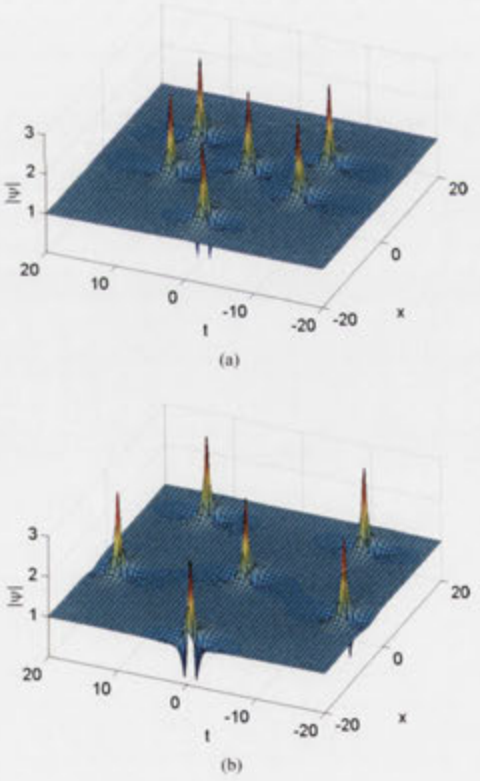

FIG. 5. (Color online) Perturbations of a third-order rogue wave cascade with $X_{12} = -25$, $X_{22} = 0$, $X_{32} = 25$, and $\kappa_1 : \kappa_2 : \kappa_3 = 1 : \sqrt{2} : \sqrt{3}$. (a) An "arrow" structure with $X_{23} = 250$. (b) A circular cluster pointing in the negative x direction with $X_{23} = 2500$.

shift to a component can deform the triangular array into an "arrow" arrangement, shown in Fig. 5(a), where three rogue wave pairs are arranged in parallel. Continuing to increase this third-order shift eventually draws one of the rogue wave quanta into the center, forming the familiar cluster shown in Fig. 5(b). In fact, larger values beyond this point will simply expand the ring of the cluster as if there were never a rogue wave cascade. This implies that structures produced by shifts of different order can coexist, but one will dominate the NLSE solution, depending on parameter values. In our previous work [28], we did not generate rogue wave cascades, so a cluster was free to grow from a central high-order peak. However, if a rogue wave cascade has been successfully produced by the right ratio of modulation frequencies and second-order shifts, then a third-order shift must be sufficiently large in order to perturb the cascade into a cluster.

The structures shown in Fig. 5 indicate how a cascade transforms into a cluster when both are "pointed" in the same direction. This requires nothing more unintuitive than a minor rearrangement of rogue wave quanta in the domain. However, if the third-order shift applied to the solution in Fig. 3(a) is reversed in sign, the three peaks located in the $x < 0$ half-plane must eventually flip with respect to the t axis in order to form a cluster that is a reflection of the one in Fig. 5(b). To achieve this, the three rogue wave quanta must merge into a second-order rogue wave, as shown in Fig. 6(a). We caution that the shift value at which this transition occurs is critically dependent on the proximity of κ to zero in the numerical process. Thus, we provide the value of κ used whenever detailing this transitional structure, which is unnecessary in all other cases. Nonetheless, this is a legitimate new solution of the NLSE, and we refer to it as a "claw" structure due to its spatiotemporal appearance. Furthermore, in some respects this solution is also a semicircular cluster; it has three peaks more than a solitary second-order rogue wave, all provided by the third component, but is four peaks short of a fourth-order cluster, which would be introduced by a fourth component. It is, thus, to be expected that claw structures of higher order also exist, albeit with more numerous "digits." Regardless, a sufficiently large third-order shift once again completely converts the cascade into a circular cluster, shown in Fig. 6(b), at which point any increase of shift magnitude will extend the radius of the ring.

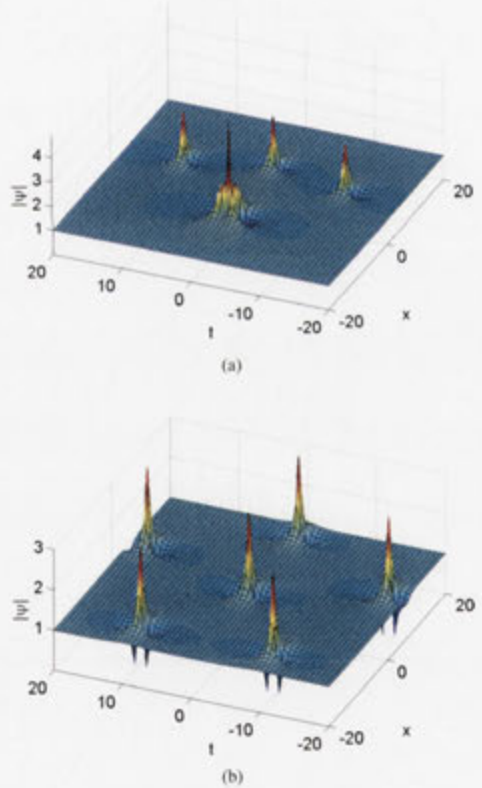

FIG. 6. (Color online) Perturbations of a third-order rogue wave cascade with $X_{12} = -25$, $X_{22} = 0$, $X_{32} = 25$, and $\kappa_1 : \kappa_2 : \kappa_3 = 1 : \sqrt{2} : \sqrt{3}$. (a) A "claw" structure with $X_{23} \approx -162.25$. This value correctly generates the solution numerically when $\kappa = 8 \times 10^{-3}$. (b) A circular cluster pointing in the positive x direction with $X_{23} = -2500$.

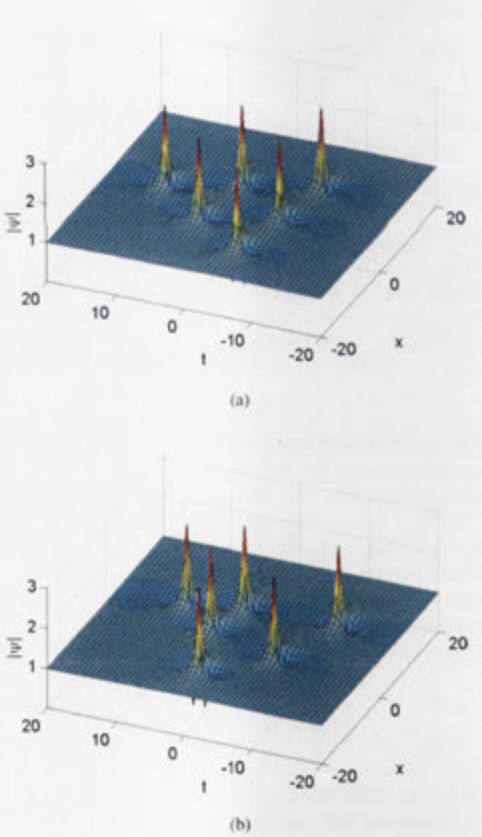

FIG. 7. (Color online) Third-order rogue wave cascades incorporating t-axis shifts, with $\kappa_1 : \kappa_2 : \kappa_3 = 1 : \sqrt{2} : \sqrt{3}$. (a) A rotation with $X_{j2} = 25(j-2)\cos(\pi/3)$ and $T_{j2} = 25(j-2)\sin(\pi/3)$. (b) A perturbation with $X_{j2} = 25(j-2)$ and $T_{23} = -125$.

As previously mentioned, the cascade solution is precariously dependent on the ratio of second-order shifts. It is possible to include t axis shifts of this order as well, but the vectorial directions of all second-order shifts must be aligned. If this is done, the rogue wave cascade can be spatiotemporally rotated to point in any direction, as shown in Fig. 7(a). However, no such restriction exists for third-order shifts. Hence, a cascade formed by second-order x-axis shifts can be perturbed by third-order t-axis shifts. This opens up a new range of asymmetrical rogue wave solutions, such as is shown in Fig. 7(b). As usual, a sufficiently large third-order shift will expand the structure into a circular cluster, neutralizing the effect of any second-order shifts.

By this stage, the possible variety of third-order rogue wave solutions is reasonably well understood. However, each additional increase of solution order introduces a greater degree of complexity. From the examples in Fig. 4, it is evident that second-order shifts can produce cascade solutions of any order. It also follows that a shift of order n applied to any component can perturb the structure and still produce a $\kappa \to 0$ rogue wave solution of the NLSE. However, the intermediate orders of shift are also expected to produce novel and elegantly arranged structures. Even without cataloguing all these solutions, we can still show numerically that the results of the Darboux process adhere to certain patterns.

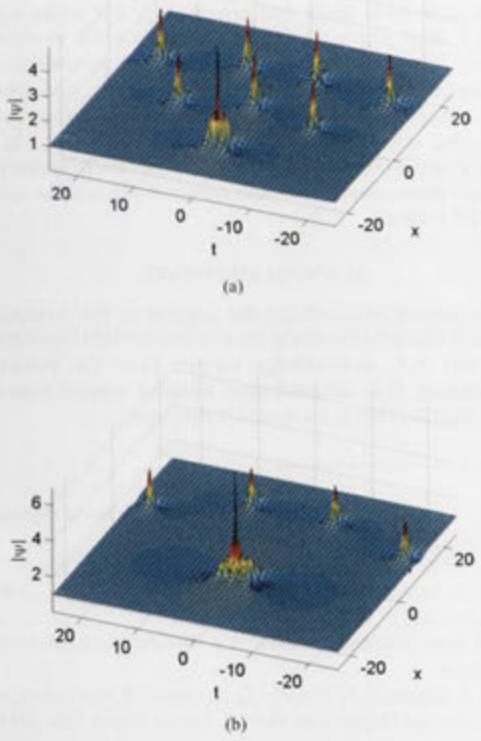

FIG. 8. (Color online) Fourth-order rogue wave claws with $X_{12} = -75$, $X_{22} = -25$, $X_{32} = 25$, $X_{42} = 75$, and $\kappa_1 : \kappa_2 : \kappa_3 : \kappa_4 = 1 : \sqrt{2} : \sqrt{3} : \sqrt{4}$. (a) Two rows of rogue wave quanta, where $X_{23} = X_{33} \approx -425$. These values correctly generate the solution numerically when $\kappa = 8 \times 10^{-3}$. (b) One row of rogue wave quanta, where $X_{23} = X_{33} \approx -1042.5$ and $X_{34} \approx -13100$. These values correctly generate the solution numerically when $\kappa = 2 \times 10^{-2}$.

Recognizing that the clawlike structure in Fig. 6(a) was generated by applying a third-order shift to the middle component so it approached the first, the middle two components of a fourth-order cascade can similarly be pushed towards the apex. In this process, three quanta belonging to two components merge and form a second-order rogue wave. The entire solution, shown in Fig. 8(a), looks identical to the claw in Fig. 6(a), except for an additional four rogue wave quanta that form a second row. Furthermore, by applying a fourth-order shift to the structure, specifically pushing the third component towards the first two, it is possible to construct a claw with only one row of quanta, shown in Fig. 8(b). The trade-off is that the focal peak transforms from a second-order to a third-order rogue wave, due to fusion with three extra rogue wave quanta. Thus, we show that rogue claw structures are generic across all orders of nonlinear superposition and display predictable features.

V. CONCLUSION

In summary, our main results are as follows:

(1) We have shown the existence of a third-order triangularly arrayed multi-rogue-wave solution, generated numerically with the recursive Darboux method. These have recently been found as particular examples by Ohta and Yang [29], although we have further identified a general prescription for these "cascade" solutions, which involves prelimit component frequencies and second-order shifts.

(2) We have extended the prescription such that the Darboux method allows us to produce rogue wave cascades of any order. In all such cases, the shifts required are still of second order. Furthermore, as shifts of order n produce circular clusters for an order n solution, this suggests that shift orders between 2 and n may be responsible for their own as-yet-undiscovered unique structures.

(3) We have further explored third-order rogue wave cascades and presented new solutions of the NLSE by including third-order terms in shifts. While the cascade prescription rigidly restricts the choice of second-order terms in shifts, the third-order terms are independent and can generate a myriad of perturbed forms. The relative strength of second-order shifts with respect to third-order shifts determines how similar the hybrid structure is to a cascade or cluster.

(4) We have shown that the new forms are not trivial and that Peregrine soliton peaks can merge to produce rather unexpected arrangements. In particular, we reveal new clawlike structures. These can also be considered as "semicircular" clusters and are indicative of an alternative class in the cluster hierarchy.

From a geometrical perspective, rogue wave cascades enrich the pattern of higher-order NLSE solutions. It is remarkable that the particular choice of NLSE in Eq. (1) produces limiting breather solutions that include not only circularly symmetric arrangements, but arrays in the shape

of equilateral triangles as well. Furthermore, these structures are all associated with certain orders of shift in Eq. (2). This allows us to speculate that other elegant arrangements may also be possible for rogue waves of order 4 and beyond, simply by constraining relative component frequencies and other orders of shift in some manner. These prescriptions can only be proved beyond doubt by analytics, but the fact that these relations and their effect on structure are numerically well evident implies that a good understanding has been achieved already.

With regard to experiment, cascade solutions are important as the first theorized rogue wave structures beyond order 3 that do not contain any substructures other than Peregrine solitons. This means that experimentalists can produce high-order arrangements without facing unduly large amplitudes. This is particularly beneficial in water wave tanks [18,19] as it is thought that wave breaking may limit the crest height with respect to the pulse width [37]. The scaling transform [20] can alleviate some of the pressure from breaking by decreasing the solution amplitude, but this comes at the cost of increasing the spatiotemporal width, which is not ideal in a tank of finite length. For this reason, it is expected that it will be easier to produce cascades than circular clusters in water.

The triangular arrangement of first-order rogue waves in a cascade may also be important in optics. In one sense, such a structure has already been seen in fibre, arising from a perturbed plane wave due to beating laser frequencies [38]. Despite minor variations in shape and the unavoidable periodicity of experimental pulse sequences, the triangular nature of the observed arrays is unmistakable. These observations are naturally linked to higher-order modulation instability. However, it will not be surprising if an ideal cascade emerges from increasing the beat period, much as an Akhmediev breather served as a pragmatic forerunner of an ideal rogue wave [17]. Furthermore, this triangular symmetry may be far more fundamental to nonlinear optics in general, with similar shapes produced experimentally from wave interactions in transverse pattern systems [39,40].

In any case, the increased number of peaks in a rogue wave cascade relative to that of circular cluster could prove relevant to the real world in its own way. If encountered in the ocean, an order n rogue wave cascade has $n(n+1)/2$ chances to impact a vessel, as opposed to $2n$ chances for a circular cluster (where $n > 2$). Worse yet, if the event is first encountered at a spatiotemporal vertex, the sea will only become rougher. Furthermore, considering that the possibility of peaks arising stochastically becomes smaller for higher orders, a cascade may be the typical form of complex rogue wave encountered in the ocean, much like the ubiquitous "three sisters" phenomenon. As for photonics, producing a cascade may be a way to transmit signals produced by the same initial condition to different locations along the fiber. Alternatively, rogue wave cascades could be used to load-test materials in progressive steps with intense pulses. Whatever the eventual application, a detailed knowledge of possible rogue wave superpositions is no less important than that of multi-soliton solutions. While we have a complete understanding of the latter, conveniently aided by solitonic persistence in the time domain, multi-rogue-wave solutions are far more diverse and still require significant efforts to both comprehend and categorize.

In conclusion, we have studied a subset of higher-order NLSE rogue wave solutions that manifests itself as a triangular array of first-order rogue waves. We have also shown that the free real parameters that govern these structures are independent from those that produce circular rogue wave clusters. With particular emphasis on third-order structures, we have shown that careful modification of all parameters can produce cluster, claw-like and cascade structures, with a wide variety of intermediate patterns included. In this way, we move yet another step closer to understanding the full hierarchy of NLSE rogue wave solutions, which progressively appears to be much more complicated than the painfully familiar world of NLSE solitons.

ACKNOWLEDGMENTS

The authors acknowledge the support of the Australian Research Council (Discovery Project number DP110102068). N.A. and A.A. acknowledge support from the Volkswagen Stiftung. N.A. acknowledges financial support from an Alexander von Humboldt Award (Germany).

[1] P. Müller, C. Garrett, and A. Osborne, Oceanography **18**, 66 (2005).

[2] I. Nikolkina and I. Didenkulova, Nat. Hazards: Earth Syst. Sci. **11**, 2913 (2011).

[3] E. Pelinovsky, E. Shurgalina, and N. Chaikovskaya, Nat. Hazards Earth Syst. Sci. **11**, 127 (2011).

[4] I. Didenkulova, Boreal Environ. Res. **16**, 138 (2011).

[5] K. B. Dysthe and K. Trulsen, Phys. Scr., T **82**, 48 (1999).

[6] N. Akhmediev, A. Ankiewicz, and J. M. Soto-Crespo, Phys. Rev. E **80**, 026601 (2009).

[7] H. S. Chiu, K. W. Chow, and C. H. Tsang, in *Proceedings of the 33rd IAHR Congress, 2009* (Curran Associates, Inc., Red Hook, NY, 2010), pp. 6232–6239.

[8] A. R. Osborne, *Nonlinear Ocean Waves and the Inverse Scattering Transform* (Elsevier, Amsterdam, 2010).

[9] E. Pelinovsky and C. Kharif, *Extreme Ocean Waves* (Springer, Berlin, 2008).

[10] C. Garrett and J. Gemmrich, Phys. Today **62**, 62 (2009).

[11] D. R. Solli, C. Ropers, P. Koonath, and B. Jalali, Nature **450**, 1054 (2007).

[12] M. Shats, H. Punzmann, and H. Xia, Phys. Rev. Lett. **104**, 104503 (2010).

[13] V. B. Efimov, A. N. Ganshin, G. Kolmakov, P. McClintock, and L. Mezhov-Deglin, Eur. Phys. J. Special Topics **185**, 181193 (2010).

[14] Y. V. Bludov, V. V. Konotop, and N. Akhmediev, Phys. Rev. A **80**, 033610 (2009).

[15] D. Peregrine, J. Austral. Math. Soc. Ser. B **25**, 16 (1983).

[16] V. Shrira and V. Geogjaev, J. Eng. Math. **67**, 11 (2010).

[17] B. Kibler, J. Fatome, C. Finot, G. Millot, F. Dias, G. Genty, N. Akhmediev, and J. M. Dudley, Nat. Phys. **6**, 790 (2010).

[18] A. Chabchoub, N. P. Hoffmann, and N. Akhmediev, Phys. Rev. Lett. **106**, 204502 (2011).
[19] A. Chabchoub, N. Hoffmann, M. Onorato, and N. Akhmediev, Phys. Rev. X **2**, 011015 (2012).
[20] N. Akhmediev, A. Ankiewicz, and M. Taki, Phys. Lett. A **373**, 675 (2009).
[21] A. Ankiewicz, D. J. Kedziora, and N. Akhmediev, Phys. Lett. A **375**, 2782 (2011).
[22] A. Ankiewicz, P. Clarkson, and N. Akhmediev, J. Phys. A-Math. Theor. **43**, 122002 (2010).
[23] C. Kharif and E. Pelinovsky, Eur. J. Mech. B-Fluids **22**, 603 (2003).
[24] K. Dysthe, H. E. Krogstad, and P. Müller, Annu. Rev. Fluid Mech. **40**, 287 (2008).
[25] F. T. Arecchi, U. Bortolozzo, A. Montina, and S. Residori, Phys. Rev. Lett. **106**, 153901 (2011).
[26] P. Dubard, P. Gaillard, C. Klein, and V. Matveev, Eur. Phys. J. Spec. Top. **185**, 247 (2010).
[27] P. Gaillard, J. Phys. A **44**, 5204 (2011).
[28] D. J. Kedziora, A. Ankiewicz, and N. Akhmediev, Phys. Rev. E **84**, 056611 (2011).
[29] Y. Ohta and J. Yang, Royal Soc. London Proc. Ser. A **468**, 1716 (2012).
[30] P. Dubard and V. B. Matveev, Nat. Hazards Earth Sys. **11**, 667 (2011).
[31] V. B. Matveev and M. Salle, *Darboux Transformations and Solitons* (Springer-Verlag, Berlin, 1991).
[32] N. Akhmediev and N. V. Mitskevich, IEEE J. Quantum Electron. **27**, 849 (1991).
[33] N. Akhmediev, J. M. Soto-Crespo, and A. Ankiewicz, Phys. Lett. A **373**, 2137 (2009).
[34] H. C. Yuen and B. M. Lake, Ann. Rev. Fluid Mech. **12**, 303 (1980).
[35] D. J. Kedziora, A. Ankiewicz, and N. Akhmediev, Phys. Rev. E **85**, 066601 (2012).
[36] P. Gaillard (2012), preprint: hal-00664052, version 1-28 Jan 2012.
[37] A. V. Babanin, T. Waseda, I. Shugan, and H.-H. Hwung, ASME Conf. Proc. **2**, 409 (2011).
[38] M. Erkintalo, K. Hammani, B. Kibler, C. Finot, N. Akhmediev, J. M. Dudley, and G. Genty, Phys. Rev. Lett. **107**, 253901 (2011).
[39] U. Bortolozzo, L. Pastur, P. L. Ramazza, M. Tlidi, and G. Kozyreff, Phys. Rev. Lett. **93**, 253901 (2004).
[40] P. L. Ramazza, U. Bortolozzo, and L. Pastur, J. Opt. A: Pure Appl. Opt. **6**, S266 (2004).

Epilogue

Triangular rogue wave cascades possibly remain the most enigmatic of NLSE solutions presented within this thesis [4]. This is simply because, unlike circular clusters [2] and the more complicated geometries [6] presented in Chapter 6, it does not appear to be difficult to obtain these arrangements. A cascade inherently consists of nothing but first-order Peregrine breathers, with no statistically improbable fusions involved. Yet the physics-based implementation of the Darboux scheme in this thesis does not hint at the geometric array, on account of its 'existence condition' being extremely inaccessible to arbitrary selection of shift and frequency parameters.

This methodological disadvantage with respect to a Wronskian-based procedure [85, 88] was mentioned previously in the epilogue of Chapter 2, but it is worth stressing here how remarkable that fact is. Indeed, the basic high-order rogue wave solution of the alternative scheme, with all 'phase' parameters set to zero, is a cascade [86]. This means that the complicated linear relation detailed in this chapter (i.e. Eq. (4)) can be considered a natural parametric 'origin' under a particular mathematical redefinition of nonlinear superposition.

Of course, both implementations of Darboux transformations are fundamentally useful because they are able to generate select solutions of the NLSE in exact form. This is only possible because specific mathematical variables, so-called component functions, can be defined analytically throughout space and time. In contrast, a lot of NLSE solution analysis operates on numerical propagation methods applied to an initial profile, with the Split-step Fourier Method (SSFM) as one commonly-used possibility [104, 105]. This is because the vast majority of interesting possible initial conditions will not avoid descending into endless chaotic behaviour and cannot be written in closed form. Even then, breather phenomena are still notoriously difficult to examine, as the slightest numerical error is equivalent to a perturbation of the background that eventually surges into false peaks of modulational instability [106]. Dissociating true events from false artefacts is complicated, as Fig. 4.1a demonstrates with the numerical propagation of an initial analytic profile for the Peregrine breather.

Nonetheless, the point here is that triangular cascades are approximated with surprising ease, even in the case of numerical propagation, as exemplified by the use of a 'beating-type' perturbation as an initial condition in Fig. 4.1b. Indeed, structures like circular clusters may require particularly complicated profiles, but cascade-like wavefunctions do not appear to need them. In some cases, it is even easier to generate the perfectly equidistant triangular arrangement than it is to fuse Peregrine breathers together [107]. It is simply sufficient to excite so-called higher-order modulational instability processes, as experimentally demonstrated in optical fibre [76]. So perhaps this is why wavefunctions simulating cascades appear so often in the literature. Truly localised rogue wave cascades probably possess initial conditions that are the closest approximations to beating-type waveforms. These latter oscillations are ubiquitous in nature and experiment, formed in one instance by interference from lasers of different frequencies [13]. However, this hypothesis for cascade prevalence

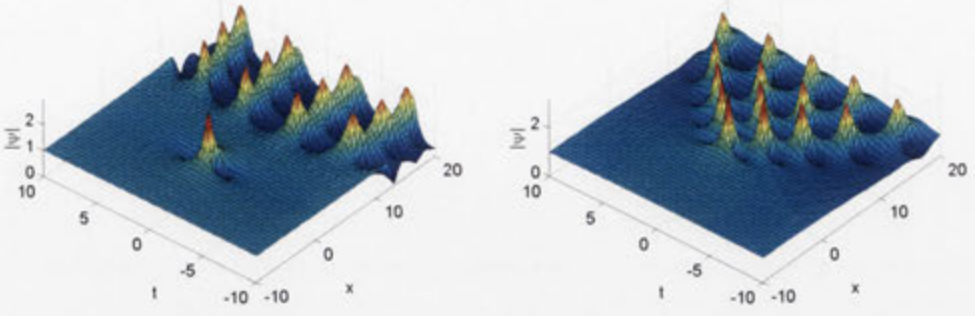

(a) (b)

Figure 4.1: Numerical solutions generated via an adaptive time-step implementation of the Split-step Fourier Method (SSFM), with an error tolerance of 1%. (a) Initial condition is the profile of an unshifted rogue wave (i.e. Eq. (6) in the degenerate paper [3]) at $x = -10$. (b) Initial condition is a beating perturbation, $\psi(t) = (1 + 0.01\exp(i\omega t))\exp(ix)$ with $\omega = 200\pi/(3^7 - 1)$, at $x = -10$. The influence of errors does not visibly arise for this case until outside the depicted domain.

will require further mathematical study to confirm.

Ultimately, while the novelty of cascade solutions is arguable, their development is a step towards developing a multi-rogue wave hierarchy. Furthermore, attaining an understanding of how they function in the Darboux scheme is not in vain, for it is the subsequent concept of hybridisation, in this chapter, that is most significant for the field. Certainly, prior to this publication, exact rogue wave solutions were always reported to possess clear symmetries. Arbitrary arrangements could seemingly be constructed numerically, but were never properly isolated from noisy and chaotic backgrounds. In contrast, with the revelation that the existence condition for a cascade typically depends on shifts proportional to a different power of modulation frequency than that for a circular cluster, it is now known that the 'triangularity' and 'circularity' of a multi-rogue solution with fixed frequency ratio can be tuned independently of each other. Based on this concept, higher-order versions of semi-circular clusters have since been presented [89]. Moreover, this understanding hints at the fact that many more arbitrary arrangements of 6, 10, 15, 21 or 28 Peregrine breathers (and so on) can be classed as legitimate rogue wave solutions of the NLSE. The promising possibilities of hybridisation are discussed further in Chapter 6.

Chapter 5

The Phase Patterns of Higher-order Rogue Waves

Prologue

At this stage of the thesis, both circular cluster [2] and triangular cascade [4] arrangements of rogue wave 'quanta' have been presented. Chronologically, the discovery of the latter set was particularly useful as it hinted towards the construction of many more fundamental NLSE solutions that could be catalogued according to relevant parametric relations. This hierarchy, as the core result of this thesis, is discussed in Chapter 6. However, a few extra matters need to be addressed first, relating to the observable behaviour of these extreme events.

Most importantly, the NLSE only describes the evolution of a wave envelope in both hydrodynamic and optical contexts, which means that the underlying carrier wave has largely been neglected thus far in the thesis. This is not necessarily a severe oversight with electromagnetic waves, as frequencies are typically so high that only squared amplitudes (a.k.a. intensities) are measured. Discerning phase information generally requires interferometry. However, the wavelength of the carrier is typically much larger in ocean waves, often with multiple crests distinguishable under a peak of envelope modulation [62]. It is thus of interest to consider how a multi-rogue wave structure modifies the underlying background beyond its simple amplitude effects, especially when the phase-dependent steepness is arguably the real 'destructive' characteristic [57, 108].

This chapter, as a published manuscript [5], explores complex-plane trajectories of high-order rogue wave solutions, albeit without the plane wave factor. It is an extension of an earlier investigation regarding the Peregrine soliton, which concluded that an observer hit by a first-order rogue wave would experience a homoclinic orbit in phase space, otherwise known as an aggregate phase shift of 2π [109]. In physical terms, this represents individual crests in a carrier wave being rapidly forced along their sequential wavetrain by one wavelength [110], with hypothetically violent consequences. This is only compounded by the fact that rogue waves of order n are capable of applying a maximum phase shift of $2\pi n$. However, this is somewhat mitigated by the fact that these effects are demarcated by the zero-amplitude envelope troughs of the spatiotemporally localised solutions, realised as points of unusually calm ocean.

Turning to a more theoretical perspective, analysis of this type proves particularly convenient for examining the 'anatomy' of a rogue wave under potentially confusing amplitude information. For instance, it is revealed in this chapter how each quantum maintains its distinct localisation, even in a fused triplet form. The individual Peregrine breathers always arrange themselves to avoid surpassing the maximum allowable phase shift of $2\pi n$ with their overlap. Therefore, considering that the total phase shift for each quantum also happens to occur over a short time period, it may be possible to probe intensifying rogue wave behaviour in a chaotic wave field via this methodology, potentially avoiding a particularly disastrous convergence of individual extreme effects.

IOP PUBLISHING JOURNAL OF OPTICS
J. Opt. **15** (2013) 064011 (9pp) doi:10.1088/2040-8978/15/6/064011

The phase patterns of higher-order rogue waves

David J Kedziora, Adrian Ankiewicz and Nail Akhmediev

Optical Sciences Group, Research School of Physics and Engineering, The Australian National University, Canberra ACT 0200, Australia

E-mail: djk105@rsphysse.anu.edu.au

Received 14 January 2013, accepted for publication 19 April 2013
Published 4 June 2013
Online at stacks.iop.org/JOpt/15/064011

Abstract
We investigate the phase profiles of rogue wave solutions to the nonlinear Schrödinger equation, all produced via the Darboux transformation scheme. We focus specifically on the second-order rogue wave, in both origin-centred and fissioned form, and extrapolate the results for higher-order structures. In particular, a rogue wave solution of order n can be decomposed into $n(n+1)/2$ Peregrine breathers, and each peak applies an additive phase shift of 2π to the underlying plane wave background. Yet it is evident that no evolution path can be phase shifted beyond $2\pi n$. We show that a fused rogue wave arranges its components to avoid any contradiction in this matter. We also show that the phase profile for any structure in the rogue wave hierarchy can be determined by examining phase bifurcations marked by zero-amplitude troughs.

Keywords: rogue waves, nonlinear optical effects, phase shifts

(Some figures may appear in colour only in the online journal)

1. Introduction

As with any other wave, rogue waves are characterized by both their amplitude and phase profiles. Yet, in popular culture, there is a fixation on the maximum amplitude of the extreme event, considering that this is the parameter that usually justifies its name. Indeed, a rogue wave is supposed to have a higher amplitude than other waves in the same field, as is well established in oceanography with the '2.2 times significant wave height' rule [1, 2]. Consequently, most theoretical treatments of a rogue wave focus on amplitude envelopes, rarely going beyond simple acknowledgment of the underlying carrier wave and its frequency. In many ways this is an oversight, taking into account that the maximum amplitude of the envelope is not necessarily the maximum amplitude of the carrier. Moreover, the second parameter that characterizes the killing strength of a rogue wave is its steepness. This is described by the front slope of each oscillation peak in the carrier. Naturally, the steepness not only depends on the amplitude profile of the envelope but also is strongly dependent on its phase profile. It follows that an amplitude investigation has to always be supplemented by a study of phase in order to truly estimate the impact of a rogue wave.

Most fundamental theoretical descriptions of a freak wave revolve around the nonlinear Schrödinger equation (NLSE). In the case of its simplest rogue wave solution, commonly referred to as either a Peregrine breather or Peregrine soliton [3], the phase profiles are relatively simple [4]. Crucially, there is a phase shift of 2π along its central path of evolution. This significant phase shift makes the wave much steeper than if we ignored it. Moreover, the Peregrine breather is generally considered as only a first-order rogue wave solution and can undergo processes of nonlinear superposition to become more complicated. For the simplest 'origin-centred' higher-order solutions [5], the phase shift is intuitively additive. For example, the central evolution path is shifted by 4π for second order, 6π for third order, and so on [6]. As the value of a phase shift increases, the corresponding steepness becomes more drastic. Furthermore, higher-order solutions attain more degrees of freedom pertaining to the shape of their amplitude profiles [7–9], resulting in phase-shift profiles that are also complicated functions of time and space, often involving a number of possible phase jumps across the entire rogue wave

J. Opt. **15** (2013) 064011 D J Kedziora *et al*

pattern. The phase shifts of such arrangements have not been paid much attention before, but they certainly require special study.

This work provides some initial contribution towards developing this useful knowledge. Although the above ideas are contextualized for water waves, they are also equivalently suitable in optics. Indeed, the carrier-envelope phase difference becomes of crucial significance for ultra-short pulses [10, 11]. Rogue waves can also be short enough in duration for this parameter to play a serious role in determining interactions. Moreover, due to the complicated arrangements possible within the rogue wave hierarchy [8, 9], individual peaks within the array may have different phases and consequently different effects. Thus it is not just the aggregate phase shift that matters for the rogue wave event. The whole phase function across the entire wave must be examined carefully.

2. Theory

As mentioned in section 1, we are primarily concerned with rogue wave solutions of the NLSE. This equation serves as a basic model for nonlinear waves in many fields, including fibre optics research [12, 13]. In dimensionless form, the 1D NLSE is written as

$$\mathrm{i}\frac{\partial\psi}{\partial x}+\frac{1}{2}\frac{\partial^2\psi}{\partial t^2}+|\psi|^2\psi=0, \tag{1}$$

with the complex function $\psi(x,t)$ typically describing the wave envelope. The evolution variable here is x, based on the normalized distance along a fibre used in optical conventions, and t is accordingly defined as the retarded time in the frame moving with the pulse group velocity. However, simple linear transformation also gives the NLSE validity in water wave applications [14–16], where x is interpreted as the normalized time and t is the distance in the frame moving with the group velocity.

An effective manner of producing solutions to equation (1) arises from Darboux transformation theory [17, 18], where a 'seeding solution' generates a set of multi-parameter component functions. These can be nonlinearly superimposed n times on the seeding function to produce a new order n solution of the NLSE. The mathematical details of this recursive process have been comprehensively presented previously [19, 8]. Relevant to this work, a plane wave produces a 'breather family' of solutions that encapsulate, for first order, Akhmediev breathers (ABs), Kuznetsov–Ma (KM) solitons and the Peregrine breather. Again, these structures and their features have been displayed elsewhere [8]. It is sufficient to state that ABs are localized in x but periodically modulate the background plane wave amplitude along t, KM solitons are localized in t but modulate along x, and a Peregrine breather consists of one isolated high-amplitude peak that remains when either of the two other solutions have their modulation frequency reduced to zero. This wavefunction adheres to important criteria in that $|\psi|$ approaches the same constant for $x\to\pm\infty$ and $t\to\pm\infty$. The solution, evolving from an infinitesimal perturbation of a plane wave at $x=-\infty$, is thus considered to be a prototypical rogue wave and is shown in figure 1(a).

Originally, in the early days of NLSE rogue wave research, components were superimposed with central (x,t) coordinates in alignment [5]. The phase profiles of these 'origin-centred' solutions are examined in section 3, and these are typically considered to be traditional rogue wave solutions of the NLSE. However, once the intricacies of the zero-frequency limit were understood, individual components could be shifted along either the x or t axis, leading to many new non-traditional rogue wave configurations [8, 9]. Indeed, these component shifts revealed that a second-order rogue wave forms from the fusion of three Peregrine solitons [7], as opposed to the two that would normally be assumed from the theory of linear superposition. We henceforth describe structures formed from this concept as 'fissioned' high-order rogue waves, so as to avoid confusing phase shifts with component shifts in this work. This may in fact be an appropriate label for the more complicated structures, due to proposed particle physics associations [8, 20]. In any case, their phase-shift profiles are examined in section 4.

It is also noted that the 1D NLSE is integrable and possesses a Lax pair, which is why a Darboux transformation exists and the equation can be solved analytically. Indeed, equations have been previously provided for all basic second-order solutions in the NLSE breather family [21], and rogue wave solutions in particular possess elegant quasi-rational functional forms [5, 22]. However, higher-order solutions become cumbersome to express as equations [23] and computational investigation remains optimal for generating results. It follows that a numerical study of rogue wave solutions is highly dependent on graphical examination. While contrary to a predominant analytical culture in exploring the NLSE, such pictorially based numerical evaluations were vital in discovering both circular rogue wave arrays [8] and general parametric restrictions for the production of rogue wave cascades [9], surpassing current analytical limitations in both cases. Hence, throughout this work, we present phase profiles of rogue wave solutions that were generated numerically with the recursive Darboux scheme, based on an algebraic implementation of the theory in the appendix. However, when possible, we will also give the exact equation for the solution in general form

$$\psi_n(x,t)=\left[(-1)^n+\frac{G_n+\mathrm{i}H_n}{D_n}\right]\mathrm{e}^{\mathrm{i}x}. \tag{2}$$

3. Origin-centred rogue waves

We begin by presenting a first-order rogue wave in figure 1(a), for which three specific evolution paths are highlighted. The analytical equation for the structure, using the form in equation (2), is

$$\begin{aligned} G_1&=4, \qquad H_1=8(x-x_1),\\ D_1&=1+4(x-x_1)^2+4(t-t_1)^2. \end{aligned} \tag{3}$$

where shifts x_1 and t_1 can be set to 0, as has been done for figure 1. Shown from an alternative angle in figure 1(b), trace I

J. Opt. **15** (2013) 064011 D J Kedziora *et al*

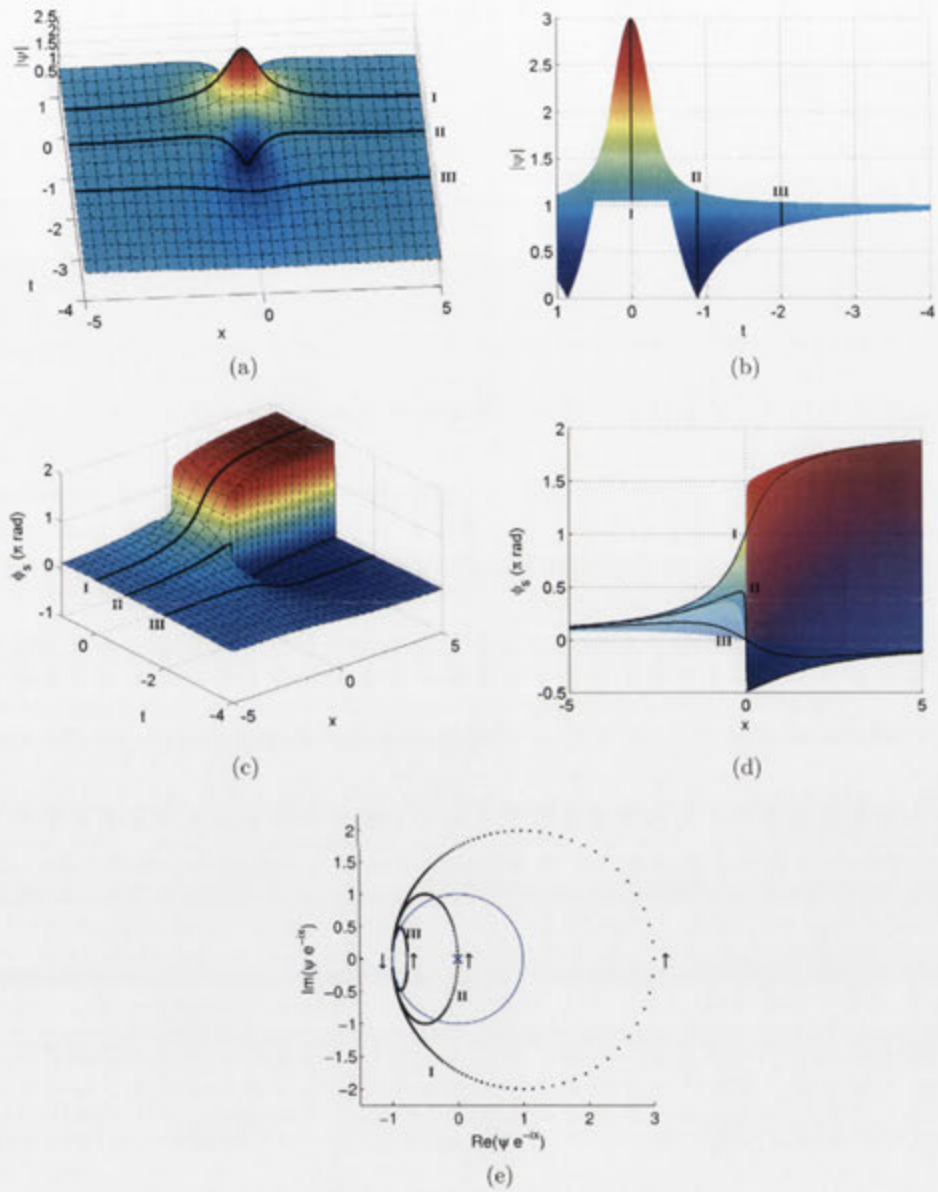

Figure 1. Evolution paths (I, II and III) and associated phase shifts (ϕ_s) along an order 1 rogue wave. (a) High-angle view of a rogue wave. (b) A rogue wave viewed down the x axis. Upper and lower curves correspond to maximum and minimum $|\psi|$ values, respectively, for a given t value. (c) High-angle view of cumulative phase shifts. (d) Cumulative phase shifts viewed from the side. (e) Phase-diagram trajectories for evolution paths I, II and III. The arrows indicate the direction of orbit. The closed circle is the locus of points where $|\psi| = 1$. The cross marks the origin.

rises from a plane wave amplitude of 1 to a maximal amplitude of 3, before symmetrically relaxing into a plane wave. Trace II similarly appears to briefly increase in amplitude, but is instead pulled down into a sharp trough with amplitude 0 before its eventual return to a plane wave state. This sharp point and its mirror image on the other side of the Peregrine soliton are the only two coordinates in the entire domain where $|\psi|$ is not smooth. It follows intuitively that these regions would be important in determining the physics of a rogue wave. By contrast, trace III lies somewhat to the edge of the rogue wave event and only passes through a mild trough.

The phase-space orbits of these evolution paths are shown in figure 1(e). However, the plane wave component is factored out from the solution for these trajectories as it simply applies a well understood x-dependent rotational effect in the complex plane. Additionally, an arbitrary coordinate-independent phase-shift term can be freely applied to the orbits, so as to rotate them by any angle with respect to

J. Opt. **15** (2013) 064011 D J Kedziora *et al*

the complex origin. In any case, it is evident that a solution arising from a perturbed plane wave will have all orbits originating from a point on the unit circle in the complex plane. Moreover, ABs and Peregrine solitons must return to a plane wave state, which means that the phase-space trajectories must also return to the unit circle. However, it is crucial to note that rogue wave solutions are distinguished from ABs by their homoclinic orbits. Although numerics does not allow evolution paths to be examined all the way to $x = \pm\infty$, figure 1(e) implies that all three traces (I, II and III) return to the same coordinate. This does not happen in the case of ABs [4].

Within the scope of this paper, it is most interesting to examine the effect of a rogue wave solution on the background plane wave. In particular, the phase of a solution is closely related to $\ln(\psi)$, which means that the complex plane origin within figure 1(e) acts as a pole. Consequently, in accordance with Cauchy's residue theorem, the total phase change around an orbit will vary depending on whether or not it encircles the origin. For heteroclinic orbits involving ABs, a plane wave will always end up phase shifted by some non-zero amount [4], but a rogue wave in a sense is simpler to analyse because the homoclinic trajectories are always closed loops. Here we define ϕ_s as the cumulative increase in phase for ψ with respect to its initial condition at $x = -\infty$. As aforementioned, we ignore the plane wave component and its linear increase in phase.

As shown in figure 1(e), evolution path III does not enclose the pole at the origin. Thus the phase addition from the plane wave perturbation may oscillate along this path, but it ultimately remains on the same branch of the complex logarithm. The integral along this closed contour is thus equivalent to a zero total phase shift. The 3D representation of ϕ_s in figure 1(c) makes this evident. In contrast, figure 1(e) shows evolution path I encircling the pole, which indicates that the orbit moves onto a new logarithm branch. This is equivalent to an aggregate difference in phase of 2π. Indeed, figure 1(c) shows that, for a well defined range of t values, a plane wave will come out of a rogue wave event with a 2π phase shift. For all other values of t, there will be no net phase shift.

Clearly, there must be a jump discontinuity between the two phase-shift regions and, indeed, this is depicted in figure 1(c) as a vertical wall of height 2π. The point at which this discontinuity between regions begins is the coordinate of the sharp trough in the rogue wave solution. As is shown in both figure 1(b) and phase space in figure 1(e), evolution path II approximately passes through this point. Technically the complex plane origin lies just outside its orbit, which means that the evolution path delineates phase-shift regions on the $\phi_s = 0$ side of the bifurcation in figure 1(c).

The jump discontinuity is examined more closely in figure 1(d), which depicts a translucent version of the ϕ_s surface in figure 1(c) viewed from the side. Evolution paths I and III progress smoothly, asymptoting to $\phi_s = 2\pi$ or 0, respectively. Evolution path II likewise proceeds smoothly until it hits the bifurcation at $x = 0$. At this point, depending on the position of the pole with respect to its phase-space orbit, the phase can advance or regress by π. Notably, aside from a translation in ϕ_s, both the upper and lower $x > 0$ paths are smooth continuations of the $x < 0$ path. Likewise, the two bifurcated paths are identical, despite the shift. Indeed, because the phase-shift landscape is smooth everywhere except for the bifurcating point, with modulus 2π [4], the Peregrine soliton is likewise a valid quasi-smooth solution of the NLSE, despite the unusual phase discontinuity.

Having understood these concepts for a Peregrine soliton, it is easy to apply the knowledge to a second-order rogue wave solution, as shown in figure 2(a). The analytical equation for this structure, using the form in equation (2), is

$$\begin{aligned}
G_2 &= \tfrac{1}{2}(80x^4 + 96x^2t^2 + 16t^4 + 72x^2 - 384xx_d + 24t^2 \\
&\quad -384tt_d - 3), \\
H_2 &= 16x^5 + 32x^3t^2 + 16xt^4 + 8x^3 - 192x^2x_d \\
&\quad - 24xt^2 + 192x_dt^2 - 384xtt_d - 15x + 48x_d, \\
D_2 &= -\tfrac{1}{24}(64x^6 + 192x^4t^2 + 192x^2t^4 + 64t^6 + 432x^4 \\
&\quad - 1536x^3x_d - 288x^2t^2 + 4608xx_dt^2 - 4608x^2tt_d \\
&\quad + 48t^4 + 1536t^3t_d + 396x^2 - 3456xx_d + 9216x_d^2 \\
&\quad + 108t^2 - 1152tt_d + 9216t_d^2 + 9),
\end{aligned} \tag{4}$$

where 'differential shifts' x_d and t_d can be set to 0, as has been done for figure 2. We note that this formula is derived, via parameters defined in the appendix, with component frequency ratio $\kappa_2 = \sqrt{2}\kappa_1$ [9]. This time there are five evolution paths present, from I to V. As depicted in figure 2(b), the first crosses the amplitude 5 peak of the solution, while the second and fourth cut through a primary and secondary sharp trough, respectively. However, the t values for paths II and IV are chosen so that they lie on the opposite sides of their respective bifurcations to the peak. It can already be foreseen at this stage that the zero-amplitude troughs will demarcate phase-shift regions as they did for the Peregrine soliton.

The key to understanding the evolution paths in phase space relies on the understanding that the second-order rogue wave is constructed via the infinite-period limit applied to a nonlinear superposition of two breather solutions [21]. Importantly, phase-space trajectories can now potentially loop around the complex plane origin twice, as in the case of path I traversing the rogue wave maximum. This is why there are two possible types of bifurcation for a second-order rogue wave. Trajectory IV in figure 2(e) separates orbits that loop once around the origin from those that do not, in a similar manner to trajectory II in figure 1(e). On the other hand, trajectory II in figure 2(e) already has one closed loop around the origin. It separates orbits that loop twice around the pole from those that do so only once.

By Cauchy's residue theorem, it is clear that evolution path II separates the region of aggregate phase shift 4π from that of 2π, and path IV does the same between 2π and 0. Indeed, figure 2(c) displays two jump discontinuities in the $t < 0$ domain, both arising at $x = 0$. Despite the increasing complexity of the ϕ_s side view in figure 2(d), it is again evident that paths II and IV each have two options along which to continue at $x = 0$, determined only by which side of the sharp trough they lie. Each pair of bifurcated paths is again

J. Opt. **15** (2013) 064011 D J Kedziora *et al*

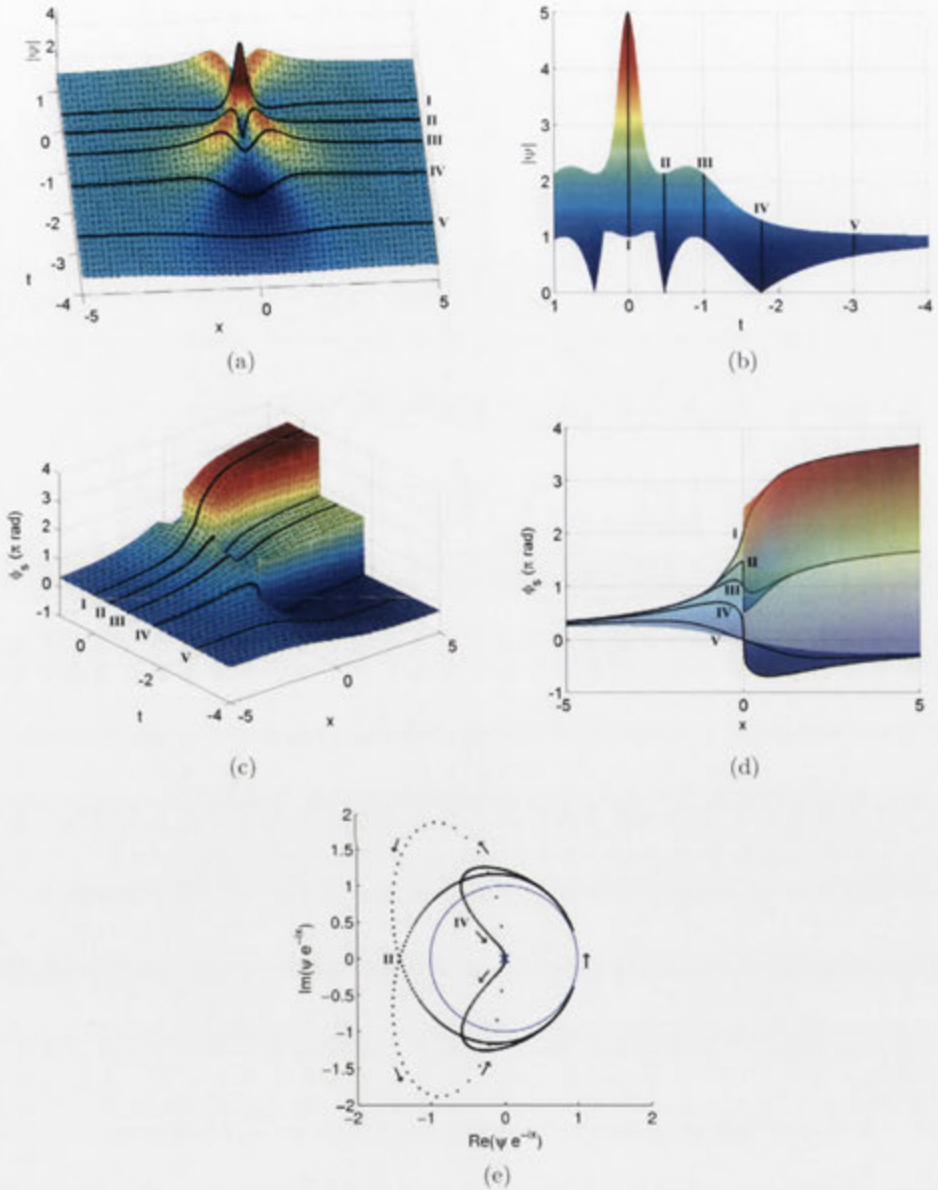

Figure 2. Evolution paths (I, II, III, IV and V) and associated phase shifts (ϕ_s) along an order 2 rogue wave. (a) High-angle view of a rogue wave. (b) A rogue wave viewed down the x axis. Upper and lower curves correspond to maximum and minimum $|\psi|$ values, respectively, for a given t value. (c) High-angle view of cumulative phase shifts. (d) Cumulative phase shifts viewed from the side. (e) Phase-diagram trajectories for evolution paths II and IV. The arrows indicate the direction of the orbit. The closed circle is the locus of points where $|\psi| = 1$. The cross marks the origin.

equal to each other and smoothly continuous with regard to their respective pre-bifurcating path, except for a $\pm\pi$ shift.

The pattern is clear for higher-order structures. An origin-centred rogue wave of order n will possess n aligned sharp troughs and corresponding bifurcation points along the t axis on either side of its central peak. An evolution path crossing the peak will ultimately experience a $2\pi n$ phase shift [6], but all other $2\pi k$ phase shifts with $0 \leq k \leq n-1$ are also available, demarcated by the n bifurcation points. For these traditional rogue wave structures, the ϕ_s surface will appear pyramidal.

4. Fissioned rogue waves

A common intuitive misconception is that, because it is constructed from two breathers, a second-order rogue wave

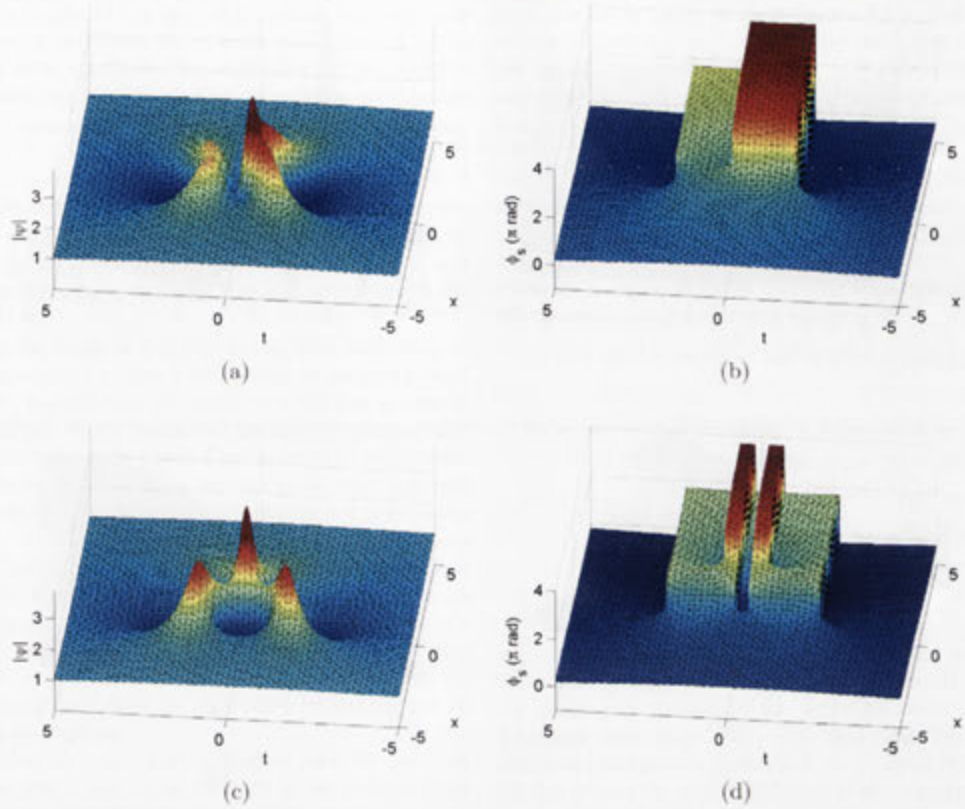

Figure 3. Weakly fissioned second-order rogue wave triplets and their associated phase shifts (ϕ_s). (a) Triplet formed by small t axis shifts. (b) Cumulative phase shift of 't axis triplet'. (c) Triplet formed by small x axis shifts. (d) Cumulative phase shift of 'x axis triplet'.

must be formed from two first-order rogue waves in nonlinear superposition. Indeed, the 4π phase shift evident in figure 2(c) suggests that two Peregrine solitons exist on top of each other, summing their 2π phase shifts. Yet it has become well established in recent times that an origin-centred second-order rogue wave can undergo 'fission' into three distinct Peregrine soliton 'quanta'. This structure is known as a rogue wave triplet and has been attained numerous times via many independent methodologies [7, 24, 25].

In accordance with our understanding of the Peregrine soliton in section 3, each quantum should (in aggregate terms) apply a 2π phase shift to a plane wave in the range of t values between its two zero-amplitude troughs. This does not actually conflict with the phase-shift profile of a second-order rogue wave, considering that two Peregrine solitons appear pressed together to produce the first 2π phase shift. Possibly due to some exclusion principle or 'rogue wave quantum pressure', these two never overlap their phase-shift segments, even under complete origin-centred 'fusion'. In contrast, the third quantum appears more mobile under the application of component shifting. For example, figure 3(a) depicts a second-order rogue wave undergoing weak fission along the t axis, analytically described by equation (4) with $(x_d, t_d) = (0, -0.05)$. It is clear from the difference between figures 3(b) and 2(c) that the third quantum is sliding to the side and overlapping one of the base 2π-shift quanta. This does not contradict the phase-shift overlap restriction, as the large peak in figure 3(a) is already beginning to separate into two quanta that centre at different values of x.

Naturally, figure 3(a) is an extreme case where the fission process forces quanta to interact along the segments bounded by their bifurcation points. However, in general, the third quantum is immediately separated in x from the other two. This is exemplified in figure 3(c), where the weak fission process occurs along the x axis and the three individual Peregrine solitons are almost immediately identifiable. This structure is analytically described by equation (4) with $(x_d, t_d) = (0.2, 0)$. Subsequently, figure 3(d) reaffirms the fact that phase shifts generated by rogue wave quanta are additive. An evolution path crossing the largest peak of the triplet will only be phase shifted by 2π, as it does not pass between a pair of troughs belonging to either of the other two quanta. However, there are still 4π phase-shift regions visible in figure 3(d), arising at (x, t) coordinates where the effects of two segments overlap, even though the segments themselves do not.

As expected, most of the interesting phase-shift combinations arise in the case of weak fission, when

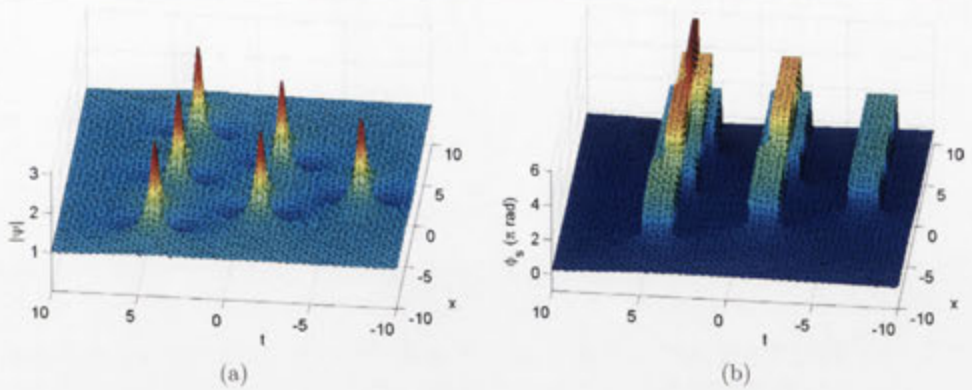

Figure 4. Slightly rotated third-order rogue wave cascade and its associated phase shifts (ϕ_s). (a) Amplitude of cascade. (b) Cumulative phase shift of cascade.

nonlinear interactions between neighbouring peaks serve to distort the amplitude profile of the event. However, rogue wave triplets are often implicitly associated with strongly fissioned second-order structures [7, 24, 25], where the three individual peaks are spatiotemporally well-separated and virtually indistinguishable from Peregrine solitons. In such a case, the phase-shift regions generally have no overlap unless two peaks enter close temporal alignment. The resulting phase-shift profile is usually nothing more than three copies of figure 1(c) at different coordinates in the domain.

Regardless, with this knowledge, we can determine the aggregate phase shift applied to a plane wave by any solution in the rogue wave hierarchy. For example, a third-order rogue wave cascade [9] is displayed in figure 4(a). Its component shifts are chosen such that the entire structure is rotated marginally and the quanta are not aligned. Specified for completeness, it is numerically generated via the process detailed in the appendix, with $\kappa_1{:}\kappa_2{:}\kappa_3 = 1{:}\sqrt{2}{:}\sqrt{3}$, $(x_1, x_2, x_3) = (0, 5, 10) \times \kappa_1^2 \cos(\theta_t)$ and $(t_1, t_2, t_3) = (0, 5, 10) \times \kappa_1^2 \sin(\theta_t)$, where $\theta_t = -3\pi/5$. It follows that the surface of ϕ_s can easily be determined by taking note of the segments bounded by bifurcation points, extending their phase shifts to $x = \infty$, and summing any overlaps. This is shown in figure 4(b).

It is worth noting that the 2π phase-shift properties are intrinsic to a rogue wave solution, irrespective of dispersion strength in the medium. In fact, we can slightly modify the NLSE in equation (1) so that it incorporates a new parameter, now written as

$$i\epsilon \frac{\partial \psi}{\partial x} + \frac{1}{2}\epsilon^2 \frac{\partial^2 \psi}{\partial t^2} + |\psi|^2 \psi = 0. \tag{5}$$

A small value of ϵ entails weak dispersion and strong nonlinear interactions. A large value represents a highly dispersive medium. To operate on this system rigorously, the Darboux scheme requires small modifications to the Lax pair, seed functions, frequency definition and transformative equation. However, the rogue wave solutions are still relatively simple to attain. In effect, solutions to equation (5) are equivalent to solutions of the NLSE that are scaled in x and t by the same constant, leaving the amplitude fixed.

It can be shown numerically that, as ϵ decreases, the width of the phase-shifting segments in figure 4 also decreases, but evolution paths traversing the segments are still shifted by 2π each time. This leads to interesting questions in the dispersionless limit, where recent results have shown that a 'gradient catastrophe' can generate structures similar to infinite-order rogue wave cascades [26], even though typical NLSE rogue wave solutions collapse to infinitesimal widths. Careful study of Riemann theta forms [27, 28] and corresponding phase profiles will be required to identify whether the two types of solution are indeed related or whether the similarities end with appearance.

5. Conclusion

In summary, our main results are as follows:

(1) We have elaborated upon previous work that noted phase-shift discrepancies induced by a first-order rogue wave [4] and have found that the sharp zero-amplitude troughs bordering the peak also serve as phase-shift bifurcations. Evolution paths that traverse the segment bounded by the two points will ultimately experience a 2π phase shift with respect to trajectories that avoid the segment.

(2) We have shown that there is no inherent contradiction for an origin-centred second-order rogue wave to be formed from the fusion of three Peregrine solitons. Two of the quanta press together and form an extended 2π phase-shift segment without ever overlapping. The third quantum overlays this with a shorter individual 2π phase-shift segment. Evolution paths can only traverse a maximum of two segments, so phase-space orbits never loop around the complex origin pole more than twice. Three quanta remained fused, but the maximum phase shift possible is 4π, in accord with the order-based additive rule.

J. Opt. **15** (2013) 064011 D J Kedziora *et al*

(3) By associating each rogue wave quantum with a 2π phase-shift segment, we have extended our ability to predict phase shifts experienced by evolution paths for any NLSE rogue wave in the hierarchy. Regions of phase shift are simply extended along the x axis and are additive where they overlap.

In summarizing such an apparently simple result, we understate several important implications of this work. For example, an order n rogue wave is separable into $n(n+1)/2$ quanta [8], each producing a 2π phase shift. Yet a $2\pi n$ phase shift is an upper bound for an order n rogue wave, whether fissioned or not. The natural consequence of this is that an NLSE rogue wave structure cannot have more than n quanta in alignment. This is perhaps why an order n cascade [9], the most grid-like shape in the known rogue wave hierarchy, is a triangular array of Peregrine solitons with sides of length n, as exemplified in figure 4(a).

Moreover, some things are simply easier to see in phase-shift space ϕ_s. When high-order rogue waves are only weakly fissioned, the individual quanta remain overlapped and their net nonlinear superposition can be confusing when viewed as an amplitude profile, as in figure 3(a). However, by tracing paths through the event and examining it in phase space, we can determine where each rogue wave quantum is located and, correspondingly, what effect it is having with regard to the entire extreme event.

This seemingly linear nature of high-order phase-shift superposition allows the extension of concepts in several areas. For example, it has been known for a while that certain phase singularities induce crest pairing for wave trains [29]. Wave dislocation in particular has been identified with first-order breathers [30] and has been proposed as an avenue to hydrodynamic rogue wave control [31]. Hence the principle in this work is likely to describe the behaviour of individual crests for rogue wave solutions in the complete hierarchy, potentially allowing seafarers to avoid unfavourable discontinuities in complex wave fields.

As for an optical context, it has been shown that laser-pumped photorefractive crystals with nonlinear mode–mode coupling produce high intensity peaks that vary statistically from typical speckle behaviour [32], instead being reminiscent of optical fibre rogue waves [33]. Generated between phase singularities, it is possible that these chaotic patterns may feature superpositions of high-order rogue waves, as opposed to individual extreme events. Further investigation with phase profiles and interference patterns may elucidate whether there is in fact mesoscopic regularity within the chaos.

In any case, phase shifts throughout a rogue wave play an important role in their interactions with the medium. Complicated phase patterns make these interactions even more involved. We have presented results here for fundamental NLSE rogue waves, but this research is expected to become even more important in the context of ultra-short optical events, where evolution is directly affected by a carrier-envelope phase relation [10, 11]. More studies are needed to fully comprehend the role of phase patterns in the growth and decay of rogue waves.

Acknowledgments

The authors acknowledge the support of the Australian Research Council (Discovery Project number DP110102068). NA and AA acknowledge support from the Volkswagen Stiftung.

Appendix. The Darboux Method

The NLSE in equation (1) can be written in Lax pair form (e.g. see ch. 2 of *Solitons* [34]):

$$R = \begin{bmatrix} r \\ s \end{bmatrix}, \qquad \frac{\partial R}{\partial t} = U \cdot R, \qquad \frac{\partial R}{\partial x} = V \cdot R,$$

$$U = \begin{bmatrix} \mathrm{i}\lambda & \mathrm{i}\psi^* \\ \mathrm{i}\psi & -\mathrm{i}\lambda \end{bmatrix},$$

$$V = \begin{bmatrix} \mathrm{i}\lambda^2 - \frac{i}{2}|\psi|^2 & \mathrm{i}\lambda\psi^* + \frac{1}{2}\frac{\partial \psi^*}{\partial t} \\ \mathrm{i}\lambda\psi - \frac{1}{2}\frac{\partial \psi}{\partial t} & -\mathrm{i}\lambda^2 + \frac{i}{2}|\psi|^2 \end{bmatrix}, \tag{A.1}$$

where λ is a complex eigenvalue. The linear system reduces to the original equation under the equality $R_{xt} = R_{tx}$.

We define the 'first-order component functions'

$$\begin{aligned} r_{1j} &= 2\mathrm{i}\mathrm{e}^{-\mathrm{i}x/2}\sin(A_{jr} + \mathrm{i}A_{ji}), \\ s_{1j} &= 2\mathrm{e}^{\mathrm{i}x/2}\cos(B_{jr} + \mathrm{i}B_{ji}), \end{aligned} \tag{A.2}$$

where functions A and B are in turn defined as

$$\begin{aligned} A_{jr} &= \frac{1}{2}\left[\arccos\left(\frac{\kappa_j}{2}\right) + (t - t_j)\kappa_j - \frac{\pi}{2}\right], \\ B_{jr} &= \frac{1}{2}\left[-\arccos\left(\frac{\kappa_j}{2}\right) + (t - t_j)\kappa_j - \frac{\pi}{2}\right], \\ A_{ji} &= B_{ji} = \frac{1}{2}\left[(x - x_j)\kappa_j\sqrt{1 - \frac{\kappa_j^2}{4}}\right], \end{aligned} \tag{A.3}$$

with $\kappa_j = 2\sqrt{1 + \lambda_j^2}$. The subscripts r and i refer to real and imaginary parts, respectively.

These component functions in equation (A.2) are the solutions of equation (A.1) when the eigenvalue is purely imaginary and ψ is equal to the plane wave seeding solution $\psi_0 = \mathrm{e}^{\mathrm{i}x}$. They also serve as basic building blocks for the construction of higher-order solutions, where the number j uniquely identifies each component. In particular, each component denoted by j is described by a set of free parameters; the corresponding eigenvalue λ_j and coordinate shifts (x_j, t_j).

A first-order solution to the system in equation (A.1) incorporates only one chosen set of free parameters and its corresponding r and s functions from equation (A.2), denoted by $j = 1$. The first-order wavefunction is thus expressed as

$$\psi_1 = \psi_0 + \frac{2(\lambda_1^* - \lambda_1)s_{11}r_{11}^*}{|r_{11}|^2 + |s_{11}|^2}. \tag{A.4}$$

An order $n > 1$ solution requires higher-order versions of the expressions for r and s. These are recursively

generated [19, 34] by

$$\begin{aligned} r_{np} &= [(\lambda_{n-1}^{*} - \lambda_{n-1})s_{n-1,1}^{*}r_{n-1,1}s_{n-1,p+1} \\ &\quad + (\lambda_{p+n-1} - \lambda_{n-1})|r_{n-1,1}|^{2}r_{n-1,p+1} \\ &\quad + (\lambda_{p+n-1} - \lambda_{n-1}^{*})|s_{n-1,1}|^{2}r_{n-1,p+1}]/(|r_{n-1,1}|^{2} \\ &\quad + |s_{n-1,1}|^{2}), \\ s_{np} &= [(\lambda_{n-1}^{*} - \lambda_{n-1})s_{n-1,1}r_{n-1,1}^{*}r_{n-1,p+1} \\ &\quad + (\lambda_{p+n-1} - \lambda_{n-1})|s_{n-1,1}|^{2}s_{n-1,p+1} \\ &\quad + (\lambda_{p+n-1} - \lambda_{n-1}^{*})|r_{n-1,1}|^{2}s_{n-1,p+1}]/(|r_{n-1,1}|^{2} \\ &\quad + |s_{n-1,1}|^{2}). \end{aligned} \tag{A.5}$$

The p subscript in equation (A.5) is used purely for enumeration and does not necessarily refer to a particular set of parameters. For example, the second-order function r_{21} is built from first-order component functions r_{11}, s_{11}, r_{12} and s_{12}, thus incorporating parameters from both the components denoted by $j = 1, 2$. Similarly, the third-order function r_{31} involves the second-order functions r_{21}, s_{21}, r_{22} and s_{22}, which, in turn, are based on r_{11}, s_{11}, r_{12}, s_{12}, r_{13} and s_{13} at the lowest order of recursion. Therefore, r_{31} constitutes parameters from all three components denoted by $j = 1, 2, 3$. In this way, equation (A.5) allows n sets of free parameters to be incorporated into an order n solution. The diagram in figure 2.2 of *Solitons* [34] can be of use in representing this sequence of calculations. Subsequently, the order n NLSE solution is generated through recursion by

$$\psi_n = \psi_{n-1} + \frac{2(\lambda_n^{*} - \lambda_n)s_{n1}r_{n1}^{*}}{|r_{n1}|^{2} + |s_{n1}|^{2}}. \tag{A.6}$$

Rogue waves of various orders arise when all κ_j in a solution uniquely approach zero. The easiest way to do this is by establishing a ratio for component frequencies, such that $\kappa_1 = c_1\kappa$, $\kappa_2 = c_2\kappa$, $\cdots$, $\kappa_n = c_n\kappa$, with $c_1 \neq c_2 \neq \cdots \neq c_n$. Applying the limit $\kappa \to 0$ takes each component frequency to zero, but always enforces the inequality required for rogue wave existence [21]. However, the construction of the 'shifted' structures in figures 3 and 4 is far more involved, with scaling of inter-peak distances additionally dependent on the frequency ratio. Details regarding the treatment of x_j and t_j in this fissioned case can be found elsewhere [8, 21, 9].

References

[1] Kharif C and Pelinovsky E 2003 *Eur. J. Mech.* B **22** 603–34
[2] Liu P C and MacHutchon K R 2008 *J. Offshore Mech. Arctic Eng.* **130** 021007
[3] Peregrine D 1983 *J. Austral. Math. Soc.* B **25** 16–43
[4] Devine N, Ankiewicz A, Genty G, Dudley J and Akhmediev N 2011 *Phys. Lett.* A **375** 4158–61
[5] Akhmediev N, Ankiewicz A and Soto-Crespo J M 2009 *Phys. Rev.* E **80** 026601
[6] Akhmediev N and Ankiewicz A 2011 *Phys. Rev.* E **83** 046603
[7] Ankiewicz A, Kedziora D J and Akhmediev N 2011 *Phys. Lett.* A **375** 2782–5
[8] Kedziora D J, Ankiewicz A and Akhmediev N 2011 *Phys. Rev.* E **84** 056611
[9] Kedziora D J, Ankiewicz A and Akhmediev N 2012 *Phys. Rev.* E **86** 056602
[10] Jones D J, Diddams S A, Ranka J K, Stentz A, Windeler R S, Hall J L and Cundiff S T 2000 *Science* **288** 635–9
[11] Cundiff S T 2007 *Nature Phys.* **3** 16–8
[12] Kibler B, Fatome J, Finot C, Millot G, Dias F, Genty G, Akhmediev N and Dudley J M 2010 *Nature Phys.* **6** 790–5
[13] Erkintalo M, Hammani K, Kibler B, Finot C, Akhmediev N, Dudley J M and Genty G 2011 *Phys. Rev. Lett.* **107** 253901
[14] Chabchoub A, Hoffmann N P and Akhmediev N 2011 *Phys. Rev. Lett.* **106** 204502
[15] Chabchoub A, Hoffmann N P, O M and Akhmediev N 2012 *Phys. Rev.* X **2** 011015
[16] Chabchoub A, Hoffmann N, Onorato M, Slunyaev A, Sergeeva A, Pelinovsky E and Akhmediev N 2012 *Phys. Rev.* E **86** 056601
[17] Matveev V B and Salle M 1991 *Darboux Transformations and Solitons* (Berlin: Springer)
[18] Akhmediev N and Mitskevich N V 1991 *IEEE J. Quantum Electron.* **27** 849–57
[19] Akhmediev N, Soto-Crespo J M and Ankiewicz A 2009 *Phys. Lett.* A **373** 2137–45
[20] He J, Zhang H, Wang L, Porsezian K and Fokas A 2012 arXiv:1209.3742
[21] Kedziora D J, Ankiewicz A and Akhmediev N 2012 *Phys. Rev.* E **85** 066601
[22] Ankiewicz A, Clarkson P A and Akhmediev N 2010 *J. Phys. A: Math. Gen.* **43** 122002
[23] Gaillard P 2012 Tenth peregrine breather solution of the nls equation preprint: hal-00743859, version 1–21 Oct 2012
[24] Dubard P and Matveev V B 2011 *Nat. Hazards Earth Syst. Sci.* **11** 667–72
[25] Ohta Y and Yang J 2012 *R. Soc. Lond. Proc. Ser.* A **468** 1716–40
[26] Bertola M and Tovbis A 2013 *Commun. Pure Appl. Math.* **66** 678–752
[27] Kamvissis S, McLaughlin K D R and Miller P D 2003 *Semiclassical Soliton Ensembles for the Focusing Nonlinear Schrodinger Equation (AM-154)* vol 154 (Princeton, NJ: Princeton University Press)
[28] Tovbis A, Venakides S and Zhou X 2004 *Commun. Pure Appl. Math.* **57** 877–985
[29] Trulsen K 1998 *J. Geophys. Res.* **103** 3143–7
[30] Karjanto N and Van Groesen E 2007 *Phys. Lett.* A **371** 173–9
[31] Andonowati K N and van Groesen E 2007 *Appl. Math. Model.* **31** 1425–43
[32] Arecchi F, Giacomelli G, Ramazza P and Residori S 1991 *Phys. Rev. Lett.* **67** 3749–52
[33] Solli D R, Ropers C, Koonath P and Jalali B 2007 *Nature* **450** 1054
[34] Akhmediev N and Ankiewicz A 1997 *Solitons: Nonlinear Pulses and Beams* (*Optical and Quantum Electronics* vol 5) (London: Chapman and Hall) chapters 3 and 4

Epilogue

Discussing carrier waves further, they are clearly important in the case of ultrashort pulses in optics [111, 112], on account of modulational peaks becoming spatiotemporally thin enough to be comparable with the carrier oscillations themselves. However, this scenario typically requires the consideration of higher-order nonlinearities and related terms anyway (i.e. extensions to the NLSE discussed in Chapter 8). In general, the phase changes of a high-frequency electromagnetic carrier wave are much more rapid than those of the complex envelope pertaining to a solution of the NLSE. On the other hand, the importance of the carrier is ubiquitous in the hydrodynamic domain, with greater comparability between its modulations and the envelope. Indeed, the surface elevation of these oscillations is typically what is observed in both wave tanks [11, 77, 98] and the ocean itself. For this reason, even though no 'dark' rogue wave has been proposed for the standard NLSE, with a trough-shaped envelope appearing like an inverted Peregrine breather (cf. dark rogue waves for extended equations in Chapter 8), it is still possible to experience a rogue wave 'hole' [113]. This simply requires the maximum value of the rogue wave envelope to be aligned with a minimum value of the sinusoidal carrier. The resulting rogue hole is just as dangerous as a rogue peak, as it is accompanied by two adjacent steep crests in the carrier wavetrain.

In terms of the analysis in this chapter, it is clear that the increasing carrier steepness of rogue wave phenomena must be linked to the complex-plane zeroes of the solution, namely the envelope troughs. Certainly, complex analysis of rogue waves has previously led to the discovery of many interesting mathematical features of rogue waves [70], but the implications here are simple. Zero-amplitude troughs allow for phase-jump discontinuities to exist between adjacent evolution trajectories, without losing the continuity that is physically required of a rogue wave envelope. For an oceanic carrier, this gives rise to moments in space and time when the sea becomes unnaturally calm. The end result of such events is either two crests becoming one or one splitting into two, resulting in so-called 'wave dislocation' for a portion of the carrier [114]. It should be noted that this effect of phase singularities is also well known in optics and other fields [115, 116].

Consequently, the concept of wave dislocation is demonstrated here in Fig. 5.1, where an arbitrarily chosen carrier wave passes through two examples of NLSE extreme events. To reduce visual complexity, its troughs are ignored and are thus admittedly difficult to distinguish from points of zero-amplitude. However, the latter can still be identified by the fusions and splits they induce with regard to the carrier crests. Accordingly, it is clear from Fig. 5.1a that the maximum amplitude of the depicted second-order fused rogue wave belongs to an oscillation that is pushed back two wavelengths down the carrier wave, as seen with an aggregate perspective. This is what a 4π phase shift is expected to look like in the ocean, and any vessel travelling at the carrier velocity behind the shifting crest risks being suddenly hit by a steep moving 'wall of water' [117]. Even the oscillations that appear out of nowhere adjacent to the point of maximum amplitude can likewise prove destructive, due to

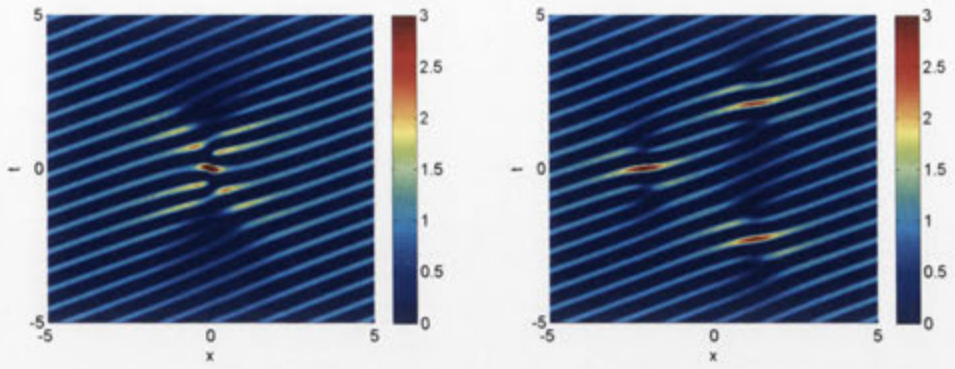

(a) (b)

Figure 5.1: Surface elevations for example carriers of second-order rogue wave solutions, ψ, in the form of $\mathrm{Re}[\psi \exp(i(10t - 5x))]$. Component frequency ratio is $\kappa_1 : \kappa_2 = 1 : 2$. Values exist outside the range of the colour bar but are ignored (set to the extremes of the colour bar) so as to reduce visual complexity and focus specifically on carrier crests. (a) Unshifted fused rogue wave. (b) Triplet with non-zero shift $x_1 = -4\kappa_1^2$.

their seemingly unpredictable nature. This is why wave dislocation occurring in the case of triplets, shown in Fig. 5.1b, can still be dangerous, despite the relatively low wave steepness. That is because spatial translations, fusions and fissions of carrier wave crests are more difficult to determine in the presence of numerous events.

Of course, while this is seemingly a significant issue, caution should be maintained in adopting an avoidance policy based on these results alone. After all, the Peregrine breather is an ideal mathematical structure [47]. It is a solution of the NLSE formed from an infinitesimal perturbation at an infinitely spatiotemporally-distant location with respect to the rogue wave peak. In reality, structures within physical domains are far more likely to be composites of numerous finite-frequency breathers. As has been previously established, complex-plane trajectories through these solutions follow heteroclinic orbits [109], meaning that phase shifts are not exactly 2π. Observing the behaviour of carrier oscillations shortly before the climax of a rogue wave event may still allow for the maximum amplitude to be avoided, but the feasibility of this can only be determined by further study.

Chapter 6

Classifying the Hierarchy of NLSE Rogue-wave Solutions

Prologue

At the time of their discovery, it appeared that circular clusters [2] would be the only possible fissioned rogue wave solutions of the NLSE. Multi-ring structures were hinted at, but these could not be properly distinguished from numerical inaccuracies in the application of the Darboux scheme. Certainly, for any compound rogue wave of third order or beyond, shifting one component alone from the others could only ever produce a circular cluster, given an appropriate infinitesimal value for its spatiotemporal perturbation. On the other hand, when the existence of triangular cascades was published [4], it became immediately clear how the other fundamental multi-rogue structures would arise. Moreover, by the start of 2013, the application of other methods had independently begun to glimpse various new Peregrine breather arrangements [72]. It would soon be necessary to devise a system capable of controllably constructing all fundamental multi-rogue wave solutions, and exhaustively categorising them.

On that note, the Darboux process had one particular advantage over other procedures [71, 86], in that the degrees of freedom required to fission a compound rogue wave were already considered physically as axial shifts of individual components. While these became unintuitively infinitesimal in the zero-frequency rogue wave limit, they were still finite in the context of low-frequency breathers. Accordingly, analogues of parametrically precarious rogue wave arrangements could first be constructed at the intersection of periodically modulating wavetrains, with relative numerical ease. Comparisons of the two forms soon allowed for existence conditions to be naturally defined for various spatiotemporally localised structures.

Again, the understanding of what ensues is reliant on the idea that the breathers used in the process of nonlinear superposition have a ratio of frequencies with common factor κ. This concept was introduced and justified in Chapter 4. It follows that the factor κ is important as a proportionality term for component shifts, despite the fact that both breather frequencies and axial translations physically approach zero in the $\kappa \to 0$ rogue wave limit. In particular, provided that the right relations exist between component shifts and the squared coefficients of the modulation frequency ratio, κ^2 proportionality is responsible for the production of triangular cascades [4].

Therefore, iterative logic suggests that component translations with a κ^4 factor might be relevant for new NLSE solutions, with the same situation for κ^6, κ^8, and so on. Sure enough, exploration with this concept reveals many novel structures.

This chapter, as a published manuscript [6], presents the core result of this thesis. Specifically, extreme events modelled by the NLSE and composed of multiple rogue wave quanta, each representing an instance of modulational instability in the form of a Peregrine breather, can be deterministically generated via the Darboux scheme and classified according to spatiotemporal geometries. This statement can be elaborated as follows:

1. If every constituent component pertaining to a rogue wave of order n is shifted by a finite amount (i.e. κ^0 proportionality), then the shifts must be identical in value to maintain a structure of order n. This scenario is equivalent to a spatiotemporal translation of the entire compound structure.

2. If every component for the same structure is shifted with κ^2 proportionality, the values of the relevant shift coefficients must be linearly related to the squared coefficients of the frequency ratio, so as to maintain a structure with finite spatiotemporal circumradius. This scenario is equivalent to a rogue wave fission process producing a triangular cascade [4].

3. If every component is shifted with κ^4 proportionality, the relevant relation must now be quadratic to maintain a parametrically stable wavefunction. This scenario reproduces fission into a five-sided array of rogue wave quanta.

4. By induction, $\kappa^{2(m-1)}$ proportionality requires the relevant relation to be a polynomial with order $m-1$, so as to maintain parametric stability. This scenario reproduces fission into a rotationally quasi-symmetric array of rogue wave quanta with $2m-1$ sides.

In essence, a rogue wave of order n can be spatiotemporally arranged as a triangular cascade, a pentagram, a heptagram, and so on, as long as certain 'existence conditions' are met. This effectively categorises NLSE solutions, in that a wavefunction formed from 'shifts of order m' possesses rotational symmetry of degree $2m-1$.

Naturally, this is a dense result with many corollaries, also discussed in the paper. These include the fact that:

- Circular clusters [2] actually correspond to a rogue wave arrangement with the greatest degree of rotational symmetry possible for a solution of the relevant order.

- Symmetry restrictions constrain the ways in which the total number of quanta in the compound solution can be arranged. It is thus possible to extrapolate the shape of any extreme-order rogue wave, regardless of the shift order involved in the relevant fission process.

- No two existence conditions use the same shift coefficients. For instance, it is possible to spatially translate one component by $2+3\kappa^2+5\kappa^4+8\kappa^6$ and

still adhere to conditions required for structural translation, as well as cascade, pentagram and heptagram fission, provided shifts are chosen appropriately for other components.

This last point is of great interest. It effectively implies that the fundamental rogue wave NLSE solutions designated by the existence conditions can be thought of as a nonlinear-style basis set. Indeed, applying two or more existence conditions with non-zero scaling coefficients can hybridise symmetry features to produce wavefunctions of claw-like [4] or multi-ring form. Consequently, this chapter indicates how to produce seemingly arbitrary multi-rogue wave arrangements that are guaranteed adherents of NLSE physics.

PHYSICAL REVIEW E **88**, 013207 (2013)

Classifying the hierarchy of nonlinear-Schrödinger-equation rogue-wave solutions

David J. Kedziora,* Adrian Ankiewicz, and Nail Akhmediev

Optical Sciences Group, Research School of Physics and Engineering, The Australian National University, Canberra ACT 0200, Australia

(Received 22 January 2013; revised manuscript received 28 March 2013; published 30 July 2013)

We present a systematic classification for higher-order rogue-wave solutions of the nonlinear Schrödinger equation, constructed as the nonlinear superposition of first-order breathers via the recursive Darboux transformation scheme. This hierarchy is subdivided into structures that exhibit varying degrees of radial symmetry, all arising from independent degrees of freedom associated with physical translations of component breathers. We reveal the general rules required to produce these fundamental patterns. Consequently, we are able to extrapolate the general shape for rogue-wave solutions beyond order 6, at which point accuracy limitations due to current standards of numerical generation become non-negligible. Furthermore, we indicate how a large set of irregular rogue-wave solutions can be produced by hybridizing these fundamental structures.

DOI: 10.1103/PhysRevE.88.013207 PACS number(s): 05.45.Yv, 47.20.Ky, 42.65.−k

I. INTRODUCTION

The nonlinear Schrödinger equation (NLSE) has become one of the most studied partial differential equations since its inception in the 1960s. A major part of this appeal stems from its wide variety of applications in various branches of physics. Indeed, the universality of this equation has resulted in many common phenomena being discovered in optics, oceanography, superfluids, and even atmospheric science. Of particular historical note, it was one of the first known integrable equations admitting the existence of solitons. Since then, their nonlinear superpositions with each other and with radiation have been intensively studied. More recently, significant attention has been directed to rogue-wave solutions. These are marked by brief "bursts" of large amplitude, localized in both space and time, on an otherwise quiescent background. This unique feature makes them effective prototypes for describing notorious rogue waves in the ocean [1,2]. Moreover, these solutions have found substantial utility in other fields of science where we find unexpected high-impact extreme events.

In addition to spatiotemporal localization, another main feature of this class of solutions is their hierarchical structure. The lowest-order solution is known as a Peregrine breather (or soliton) [3], which is described by a simple quasirational expression. The second-order solution was first introduced in 1985 [4] and has recently been presented again in the context of freak waves [5]. Further progress in revealing higher-order solutions has mostly revolved around the development of mathematical techniques that can ideally represent the whole set in explicit form. Certainly, the rational solutions require a special approach that differs from those used to obtain multisoliton solutions. Several methods have been considered in the quest for deriving the whole hierarchy [6–10], but there is no consensus to date that any one of them has an explicit advantage over the others. Moreover, despite much effort being placed into obtaining the hierarchy, we can conclude that there is currently no complete classification of higher-order rogue-wave solutions. Thus, continued investigation is required in order to better understand the rogue-wave phenomenon.

On the practical side, a series of recent experiments has shown that rogue waves can be produced in a water-based environment. The Peregrine breather, the second-order rogue wave, and solutions up to order 5 have been observed in experiments [11–13]. The Peregrine breather similarly has been generated in optics [14,15] and magnetoplasma [16,17]. Thus, the validity of the simplest rogue-wave solutions has been experimentally confirmed. This also means that the theoretical classification of the whole hierarchy of rogue waves is crucial for further developments in this area of research.

One significant discovery in this regard is that there are no higher-order solutions that are physically separable into 2,4,5,7,8,9, ... elementary Peregrine breathers. Their number is well defined [18,19] and given by the simple expression $n(n+1)/2$, where n is the order of the solution. Following this rule, we can have rogue-wave triplets, sextets, dectets, and so on [18–20], but composites of any other number are not allowed under the NLSE. Another important theoretical result is that these elementary parts of the higher-order rogue waves do not need to be localized at the same position but can be arrayed spatiotemporally in elegant geometries [9,10,19,20]. Nonetheless, despite the discovery of these interesting general facts, there is neither any systematic categorization of the NLSE rogue-wave hierarchy nor a description of how to routinely produce all geometric forms via any particular method. Search strategies may become particularly complicated when exact analytic solutions turn out to be too cumbersome to manipulate. In such a case, it naturally ensues that rogue-wave profiles must be investigated numerically.

This work is the continuation of our previous efforts in finding higher-order NLSE rogue-wave solutions [18–21]. It is based on the Darboux method [22], which remains an efficient technique despite the development of alternative methods. Most importantly, our present research is summative. It provides a classification that is a crucial step in predicting solutions from an infinite array of fundamental rogue-wave structures. The level of predictive power seen in our approach is a necessity in the present state of rogue-wave science, which faces a multiplicity of methods and a haphazard collection of particular solutions presented by various authors. Via the introduction of our scheme, we show that each solution is within easy numerical reach, while our classification is sufficient to indicate trends for higher-order solutions.

*Corresponding author: djk105@rsphysse.anu.edu.au

By nontrivially modifying parameters related to physical shifts in the scheme and relating them to frequency ratios of individual components, we have extended higher-order rogue-wave patterns beyond circular clusters [19] and triangular cascades [20]. Some of these new structures have been independently obtained via an alternative methodology [10]. Here we have modified the Darboux scheme used in our previous works. Namely, the technique is reconsidered using our new "polynomials of existence" concept. The reasoning behind this is twofold: it introduces what is arguably a complicated idea and also proves consistency with previous results. Section III of our present work shows that even "simple" rogue-wave structures comply with our newly found rule.

The rules governing these structures can be extrapolated far beyond the general solution of order 6, where numerical limitations start to be noticeable. Moreover, irregular rogue-wave solutions that also exist can now be interpreted as "hybridized" versions of the fundamental profiles obtained in the analysis. In this way, we, first, broaden and improve our current theoretical understanding of rogue waves and, second, set classification standards that may become useful in the analysis of rogue-wave hierarchies pertaining to related equations, such as the Hirota [23] or Sasa-Satsuma systems [24].

II. THEORY

We begin by expressing the dimensionless 1D NLSE as

$$i\frac{\partial\psi}{\partial x}+\frac{1}{2}\frac{\partial^2\psi}{\partial t^2}+|\psi|^2\psi=0, \tag{1}$$

with the wave envelope described by the complex function $\psi(x,t)$. The variables here are named in accordance with fiber optic convention [14,15], where x is the normalized distance along the fiber and t is the retarded time in the frame moving with the pulse group velocity. Alternatively, in water wave applications [11–13], x is interpreted as the normalized time while t is the distance in the frame moving with the group velocity. In either case, a simple linear transformation involving group velocity allows us to find the relation between both conventional forms and their variables. Perhaps a more important observation is the choice of particular coefficients in front of each term in Eq. (1), considering that this particular choice is responsible for the circular nature of emergent spatiotemporal patterns [19].

Clearly, the nonlinearity in the equation complicates routine analytic solving processes. Fortunately, to find involved solutions of Eq. (1), we can start with simple ones and build on them with the Darboux method. The technique is well described in the literature [22,25] and the specific formalism we use in this work has been expressly detailed previously [19,26]. It is also provided here in Appendix A. Conceptually, the procedure uses a seeding solution to the evolution equation, such as a plane wave ($\psi=e^{ix}$), and generates a first-order "building block." In this case, the fundamental component is a breather, from which all higher-order solutions can be constructed. For simplicity, we have fixed the amplitude of the seeding plane wave at 1 in this work, but it can always be made arbitrary after the final stage of construction via a scaling transformation [5].

It follows that a nonlinear superposition of order n requires n first-order components. Hence, we give the label j for each component, such that $1\leqslant j\leqslant n$. Each component can be translated by an amount x_j or t_j along the x or t axes, respectively. Most importantly, each first-order breather is governed by a complex eigenvalue l_j. The real part of this eigenvalue aligns the breather at a finite angle with the x and t axes while the imaginary part sets its amplitude. However, the modulation period for a NLSE breather depends on the ratio between breather and background amplitudes. Therefore, with the background plane wave restricted to amplitude 1, the imaginary part of the eigenvalue directly controls breather frequency. Additionally, we restrict ourselves to zero-angle alignment in this work, so we henceforth assume l_j is purely imaginary. Complex eigenvalues can still be easily deployed in the Darboux scheme [26], but this current restriction does allow the modulation frequency of a breather to be defined simply as $\kappa_j=2\sqrt{1+l_j^2}$.

When $0<\mathrm{Im}(l_j)<1$, the frequency κ_j is real. The resulting first-order solution, called an Akhmediev breather (AB), is localized in x and periodic in t. A nonlinear superposition of three such ABs parallel to each other is shown in Fig. 1(a). Alternatively, when $\mathrm{Im}(l_j)>1$ and the frequency κ_j is purely imaginary, the solution is called a Kuznetsov-Ma (KM) soliton. In contrast to the AB, it is localized in t but periodic in x. The KM soliton has been displayed individually in Fig. 1 of our previous work [19]. We mention again that, for the general case of complex l_j, the oscillating soliton is located at a finite angle to the x and t axes.

In each case, the modulation frequency can be controlled by the eigenvalue. The period of the AB solution increases when $\kappa_j\to 0$, as can be seen from the examples shown in Fig. 1. In the limit of $l_j\to i$ ($\kappa_j\to 0$), the period of both the ABs and KM solitons goes to infinity and, in the first-order scenario, only one isolated peak remains. Such a solution is known as a Peregrine soliton and is considered to be the prototype of a first-order rogue wave. In Fig. 1(c), which depicts a nonlinear superposition of three $\kappa_j\to 0$ ABs, six Peregrine solitons appear simultaneously.

For higher-order rogue-wave solutions, several facts have already been previously established:

(1) All nonlinear superpositions of ABs and KM solitons in the rogue-wave limit ($\kappa_j\to 0,\forall j$) are reduced to a pattern of peaks, with each appearing as a Peregrine soliton or some nonlinear combination thereof. Then, naturally, the first-order rogue wave can be effectively considered as a "quantum" of the whole structure [20].

(2) The number of such quanta in an order n solution is not n, as one would expect when applying ordinary knowledge of multisoliton theory. Contrary to these expectations, the number of such quanta is $n(n+1)/2$. Figure 1(c) is a direct confirmation of this simple rule, representing the case for $n=3$.

(3) In inverse scattering theory, no two components with unique j can coexist with equal eigenvalues l_j. When this happens, the solution is undefined. The case has to be considered as degenerate and a special technique has to be used to resolve the uncertainty [21]. One of the ways to deal with the common $\kappa_j\to 0$ limit in the multirogue-wave case is to assume that $\kappa_j=k_j\times\kappa$, with unique values of k_j for

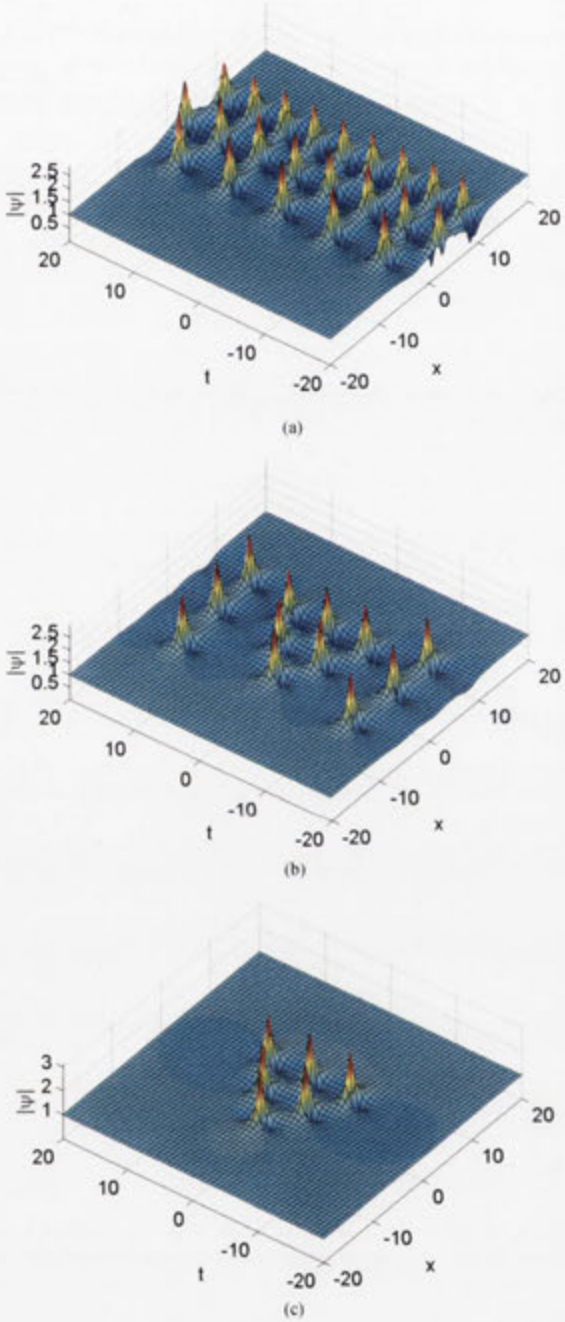

FIG. 1. (Color online) Step-by-step snapshots of the infinite-period limit applied to a triple AB superposition. Modulation frequencies are $\kappa_1 = \kappa$, $\kappa_2 = \sqrt{2}\kappa$, and $\kappa_3 = \sqrt{3}\kappa$. The shifts are $x_1 = 0, x_2 = 5\kappa^2$, and $x_3 = 10\kappa^2$. (a) $\kappa = 0.8$; (b) $\kappa = 0.5$; (c) $\kappa \approx 0$.

each j and with the ordering $k_1 < k_2 < \cdots < k_n$. As the common factor κ goes to zero, in the limit, all κ_j will be within the modulation instability band [26] no matter how many components are involved. From the successive changes leading to Fig. 1(c), we can conjecture that each component j contributes j rogue-wave quanta to the higher-order solution. This conjecture would justify the observed number of quanta, $n(n+1)/2$, in the whole superposition.

(4) Higher-order rogue-wave patterns are precariously dependent on the component shifts. An example is the third-order "triangular cascade" [20] shown in Fig. 1(c). Obtained from three ABs in the rogue-wave limit, this particular solution appears only when the shifts are scaled according to $x_j \propto \kappa^2$. If the shifts are proportional to other orders of frequency, the pattern changes. One such possibility (for $x_j \propto \kappa^4$) leads to a circular cluster [19]. More generally (e.g., for $x_j \propto \kappa^0$), the pattern may expand to the infinity horizon of the x and t plane when $\kappa \to 0$. A reduced number of peaks then will remain visible from the whole set. However, the remaining number of quanta should still be $i(i+1)/2$, where $i \leqslant n-2$ for an order n solution.

This fourth concept is highly unintuitive due to the intricacies of the rogue-wave limit. It motivates the unique redefinition of shifts as even-order expansions in the κ variable,

$$\begin{aligned} x_j &= \sum_{m=1}^{\infty} \kappa^{2(m-1)} X_{jm} \\ &= X_{j1} + X_{j2}\kappa^2 + X_{j3}\kappa^4 + \cdots, \\ t_j &= \sum_{m=1}^{\infty} \kappa^{2(m-1)} T_{jm} \\ &= T_{j1} + T_{j2}\kappa^2 + T_{j3}\kappa^4 + \cdots, \end{aligned} \tag{2}$$

where the coefficients X_{jm} and T_{jm} are constants. When $\kappa \to 0$, it follows that $x_j \to X_{j1}$ and $t_j \to T_{j1}$, i.e., all higher-order terms contribute negligibly to a physical component shift. Thus, one can mistakenly conclude that the extra shift coefficients have no impact on the NLSE rogue waves. However, analytic application of the rogue-wave limit shows that the values of the expansion coefficients are actually allowed to enter the solution [21]. Consequently, the structure of the resulting pattern depends on them.

When either X_{jn} or T_{jn} is nonzero for a single component in an order n solution, a basic higher-order rogue wave expels a ring of Peregrine solitons from the central structure. The solution then becomes a circular cluster [19]. However, in general, all expansion coefficients in Eq. (2) with $1 \leqslant m \leqslant n$ are important in determining the structure of an order n rogue wave, provided that the prelimit component frequencies are all in appropriate ratio. The triangular cascade in Fig. 1(c) is a prime example. It is a third-order solution, but it requires a certain ratio of $k_1 : k_2 : k_3$ and depends on the $m = 2$ expansion coefficients [20].

Below, we refer to the expansion coefficients X_{jm} as shifts of order m. For simplicity, we will set all $T_{jm} = 0$ unless otherwise stated. This does not affect the generality of our results as all rogue-wave patterns can be rotated in the x and t plane [20]. For these cases, the expansion coefficients of same order for x and t must be functionally related. In this work, we present all possible fundamental NLSE rogue-wave structures up to order 6, providing the relations between shifts

and frequencies that ensure their existence. By induction, we extend these patterns beyond order 6.

III. THE POLYNOMIALS OF EXISTENCE

The basic set of rogue-wave structures up to order 6 is shown in Fig. 2. Each image is a top-view false-color contour plot of an order n rogue wave constructed using only order m shifts. The latter mathematical restriction defines the basic set solutions (BSS). Section V gives further appearance-based justification for this natural choice of the BSS. Here, we present numerical evidence for how the structures of each column exist only if, for column m, there is a polynomial relation of order $m-1$ between the order m component shift values (X_{jm}) and the squared ratio coefficients of the modulation frequencies (k_j^2).

The images in the first column of Fig. 2 depict translations of traditional "fused" rogue waves [27], with the largest possible amplitude for each order n at the center of each wave function. The existence condition for such structures is simple: All components must have the same constant (or zero) shift. Nonzero shifts will simply translate the total structure in space and time from the origin. Any difference in the component shift values causes the solution to disappear. Specifically, the substructures that form the rogue wave in the $\kappa_j \to 0$ limit cannot coexist and repel each other to infinity, thus effectively reducing the order of the remnant composite rogue wave [19]. Therefore, the lowest-order shifts X_{j1} and T_{j1} must be equal for all j.

Rogue waves of order 4 are shown in Fig. 3(b). Three separate solutions are presented on the same plot to save space. The corresponding shift and frequency parameters for each solution are illustrated in Fig. 3(a). As discussed, all four components for each rogue wave must have the same X_{j1} value. The components must also have different prelimit modulation frequencies [21]. For example, rogue wave II has four components with a frequency ratio of $\kappa_1 : \kappa_2 : \kappa_3 : \kappa_4 = 1 : \sqrt{2} : \sqrt{3} : \sqrt{4}$, all with $X_{j1} = -5$. As a result, rogue wave II is located at $(x,t) = (-5,0)$ in Fig. 3(b). Choosing four coordinates on a line with a certain X_{j1} places the total structure at $x = X_{j1}$. This remains true if a component has a negative k_j^2 value, as it simply means that the prelimit ($\kappa \neq 0$) component frequency κ_j is imaginary. This is equivalent to saying that component 3 of rogue wave III was a KM soliton rather than an AB before application of the $\kappa \to 0$ limit.

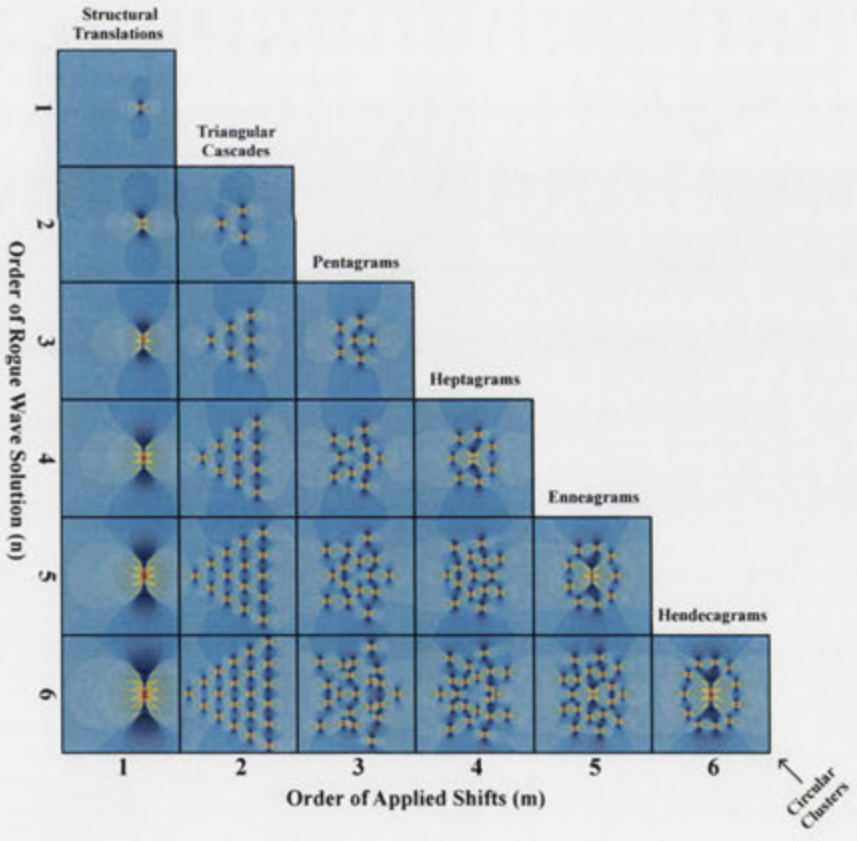

FIG. 2. (Color online) Overview of all fundamental rogue-wave solutions up to order 6. Structures in the first column appear off-center due to physical translations induced by first-order shifts. All other solutions are centered at the origin due to higher-order shifts being associated solely with fission effects. Structures belonging to column m (for $m > 1$) have effective radial symmetry of order $2m-1$. Each circular cluster along the diagonal ($n = m$) displays a ring of $2m-1$ Peregrine solitons around a central rogue wave of order $m-2$ (for $m > 2$).

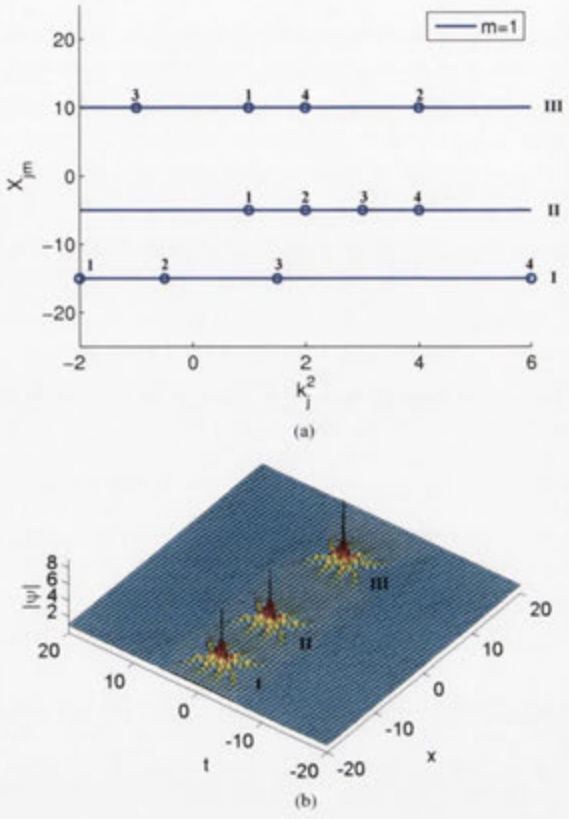

FIG. 3. (Color online) (a) Possible parameter choices for rogue waves of order 4 illustrated by circles. Vertical axis represents the first-order shift (X_{j1}) while the squared modulation frequency ratio coefficient (k_j^2) of each component is shown along the horizontal axis. The number above each circle is the component index (j). (b) A graphical superposition of the resulting rogue waves. Rogue waves I, II, and III are located at $x = X_{j1}$.

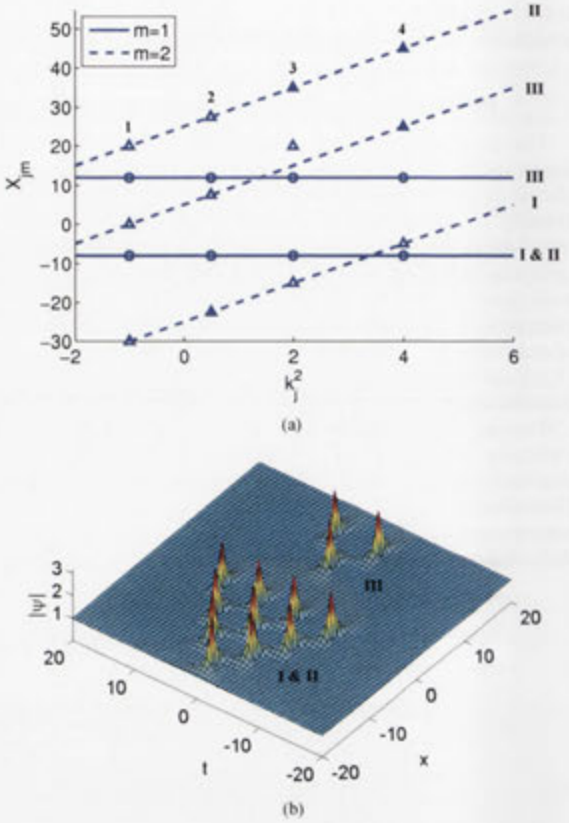

FIG. 4. (Color online) (a) Parameter choices for three instances of fourth-order rogue waves (I, II, and III). The components have the same squared modulation frequency ratio coefficients (k_j^2) for each of the three rogue waves. Thus, each column of coordinates is associated with a single component (denoted by index j). The ordinate of each circle and triangle is the first- and second-order shift (X_{j1} and X_{j2}), respectively, of each component. Lines represent the polynomial relations required for existence. (b) Overlay of resulting rogue waves I, II, and III. This is a graphical superposition of three different solutions, not a single solution. Two of them (I and II) are identical.

Similarly, rogue wave I forms in the intersection of two KM solitons and two ABs. Furthermore, the ordering of component frequencies is arbitrary. It does not have to be monotonic with respect to component index. Rogue wave III in Fig. 3 is an example of this.

The second column in Fig. 2 illustrates the simplest cases when higher-order shifts result in nontrivial structures. With various forerunners elsewhere [9,28], these triangular cascades were investigated in detail within our previous work [20]. It was found that these structures could be generated via the Darboux method with X_{j2} shifts alone. In particular, with the ordering $X_{12} < X_{22} < \cdots < X_{n2}$, and d_j denoting the second-order "differential shift" between the components j and $j+1$, a rogue-wave cascade is always produced in the $\kappa \to 0$ limit, provided that

$$\kappa_j : \kappa_{j+1} : \kappa_{j+2} = k_j : k_{j+1} : \sqrt{\frac{(d_j + d_{j+1})k_{j+1}^2 - d_{j+1}k_j^2}{d_j}}, \tag{3}$$

for all j ranging from 1 to $n-2$. It is evident that Eq. (3) is nothing but a linear relationship between the squared modulation frequency ratio coefficients (k_j^2) and second-order shifts. Indeed, Fig. 4 shows how triangular cascades can be constructed with adherence to this rule.

Standard fused rogue waves, such as those shown in Fig. 3(b), implicitly have X_{j2} set to zero for all j. This would be represented by a dashed $y = 0x + 0$ line in Fig. 3(a). If this line is modified in parameter space, as shown in Fig. 4(a), a higher-order rogue wave splits into a triangular array of Peregrine solitons. The y intercept of each line does nothing to affect the structure. Rogue waves I and II, translated to $x = -8$, have second-order shifts that lie on a $y = 5x - 25$ and $y = 5x + 25$ line, respectively. Yet the overlay in Fig. 4(b) shows that the two wave functions remain identical. On the

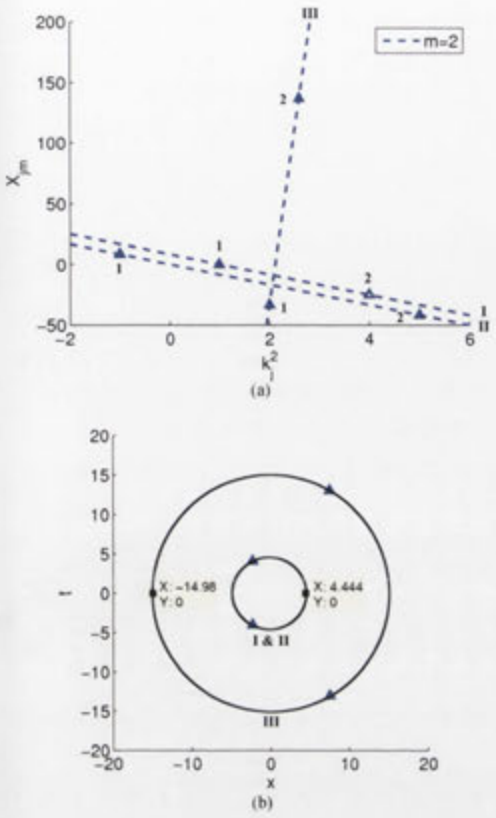

FIG. 5. (Color online) (a) Parameter choices for three rogue waves (I, II, and III) of order 2, shifted by X_{j2} alone. Coordinates of each triangle represent the second-order shift (X_{j2}) and the squared modulation frequency ratio coefficient (k_j^2) of each component, where the number near the triangle is the component index (j). Lines represent the polynomial relation required for existence. (b) The maxima of rogue waves I, II, and III in the x and t plane. Circumcircles are drawn for each triangular cascade.

other hand, it is crucial that all components have shifts that lie on the same polynomial of existence.

Rogue wave III is an example of where the rule is broken, with the value of X_{32} being five dimensionless units greater than what is required. This is represented in Fig. 4(a) by a triangular marker deviating from the dashed line denoted as III. As discussed with first-order shifts, the resulting structure is shown in Fig. 4(b) as a diminished rogue wave of second order. Moreover, this reduction in order is instantaneous in the $\kappa \to 0$ limit for any deviation. It appears necessary that any shifts belonging to a particular order must lie exactly on the relevant existence polynomial in parameter space.

Notably, the existence polynomial for second-order shifts has an extra degree of freedom relative to the one for first-order shifts, this being the slope of the line. In the case of Fig. 4(b), all three rogue waves are oriented in the same direction, due to the positive gradients of the $m = 2$ lines in Fig. 4(a). However, as the slope decreases to zero, the peaks merge together to form a fused rogue wave. If the gradient becomes negative, as with rogue waves I and II in Fig. 5(a), the solution again expands into a cascade but is now oriented in the opposite direction, as the three peaks in the center of Fig. 5(b) demonstrate.

To ensure consistency with previous work [18,19], we note that the circumradius of a second-order cascade (and cluster) was derived as

$$R \approx 2^{2/3}\left(x_d^2 + t_d^2\right)^{1/6}, \tag{4}$$

where $x_d = X_{12} - X_{22}$ and $t_d = T_{12} - T_{22}$. However, it was realized in later work that the scaling of shifts depends on the component frequencies established before the $\kappa \to 0$ limit [21]. This means that Eq. (4) is valid for a $\kappa_1 : \kappa_2 = 1{:}2$ ratio, used in the original analytic derivations, but must be recalculated for other prelimit ratios.

To demonstrate this, rogue wave I in Fig. 5(a) uses the original frequency ratio and has a value of 25 for x_d. The resulting circumradius, shown in Fig. 5(b), is $R \approx 4.444$, which is in reasonable agreement with the expected 4.6416 value. However, rogue wave II possesses a larger x_d value for a different prelimit frequency ratio and produces an identical wave function. In any case, the linear nature of the existence polynomial means that Eq. (4) can be used to engineer structures of any radius. Indeed, the second-order shifts of rogue wave III in Fig. 5(a) lie on the line $y = (850/3)x - 600$, which corresponds to $x_d = 850$ for the definitions used in Eq. (4). Accordingly, the circumradius of cascade III is approximately 15 in Fig. 5(b), as expected.

IV. PENTAGRAMS AND BEYOND

In the previous section, we established that an order $m - 1$ polynomial relationship between order m shifts and the squared ratio coefficients of component modulation frequencies results in both rogue-wave translations ($m = 1$) and cascades ($m = 2$). Deviations from these polynomials produce rogue waves of decreased order. However, both traditional fused structures [27] and cascades [9,20] are relatively well known at this stage. Fortunately, the aforementioned existence polynomials indicate a way to predictably generate more complicated structures that have only been glimpsed via other methods [10].

For example, forming a parabolic relationship between third-order shifts and k_j^2 is the natural next step, as shown in Fig. 6(a). Indeed, applying this polynomial restriction expands a standard fused rogue wave into a structure with effective pentaradial symmetry, shown for fourth order in Fig. 6(b), which we refer to as a rogue-wave pentagram. The top view of this wave function is the second image of the third column in Fig. 2.

As should be evident by this stage, it is only the order $m - 1$ derivative of the order $m - 1$ existence polynomial for X_{jm} that has any effect on the shape of the rogue wave. In the case of Fig. 6(a), all three parabolic curves have the same curvature for the same k_j^2 value, despite generally differing on slope and X_{jm} value. Consequently, the three rogue-wave pentagrams are identical in Fig. 6(b). However, as expected, the pentagram can be expanded in spatiotemporal size by choosing a parabola with increased curvature, and a vertically inverted

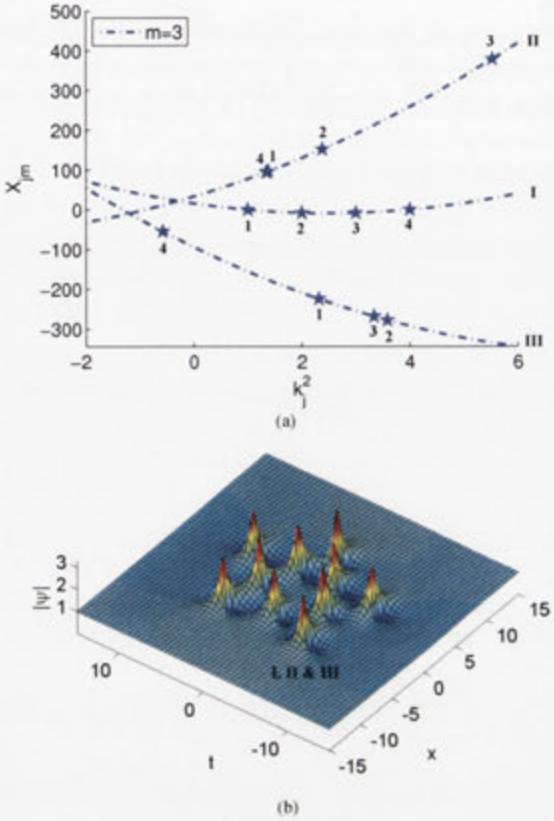

FIG. 6. (Color online) (a) Parameter choices for three rogue waves (I, II, and III) of order 4, shifted by X_{j3} alone. Coordinates of each star represent the third-order shift (X_{j3}) and the squared modulation frequency ratio coefficient (k_j^2) of each component, where the number near the star is the component index (j). Curves represent the polynomial relation required for existence. (b) Overlay of resulting rogue waves I, II, and III. This is a graphical superposition, but, as all three rogue waves are identical, this can also be considered a true solution.

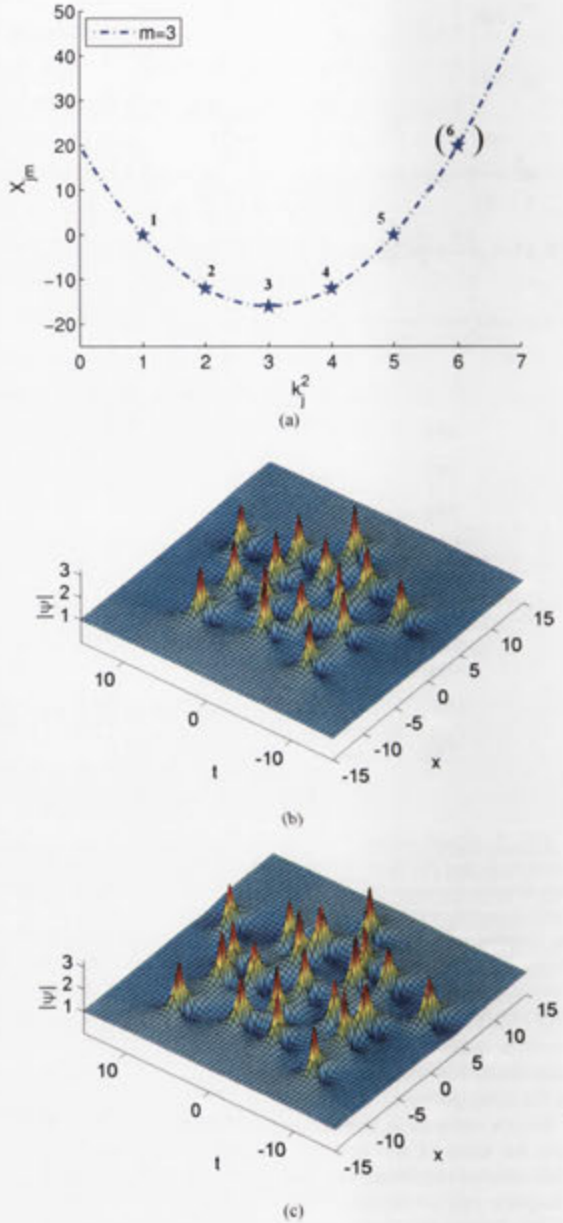

FIG. 7. (Color online) (a) Parameter choices for high-order rogue-wave pentagrams produced by X_{j3} shifts alone. Coordinates of each star represent the third-order shift (X_{j3}) and the squared modulation frequency ratio coefficient (k_j^2) of each component, where the number near the star is the component index (j). Curves represent the polynomial relation required for existence. (b) An order 5 pentagram generated with components 1 to 5. (c) An order 6 pentagram generated with components 1 to 6.

polynomial generates a pentagram that points in the opposite direction.

In general, the procedure for generating higher-order structures with pentaradial symmetry is to continue choosing extra components that adhere to the parabolic relation between third-order shifts and k_j^2. For example, Fig. 7(a) shows five components that obey the relation, thus producing the rogue-wave pentagram in Fig. 7(b), which is also displayed elsewhere [10]. However, Fig. 7(a) also shows a sixth component on the same existence polynomial, which contributes to the sixth-order pentagram in Fig. 7(c) being formed from six $\kappa \to 0$ ABs. Therefore, along with the similar extension of cascade forms [20], it is not hard to produce pentagram structures of any order.

The structures within each successive column of Fig. 2 follow the same trend. Second-order shifts are associated with triradial symmetry and triangular cascades, third-order shifts are associated with pentaradial symmetry and pentagrams, and, hence, order m shifts are associated with peak arrangements that are effectively identical following rotations of $2\pi/(2m-1)$. Rogue-wave heptagrams thus are generated

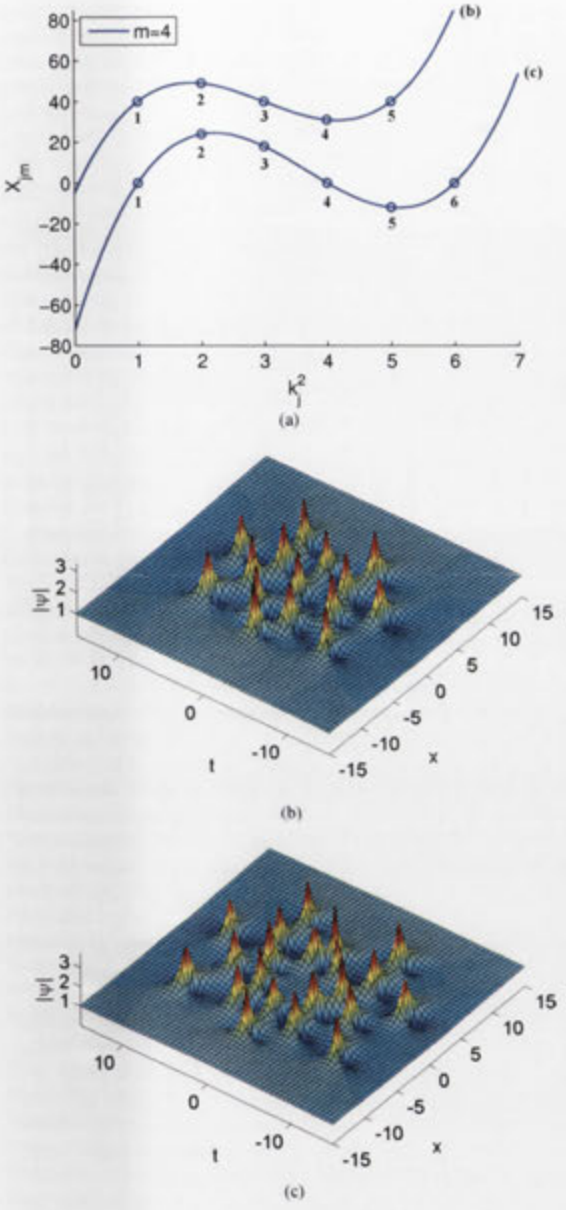

FIG. 8. (Color online) (a) Parameter choices for high-order rogue-wave heptagrams produced by X_{j4} shifts alone. Coordinates of each circle represent the fourth-order shift (X_{j4}) and the squared modulation frequency ratio coefficient (k_j^2) of each component, where the number near the circle is the component index (j). Curves represent the polynomial relation required for existence. (b) Rogue wave of order 5. (c) Rogue wave of order 6.

from cubic relations involving squared component frequencies and fourth-order shifts, as shown in Fig. 8(a). As usual, only the fourth-order derivative of the polynomial appears to have any effect on structural spacing. A rogue-wave heptagram recursively generated from five ABs is shown in Fig. 8(b), while a sixth-order heptagram is shown in Fig. 8(c). The limits of numerical accuracy lead to a minor distortion of shape in the latter case, but both wave functions still display concentric rings, each with seven rogue-wave quanta.

This existence polynomial technique can be extended indefinitely, with a quartic relationship between X_{j5} and k_j^2 in Fig. 9(a) leading to the generation of rogue-wave enneagram I in Fig. 9(b). In combination with previous circular cluster [19] and triangular cascade results [20], these new solutions cover all the fundamental structures up to order 6, as displayed in

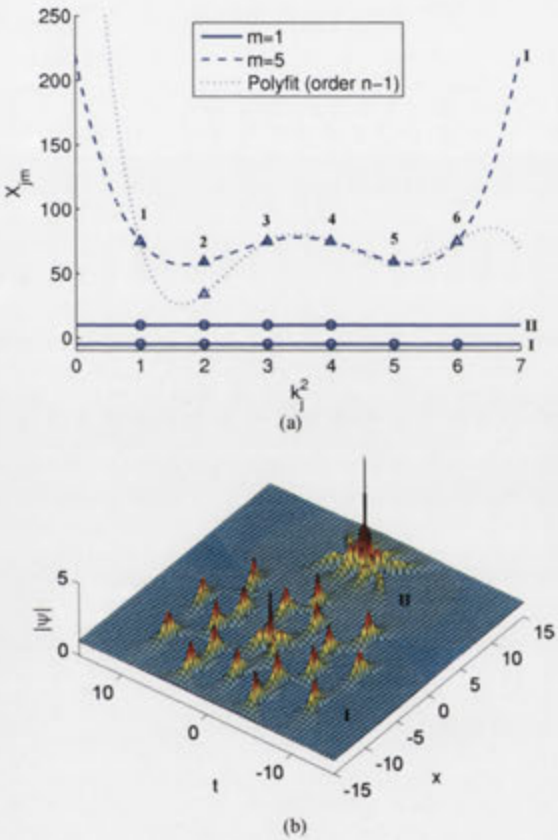

FIG. 9. (Color online) A rogue wave of order 6, shifted by X_{j1} and X_{j5} alone, and a rogue wave of order 4, shifted by X_{j1} alone. (a) Parameter choices for rogue waves I and II. The components (where they exist) have the same squared modulation frequency ratio coefficients (k_j^2) for each of the two rogue waves. Thus each column of coordinates is associated with a single component (denoted by index j). The ordinate of each circle and triangle is the first- and fifth-order shift (X_{j1} and X_{j5}) of each component, respectively. Continuous lines and dashed curves represent the polynomial relations required for existence. The dotted line represents an order 5 polynomial fit of the X_{j5} shifts for rogue wave I when component 2 is perturbed. (b) Overlay of resulting rogue waves I and II. This is a graphical superposition, not a true solution.

Fig. 2. However, this understanding can be extended even further for higher orders and "hybrids."

V. EXTRAPOLATION AND HYBRIDIZATION

By associating each fundamental type of rogue-wave solution with a unique well-defined parameter in the Darboux generation scheme, we can visualize the trends in Fig. 2 and extend the patterns beyond order 6. We already know from Sec. IV that an order m shift is associated with radial symmetry of degree $2m-1$, which allows for the natural subdivision of fundamental solutions based on appearance. Moreover, the simplest nontrivial structure of any shift order appears to be a circular cluster, which is consistent with the notion of having $2m-1$ rogue-wave quanta in a ring [19]. Hence, we know that an order n structure with order n shifts alone will display an order $n-2$ peak (with amplitude $2n-3$) surrounded by $2n-1$ Peregrine solitons.

Conveniently, the existence polynomial theory explains why rogue waves are susceptible to shedding a ring of rogue-wave quanta for poorly chosen shifts. If we only let one order of shift be nonzero for all components, thus writing $x_j = X_{jm}\kappa^{2(m-1)}$, then this can always be expressed in terms of order n shifts, specifically $x_j = X_{jm}\kappa^{2(m-n)}\kappa^{2(n-1)}$, which in turn implies $X_{jn} = X_{jm}\kappa^{-2(n-m)}$. If X_{jm} is well chosen so as to adhere to the relevant existence polynomial, then we can consider it a finite contribution to a noncluster fundamental shape, such as in the case of fifth-order shifts in Fig. 9(a) producing the enneagram in Fig. 9(b). However, if X_{jm} fails to contribute in this way, such as by one component being perturbed from the existence polynomial, then the shifts must still have an effect of some sort. Indeed, there will always be an order $n-1$ polynomial that is capable of fitting n coordinates in parameter space, as shown in Fig. 9(a), which means that any "badly" generated structure will always default to circular cluster form. But as X_{jm} is nonzero and $n > m$, $\kappa \to 0$ will take all X_{jn} to infinity via the aforementioned relation. This effectively becomes an infinite contribution to a circular cluster shape, which manifests as a structure with infinite radius for its outer ring [19]. Thus, in such a case, an order $n-2$ structure is always left behind in the rogue-wave limit. For example, a perturbation of frequency or shift for enneagram I in Fig. 9(b) results in a fourth-order rogue wave similar to II.

Acknowledging this issue, we henceforth assume that shift orders adhere strictly to existence polynomials, resulting in finite contributions to relevant structures. The $n(n+1)/2$ rogue-wave quanta that constitute the structures of order n in Fig. 2 can then be subdivided into rings of $2m-1$ quanta, for sufficiently large shifts of order m, and a remnant that appears as a fused central peak. It is soon evident from Table I that certain patterns arise for increasing solution orders. For instance, the number of rogue-wave quanta in the center of a triangular cascade cycles through (0,1,0) for each successive triplet of solution order, starting with 0, 1, and 2. It follows that the center of a pentagram cycles through (0,1,3,1,0) merged rogue-wave quanta, and a heptagram center similarly cycles forwards and backwards between a zero- and third-order rogue wave. For this same reason, the enneagram in Fig. 9(b) is not solely composed of first-order Peregrine solitons. We thus can extrapolate that structures related to an order m shift iterate through cycles of length $2m-1$, where the central peak oscillates between a rogue wave of order 0 and $m-1$.

TABLE I. The structure of rogue wave arrays for various orders and shifts. The first column denoted as S.O. is the solution order. The second column (Qu.) denotes the number of rogue-wave quanta in the solution. The rest of the columns on the right, marked as SAm, show how the structure is arrayed when the order m shifts are sufficiently large. The elements of these columns are presented in the format $q_r \times r + q_c$, where q_r is the number of quanta per "ring," r is the number of rings, and q_c is the number of quanta fused into a central peak. Data beyond the solution of order 6 have been extrapolated.

S.O.	Qu.	SA1	SA2	SA3	SA4	SA5
0	0	**0**	$3\times0+\mathbf{0}$	$5\times0+\mathbf{0}$	$7\times0+\mathbf{0}$	$9\times0+\mathbf{0}$
1	1	**1**	$3\times0+\mathbf{1}$	$5\times0+\mathbf{1}$	$7\times0+\mathbf{1}$	$9\times0+\mathbf{1}$
2	3	**3**	$3\times1+\mathbf{0}$	$5\times0+\mathbf{3}$	$7\times0+\mathbf{3}$	$9\times0+\mathbf{3}$
3	6	**6**	$3\times2+\mathbf{0}$	$5\times1+\mathbf{1}$	$7\times0+\mathbf{6}$	$9\times0+\mathbf{6}$
4	10	**10**	$3\times3+\mathbf{1}$	$5\times2+\mathbf{0}$	$7\times1+\mathbf{3}$	$9\times0+\mathbf{10}$
5	15	**15**	$3\times5+\mathbf{0}$	$5\times3+\mathbf{0}$	$7\times2+\mathbf{1}$	$9\times1+\mathbf{6}$
6	21	**21**	$3\times7+\mathbf{0}$	$5\times4+\mathbf{1}$	$7\times3+\mathbf{0}$	$9\times2+\mathbf{3}$
7	28	**28**	$3\times9+\mathbf{1}$	$5\times5+\mathbf{3}$	$7\times4+\mathbf{0}$	$9\times3+\mathbf{1}$
8	36	**36**	$3\times12+\mathbf{0}$	$5\times7+\mathbf{1}$	$7\times5+\mathbf{1}$	$9\times4+\mathbf{0}$
9	45	**45**	$3\times15+\mathbf{0}$	$5\times9+\mathbf{0}$	$7\times6+\mathbf{3}$	$9\times5+\mathbf{0}$
10	55	**55**	$3\times18+\mathbf{1}$	$5\times11+\mathbf{0}$	$7\times7+\mathbf{6}$	$9\times6+\mathbf{1}$
...	...	...	...	...	...	...

It is also clear from Table I that the number of rings added per solution order increases by one after the point in every cycle where the center reaches maximum order. For instance, cascades begin adding individual triplets at order 2 and pairs of triplets at order 5. Consistent with this, the single-ring circular cluster happens to occur immediately following the maximum of the very first cycle, thus also explaining its order $m-2$ central peak. By combining all these trends, we can predict the layout of any fundamental rogue-wave solution affected by shifts. For example, an order 18 hendecagram, generated by order 6 shifts, should have a central third-order rogue-wave peak surrounded by 15 rings of 11 quanta each.

All this discussion of shape is fundamental to understanding the physics of rogue-wave NLSE structures. For one thing, maximum amplitudes of each solution and shift order are already implicitly encoded in Table I. For example, an order 7 pentagram (SA3 column) has a central peak of three fused quanta, which can be correlated with a second-order rogue wave via the SA1 column. Knowing that an order n fused rogue wave has an amplitude of $2n+1$, this means that the structure possesses a sharp spike of amplitude 5. Furthermore, with the information presented in this work, it is also possible to extrapolate backwards from shape so as to determine how many breathers are interacting to form a rogue wave and how they are spatiotemporally located with respect to each other.

This backward extrapolation becomes particularly relevant with the realization that experimentally produced NLSE rogue-wave structures are unlikely to ever truly be ideal. This means that κ in Eq. (2) is small but not zero, and both modulation frequencies and the different orders of shift manifest as actual physical observables pertaining to component breathers rather than mere theoretical abstractions. Moreover, as demonstrated

in the simplest case within Sec. III, the circumradius of a rogue wave "ring" is dependent on the highest-order coefficient of an existence polynomial. With the appropriate constant of proportionality determined, these results enable an effective bijection between simple breather arrangements and complex rogue waves of any spatiotemporal size.

In any case, we have thus far only discussed rogue waves associated with unique orders of shift in Eq. (2), having referred to them as "fundamental" structures (BSS) that obey the NLSE. However, the effects of different shift orders are independent, associating the set of X_{jm} and T_{jm}, for all j and for each $m \leqslant n$, with a degree of freedom in the determination of rogue-wave shape. This has been implied to some extent by Figs. 4 and 9, where X_{j1} has shifted entire wave functions without destabilizing the arrangements generated by other orders of shift. However, previous work with "claw structures" [20] has shown that this is not exclusive to first order, and any combination of fundamental wave functions can be mixed to generate a nontrivial hybrid rogue wave with shared features.

We originally postulated that single-ring clusters could be further split into multiple rings, with consecutive concentric shells differing by four Peregrine solitons [19]. Such an arrangement is nothing more than circular clusters within circular clusters, and this is achieved by making X_{jm} adhere to a nonzero order $m-1$ polynomial for $m = n, n-2, n-4, \ldots$, all the way down to second or third order. The only technicality is that each higher-order shift must be sufficiently large to pull out a ring of quanta. Due to the relative parametric ease by which circular clusters are generated, examples of the resulting multiring structures can be seen elsewhere [10]. Moreover, circular clusters are simple to hybridize in general. With sufficiently large X_{jn} and T_{jn} for an order n rogue wave, the central peak can be modified independently of the ring by any order of shift from 2 to $n-2$. For example, a sixth-order circular cluster, generated with nonzero T_{j6}, has its central peak arrayed into a fourth-order cascade via nonzero T_{j2}. This is shown in Fig. 10(a). Alternatively, the center can instead become a fourth-order pentagram via nonzero T_{j3}, as shown in Fig. 10(b).

This concept of decomposition has been independently verified elsewhere [10], but, because of the existence polynomial and hybridization theory outlined here, we can systematically extend this to construct many more unexpected NLSE rogue-wave solutions. It is clear that circular cluster hybrids are relatively simple to understand and extrapolate. The outermost ring draws out $2n-1$ rogue-wave quanta from $n(n+1)/2$, and leaves behind $(n-2)(n-1)/2$ quanta that can be rearranged into any order $n-2$ structure. However, if the highest order of nonzero shift is below n, then there is an attempt to exclude less than $2n-1$ quanta in a circular ring, which leaves behind an irregular number of quanta in the center. If left as a fundamental structure, the resulting rogue-wave arrangement is still regular and circular, as shown in Fig. 2. But hybridizing structures in general will result in a competition between features, only won decisively if one order of shift dominates the other. The higher degrees of symmetry will often break, resulting in bilateral rogue-wave arrangements [20]. Despite this, there are many hybrid structures that display elegant geometries. For example, a T_{j2} triangular cascade and a T_{j5} enneagram both

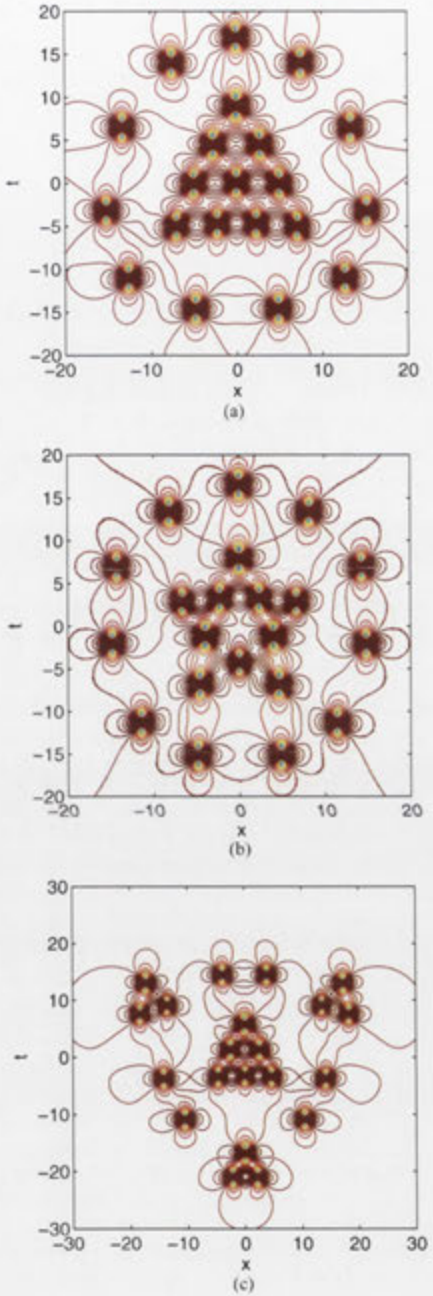

FIG. 10. (Color online) Contour plots of sixth-order hybrid rogue waves, shifted in the t axis, with $k_j = \sqrt{j}$. (a) Ringed cascade. T_{j2} and T_{j6} adhere to $y = 3.75(x-1)$ and $y = 1750(x^5 - 20x^4 + 155x^3 - 580x^2 + 1044x - 720)$, respectively, with respect to squared modulation frequency ratio coefficients (k_j^2). (b) Ringed pentagram. T_{j3} adheres to $y = 1.5(4x^2 - 28x + 24)$ with respect to k_j^2. T_{j6} is the same as for the ringed cascade. (c) Cascade-enneagram hybrid. T_{j2} and T_{j5} adhere to $y = -20(x-1)$ and $y = 500(2x^4 - 28x^3 + 134x^2 - 252x + 144)$, respectively, with respect to k_j^2.

share triradial symmetry. Thus, as Fig. 10(c) shows, mixing the structures retains that symmetry.

VI. CONCLUSION

In summary, our main results are as follows:

(1) Within the context of the Darboux scheme, we have shown that spatial and temporal axis shifts of breather components can be written as expansions involving frequency, and each coefficient within the expansion is responsible for a unique form of fundamental rogue-wave solution to the NLSE. We have named these coefficients "shifts of order m," whereby $m = 1$ is responsible for global structure translations, $m = 2$ is responsible for triangular cascades [20], $m = 3$ is responsible for pentagrams, and so on, as detailed in Fig. 2. For a rogue wave composed of n breathers, the $m = n$ shift is associated with a circular cluster [21]. Higher-order shifts beyond this do not appear to affect the structure of a rogue wave.

(2) We have shown numerically that, for rogue-wave structures of shift order $m < n$ to exist without defaulting to a circular cluster with infinite circumradius, the shifts of order m must fit a polynomial of order $m - 1$ with respect to the squared coefficients of the ratio between prelimit component frequencies. The spatiotemporal size of the resulting rogue-wave arrangement is determined by the order $m - 1$ derivative of the polynomial, but no other derivative appears to have any effect. The sign and ordering of ratio coefficients similarly do not affect the shape of the rogue wave.

(3) We have found that the arrangements of fundamental rogue-wave solutions have a radial symmetry of degree $2m - 1$ for shift orders $m > 1$. The wave functions form spatiotemporal concentric rings, each made from a multiple of $2m - 1$ Peregrine solitons, and any remaining quanta fuse in the center to appear as a rogue wave of up to order $m - 1$. Using the trends shown in Table I, we are, hence, able to extrapolate and predict the large-scale structure of extreme high-order rogue waves.

(4) By realizing that each coefficient of the shift expansion is an independent degree of freedom in determining rogue-wave arrangement, we are able to continue generating valid NLSE solutions by "hybridizing" fundamental structures associated with different orders of shift. Indeed, provided that one order of shift does not dominate another, the resulting wave function expresses features from all fundamental constituents. Circular clusters are particularly amenable to hybridization, with additional lower-order shifts modifying the central peak in regular fashion. However, other elegant geometries are also possible when radial symmetries share a common factor in degree beyond bilateral symmetry.

Our study shows that the world of rogue waves is significantly more complicated than the world of solitons. Their growth-decay cycle in both space and time makes them unique formations in physics, with a range of applicability that still waits to be discovered. At the very least, their intricate spatiotemporal structure makes them attractive objects of study from an aesthetic point of view. As of such, the world of rogue waves can be considered a fusion of art and science.

ACKNOWLEDGMENTS

The authors acknowledge the support of the Australian Research Council (Discovery Project number DP110102068). N.A. and A.A. acknowledge support from the Volkswagen Stiftung.

APPENDIX: THE DARBOUX METHOD

The NLSE in Eq. (1) can be written in Lax pair form (e.g., see Chap. 2 of Ref. [29]):

$$\frac{\partial R}{\partial t} = UR, \quad \frac{\partial R}{\partial x} = VR,$$
$$R = \begin{bmatrix} r \\ s \end{bmatrix}, \quad U = \begin{bmatrix} il & i\psi^* \\ i\psi & -il \end{bmatrix}, \tag{A1}$$
$$V = \begin{bmatrix} il^2 - \frac{i}{2}|\psi|^2 & il\psi^* + \frac{1}{2}\frac{\partial \psi^*}{\partial t} \\ il\psi - \frac{1}{2}\frac{\partial \psi}{\partial t} & -il^2 + \frac{i}{2}|\psi|^2 \end{bmatrix},$$

where l is a complex eigenvalue. The linear system reduces to the original equation under the equality $R_{tx} = R_{xt}$.

We define the "first-order component functions" as follows:

$$r_{1j} = 2ie^{-ix/2}\sin(A_{jr} + iA_{ji}),$$
$$s_{1j} = 2e^{ix/2}\cos(B_{jr} + iB_{ji}), \tag{A2}$$

where functions A and B are in turn defined as

$$A_{jr} = \frac{1}{2}\left[\arccos\left(\frac{\kappa_j}{2}\right) + (t - t_j)\kappa_j - \frac{\pi}{2}\right],$$
$$B_{jr} = \frac{1}{2}\left[-\arccos\left(\frac{\kappa_j}{2}\right) + (t - t_j)\kappa_j - \frac{\pi}{2}\right], \tag{A3}$$
$$A_{ji} = B_{ji} = \frac{1}{2}\left[(x - x_j)\kappa_j\sqrt{1 - \frac{\kappa_j^2}{4}}\right],$$

with $\kappa_j = 2\sqrt{1 + l_j^2}$. The subscripts r and i refer to real and imaginary parts, respectively.

These component functions in Eq. (A2) are the solutions of Eq. (A1) when the eigenvalue is purely imaginary and ψ is equal to the plane-wave seeding solution $\psi_0 = e^{ix}$. They also serve as basic building blocks for the construction of higher-order solutions, where the number j uniquely identifies each component. In particular, each component denoted by j is described by a set of free parameters, the corresponding eigenvalue l_j, and coordinate shifts (x_j, t_j).

A first-order solution to the system in Eq. (A1) incorporates only one chosen set of free parameters and its corresponding r and s equations from Eq. (A2), denoted by $j = 1$. The first-order wave function thus is expressed as

$$\psi_1 = \psi_0 + \frac{2(l_1^* - l_1)s_{11}r_{11}^*}{|r_{11}|^2 + |s_{11}|^2}. \tag{A4}$$

An order $n > 1$ solution requires higher-order versions of the expressions for r and s. These are recursively generated [26,29] by

$$\begin{aligned} r_{np} = {} & [(l_{n-1}^* - l_{n-1})s_{n-1,1}^* r_{n-1,1}s_{n-1,p+1} \\ & + (l_{p+n-1} - l_{n-1})|r_{n-1,1}|^2 r_{n-1,p+1} \\ & + (l_{p+n-1} - l_{n-1}^*)|s_{n-1,1}|^2 r_{n-1,p+1}]/ \\ & (|r_{n-1,1}|^2 + |s_{n-1,1}|^2), \end{aligned}$$

$$\begin{aligned} s_{np} = {} & [(l_{n-1}^* - l_{n-1}) s_{n-1,1} r_{n-1,1}^* r_{n-1,p+1} \\ & + (l_{p+n-1} - l_{n-1}) |s_{n-1,1}|^2 s_{n-1,p+1} \\ & + (l_{p+n-1} - l_{n-1}^*) |r_{n-1,1}|^2 s_{n-1,p+1}] / \\ & (|r_{n-1,1}|^2 + |s_{n-1,1}|^2). \end{aligned} \tag{A5}$$

The p subscript in Eq. (A5) is used purely for enumeration and does not necessarily refer to a particular set of parameters. For example, the second-order function r_{21} is built from first-order component functions r_{11}, s_{11}, r_{12}, and s_{12}, thus incorporating parameters from both the components denoted by $j = 1,2$. Similarly, the third-order function r_{31} involves the second-order functions r_{21}, s_{21}, r_{22}, and s_{22}, which, in turn, are based on r_{11}, s_{11}, r_{12}, s_{12}, r_{13}, and s_{13} at the lowest order of recursion. Therefore, r_{31} constitutes parameters from all three components denoted by $j = 1,2,3$. In this way, Eq. (A5) allows n sets of free parameters to be incorporated into an order n solution. The diagram in Fig. 2.2 of Ref. [29] can be of use in representing this sequence of calculations. Subsequently, the order n NLSE solution is generated through recursion by

$$\psi_n = \psi_{n-1} + \frac{2(l_n^* - l_n) s_{n1} r_{n1}^*}{|r_{n1}|^2 + |s_{n1}|^2}. \tag{A6}$$

From a numerical perspective, the appearance of rogue-wave solutions can be determined by using values of κ_j that are as close to zero as computationally feasible. In this work, it is vital that individual κ_j values are still in a predetermined ratio, no matter how small they are. Shifts x_j and t_j are also dependent on powers of κ_j, via Eq. (2), and will likewise be close to zero.

[1] J. Cartwright and H. Nakamura, Notes Rec. Roy. Soc. **63**, 119 (2009).

[2] C. Kharif, E. Pelinovsky, and A. Slunyaev, *Rogue Waves in the Ocean* (Springer, Berlin, 2009).

[3] D. Peregrine, J. Austral. Math. Soc. Ser. B **25**, 16 (1983).

[4] N. Akhmediev, V. M. Eleonskii, and N. E. Kulagin, Zh. Eksp. Teor. Fiz. **89**, 1542 (1985) [Sov. Phys. JETP **62**, 894 (1985)].

[5] N. Akhmediev, A. Ankiewicz, and M. Taki, Phys. Lett. A **373**, 675 (2009).

[6] P. Dubard, P. Gaillard, C. Klein, and V. Matveev, Eur. Phys. J. Spec. Top. **185**, 247 (2010).

[7] P. Dubard and V. B. Matveev, Nat. Hazard Earth Syst. Sci. **11**, 667 (2011).

[8] P. Gaillard, J. Phys. A Math. Gen. **44**, 435204 (2011).

[9] Y. Ohta and J. Yang, Roy. Soc. Lond. Proc. Ser. A **468**, 1716 (2012).

[10] J. S. He, H. R. Zhang, L. H. Wang, K. Porsezian, and A. S. Fokas, Phys. Rev. E **87**, 052914 (2013).

[11] A. Chabchoub, N. P. Hoffmann, and N. Akhmediev, Phys. Rev. Lett. **106**, 204502 (2011).

[12] A. Chabchoub, N. P. Hoffmann, M. Onorato, and N. Akhmediev, Phys. Rev. X **2**, 011015 (2012).

[13] A. Chabchoub, N. Hoffmann, M. Onorato, A. Slunyaev, A. Sergeeva, E. Pelinovsky, and N. Akhmediev, Phys. Rev. E **86**, 056601 (2012).

[14] B. Kibler, J. Fatome, C. Finot, G. Millot, F. Dias, G. Genty, N. Akhmediev, and J. M. Dudley, Nat. Phys. **6**, 790 (2010).

[15] M. Erkintalo, K. Hammani, B. Kibler, C. Finot, N. Akhmediev, J. M. Dudley, and G. Genty, Phys. Rev. Lett. **107**, 253901 (2011).

[16] P. Shukla and W. Moslem, Phys. Lett. A **376**, 1125 (2012).

[17] R. Sabry, W. M. Moslem, and P. K. Shukla, Phys. Rev. E **86**, 036408 (2012).

[18] A. Ankiewicz, D. J. Kedziora, and N. Akhmediev, Phys. Lett. A **375**, 2782 (2011).

[19] D. J. Kedziora, A. Ankiewicz, and N. Akhmediev, Phys. Rev. E **84**, 056611 (2011).

[20] D. J. Kedziora, A. Ankiewicz, and N. Akhmediev, Phys. Rev. E **86**, 056602 (2012).

[21] D. J. Kedziora, A. Ankiewicz, and N. Akhmediev, Phys. Rev. E **85**, 066601 (2012).

[22] V. B. Matveev and M. Salle, *Darboux Transformations and Solitons* (Springer-Verlag, Berlin/Heidelberg, 1991).

[23] A. Ankiewicz, J. M. Soto-Crespo, and N. Akhmediev, Phys. Rev. E **81**, 046602 (2010).

[24] U. Bandelow and N. Akhmediev, Phys. Lett. A **376**, 1558 (2012).

[25] N. Akhmediev and N. V. Mitskevich, IEEE J. Quantum Electron. **27**, 849 (1991).

[26] N. Akhmediev, J. M. Soto-Crespo, and A. Ankiewicz, Phys. Lett. A **373**, 2137 (2009).

[27] N. Akhmediev, A. Ankiewicz, and J. M. Soto-Crespo, Phys. Rev. E **80**, 026601 (2009).

[28] A. Calini and C. Schober, Phys. Lett. A **298**, 335 (2002).

[29] N. Akhmediev and A. Ankiewicz, *Solitons: Nonlinear Pulses and Beams*, Vol. 5 of Optical and Quantum Electronics (Chapman & Hall, London, 1997), Chaps. 3–4.

Epilogue

Despite the summative nature of this chapter, the development of the rogue-wave hierarchy with a physically based Darboux-transformation perspective leads to several interesting conclusions worth expanding. For instance, the establishment of so-called existence conditions provides a good reason why circular clusters were chronologically discovered first [2], in that it is always possible to fit a polynomial of order $n-1$ through n 'parametric coordinates'. More specifically, a fused rogue wave [69] is a 'trivial' case that simultaneously adheres to all existence conditions (with zero spatiotemporal circumradius), but one shifted component alone is enough to break every single relevant polynomial relation except the one pertaining to circular clusters.

Of course, in the $\kappa \to 0$ limit, spatiotemporal shifts proportional to κ^a rather than κ^b will be considered infinitely too large to produce a structure relevant to the order of the latter exponent b, in the case of $a < b$. But, as the Darboux scheme in this thesis has been implemented numerically with small but technically finite κ values, this error factor is no longer infinite. Choosing the wrong exponent would still replicate the right geometry, just with a false spatiotemporal circumradius. Indeed, this is a major reason why numerical techniques have proved somewhat more enlightening than analytics for the exploration of multi-rogue wave NLSE solutions [86, 88]. Put simply, a misguided notion that a rogue triplet depends on finite shifts (i.e. proportional to κ^0 rather than κ^2) will still reproduce its features for $\kappa \neq 0$. This step in the right direction can then be subsequently refined with numerical techniques, such as determining what κ exponent is required to keep the circumradius independent of variations in the value of κ. Likewise, finite shifts are sufficient to use as an exploratory first step for triangular cascades [4], before constraining their parametric dependencies, but the contrasting issue for this case is that arbitrary shift choices will rarely be fitted by the relevant polynomial of existence. This explains the difference in methodological advantages discussed in Chapter 4.

Beyond this, many mysteries are yet to be explored. All investigations of these multi-rogue wave solutions have thus far been primarily efforts of discovery, deriving them mathematically. While this chapter presents the most complete picture to date of all the high-order possibilities, future directions will need to include studies aimed at understanding why they arise in these forms. Analysis of energetics has previously been proposed in Chapter 2 as one avenue towards comprehending the circular geometries involved, but the physical interpretation of shift 'orders' is an open problem. Perhaps they will always be considered as mathematical consequences of limit theory and thus unimportant in practice.

Certainly, if rogue wave formations are to be considered as structures arising at the intersection of more physically realistic breathers, the unintuitive intricacies of 'infinitesimal orders' can be neglected. For example, four NLSE solutions are depicted in Fig. 6.1, each constructed from four low-frequency ABs. The x-axis shifts range from those required for a triangular cascade in Fig. 6.1a to those required for a pentagram in Fig. 6.1d, with linear interpolation for the intermediate two structures. All shifts are finite here, yet the perfect geometries of multi-rogue waves are still

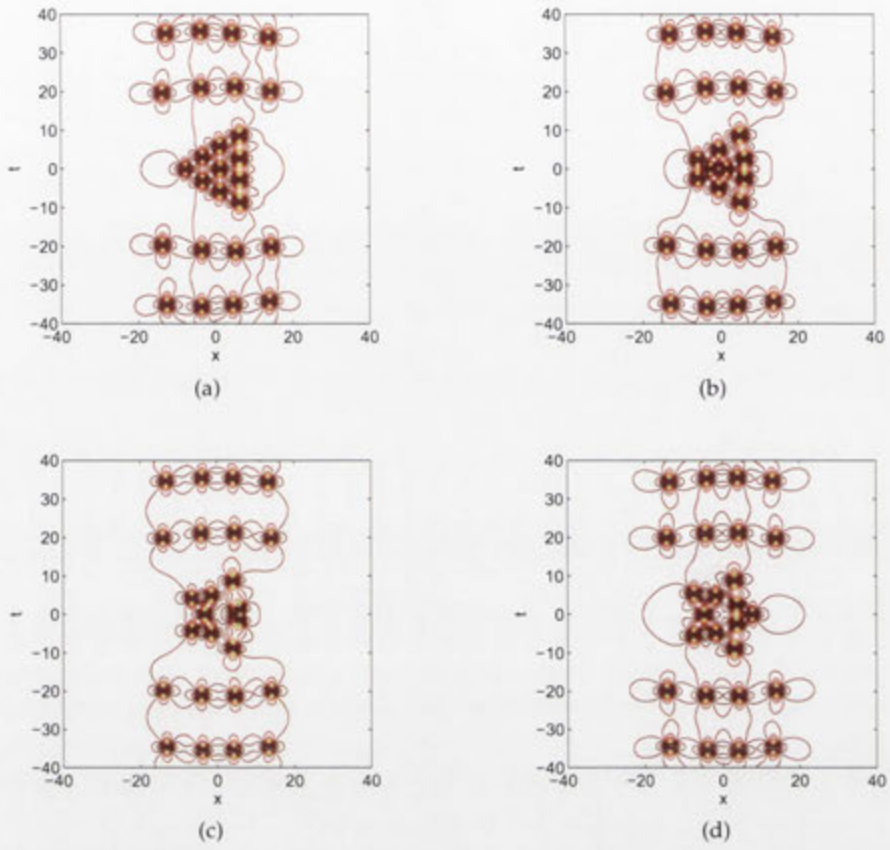

Figure 6.1: Contours of fourth-order breathers with frequencies $\kappa_j = \sqrt{j}/3$. (a) Cascade intersection. Shifts are $(x_1, x_2, x_3, x_4) \approx (0, 0.5556, 1.1111, 1.6667)$. (b) Shifts are $(x_1, x_2, x_3, x_4) \approx (0, 0.2716, 0.6420, 1.1111)$. (c) Shifts are $(x_1, x_2, x_3, x_4) \approx (0, -0.0123, 0.1728, 0.5556)$. (d) Pentagram intersection. Shifts are $(x_1, x_2, x_3, x_4) \approx (0, -0.2963, -0.2963, 0)$.

well approximated. This is despite the fact that, in the rogue wave limit, the cascade shifts would need to be infinitesimal (i.e. proportional to κ^2). Any deviation from the relevant existence condition, destroying the cascade but retaining κ^2 proportionality, would be equivalent to creating a circular cluster with infinite circumradius. Accordingly, it would definitely not be possible to create a rogue wave pentagram without jumping to a higher order of 'infinitesimality'. Yet, when κ is finite, none of these conceptual difficulties are particularly problematic. Indeed, as the first Peregrine breather demonstrated in optical fibre was technically an AB with very low modulation frequency [13], the shifts for higher-order structures can genuinely be thought of as physical spatiotemporal translations.

In any case, it is worth mentioning that Figs. 6.1b and 6.1c still represent legitimate rogue wave solutions at the intersection of the four breathers. They are not

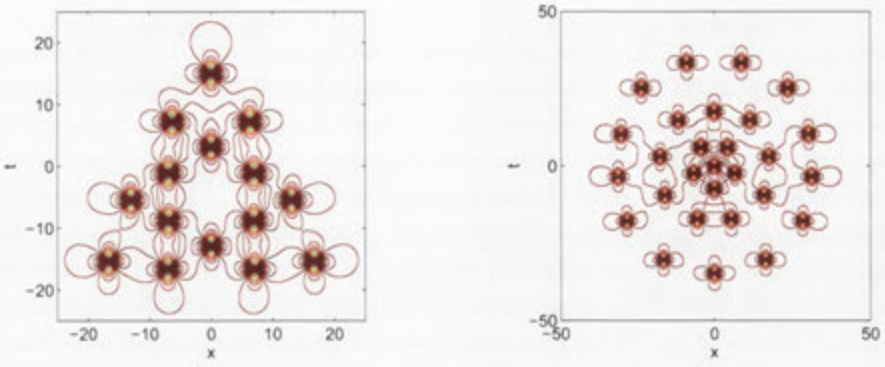

Figure 6.2: Contours of higher-order rogue wave 'hybrids'. Component frequencies are $\kappa_j = \kappa\sqrt{j}$. (a) Fifth-order triquetra. Shifts are $t_j = -5 + 20(j-1)\kappa^2 + 1250(j^4 - 14j^3 + 67j^2 - 126j + 72)\kappa^8$. (b) Seventh-order multi-ring structure. Shifts are $t_j = -0.3(10j)^2\kappa^4 + 0.6(10j)^4\kappa^8 - 12(10j)^6\kappa^{12}$.

fundamental structures, but are arrays formed from a mixture of triangular and pentagonal geometries. Accordingly, the research presented in this chapter is not just important for categorising numerous standard multi-rogue wavefunctions [71, 72]. It also completely specifies the 'palette' of geometries that can be used for hybridisation. With this understanding, it is simple to create a structure in the shape of a triquetra, as shown in Fig. 6.2a, by tuning existence conditions that specify $2\pi/3$ and $2\pi/9$ rotational symmetries. A global shift of -5 is only added for visual purposes.

Additionally, hybridisation also provides the methodology to prove the hypothesis of multi-ring structures in Chapter 2. Their existence was independently reported elsewhere [72], while the publication here simply described how to create them [6]. However, an explicit example of a seventh-order case is shown in Fig. 6.2b, with the κ^{12} proportionality in the shifts extracting the outermost ring of 13 'quanta', κ^8 relating to the second ring of 9 and κ^4 being associated with central ring of 5. The choice of signs on each shift coefficient are chosen to alternate the directions in which the rings point, while the degrees of rotational symmetry for each layer support why each κ exponent is chosen as is. Clearly, these patterns are regular and appear analogous to the atomic-based sequences described earlier [2], but speculations of a link are for future study.

Ultimately, what is perhaps most important is that this work proves that an expansive and possibly exhaustive set of multi-rogue wave solutions can be generated via the Darboux scheme. While analytic equations are exact and possible, they are also large and cumbersome. Instead, the numerical implementation deployed in this thesis is a routine procedure to construct these wavefunctions within a specified domain. It is thus not complicated to take a profile for a sufficiently negative value of x and propagate this initial condition within an experimental set-up. This is what

has been done previously in a wave tank [77], with appropriate hydrodynamic conventions and dimensionalisation. Thus it is only a matter of time before complicated rogue wave arrangements are engineered in practice.

Chapter 7

Rogue Waves and Solitons on a Cnoidal Background

Prologue

The publications thus far in this thesis have detailed the process by which rogue wave solutions of the NLSE have been constructed and classified. Remarkably, given the physical constraints inherent within the relevant nonlinear system, fundamental arrangements have been categorised into a hierarchy [6] according to parametric relations that evidently reflect rotational symmetries. Even so, these elegant geometries can be freely mixed to array individual rogue wave quanta into seemingly arbitrary patterns, with the Darboux scheme providing the guarantee that these are all true solutions of the NLSE. A vital question then arises; how universal is this rogue wave hierarchy?

This is not an easy problem to address and is currently a topic of ongoing research. Certainly, there are many nonlinear systems that do not even host the standard Peregrine soliton, such as the shallow water Korteweg-de Vries (KdV) equation [85], so limitations do exist. At the same time, extensions of the NLSE such as the Hirota equation [118, 119] do seem to maintain superficially modified versions of the same hierarchy. Given this, a concerted effort within the scientific community is currently underway to identify analogues of high-order spatiotemporally localised structures within various systems. This is further detailed in Chapter 8.

Even so, not all is yet understood about rogue wave solutions within the simple NLSE case itself. For instance, it is well known that plane waves perturbed with noise exhibit chaotic rogue wave behaviour, but variations on the shape of the background have rarely been investigated. This is partially because Darboux theory had traditionally been explored via analytical means. So, while zero amplitude and a plane wave were two trivial seeding solutions that generated exact expressions for solitons [87] and breathers [59], respectively, other backgrounds led to intractable mathematics. Accordingly, solitons and breathers were long considered as distinct classes of wavefunctions in the literature, despite the fact that their seeds were two end-points along a smoothly transformable spectrum of periodic solutions involving Jacobi elliptic functions [120]. Naturally, this was an oversight worth addressing, because these so-called 'cnoidal' waves further generalise representations of both shallow-depth hydrodynamic surface oscillations [45] and optical signals in waveguides [121]. Such

an exploration was also expected to reveal the vital 'missing link' between solitonic and rogue wave structures.

This chapter, as a published manuscript [7], uses the Darboux scheme to find new NLSE solutions generated on a cnoidal background. Because the seed is translationally invariant along the evolution axis, apart from a plane wave factor, it is possible to analytically determine half of the first-order component functions used in the construction process. Numerical propagation methods must still be involved, but only initially and along the transverse axis alone. Consequently, there is little computational overhead added and all the benefits of Darboux-theory nonlinear superposition remain, including the avoidance of error by solely relying on algebraic operations.

As previously mentioned, the cnoidal seed varies between a zero background and a plane wave [120], forming a one-soliton background in the middle of this range. The breather dynamics of interest to this thesis actually occur for seeding solutions between the soliton and the plane wave, where the background is differentiable across the entire spatiotemporal domain and wave energy is readily mobile. It is revealed that:

- The oscillations of these cnoidal functions do indeed support spatiotemporally localised waves, although the constituent components must possess imaginary eigenvalues of smaller magnitude than in the plane wave case.
- A locus of points can be drawn through cnoidal parameter space for which typical 'concentrated' rogue wave solutions exist. One end-point is the standard Peregrine breather, while the other is the well-known degenerate two-soliton solution.
- This locus continues further through parameter space, revealing an unexpected new class of 'diffuse' rogue wave solutions that have no analogue when the background is a plane wave. Their appearance is also highly unusual, in that the 'super-envelope' of their oscillating envelope resembles rotated breathers and rogue waves.

Ultimately though, this chapter concludes on the point that all fundamental arrangements from the rogue wave hierarchy [6] are reproducible on a cnoidal background, further extending the known generality of the classification scheme.

Eur. Phys. J. Special Topics **223**, 43–62 (2014)

DOI: 10.1140/epjst/e2014-02083-4

THE EUROPEAN PHYSICAL JOURNAL SPECIAL TOPICS

Review

Rogue waves and solitons on a cnoidal background

D.J. Kedziora[a], A. Ankiewicz, and N. Akhmediev

Optical Sciences Group, Research School of Physics and Engineering, The Australian National University, Canberra ACT 0200, Australia

Received 11 September 2013 / Received in final form 25 November 2013
Published online 23 January 2014

Abstract. Solutions of the nonlinear Schrödinger equation, appearing as rogue waves on a spatially-periodic background envelope, are obtained using the Darboux transformation scheme. Several particular examples are illustrated numerically. These include soliton and breather solutions on a periodic background as well as higher-order structures. The results enrich our knowledge of possible analytic solutions that describe the appearance of rogue waves in a variety of situations.

This work is prepared on the occasion of Prof. Helmut Brand's 60th birthday. He has made significant contributions to the science of solitons and his ideas have inspired our research into localised formations in various physical contexts.

1 Introduction

Solitons and rogue waves are generally considered to be two distinct phenomena in both oceanography and optics, as well as other fields involving nonlinear wave evolution. Certainly, the former encapsulates waves that keep their shape across all time, while the latter describes distinctly one-off occurrences, involving unpredictable high-amplitude bursts of energy. Even the motivations for their study differ, contrasting the development of lossless energy transport with the generation and avoidance of energetic focal points.

Naturally, this distinction extends to theoretical investigations, where the nonlinear Schrödinger equation (NLSE) is commonly used to model both phenomena. Traditional solitons propagate on a constant background, while so-called "breathers" arise from plane wave perturbations. The latter group includes the well-studied rogue wave prototype known as both the Peregrine soliton and breather [1]. However, in practice, both sets of solutions may be neither as unrelated nor adequately representative of reality as commonly thought. In fact, a zero amplitude background and a plane wave, upon which these solutions are built, are simply two limiting cases in a spectrum of waves involving Jacobi elliptic functions. From a statistical perspective,

[a] e-mail: david.kedziora@anu.edu.au

these "cnoidal" oscillations appear far more common in the ocean than any idealised background with constant amplitude. It is also not uncommon for an optical cnoidal wave to appear in a fibre as a regular train of solitonic pulses.

These questions then arise: how do varying cnoidal backgrounds perturb both solitons and breathers, and are there rogue wave analogues when the amplitude envelope of the rest of the wave field is no longer flat? Previous investigations have attempted NLSE generalisations involving doubly-periodic cnoidal waves [2–4], but we focus on spatial periodicity alone [5] due to the sufficient richness of its parameter space. We also make use of the Darboux transformation method [6,7], a recursive process that allows for the nonlinear superposition of NLSE solutions. Due to the complexity of Jacobi elliptic functions, numerical procedures substitute for analytical deficiencies and aid in graphically examining a number of new cnoidal soliton and breather waves.

Most importantly, by enforcing a zero limit on the modulation frequency of cnoidal breathers, we link the Peregrine soliton to the degenerate soliton via a range of cnoidal waves, all possessing a single spatiotemporally localised high-amplitude peak. The parametric curve behind this relation extends even further to a unique class of "diffuse" rogue waves with unintuitive appearance, where the extreme event is spread spatially over multiple crests. Finally, we confirm that higher-order "fissioned" rogue waves [8,9] still adhere to the same parametric relations when nonlinearly superimposed upon a cnoidal background.

2 Theory

2.1 The NLSE Lax Pair

The 1D NLSE is written in optical notation as

$$i\psi_x + \frac{1}{2}\psi_{tt} + |\psi|^2\psi = 0, \tag{1}$$

where x is the normalised distance along a waveguide and t is the retarded time in the frame moving with the pulse group velocity. In oceanographic convention, x is instead interpreted as the normalised time while t is the distance in the frame moving with the group velocity. Simple linear transformation allows conversion between forms, and, in both cases, complex function $\psi(x,t)$ typically describes the wave envelope. However, as a nonlinear equation, the NLSE can be difficult to solve using analytical techniques. Complications are thus circumvented by expressing the equation in Lax Pair form,

$$\begin{gathered}
\frac{\partial R}{\partial t} = U \cdot R, \quad \frac{\partial R}{\partial x} = V \cdot R, \\
R = \begin{bmatrix} r \\ s \end{bmatrix}, \quad U = \begin{bmatrix} i\lambda & i\psi^* \\ i\psi & -i\lambda \end{bmatrix}, \\
V = \begin{bmatrix} i\lambda^2 - \frac{i}{2}|\psi|^2 & i\lambda\psi^* + \frac{1}{2}\frac{\partial \psi^*}{\partial t} \\ i\lambda\psi - \frac{1}{2}\frac{\partial \psi}{\partial t} & -i\lambda^2 + \frac{i}{2}|\psi|^2 \end{bmatrix},
\end{gathered} \tag{2}$$

where $R_{tx} = R_{xt}$ and the associated zero-curvature equation, $U_x - V_t + U \cdot V - V \cdot U = 0$, return the NLSE in Eq. (1).

The Darboux scheme is but one of several methods that operate on Eq. (2) to produce high-order solutions of the NLSE, doing so in this case via the transformation of lower-order wavefunctions [6]. Specifically, the Lax Pair is solved for a trivial seeding solution $\psi = \psi_0$, and the resulting r and s functions become the "building blocks" for a hierarchy of solutions [7,8,10]. Via this mechanism, an order n wavefunction is produced from the recursive nonlinear superposition of n individual components, uniquely identified by $1 \leq j \leq n$. We henceforth emphasise the uniqueness of fundamental components by relabelling the Lax Pair solutions as r_{1j} and s_{1j}, with λ_j as corresponding eigenvalue.

Importantly, the well-known NLSE solitonic hierarchy [7] arises from seeding solution $\psi_0 = 0$, while a more recently discovered family of breather solutions [11,12] is built from the plane-wave background $\psi_0 = e^{ix}$. The latter set includes the Peregrine soliton, a well-studied prototype of a rogue wave [1]. These two hierarchies have generally been considered as distinct entities in the field of NLSE solutions. However, they are actually two opposite limiting cases in a wide spectrum of NLSE-adherent wavefunctions, known generally as cnoidal waves.

To examine the transition between the iconic hierarchies, we note that the NLSE has two basic solutions involving Jacobi elliptic functions [5],

$$\begin{aligned} \psi_{\mathrm{cn}}(x,t) &= g\,\mathrm{cn}(t-t_p,g)e^{i(x-x_p)(g^2-\frac{1}{2})}, \\ \psi_{\mathrm{dn}}(x,t) &= \mathrm{dn}(t-t_p,g)e^{i(x-x_p)(1-\frac{g^2}{2})}, \end{aligned} \tag{3}$$

where, if $u = \int_0^\phi \left(1 - g^2\sin^2(\theta)\right)^{-1/2} d\theta$, the Jacobi functions are defined here as $\mathrm{sn}(u,g) = \sin(\phi)$, $\mathrm{cn}(u,g) = \cos(\phi)$ and $\mathrm{dn}(u,g) = \sqrt{1-g^2\sin^2(\phi)}$. Due to notational differences in the literature, we stress that g here is the "elliptic modulus" and g^2 serves as the "elliptic parameter". From here on in we also set $x_p = t_p = 0$, noting that these variables are nothing more than phase-shifts to the underlying background of the solutions we seek.

Provided that u is real, the Jacobi elliptic functions are also real within the range $0 \leq g \leq 1$. From $g = 0$ to $g = 1$, $\mathrm{cn}(u,g)$ varies between $\cos(u)$ and $\mathrm{sech}(u)$. Similarly, from $g = 1$ to $g = 0$, $\mathrm{dn}(u,g)$ varies between $\mathrm{sech}(u)$ and 1. Therefore, $\psi_{\mathrm{cn}}(x,t)$ and $\psi_{\mathrm{dn}}(x,t)$ represent together a smooth transition from the zero-background seed of the solitonic hierarchy to the plane-wave seed of the rogue wave breather family. Notably, the "halfway point" $g = 1$ limit, where both basic solutions converge, generates an equation of soliton form.

It is important to mention that the use of the NLSE generally assumes a carrier wave that underlies the envelope described by ψ in Eq. (1). In this work, we assume the carrier has sufficiently high frequency so that its wavelength is smaller than that of the cnoidal background. This allows the oscillations of the Jacobi elliptic functions to be seen in a physical wave field.

2.2 Lax Pair solutions: $\psi_0 = \psi_{\mathrm{dn}}$

Now, for the $\psi_0 = \psi_{\mathrm{dn}}$ branch, the r and s functions that solve the Lax Pair in Eq. (2) are of the form

$$\begin{aligned} r_{1j}(x,t) &= a_{1j}(x,t)e^{\frac{ix}{4}(g^2-2)}, \\ s_{1j}(x,t) &= b_{1j}(x,t)e^{-\frac{ix}{4}(g^2-2)}. \end{aligned} \tag{4}$$

Noting this transformation, the Lax Pair reduces to

$$\begin{aligned}
a_t &= i\lambda a + ib\,\mathrm{dn}(t,g),\\
b_t &= -i\lambda b + ia\,\mathrm{dn}(t,g),\\
a_x &= \frac{1}{2}ia\left(2\lambda^2 + g^2\left(\mathrm{sn}^2(t,g) - \frac{1}{2}\right)\right) + b\left(i\lambda\,\mathrm{dn}(t,g) - \frac{g^2}{2}\mathrm{sn}(t,g)\mathrm{cn}(t,g)\right),\\
b_x &= -\frac{1}{2}ib\left(2\lambda^2 + g^2\left(\mathrm{sn}^2(t,g) - \frac{1}{2}\right)\right) + a\left(i\lambda\,\mathrm{dn}(t,g) + \frac{g^2}{2}\mathrm{sn}(t,g)\mathrm{cn}(t,g)\right). \qquad (5)
\end{aligned}$$

We exclude the j subscripts here for the sake of readability. These four first-order differential equations (DEs) then reduce to two of second order,

$$\begin{aligned}
f_{tt} &= -g^2\frac{\mathrm{sn}(t,g)\mathrm{cn}(t,g)}{\mathrm{dn}(t,g)}f_t - \left(\lambda^2 + \mathrm{dn}^2(t,g) - Fig^2\lambda\frac{\mathrm{sn}(t,g)\mathrm{cn}(t,g)}{\mathrm{dn}(t,g)}\right)f,\\
f_{xx} &= -\lambda^2\left(1 + \left(\lambda - \frac{g^2}{4\lambda}\right)^2\right)f, \qquad (6)
\end{aligned}$$

where $F = +1$ for $f = a$ and $F = -1$ for $f = b$. The latter equation can be solved exactly for all values of g, completely determining the shape of r and s functions along the x axis. However, the former is more complicated and only has a particularly simple answer when $g = 0$. Fortunately, provided that we have a profile of a and b, along with their t derivatives, for a fixed value of t, it is possible to numerically evolve them backwards and forwards through space via typical numerical procedures. An appropriate initial profile is also simple to attain for $t = 0$, as $\mathrm{sn}(0,g) = 0$ and $\mathrm{dn}(0,g) = 1$. For this fixed value, the first expression in Eq. (6) reduces to the Lax Pair equation related to a plane-wave seed [11], which is exactly solvable. The end result is that the $t = 0$ profiles and derivatives are defined by

$$\begin{aligned}
a_{1j}|_{t=0} &= Ae^{i(\chi_j + \kappa_j\lambda_j(x - x_{sj}))} - Be^{-i(\chi_j + \kappa_j\lambda_j(x - x_{sj}))},\\
b_{1j}|_{t=0} &= Ae^{i(-\chi_j + \kappa_j\lambda_j(x - x_{sj}))} + Be^{-i(-\chi_j + \kappa_j\lambda_j(x - x_{sj}))},\\
a_{1j,t}|_{t=0} &= i\left(\lambda_j a_{1j}|_{t=0} + b_{1j}|_{t=0}\right),\\
b_{1j,t}|_{t=0} &= -i\left(\lambda_j b_{1j}|_{t=0} - a_{1j}|_{t=0}\right), \qquad (7)
\end{aligned}$$

where $\kappa_j = \sqrt{1 + (\lambda_j - \frac{g^2}{4\lambda_j})^2}$ and $\chi_j = \arccos(\kappa_j)/2$. With foresight, we also choose the phase-shift constants to be $A = \exp(-i\pi/4)$ and $B = \exp(i\pi/4)$, so that the amplitude maximum of the standard solutions we seek is located at the origin of the (x,t) plane. Regardless, via standard numerical DE solvers operating upon Eq. (7), it is possible to determine the r and s functions compatible with $\psi_0 = \psi_{\mathrm{dn}}$ across the entire (x,t) plane.

We note that Eq. (7) includes an arbitrary temporal shift x_{sj} as the second parameter crucial to the description of individual components. A corresponding spatial shift can also be included, but provides additional numerical complication for a negligible gain in understanding. Therefore, in the context of this work, individual components that constitute a higher-order NLSE solution can be tuned solely by eigenvalue λ_j and x-axis origin shift x_{sj}.

2.3 Lax Pair solutions: $\psi_0 = \psi_{\mathrm{cn}}$

We now repeat the same derivation procedure for the $\psi_0 = \psi_{\mathrm{cn}}$ branch. In this case, the r and s functions are of the form

$$\begin{aligned} r_{1j}(x,t) &= a_{1j}(x,t)e^{-\frac{ix}{4}(2g^2-1)}, \\ s_{1j}(x,t) &= b_{1j}(x,t)e^{\frac{ix}{4}(2g^2-1)}, \end{aligned} \tag{8}$$

resulting in a Lax Pair reduction to

$$\begin{aligned} a_t &= i\lambda a + ibg\,\mathrm{cn}(t,g), \\ b_t &= -i\lambda b + iag\,\mathrm{cn}(t,g), \\ a_x &= \frac{1}{2}ia\left(2\lambda^2 + g^2\mathrm{sn}^2(t,g) - \frac{1}{2}\right) + bg\left(i\lambda\,\mathrm{cn}(t,g) - \frac{1}{2}\mathrm{sn}(t,g)\mathrm{dn}(t,g)\right), \\ b_x &= -\frac{1}{2}ib\left(2\lambda^2 + g^2\mathrm{sn}^2(t,g) - \frac{1}{2}\right) + ag\left(i\lambda\,\mathrm{cn}(t,g) + \frac{1}{2}\mathrm{sn}(t,g)\mathrm{dn}(t,g)\right), \end{aligned} \tag{9}$$

where we again exclude j subscripts. Similar to the ψ_{dn} branch, these four first-order DEs can be rewritten as

$$\begin{aligned} f_{tt} &= -\frac{\mathrm{sn}(t,g)\mathrm{dn}(t,g)}{\mathrm{cn}(t,g)}f_t - \left(\lambda^2 + g^2\mathrm{cn}^2(t,g) - Fi\lambda\frac{\mathrm{sn}(t,g)\mathrm{dn}(t,g)}{\mathrm{cn}(t,g)}\right)f, \\ f_{xx} &= -\lambda^2 g^2\left(1 + \frac{1}{g^2}\left(\lambda - \frac{1}{4\lambda}\right)^2\right)f, \end{aligned} \tag{10}$$

for $f = a$ and b. As before, the latter equation is easily solvable, giving an exact expression for r and s along the x axis. In contrast, the former requires numerical techniques to solve, but only a profile and derivative of a and b for a fixed value of t are needed. This is simple to derive, noting that $\mathrm{sn}(0,g) = 0$ and $\mathrm{cn}(0,g) = 1$ reduces the first expression in Eq. (10) to one with a trivial solution. Explicitly, the corresponding $t = 0$ profile and derivatives for the ψ_{cn} branch are

$$\begin{aligned} a_{1j}|_{t=0} &= Ae^{i(\chi_j + \kappa_j\lambda_j(x - x_{sj}))} - Be^{-i(\chi_j + \kappa_j\lambda_j(x - x_{sj}))}, \\ b_{1j}|_{t=0} &= Ae^{i(-\chi_j + \kappa_j\lambda_j(x - x_{sj}))} + Be^{-i(-\chi_j + \kappa_j\lambda_j(x - x_{sj}))}, \\ a_{1j,t}|_{t=0} &= i\left(\lambda_j a_{1j}|_{t=0} + gb_{1j}|_{t=0}\right), \\ b_{1j,t}|_{t=0} &= -i\left(\lambda_j b_{1j}|_{t=0} - ga_{1j}|_{t=0}\right), \end{aligned} \tag{11}$$

where $\kappa_j = g\sqrt{1 + \frac{1}{g^2}\left(\lambda_j - \frac{1}{4\lambda_j}\right)^2}$ and $\chi_j = \arccos(\frac{\kappa_j}{g})/2$. As with the other branch, we choose $A = \exp(-i\pi/4)$ and $B = \exp(i\pi/4)$.

2.4 The Darboux transformation

With r and s now able to be completely determined for either branch of seeding cnoidal solution, the Darboux scheme allows wavefunctions of any order to be generated. For a "first-order" solution, only one set of functions is required, which combine with the seed solution via the transformative equation

$$\psi_1 = \psi_0 + \frac{2(\lambda_1^* - \lambda_1)s_{11}r_{11}^*}{|r_{11}|^2 + |s_{11}|^2}. \tag{12}$$

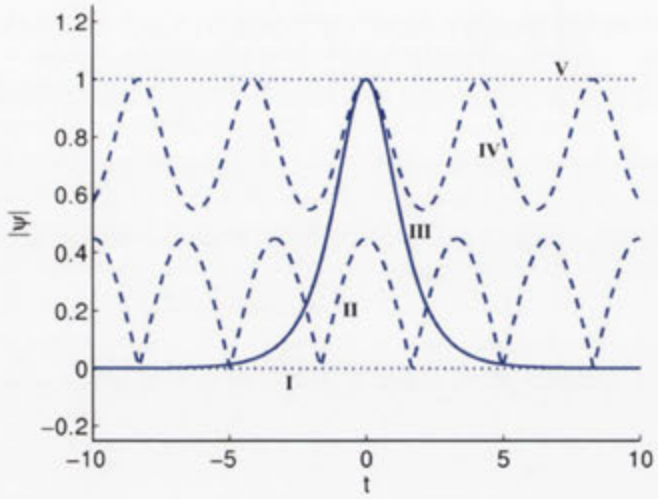

Fig. 1. Amplitude envelope cross-sections of zero-order NLSE solutions, according to Eq. (3). (I) Zero background ψ_{cn} with $g = 0$. (II) Cnoidal wave ψ_{cn} with $g = \sqrt{0.2}$. (III) Solitonic ψ_{cn} or ψ_{dn} with $g = 1$. (IV) Cnoidal wave ψ_{dn} with $g = \sqrt{0.7}$. (V) Plane wave ψ_{dn} with $g = 0$.

However, higher-order solutions require higher-order component functions, all recursively generated from lower orders by the relation

$$\begin{aligned} r_{np} = &\Big[\left(\lambda_{n-1}^{*} - \lambda_{n-1}\right) s_{n-1,1}^{*} r_{n-1,1} s_{n-1,p+1} + \left(\lambda_{p+n-1} - \lambda_{n-1}\right) |r_{n-1,1}|^2 r_{n-1,p+1} \\ &+ \left(\lambda_{p+n-1} - \lambda_{n-1}^{*}\right) |s_{n-1,1}|^2 r_{n-1,p+1} \Big] / \left(|r_{n-1,1}|^2 + |s_{n-1,1}|^2\right), \\ s_{np} = &\Big[\left(\lambda_{n-1}^{*} - \lambda_{n-1}\right) s_{n-1,1} r_{n-1,1}^{*} r_{n-1,p+1} + \left(\lambda_{p+n-1} - \lambda_{n-1}\right) |s_{n-1,1}|^2 s_{n-1,p+1} \\ &+ \left(\lambda_{p+n-1} - \lambda_{n-1}^{*}\right) |r_{n-1,1}|^2 s_{n-1,p+1} \Big] / \left(|r_{n-1,1}|^2 + |s_{n-1,1}|^2\right). \end{aligned} \tag{13}$$

With these, increasing the order of an NLSE solution is simply encapsulated by

$$\psi_n = \psi_{n-1} + \frac{2(\lambda_n^{*} - \lambda_n) s_{n1} r_{n1}^{*}}{|r_{n1}|^2 + |s_{n1}|^2}, \tag{14}$$

where the eigenvalues and x-axis shifts of all constituent components have been incorporated into the wavefunction by Eq. (13). The end result is a complicated order n solution of the NLSE, provided by a fusion of analytical and numerical techniques.

3 Results

3.1 Cnoidal seed functions

The zero-order solutions to the NLSE, presented in Eq. (3), serve as the background to any increasingly complicated higher-order solutions generated via the Darboux transformation process. Their amplitude profiles are independent of x, which means that the unchanging shape of their t-axis cross-sections can be displayed simply in Fig. 1. For $g = 0$, the ψ_{cn} seed is compressed to zero amplitude, denoted by cross-section I. Increased values of g allow the periodicity of the cnoidal function to appear,

as evident with cross-section II. Indeed, when the elliptic modulus is 0.5, the maximum amplitude of the function reaches 0.5. Also noteworthy is the fact that the modulus operation forces zero-amplitude points along the function to be non-differentiable, which can prove problematic for numerical solvers in the ψ_{cn} regime. Nonetheless, the spatial oscillation is clearly evident and its frequency decreases for $g \to 1$. In the actual limit, only one peak remains with the appearance of a sech profile, and this basic soliton is shown by cross-section III.

According to the seed definitions and the description of the Darboux scheme in Sect. 2, this ψ_0 solitonic seed is also a particular case of ψ_1 for a zero-background seed [7], specifically where $\lambda_1 = 0.5i$ and $x_{s1} = 0$. Hence there is a very special redundancy of solution hierarchies, in that ψ_n built upon $\psi_{\mathrm{cn}}|_{g=0}$ is equivalent to ψ_{n-1} based on $\psi_{\mathrm{cn}}|_{g=1}$, provided that one component from the constituents of the former has parameters fixed at $\lambda_j = 0.5i$ and $x_{sj} = 0$, for any particular value of j. In any case, this soliton is also a $g = 1$ limit of the ψ_{dn} branch. Within this complementary regime, for decreased values of the elliptic modulus, the frequency of spatial oscillation once again increases and the minimum amplitude of the wavefunction rises above zero. Cross-section IV in Fig. 1 exemplifies this type of cnoidal wave, and a value of $g = \sqrt{0.75}$ marks the point at which the minimum amplitude is 0.5. Finally, for $g = 0$, the spatial modulation is compressed so that ψ_{dn} becomes a plane wave, as shown by cross-section V. Therefore, it is clear that varying g across both branches allows a smooth transition between cnoidal solutions, from zero-background to plane wave and through a particular case of basic soliton.

3.2 Cnoidal solitons

We now examine first-order solutions transformed from the seeds. In doing so, our parameter space involves λ_1 and g for both cnoidal branches. Of course, there was no restriction made on the eigenvalue in Eq. (2), which means that the Darboux transformation method works for complex λ_j. However, the real part of the eigenvalue only affects the angle of alignment between NLSE solutions and spatiotemporal axes. We thus enforce that λ_j be purely imaginary with $\mathrm{Im}(\lambda_j) \geq 0$. This allows parameter space to be two-dimensional, without discarding any important results. The regions we investigate are depicted in Fig. 2, along with parametric coordinates for every first-order solution displayed in this work.

Of this domain, the zero-background $g = 0$ edge of the ψ_{cn} branch is most well-known, with ψ_1 from the Darboux scheme corresponding to nothing more than sech-type solitons. Because they are time-independent and shape-preserving, it is sufficient to display sample cross-sections in Fig. 3a. Notably, it is clear that the imaginary part of the eigenvalue tunes the height of the soliton, with a peak amplitude of $\mathrm{Im}(2\lambda_1)$. Correspondingly, a decreased value of λ_1 stretches out the width of the soliton instead.

However, as the elliptic modulus increases and the background assumes the appearance of wavefunction II in Fig. 1, the nonlinearly superimposed soliton interacts with the nearest spatial oscillations. As a result, the shape of the soliton becomes temporally modulated, as shown by structure PS in Fig. 3b. In fact, within the range of $0 < g \leq 1$, the shape of the central peak can be heavily perturbed by its nearest 'neighbours'. Nonetheless, for $\mathrm{Im}(\lambda_1) > 0.5$, the soliton is generally too spatially compact to interact significantly with distant oscillations, even when the cnoidal peaks approach their maximal amplitude of 1. Moreover, the peak amplitude of the cnoidal background scales according to g, which means that, within the range of $0 \leq g \leq 1$ for the ψ_{cn} branch, a soliton with eigenvalue greater than $0.5i$ will always be taller than the background around it.

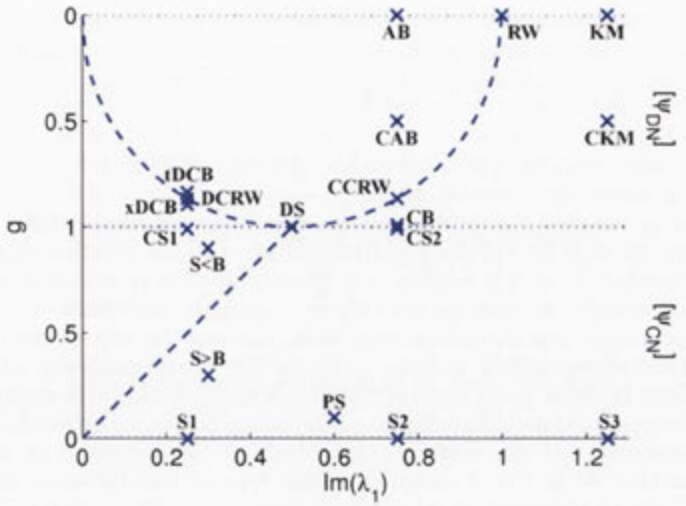

Fig. 2. Parameter space and sample coordinates for first-order NLSE solutions, across eigenvalue λ_1 and elliptic modulus g, with both branches of cnoidal seeding solution represented. Dashed line in ψ_{cn} region marks where soliton and background have same peak amplitudes. Dashed line in ψ_{dn} region denotes "rogue wave" curve. Solitons S1, S2 and S3, as well as perturbed soliton PS, are shown in Fig. 3. Soliton dominating background (S>B) and vice versa (S<B) are shown in Fig. 4. Cnoidal solitons CS1 and CS2 near the two-soliton parameter line are shown in Fig. 5. An Akhmediev Breather (AB), KM soliton (KM) and their respective cnoidal perturbations (CAB and CKM) are shown in Fig. 6. A normal rogue wave (RW), concentrated cnoidal rogue wave (CCRW) and degenerate soliton (DS), as well as a cnoidal breather near the two-soliton line (CB), are shown in Fig. 7. A diffuse cnoidal rogue wave (DCRW) is shown in Fig. 8, along with both a t- and x-periodic diffuse cnoidal breather (tDCB and xDCB, respectively).

For a more diffuse soliton with small λ_1, it may have sufficiently strong interactions over an extended domain so as to modulate distant cnoidal oscillations over time. An example of this is shown in Fig. 4a, where energy in the main peak of the soliton periodically flows into its two nearest neighbours, but adjacent cnoidal crests are also affected. Nonetheless, a sech envelope can easily be seen over the entire wavefunction. We refer to this situation as a soliton dominating the background (S>B). In contrast, a large value of elliptic modulus can produce a cnoidal wave that dwarfs the superimposed soliton (S<B), as in Fig. 4b. Many more spatial oscillations are now temporally affected by interactions between the soliton and background. This effect is primarily a consequence of the nonlinear term in the NLSE, which implies that the high-amplitude cnoidal oscillations serve as focal points for energy transfer. The end result is that the shape of the soliton appears to be washed out by the background and, in some cases, the modulations of the cnoidal wave appear infinite in two dimensions. However, within the ψ_{cn} branch, this is never truly the case. Just as the soliton tail fades to negligible values, so too does the far field return to regularity.

Because this concept of dominance is largely subjective, we choose $g = \mathrm{Im}(2\lambda_1)$ as a rough demarcation in parameter space, shown by the dashed line within the ψ_{cn} branch of Fig. 2. Solutions along this line are particularly noteworthy as the equal peak amplitudes of both background and soliton interfere so as to uniquely produce zero-amplitude troughs along the $x = 0$ evolution path. In any case, $g \to 1$ results in structures approaching typical two-soliton solutions, whether for small eigenvalues and a dominant background, shown with CS1 in Fig. 5a, or large eigenvalues

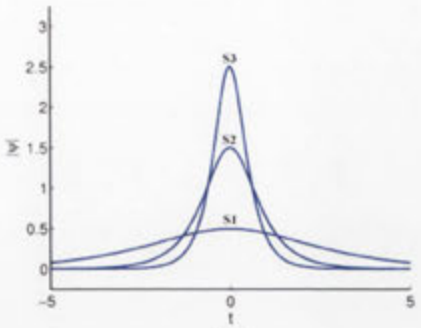

(a)

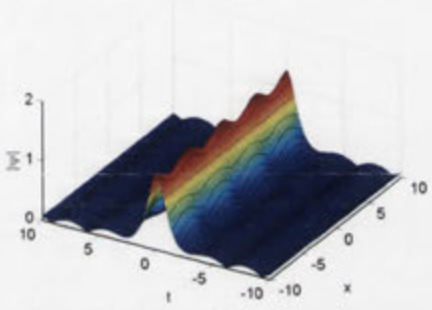

(b)

Fig. 3. First-order solitonic solutions, with $\psi_0 = \psi_{\mathrm{cn}}$. (a) Cross-sections of wavefunctions built on zero background, where $g = 0$. Soliton S1 arises when $\lambda_1 = 0.25i$, S2 when $\lambda_1 = 0.75i$, and S3 when $\lambda_1 = 1.25i$. (b) A perturbed soliton (PS) with $\lambda_1 = 0.6i$ and $g = 0.1$.

and a dominant soliton, shown with CS2 in Fig. 5b. Both cases indicate that the period of the cnoidal background increases with elliptic modulus, eventually leaving only one sech-type spatial oscillation to interact with the superimposed soliton. In the absolute limit, only the central structure of both images remains, a well-known two-soliton wavefunction periodic in both crests and "craters".

3.3 Cnoidal breathers and first-order rogue waves

While the ψ_{cn} branch of solutions extends soliton physics, particularly from the perspective of applied perturbations, it is the ψ_{dn} branch that is of primary interest to the new field of rogue wave physics. Indeed, even though periodic oscillations in Sect. 3.2 hint at the interplay between the dispersion and nonlinear terms of the NLSE, the process of modulation instability in its purest form has largely been associated with the discovery of NLSE breathers [13]. This is partly due to the presence of an underlying "basin" of energy for ψ_{dn} wavefunctions, with no zero-amplitude points evident for cross-sections IV and V in Fig. 1. This allows for easier energy transport within the NLSE wave and can result in the illusion of crests arising unexpectedly from "nowhere".

In particular, applying the Darboux transformation to a plane-wave background with an imaginary eigenvalue in the range $0 < \mathrm{Im}(\lambda_1) < 1$ produces the so-called Akhmediev Breather (AB), displayed in Fig. 6a. This event is localised in time and periodic in space, arising from an infinitesimal periodic perturbation of a plane wave at

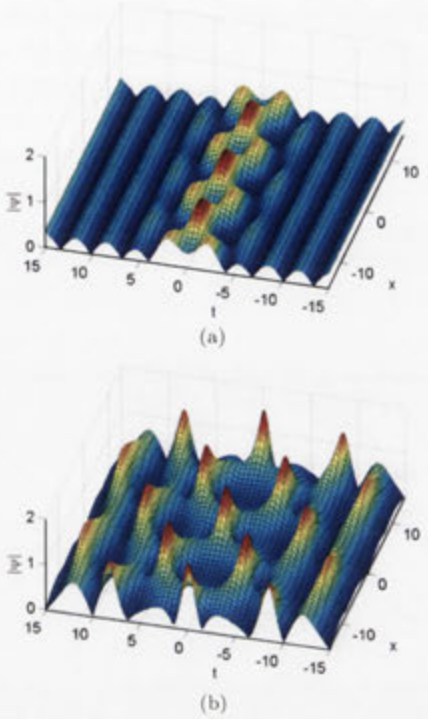

Fig. 4. First-order cnoidal solitonic solutions, with $\psi_0 = \psi_{\mathrm{cn}}$. (a) Soliton with $\lambda_1 = 0.3i$ dominates $g = 0.3$ background (S>B). (b) Soliton with $\lambda_1 = 0.3i$ dominated by $g = 0.9$ background (S<B).

$x = -\infty$. The Kuznetsov-Ma (KM) soliton is a similar structure for large $\mathrm{Im}(\lambda_1) > 1$, displayed in Fig. 6b, although it is spatially localised and temporally periodic. Most notably, ABs and KM solitons are smooth transformations of each other. As their eigenvalue λ_1 approaches i from either direction, their modulation frequency κ_1 approaches zero, resulting in a "stretching out" of wavetrains along either axis until only one central peak remains. This quasi-rational Peregrine soliton, alternatively called a Peregrine breather, is considered to be a prototypical rogue wave (RW) on account of fading into a constant background in all directions (shown later in Fig. 7b).

Increasing the elliptic modulus beyond $g = 0$ for a ψ_{dn} background perturbs the overlaid solution slightly, depending on where individual peaks are located. Most importantly, an AB appears to stretch out, as is shown with 7 peaks in Fig. 6a reducing to 5 in Fig. 6c within the plotted domain. In contrast, for a KM soliton, the 9 crests visible in Fig. 6b become 11 in Fig. 6d. These two new structures are denoted by CAB and CKM, respectively, within Fig. 2. Following the same logic, the Peregrine soliton similarly pulls in peaks from infinity along the x axis and, consequently, morphs into a cnoidal KM soliton as g increases.

From this, it is clear that the effect of variations in g appears very similar to that of variations in λ_1, at least in regard to the superstructure of the wavefunction. Certainly, for $\mathrm{Im}(\lambda_1) > 0.5$ and increasing g, the period of an AB eventually becomes infinite, meaning that further increases in the elliptic modulus must affect the frequency along the x axis. The result of this process is shown in Fig. 7a, where the background has sufficiently modified an AB so that it now appears as a KM soliton. Because of this ambiguity, we refer to it simply as a cnoidal breather (CB) in Fig. 2.

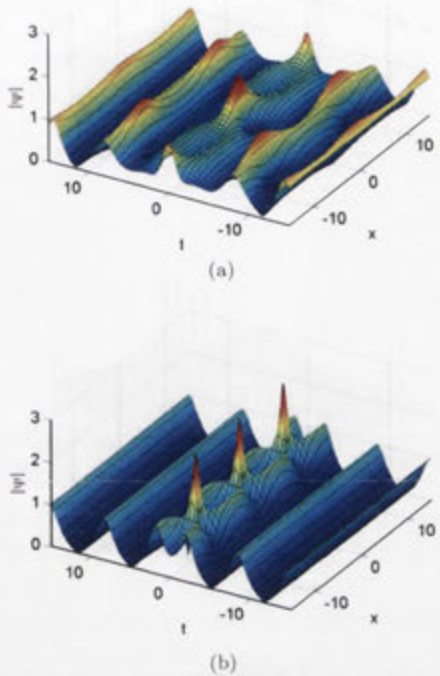

Fig. 5. First-order solutions near the two-soliton regime, with $\psi_0 = \psi_{\mathrm{cn}}$. (a) Cnoidal soliton (CS1) with $\lambda_1 = 0.25i$ and $g = 0.99$. (b) Cnoidal soliton (CS2) with $\lambda_1 = 0.75i$ and $g = 0.99$.

Of course, the extreme value of g in this particular case implies that the cnoidal background approaches its solitonic limit, which is why the spatial oscillations have become relatively distant from each other. Therefore, Fig. 5b and Fig. 7a both depict an approach towards the same two-soliton solution from their respective ψ_{cn} and ψ_{dn} branches of parameter space. Accordingly, the coordinates of the two solutions are almost identical in Fig. 2.

Now, while Fig. 7b represents an ideal rogue wave with quiescent background (RW), we can arguably stretch the definition of a first-order rogue wave so that it is considered to be a spatiotemporally localised high-amplitude burst on an otherwise predictable background. Hence, it is sufficient for the modulation frequency of the superstructure to approach zero. From the definition of κ_j in Eq. (7), this is achieved along the curve in parameter space denoted by $g^2 = 4\lambda_j(\lambda_j - i)$. This is depicted in Fig. 2 by the dashed line within the ψ_{dn} region. The Peregrine soliton exists at one endpoint of this "cnoidal rogue wave" (CRW) curve, with $g = 0$ and $\lambda_1 = i$. However, there are many more structures in this range, exemplified by the "CCRW" wavefunction in Fig. 7c, where one peak alone arises from the periodic oscillations of the background. In these cases, the central "X shape" of the wavefunction appears familiar. Indeed, at the $(g, \lambda_1) = (1, 0.5i)$ vertex of the parametric curve, it is all that is left in the domain, forming the well-known degenerate soliton (DS) in Fig. 7d. Again we note that this is a first-order solution formed from the nonlinear superposition of a $\lambda_1 = 0.5i$ soliton upon a background that is effectively the same soliton. The Darboux process does not support equal eigenvalues [11,12], so, as with

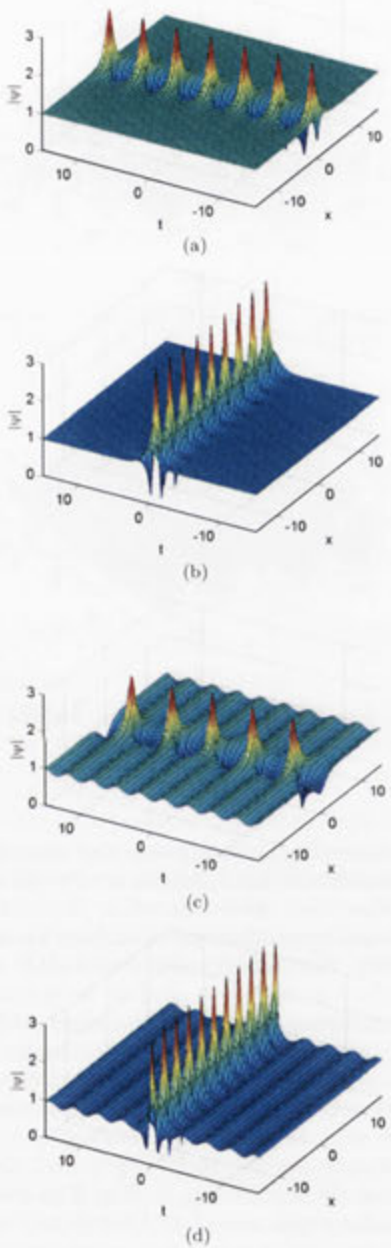

Fig. 6. First-order breathers and their cnoidal perturbations, with $\psi_0 = \psi_{\mathrm{dn}}$. (a) Regular AB with $\lambda_1 = 0.75i$ and $g = 0$. (b) Regular KM soliton with $\lambda_1 = 1.25i$ and $g = 0$. (c) Cnoidal AB (CAB) with $\lambda_1 = 0.75i$ and $g = 0.5$. (d) Cnoidal KM soliton (CKM) with $\lambda_1 = 1.25i$ and $g = 0.5$.

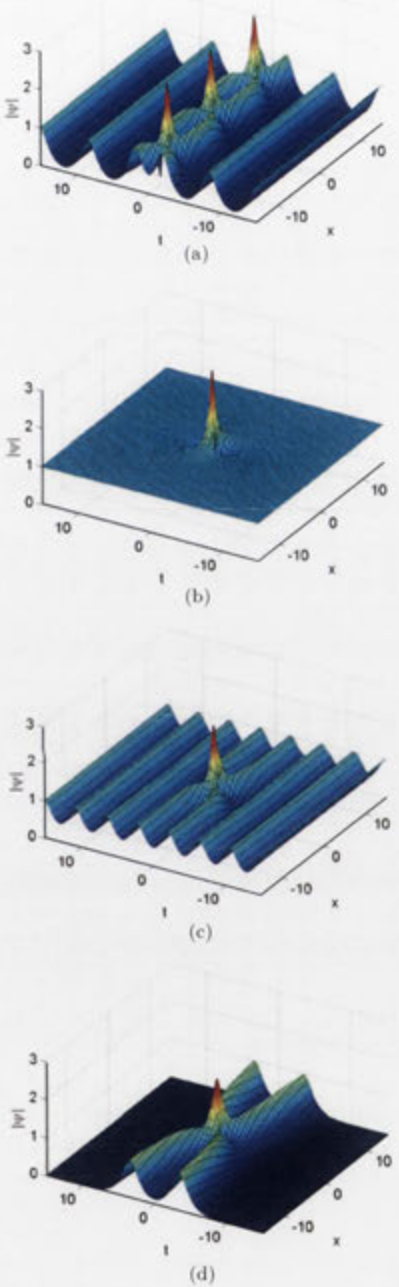

Fig. 7. First-order cnoidal breather solutions, with $\psi_0 = \psi_{\mathrm{dn}}$. (a) Cnoidal breather (CB) with $\lambda_1 = 0.75i$ and $g = 0.99$. (b) Regular rogue wave (RW) with $\lambda_1 \approx i$ and $g = 0$. (c) Typical "concentrated" cnoidal rogue wave (CCRW) with $\lambda_1 \approx 0.75i$ and $g = \sqrt{0.75}$. (d) Degenerate soliton (DS) with $\lambda_1 \approx 0.5i$ and $g = 1$. This is also technically a cnoidal rogue wave.

all CRWs, this structure can only be attained via the application of a limit, $\kappa_j \to 0$, not an actual equality.

As is evident from Fig. 7, all CRWs with $\mathrm{Im}(\lambda_1) \geq 0.5$ are simple to visually relate with the Peregrine soliton endpoint. However, the parametric CRW curve also extends in the other direction to $(g, \lambda_1) = (0, 0)$, a plane wave with a superstructure of zero differential amplitude. This means that CRWs with $\mathrm{Im}(\lambda_1) < 0.5$ are less intuitive to understand, possessing no limiting-case analogue. It is thus important to note that, in this regime, the modulation frequency κ_1 can be comparable to that of the cnoidal background for $g = 0$, implying a much sharper and more extreme transition to zero-frequency in the "rogue wave limit". In practice, this means that a number of adjacent crests for the AB are "left behind" as all others recede to infinity, effectively being maintained by a resonance effect with the cnoidal background. The resulting wavefunction is shown in Fig. 8a, which we refer to here as a diffuse cnoidal rogue wave (DCRW). We contrast this with the "concentrated" cnoidal rogue waves (CCRWs) displayed by Fig. 7 in much the same way as Fig. 4 differs from Fig. 5b; the nonlinear interactions of the superstructure appear to extend over many crests of the cnoidal background.

Because of this diffuse nature of DCRWs, their envelopes can extend over great spatiotemporal distances. But, when a more overarching view of the domain is taken, it is clear that the DCRWs behave similarly to CCRWs. Perturbing parameters into the region above the $g^2 = 4\lambda_j(\lambda_j - i)$ curve induces t-axis periodicity, as shown with tDCB in Fig. 8b, while entering the region below the curve produces x-axis periodicity, as shown with xDCB in Fig. 8c. The parametric perturbations are all displayed in Fig. 2. There are, however, crucial differences. Both Fig. 6 and Fig. 7 indicate that typical breather peaks are accompanied by adjacent troughs along the t axis, where energy has been depleted to fuel the high-amplitude bursts. In contrast, for the solutions near the DCRW curve in Fig. 8, examination of the fine structure shows that these features still remain, but the superstructure envelopes distinctly show other amplitude dips we call "cnoid voids" aligning with the diffuse peaks along the x axis. This means that Fig. 8b has the appearance of a rotated KM soliton, Fig. 8c is reminiscent of an AB, and even the second-order DCRW shown in Fig. 8d seems like a rotated version of a regular second-order rogue wave [8]. In a way, this axial inversion for the superstructure envelope preserves our understanding of eigenvalue effects. Decreased λ_1 values promote the appearance of ABs and increased values give preference to KM solitons. However, far more analysis is required to better understand this inverted appearance.

3.4 Higher-order cnoidal rogue waves

Although we avoid delving into too much depth here, the Darboux scheme set out in Sect. 2 is sufficient to generate the entire hierarchy of known rogue wave solutions [14] on a cnoidal background. The second-order DCRW in Fig. 8d is one example of this, but it is a simple "fused" case, where both constituent components are centred at the origin with no axial shifts. Alternatively, components can be independently shifted with respect to each other such that "fissioned" structures arise in the domain [8,9,15]. Notably, the cnoidal background does not change the intricacies involved in generating higher-order rogue waves, but shifts must now be appropriately dependent on the modified modulation frequency term, introduced by Eq. (7).

The key point is that, in the CCRW regime, cnoidal solutions allow for the depiction of a smooth transition between plane-wave and solitonic NLSE solutions, lending insight into rogue wave analogues. For example, the typical rogue wave triplet [15] presented in Fig. 9a does not change drastically as the elliptic modulus of the background varies. Certainly, the circular array of peaks becomes oval as the triplet is

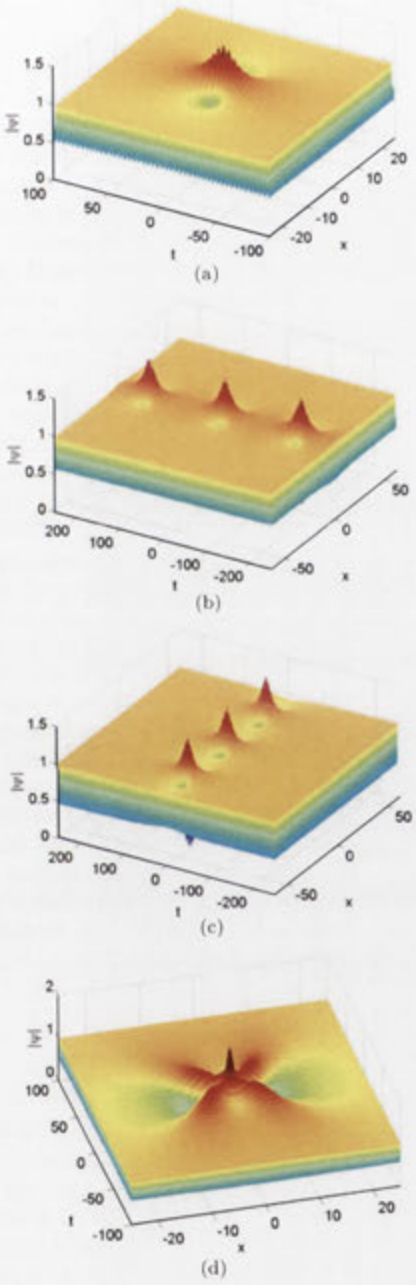

Fig. 8. Solutions in and near the diffuse cnoidal rogue wave regime, with $\psi_0 = \psi_{\mathrm{dn}}$. (a) First-order cnoidal rogue wave (DCRW) with $\lambda_1 \approx 0.25i$ and $g = \sqrt{0.75}$. (b) First-order cnoidal breather (tDCB) with $\lambda_1 = 0.25i$ and $g = \sqrt{0.7}$. (c) First-order cnoidal breather (xDCB) with $\lambda_1 = 0.25i$ and $g = \sqrt{0.8}$. (d) "Fused" second-order cnoidal rogue wave with $\lambda_1 \approx \lambda_2 \approx 0.25i$ and $g = \sqrt{0.75}$.

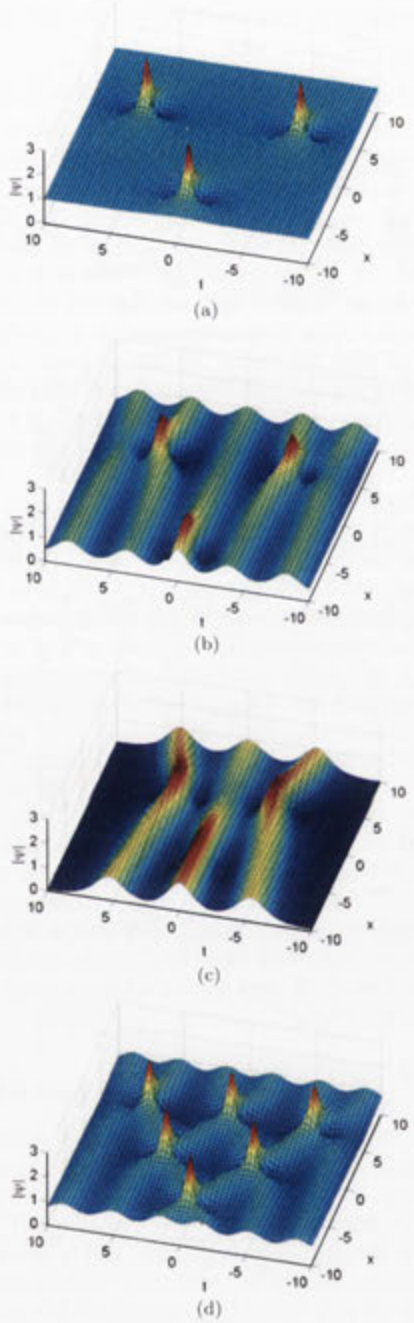

Fig. 9. Higher-order rogue wave solutions, with $\psi_0 = \psi_{\mathrm{dn}}$. Component frequencies are $\kappa_j = \kappa\sqrt{j}$, with $\kappa \approx 0$. (a) Second-order normal rogue wave triplet, for $g = 0$ and $x_j = 100(j-2)\kappa^2$. (b) Second-order cnoidal rogue wave triplet, for $g = \sqrt{0.75}$ and $x_j = 100(j-2)\kappa^2$. (c) Second-order solitonic rogue wave triplet, for $g = \sqrt{0.99}$ and $x_j = 100(j-2)\kappa^2$. (d) Third-order cnoidal rogue wave cascade, for $g = \sqrt{0.5}$ and $x_j = 25(j-1)\kappa^2$.

spatially compressed and temporally elongated, shown in Fig. 9b, but the trio of high-amplitude peaks remains visible, all the way to the solitonic extreme shown in Fig. 9c. Because a second-order solution consists of three crests in fissioned rogue wave form and three solitons in the $g = 1$ limit, the transformation in this case appears particularly clear. The energy in the system is pulled into the central soliton first, then is returned in unsustainable quantity to the two adjacent peaks, before the system returns to a stable state. This event happens only once within the entire spatiotemporal domain, and the only difference between Fig. 9a and 9c is where and how the background energy is stored.

Considering that a well-separated fissioned rogue wave of order n consists of $n(n+1)/2$ Peregrine breathers [8] and an order n solution in the $g = 1$ limit contains $n + 1$ solitons, the bijection involving energy focal points is often far less visually intuitive. Nonetheless, we have provided the framework to investigate the relationships for all higher-order rogue waves. Quasi-circular clusters of order n continue to be formed on a cnoidal background via the shifting of any component by an amount proportional to $\kappa^{2(n-1)}$, while the production of rogue wave cascades still requires the same constraint involving shifts and frequency ratios as previously established [9], an example of which is shown by Fig. 9d. The only numerical issue to note is that, upon selecting the appropriate component frequencies close to zero, the eigenvalues are derived by the expression $\lambda_j = i(\sqrt{1-\kappa_j^2} \pm \sqrt{1-\kappa_j^2-g^2})/2$. Building a solution with the $\pm$ sign regarded as a "plus" generates a CCRW, as in Fig. 9, while a "minus" produces a DCRW, as in Fig. 8d. It is thus interesting to consider the shape of high-order rogue waves formed from a mixture of both "diffuse" and "concentrated" eigenvalues, but we leave that for future investigation.

In any case, through numerical examination, the peak amplitude of all "fused" CRWs is now easy to relate to eigenvalue λ and order n. Specifically, it is $\mathrm{Im}(2\lambda n)+1$. Hence the regular rogue wave in Fig. 7b has amplitude 3, the cnoidal version in Fig. 7c has amplitude 2.5, and the degenerate soliton in Fig. 7d has amplitude 2. This is also why the first-order diffuse rogue wave in Fig. 8a has a smaller peak amplitude of 1.5 and the second-order version in Fig. 8d has an amplitude of 2. All this of course assumes that the cnoidal background has amplitude 1 under the central peak, as a spatial phase shift may instead superimpose the superstructure on a minimum of the cnoidal wave. This rule is also not much more complicated for fissioned solutions, but the amplitude of the highest crest does depend on how constituent components are arranged.

4 Conclusion

In summary, our main results are as follows:

1. We have outlined a Darboux transformation scheme for the NLSE, using spatially periodic cnoidal functions as the background for nonlinearly superimposed solutions. By varying the elliptic modulus from 0 to 1 through the ψ_{cn} branch and then back from 1 to 0 through the ψ_{dn} branch, as defined by Eq. (3), this technique allows the smooth transformation of a wavefunction background from zero amplitude to a plane wave via a lone soliton.
2. We have shown how a ψ_{cn} background affects a superimposed soliton. For solutions with large eigenvalue, the soliton is modulated via nonlinear interactions with only the nearest crests of the cnoidal wave, enforcing that its shape remains distinct and clear. In contrast, for diffuse solitons, interactions extend over a greater domain and, in the case that the elliptic modulus and corresponding peak amplitude of the background is large enough, the cnoidal wave

may visually wash out the superstructure. In any case, as the elliptic modulus approaches 1, the cnoidal background becomes a soliton and the first-order solution becomes a typical two-soliton wavefunction.

3. We have shown how a ψ_{dn} background affects a superimposed breather. For first-order solutions with sufficiently large eigenvalue ($\mathrm{Im}(\lambda) > 0.5$), increasing the elliptic modulus decreases the frequency of modulation along the spatial axis until there is only one spatiotemporally localised peak. Further increasing the elliptic modulus beyond this point increases the frequency of modulation along the temporal axis, until the first-order solution eventually becomes a two-soliton structure. The locus of these intermediate points forms a curve in parameter space, denoting a large range of rogue waves arising from a cnoidal background. This provides the missing "cnoidal link" between a Peregrine breather and a degenerate soliton.
4. We have shown that solutions with low eigenvalue ($\mathrm{Im}(\lambda) < 0.5$) are affected in a similar way by the increase of elliptic modulus. However, the locus of points in this regime, for which modulation frequency approaches zero, depicts unintuitively diffuse rogue waves. In the case of these structures, the spatiotemporal localisation extends spatially over a number of adjacent crests. While individual peaks display the usual features relating to modulation instability, including spatially aligned troughs, an envelope drawn across oscillations over a large domain reveals a pattern of depressions and protuberances in the shape of a rotated rogue wave solution.
5. In the case of higher-order rogue wave solutions, we have shown that the cnoidal background does not significantly affect the existence of these structures. Fissioned rogue waves still require shifts that depend on modulation frequency in a polynomial manner, with the only difference being that the elliptic modulus is incorporated into its definition. The peak amplitude for a fused rogue wave solution is also found to be $\mathrm{Im}(2\lambda n) + 1$, provided that it is superimposed upon a crest of the cnoidal background.

In effect, this work has explored an expansive space of solutions, all arising from waves constructed with Jacobi elliptic functions and their case-dependent interactions with both solitons and modulationally unstable perturbations. The connections between plane-wave and zero-background structures are both rich and unintuitive, and will be of particular interest in any nonlinear field that engages with cnoidal waves. The obvious example is in oceanography, where rogue waves are typically considered to be deep-water phenomena, while naturally occurring cnoidal structures are usually associated with shallow water and the KdV equation [16]. However, renormalisation strategies indicate that the two structures may be valid in either context [17], meaning that their superpositions may actually describe real-world water waves.

The applicability of our results also extends to the optical sciences, where fibre lines can transmit trains of pulses described by cnoidal waves [5]. Accordingly, new laser techniques are being developed to controllably shape signal intensity in this manner [18]. It is thus vital that the effect of perturbations on data transmission is well understood so that wavefunction stability and fidelity are maintained. Beyond this, cnoidal waves and Peregrine solitons can also be generated in Bose-Einstein condensates [19,20], indicating that our superimposed wavefunctions may similarly appear here and in a number of other fields.

In any case, with respect to the ψ_{cn} background, our results imply the possibility of a "length scale competition" arising between a soliton and a cnoidal wave, analogous to specific scenarios in other nonlinear systems [21]. For example, kink solitons in Klein-Gordon models have been shown to differentiate between a state of

entrapment within a potential well and a contrasting state of freedom, depending on how the width of the soliton compares with the basin length of the potential [22]. In similar fashion for the NLSE, the difference between solitonic dimensions and the cnoidal wavelength determines whether pulse energy remains relatively localised or is instead mobile. In the presence of inhomogeneities, intelligent tuning of the background and soliton may lead to interesting energy transport applications.

However, regarding potential future investigation, it is the influence of the ψ_{dn} background that is of greatest novelty. In particular, we stress that the diffuse rogue waves presented here have, to the best of our knowledge, not been found before. They provide an intriguing alternative to the "concentrated" forms, in that the latter is a highly destructive but relatively avoidable event, due to the presence of only one crest, while the effect of the former is low-impact but particularly wide-spread. Perhaps the solution could be used to explain the oceanic "three sisters" phenomenon [23].

Ultimately, the impact of this work is best described by highlighting the following logic. It is well known that a plane-wave background, as a solution of the NLSE with constant amplitude, is modulationally unstable. The rogue wave itself is one of the manifestations of this instability. It is possible then to think that the application of strong modulation to the initial wave profile may change the properties of the background and make it stable [5]. However, our results definitively show that even the most extreme of modulated backgrounds is unstable and subject to the generation of spatiotemporally localised amplitude bursts. This is an important implication regarding the existence of rogue waves, in that they can be generated within an NLSE-governed nonlinear system with seemingly no restriction on the background, provided that the conditions are right. From a physical point of view, this means that, assuming there is sufficient energy distributed in space to fuel the generation of a high-amplitude spike, no wave field is intrinsically safe from these extreme events.

The authors acknowledge the support of the Australian Research Council (Discovery Project number DP110102068). N.A. and A.A. acknowledge support from the Volkswagen Stiftung.

References

1. D. Peregrine, J. Austral. Math. Soc. Ser. B **25**, 16 (1983)
2. N. Akhmediev, A. Ankiewicz, Phys. Rev. A **47**, 3213 (1993)
3. K.W. Chow, Wave Motion **35**, 71 (2002)
4. K. Chow, R. Conte, N. Xu, Phys. Lett. A **349**, 422 (2006)
5. V. Aleshkevich, Y. Kartashov, V. Vysloukh, Opt. Comm. **185**, 305 (2000)
6. V.B. Matveev, M. Salle, *Darboux Transformations and Solitons* (Springer-Verlag Berlin, Heidelberg, 1991)
7. N. Akhmediev, N.V. Mitskevich, IEEE J. Quant. Electr. **27**, 849 (1991)
8. D.J. Kedziora, A. Ankiewicz, N. Akhmediev, Phys. Rev. E **84**, 056611 (2011)
9. D.J. Kedziora, A. Ankiewicz, N. Akhmediev, Phys. Rev. E **86**, 056602 (2012)
10. N. Akhmediev, J.M. Soto-Crespo, A. Ankiewicz, Phys. Lett. A **373**, 2137 (2009)
11. N. Akhmediev, A. Ankiewicz, J.M. Soto-Crespo, Phys. Rev. E **80**, 026601 (2009)
12. D.J. Kedziora, A. Ankiewicz, N. Akhmediev, Phys. Rev. E **85**, 066601 (2012)
13. J. Dudley, G. Genty, F. Dias, B. Kibler, N. Akhmediev, Opt. Expr. **17**, 21497 (2009)
14. D.J. Kedziora, A. Ankiewicz, N. Akhmediev, Phys. Rev. E **88**, 013207 (2013)
15. A. Ankiewicz, D.J. Kedziora, N. Akhmediev, Phys. Lett. A **375**, 2782 (2011)
16. R. Wiegel, J. Fluid Mech. **7**, 273 (1960)
17. D. Clamond, J. Fluid Mech. **489**, 101 (2003)
18. M. Wilson, V. Aboites, A.N. Pisarchik, F. Ruiz-Oliveras, M. Taki, Appl. Phys. Expr. **4**, 112701 (2011)

19. P. Leboeuf, N. Pavloff, Phys. Rev. A **64**, 033602 (2001)
20. Y.V. Bludov, V. Konotop, N. Akhmediev, Eur. Phys. J. Special Topics **185**, 169 (2010)
21. S. Cuenda, A. Sánchez, Chaos: An Interdisciplinary J. Nonlinear Sci. **15**, 023502 (2005)
22. M.A. García-Ñustes, I. Rondón, J.A. González, R. Chacón, J. Phys.: Conf. Ser. **246**, 012008 (2010)
23. I. Nikolkina, I. Didenkulova, Nat. Hazards Earth Syst. Sci. **11**, 2913 (2011)

Epilogue

It is clear that the research presented in this chapter has a very large scope, discussing constructed NLSE solutions on a range of backgrounds. These periodic seeds, based on Jacobi elliptic functions, are effectively two separate regimes that are linked so that they are transformably continuous [120]. One branch is described by a $\mathrm{cn}(t, g)$ function, oscillating along the optical t axis and parametrised by g. This ranges from a $g = 0$ plane wave to a $g = 1$ soliton and typically resembles a periodic series of intermediate-amplitude crests, with non-differentiable zero-amplitude points between consecutive peaks. The associated results are then likely to be of interest to soliton studies, as the background starts to resemble a series of pulses for large values of g [122]. All nonlinearly superimposed components in this parameter regime also resemble solitons themselves, so the complicated beating structures may have implications regarding localised energy transfer and optical signal interference [123, 124], among other more speculative applications.

However, it is the background related to $\mathrm{dn}(t, g)$ that is of greatest interest to the narrative within this thesis. Ranging from a $g = 0$ plane wave to the aforementioned $g = 1$ soliton, NLSE solutions constructed with this seed must necessarily describe a smooth transformation between breathers and solitonic wavefunctions. To some extent, this relationship between both classes of localised solutions has already been discussed in the epilogue of Chapter 3. However, this work extends that idea and demonstrates that rogue waves themselves are actually analogous to the collisions between solitons. Indeed, the peaks of the latter are phase alignments of interacting pulses, while the former spatiotemporally localised structures can be considered products of beating between the plane wave and a separate wavefunction. This mysterious component can be considered a soliton when the product is a KM breather [81, 82], but this cannot be carelessly extended to the scenario of ABs, since energy conservation laws preclude the existence of any x-localised zero-background solution. Regardless, this indicates that any multi-rogue wave NLSE solution of order n can be reproduced in the collision of $n + 1$ solitons.

The implications of this are numerous. Amplitude relations have already been noted [7], but this concept hints at the reasons why there is a particular number of Peregrine breathers fused in a multi-rogue wavefunction. If solitons are considered to travel along a linear spatiotemporal path, two will only ever intersect a maximum of one time, three can collide thrice, four have six crossing points, and so on. Concisely put, $n + 1$ solitons can produce a maximum of $n(n + 1)/2$ collisional peaks. This is a significant revelation that provides an alternate perspective to the one based on breather asymmetry in Chapter 3.

Thus it is shown in this chapter that other types of background do not necessarily invalidate the rogue wave hierarchy [6]. In fact, a cnoidal seed involving $\mathrm{dn}(t, g)$ appears to even double the hierarchy of spatiotemporally localised solutions, although the new set of structures is more debatable as a prototypical class representing rogue wave behaviour. For instance, the consecutive ripples of a first-order 'diffuse' rogue wave are certainly spatiotemporally localised, but the maximum amplitude is below

that of a degenerate soliton [99, 100]. This means that a basic diffuse rogue wave does not fulfil the hydrodynamic criterion based on significant wave height [20, 30, 31]. On the other hand, higher-order versions can be constructed to superimpose components up to an arbitrarily large amplitude [69]. Moreover, with the envelope almost resembling a second-order version of the carrier wave discussed in Chapter 5 and the localisation of the diffuse rogue wave extending over a large spatiotemporal domain, this newly-discovered set of structures could potentially represent extreme events that have even more impact.

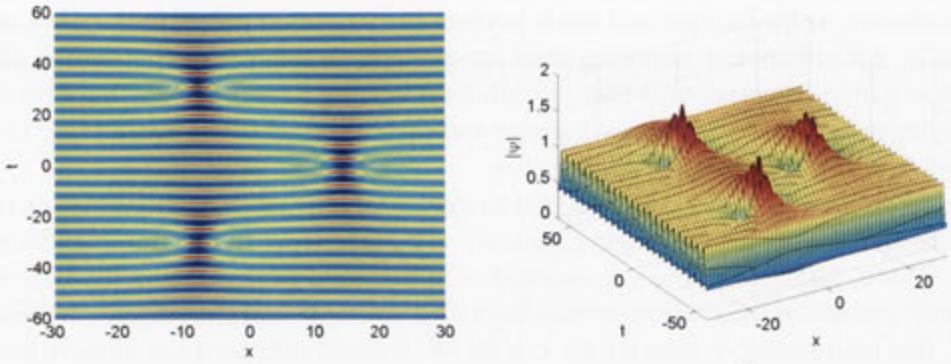

(a) (b)

Figure 7.1: A diffuse rogue wave triplet, with $g = \sqrt{0.85}$, $\kappa_1 = \kappa$, $\kappa_2 = \kappa\sqrt{2}$ and numerical limit $\kappa \to 0$. Modified modulation frequency κ_j is related to both cnoidal parameter g and eigenvalue λ_j via Eq. (7) in cnoidal paper [7]. Non-zero shifts are $x_1 = 100\kappa^2$. (a) Top view. (b) Angled view.

As already mentioned, these NLSE solutions seem to be classifiable into their own version of the standard rogue wave hierarchy. For instance, two perspectives of a diffuse rogue triplet are shown in Fig. 7.1. As is expected [1], the spatiotemporal shift of a component must still be proportional to κ^2 for this solution, although it must be noted that the definition of modulation frequency is slightly modified within the publication in this chapter [7], so as to incorporate cnoidal parameter g. It is nonetheless clear from Fig. 7.1a that the typical features of modulational instability are still present in these unusual structures. The blue colours representing low amplitudes indicate that troughs still accompany peaks of intensity along the t axis, but this does not explain why the 'super-envelope' of envelope oscillations in Fig. 7.1b resembles a rotated version of the rogue triplet. Certainly, the troughs of the super-envelope are adjacent to the three crests along the evolution axis x. This would never be allowed in the case of a plane wave background, as energy conservation would clearly be violated. Yet, remarkably, the cnoidal oscillations allow for this uncanny resemblance to arise. It may be possible then that doubly-periodic cnoidal functions [125, 126] also host their own versions of a diffuse rogue wave. An investigation of these seeds would inevitably lose the analytic advantage that the Darboux

scheme affords singly periodic cnoidal backgrounds, forcing the methodology to rely solely on numerical propagation. But perhaps even more complicated spatiotemporally localised solutions can be thus attained, possibly in the form of further rotated 'super-super-envelopes'.

Of course, at this stage, speculation must give way to patience and further investigation. It is at least evident that varying the background to a multi-rogue wave solution can potentially enrich the possible situations in which extreme events can arise, as well as their appearances themselves.

Chapter 8

The Future of the Hierarchy

Although the fundamental categorisation scheme of NLSE multi-rogue wave solutions was established in Chapter 6, and subsequently proved to be reasonably robust regarding variations of the plane wave background in Chapter 7, its study is far from over. Certainly, as research intensifies into numerous wave evolution equations, one of the most important questions at the current time is: how ubiquitous is the rogue wave hierarchy within nonlinear systems in general?

This chapter is intended as a brief and non-exhaustive discussion of this issue. Few mathematical details are provided, as it merely aims to preview several investigative pathways that have opened up in the aftermath of the core discoveries within this thesis. Certainly, the showcased results have been compiled into articles that are either published or on the verge of submission. With that preface, there are three simple ways to extend the standard NLSE. One is to modify the domain, either adding dimensions or changing the definitions of ones that already exist. To this end, rogue waves of the discrete NLSE are discussed in Sec. 8.1. Another way is to couple the NLSE to the evolution of extra wavefunctions. Resonance between a 'long wave' and a 'short wave' is an example of this and is detailed in Sec. 8.2. Finally, one can simply keep extending the NLSE with higher-order nonlinearities and other terms, in an effort to better approximate the physics of wave evolution within various domains. Progress in deriving and solving an integrable NLSE of infinite order is summarised in Sec. 8.3.

These three research directions ensure that the heretofore understood concepts of NLSE dispersion and cubic nonlinearity, along with their effects on modulational instability and rogue wave evolution, are not discarded. At the same time, they constitute significant steps forward in the theory of multi-rogue waves, forming a compromise between novelty and tractability.

8.1 Discretisation and Spectral Interference

Higher dimensional versions of the NLSE are sometimes seen as a holy grail of research in the field. Certainly, while the 1D version has proven to be remarkably useful in describing hydrodynamic waves and optical signals in a variety of contexts, as well as other phenomena in numerous physical domains, it cannot give a full picture of all the possible extreme events that can arise. For instance, there are definitely numerous spots in the ocean where group velocity vectors may cross as

a result of coastal diffraction [127, 128]. Accordingly, the 2D hyperbolic NLSE is one such higher-dimensional system investigated, albeit with a so-called 'hyperbolic' term to distinguish between the anomalous and normal dispersion affecting oscillations travelling with and across the wave group, respectively [129, 130]. Moreover, this is just for surface waves. There is similarly plenty of interest in rogue waves that arise in three spatial dimensions [131, 132].

However, there is a major caveat here. Most investigations of higher-order systems must be done via numerical propagation or similar techniques. This is because they lack a crucial property called integrability [133, 134]. This mathematically deep concept has many implications regarding features such as conserved quantities. Moreover, it is a prerequisite for numerous solution-generating procedures including the Darboux scheme [84, 135]. This is why the 1D NLSE can be exactly solved, but the standard 2D NLSE remains obtuse. This is not to say that concerted efforts have not wrangled integrability from higher-dimensional nonlinear systems, but these successes have generally been achieved via the contrived inclusion of generally unphysical terms. Analytic triumphs in this topic are few and infrequent.

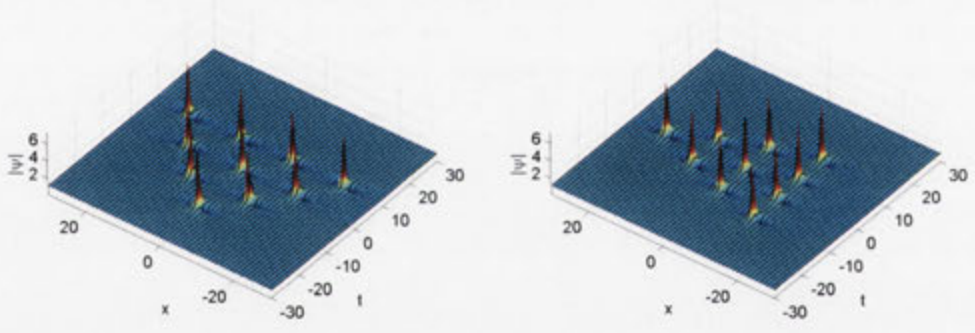

Figure 8.1: Fourth-order Ablowitz-Ladik triangular cascades constructed via the Darboux scheme, with $h = 1$, so that $x = n$. (a) Shifts along the t axis. (b) Same shifts along the x axis.

On the other hand, discretisation has seen much greater progress in rogue wave theory [136–138]. The resulting nonlinear systems face the issue of limited applicability, but spatially discrete domains can still be found in various physical contexts that involve lattice potentials [139]. Given this, the generalised Ablowitz-Ladik (AL) system is one such discretisation of the NLSE [140], expressed as

$$i\frac{\partial \psi_n}{\partial t} + \frac{1}{2h^2}\left(\psi_{n-1} - 2\psi_n + \psi_{n+1}\right) + \frac{1}{2}\left(\psi_{n-1} + \psi_{n+1}\right)|\psi_n|^2 = 0 \tag{8.1}$$

in traditional (i.e. non-optical) convention, where evolution is along the t axis. As to variable n, it is an index that denotes the nodes of a lattice along the spatial x axis,

with adjacent gridpoints separated by a distance of h.

Compensating for the variable changes, this equation reduces to the continuous NLSE in the $h \to 0$ limit. Moreover, it is integrable, which means that the nonlinear system can be written in 'Lax pair' format. Darboux transformations can subsequently be established [141, 142]. Naturally, these have a different form from that found using the methodology employed in this thesis [2, 5, 6], but the conceptual procedure is the same. A plane wave is a trivial solution of Eq. (8.1) and leads to the derivation of first-order discrete breather components. Subsequently, the recursive process and application of zero-frequency limits lead to the standard rogue wave structures presented in Chapter 6. As an example, triangular cascades [4] are shown in Fig. 8.1. They are technically only defined along the depicted black lines, representing a lattice with grid-spacing $h = 1$, but, without delving into details, they have analytic continuations that are defined for the entire spatiotemporal domain. As is apparent, the differences between continuous and discrete rogue waves are few, including the fact that lattice-spacing h affects the amplitude and steepness of each rogue wave quantum, as well as the fact that an increasing h value stretches out arrays of rogue waves along the spatial axis.

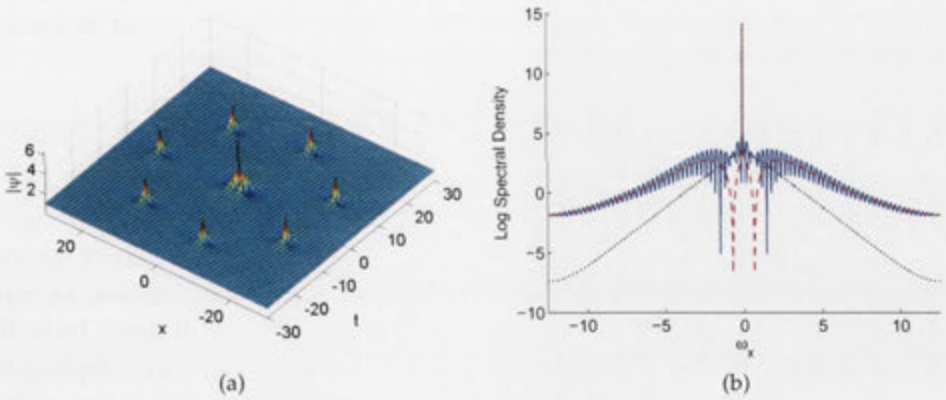

(a) (b)

Figure 8.2: Spectral interference pattern for a first-order and second-order AL rogue wave in alignment, as part of a numerically generated fourth-order rogue wave heptagram. Lattice spacing is $h = 1/4$, so that $x = n/4$. (a) Wavefunction in spatiotemporal domain. Grid does not represent lattice and is a visual aid. (b) Solid blue line represents spectrum for profile at $t = 0$. The dotted black and dashed red lines denote spectra for first-order and fused second-order rogue waves, respectively, with $h = 1/4$.

Of course, an exploration of discrete rogue waves may be of limited appeal to a general scientific audience more interested in phenomena within a continuous context. However, the set-up of this problem is well-suited to investigate spectra, as most numerical applications of the Fourier transform are technically discrete. Interestingly, despite differences in spatiotemporal shapes, the spectral profile of a discrete

Peregrine breather at its maximum amplitude is almost identical to the well-known triangular shape associated with the continuous version [143]. This holds true for all multi-rogue spectra, provided that h is not overly large.

Now, based on the knowledge gained during the course of study detailed in this thesis, it is possible to investigate more complicated spectral effects that were not attainable previously. For instance, constructing a fourth-order discrete heptagram with the Darboux scheme is a routine matter, utilising an appropriate existence condition [6] that is tailored for the discrete AL system. The resulting circular cluster [2] is shown in Fig. 8.2a, although there are too many individual lattice points compressed in the domain to also depict the solution in discrete form. In any case, the discrete Fourier transform (DFT) of the profile at $t = 0$ is shown in Fig. 8.2b. Remarkably, it is a clear beating shape formed from the interference pattern of spectra pertaining to both a first-order and a second-order rogue wave, also shown in the same image. This is particularly curious because two localised structures (e.g. delta functions) in the frequency domain typically correspond to a beating structure in the spatiotemporal domain. Here, the converse is occurring. Localisations in space and time are inducing interference patterns in the frequency domain. Thus this exploration of a discrete system has inadvertently developed a greater understanding of Fourier physics with respect to continuous NLSE rogue wave solutions. At the very least, it is now possible to confirm that the rogue wave hierarchy is not necessarily invalidated by a discretised domain.

8.2 Rogues in Resonance

Coupling the NLSE to other equations is another way to extend standard theories. It is also generally less challenging than dealing with dimensional issues, as maintaining integrability is arguably simpler in many of these cases. Indeed, including an extension such as polarisation into optical models is often done by coupling one wavefunction that obeys the NLSE with another. An example of this is the widely-studied Manakov equation [144–146]. The full picture of a rogue wave must then be synthesised from two or more separately-visualised spatiotemporally localised structures.

From a technical perspective, the simplest procedures of coupling amount to vectorising a wavefunction, which accordingly increases the size of the NLSE Lax pair matrices (i.e. Eq. (A2) in the clusters paper [2]) but does not sacrifice the tractability of solution-generating methods. However, this is not the only way to increase the complexity of a Lax pair. The inclusion of some higher-order terms are sufficient to induce this consequence, as in the case of the Sasa-Satsuma equation [147, 148]. More generally, non-trivial couplings tend to have this effect as well, such as the 'long-short wave resonance' equation (LSWRE) [149, 150], expressed as

$$\frac{\partial A}{\partial t} = \frac{\partial |B|^2}{\partial x},$$

$$i\frac{\partial B}{\partial t} + \frac{1}{2}\frac{\partial^2 B}{\partial x^2} + AB = 0. \tag{8.2}$$

This is again written here in traditional (i.e. non-optical) convention, where t is the evolution variable. Function A is the real-valued long wave and B is the complex-valued envelope of the short wave.

This nonlinear system is one focus of collaborative research initially inspired by the circular clusters result in this thesis [2]. Indeed, Eq. (8.2) is of interest to multi-rogue studies as it can be used to model physical interactions between the oscillations on the surface of a two-layer fluid (i.e. B) and a wave in the interface (i.e. A) [151, 152]. Unsurprisingly, because of the similarity between the LSWRE and the standard NLSE, the analogue of a Peregrine breather was eventually identified, albeit derived via the alternative Hirota bilinear method [8]. To date, there has not been overwhelming success with establishing a hierarchy for the system with the Darboux scheme. This is because the aforementioned increase in the complexity of Lax pair matrices, from a size of 2×2 for the NLSE to 3×3 for the LSWRE, provides many difficult obstacles.

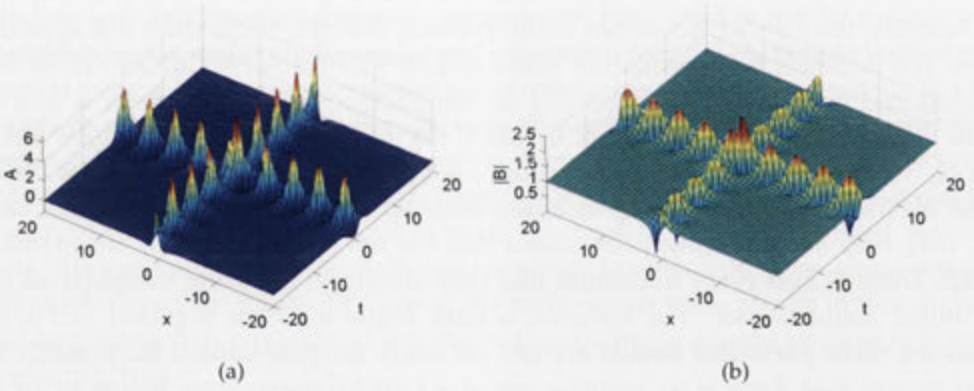

Figure 8.3: An intersection of an AB and KM breather in the long-short wave resonance equation (LSWRE). (a) Long wave A. Background is $A_0 = 0$. (b) Short wave B. Background is $B_0 = 1$.

For one thing, without dwelling on the details, there does not appear to be an 'elementary' Darboux method for the scheme. A 'binary' version must be employed instead, which is highly involved [153, 154]. This complication is compounded by the fact that there are now three functions to deal with for each first-order component (cf. r_{1j} and s_{1j} of Eq. (A4) in the clusters paper [2]). The eigenvalue space is also more convoluted. Whereas axially-aligned NLSE ABs and KM breathers are parametrically constrained by a straight line in the complex plane (i.e. purely imaginary eigenvalues), the parametric locus of LSWRE ABs and KM breathers consists of fully complex eigenvalues and is not smoothly continuous. However, while not necessar-

ily elegant, this alone is numerically surmountable. An image of intersecting LSWRE breathers is shown in Fig. 8.4.

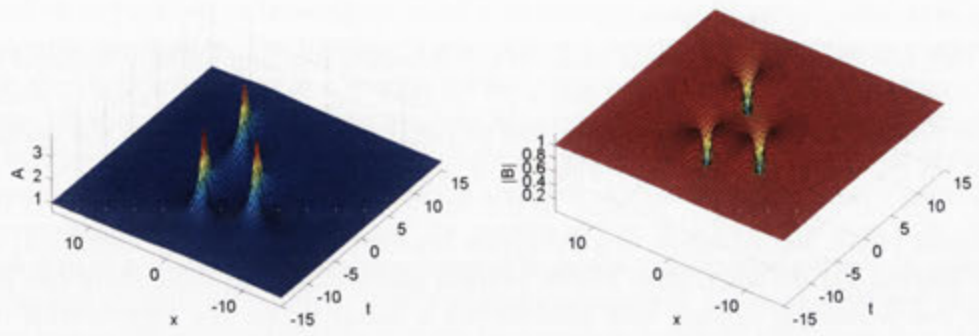

Figure 8.4: A dark rogue wave triplet of the LSWRE. (a) Long wave A. Background is $A_0 = 1$. (b) Short wave B. Background is $B_0 = \exp(i\sqrt{2}x)$.

Notably, the LSWRE possesses many features that the NLSE does not appear to have. For instance, the modulation peaks of LSWRE breather solutions can be augmented and even inverted, depending on the background amplitude of A and the plane wave parameters that seed B. In fact, if the backgrounds of Eq. (8.2) are $A_0 = 1$ and $B_0 = \exp i\sqrt{2}x$, it is possible to reproduce a maximally 'dark' rogue wave. While these inverted spatiotemporally-localised envelopes are nothing new at this stage [73, 155], they are still wave phenomena that are not encapsulated by the standard NLSE. There is also every indication that they adhere to the same hierarchy as that of 'bright' rogue waves. For instance, a dark rogue triplet is depicted in Fig 8.4. However, these particular results are not yet ready for publication, for possibly the same reason that there is no mention yet of a LSWRE rogue wave hierarchy in the literature. Specifically, the identification of exact component shifts to align multiple rogue waves at the origin is proving to be a tremendous mathematical challenge, seemingly intractable via current methodologies and computational power. This is why the collision peak in Fig. 8.3 is not symmetric. The problem here is that, without fused versions of higher-order rogue waves, a classification hierarchy cannot be considered systematic.

Curiously, the LSWRE is not the only nonlinear system stymied by this analytic obstacle. The Sasa-Satsuma equation also resembles the resonance equation in numerous ways [147, 156], seemingly on account of both its 3×3 Lax pair matrices and deeper mathematical symmetries, and similarly appears to suffer component alignment issues. Nonetheless, both equations remain appealing objects of study despite their challenge. Certainly, a 3×3 Lax pair matrix extends the possible types of wave behaviour beyond the NLSE case, providing hints towards the existence of so-called 'Y breathers', angled wavetrain reflections and other exotic phenomena [157, 158].

Thus, a potential breakthrough in this direction may not only lead to a plain confirmation of the same rogue wave hierarchy in a new nonlinear system, but also give rise to novel spatiotemporally localised structures that only exist due to the effect of coupling and extended physics.

8.3 The Endless NLSE

To conclude the preview of future directions in this chapter, it is worth acknowledging the fact that the standard NLSE is but an approximation of wave behaviour that relies on numerous assumptions. It is indeed a universal equation, but it restrictively describes the dynamics of slowly-varying quasi-monochromatic wave packets in dispersive weakly-nonlinear media. These foundations quickly fail in numerous contexts, such as when dealing with ultrashort pulses in optics [111, 112] or water waves with a broad spectral band [159, 160]. Consequently, there are many ways to extend the NLSE so as to better model phenomena in various domains.

In line with this research direction, rogue waves have been found for models that incorporate higher-order nonlinearites and dispersion terms [118, 161], as well as systems that possess gauge transformations into relevant extended equations [162]. One example of a nonlinear system that has been studied as part of a collaborative effort stemming from the research in this thesis is the Chen-Lee-Liu (CLL) equation [163], a type of 'derivative NLSE' [164, 165]. However, it is a complicated system, requiring a 'binary' Darboux scheme, and, as of such, has thus far only been solved with the Hirota bilinear method [9]. Nonetheless, research interest into these equations has blossomed. Given the impact of some of the multi-rogue wave results in this study, it is not surprising that hierarchical structures are also being sought in these nonlinear systems [92, 166].

Progress with some of these equations is challenging. As mentioned in Sec. 8.2, certain higher-order terms can modify Lax pairs and corresponding Darboux transformations to induce greater analytic difficulty. In fact, most arbitrary extensions will break the integrability of the system altogether [133, 134] and preclude any easy way to produce exact solutions, even if the terms they introduce are physically appropriate. Given this, it is worthwhile to investigate NLSE extensions that maintain Lax pair simplicity and keep the corresponding Darboux scheme in this thesis fixed. Indeed, the standard NLSE is but a second-order manifestation of a so-called Ablowitz-Kaup-Newell-Segur (AKNS) class of equations [167]. Instead of being restricted by second-order dispersion and the cubic nonlinearity, it is possible to derive the equation of any order in the AKNS set [168] as

$$i\frac{\partial \psi}{\partial t} + \sum_{j=0}^{n} f_j K_j = 0, \tag{8.3}$$

with

$$\begin{aligned} K_j &= -(-i)^j \frac{\delta p_{j+1}}{\delta \psi^*}, \\ p_{j+1} &= \psi \frac{\partial}{\partial x}\left(\frac{p_j}{\psi}\right) + \sum_{j=j_1+j_2} p_{j_1} p_{j_2}. \end{aligned} \tag{8.4}$$

The initial function to launch the recursive process must be $p_1 = \psi\psi^*$ and the use of the 'functional derivative' is required; it is defined as

$$\frac{\delta}{\delta \psi^*} = \frac{\partial}{\partial \psi^*} + \sum_{j=1}^{\infty} (-1)^j \nabla^{(j)} \left(\frac{\partial}{\partial \left(\nabla^{(j)} \psi^* \right)} \right). \tag{8.5}$$

Keeping with the theme of this chapter, these equations are defined in traditional (i.e. non-optical) convention with t as the evolution variable.

Now, this set of expressions appears involved, but it is a compact way of reproducing a number of integrable equations, with f_j serving as a coefficient to select and scale desirable terms for the relevant model of wave evolution. For instance, setting $f_2 = 1/2$ for the corresponding $K_2 = 2|\psi|^2\psi + \psi_{xx}$ generates the NLSE used in this thesis, provided that all other f_j coefficients are zero and the x and t variables are swapped. The Hirota equation [118] then simply requires $K_3 = i(6|\psi|^2\psi_x + \psi_{xxx})$ to be included in Eq. (8.3). A higher-order Laksmanan-Porsezian-Daniel (LPD) equation [169, 170] follows when f_4 is non-zero, and so on. Research into the quintic version of the NLSE is currently underway, but the most important point here is that a corresponding Lax pair, representing the NLSE far beyond to infinite order, has been recursively established. As the Darboux scheme in this thesis does not change for the AKNS system of any order, it is possible to attain a generalised first-order rogue wave in the form

$$\begin{aligned} N_1 &= 4\left(1 + 2i\delta_{r1} t\right), \\ D_1 &= 1 + 4\delta_{r1}^2 t^2 + 4\left(x - v_{r1} t\right)^2, \\ \psi_1 &= \left[\frac{N_1}{D_1} - 1\right] e^{i\omega_p t}, \end{aligned} \tag{8.6}$$

with associated factors

$$\begin{aligned} v_{r1} &= \sum_{j=0}^{\lfloor (n-2)/2 \rfloor} -(-1)^j f_{2j+1} \frac{(2j+1)!}{(j!)^2}, \\ \delta_{r1} &= \sum_{j=0}^{\lfloor (n-1)/2 \rfloor} 2(-1)^j f_{2j+2} \frac{(2j+1)!}{(j!)^2}, \\ \omega_p &= \sum_{j=0}^{\lfloor n/2 \rfloor} (-1)^{j+1} f_{2j} \frac{(2j)!}{(j!)^2}, \end{aligned} \tag{8.7}$$

and where $\lfloor ... \rfloor$ is the floor function. It follows that, if $f_2 = 1/2$ is fixed as the only non-zero coefficient, then Eq. (8.6) becomes consistent with the equation for a standard Peregrine breather (i.e. Eq. (6) in the degenerate paper, with $x \leftrightarrow t$).

While only previewed here, this derivation is a significant result. It describes how each group of higher-order terms in an integrable AKNS-based NLSE affects the growth and relative velocity of a rogue wave quantum. This understanding is expected to be transferable to the case of compound extreme events. Granted, the practicality of integrable higher-order nonlinear Schrödinger equations appears to diminish as they become ever more complicated, but they may yet produce the closest exact-form approximations to extreme events in highly nonlinear domains. From a mathematical perspective, they also indicate how various combinations of terms can affect solutions formed from the phenomenon of modulational instability.

Ultimately, every investigation described in this chapter attempts to aid in developing a broader understanding of multi-rogue waves, whether immediately applicable or not. Moreover, it is at least clear that the rogue wave hierarchy developed and presented in this thesis [6] is significantly general, valid for numerous extensions to, and deviations from, the standard NLSE.

Chapter 9

Conclusion

At its core, this thesis has presented an investigation into general high-order rogue wave solutions of the 1D nonlinear Schrödinger equation (NLSE). These appear as spatiotemporally localised clusters of high-amplitude surges, all arising from modulationally unstable perturbations on a plane wave background. Moreover, they are complicated nonlinear superpositions of Peregrine breathers; such a breather is the base-case structure considered to represent a single rogue wave 'quantum'. Accordingly, these new solutions are promising models for situations in which the physical effects of individual extreme events combine, such as a hypothetical cascade of freak waves in the deep ocean or a chaotic sequence of intensity bursts within an optical waveguide. They possess fundamental forms, categorisable by rotational symmetries in their spatiotemporal geometry, and can be hybridised into seemingly arbitrary arrangements of rogue wave quanta. The only apparent restrictions on their evolution dynamics have been elaborated in this study.

Summary

Each major chapter of this thesis has presented results relating to this research in the form of a journal publication. Together, they have aimed to form a cohesive narrative of investigation up to and beyond the establishment of the novel rogue wave hierarchy. The crucial features of this dissertation are thus summarised below.

- There exists a mathematical procedure for the construction of complicated NLSE solutions based on the concept of Darboux transformations. This scheme, as implemented in this thesis, was first introduced within the publication [2] presented in Chapter 2 and has been detailed again in subsequent articles [5, 6]. It takes a trivial seeding solution to the nonlinear system and determines a set of first-order component functions that are compatible with the background, from which simple first-order solutions of the NLSE can be algebraically derived. More importantly, the Darboux scheme can work recursively to nonlinearly superimpose n first-order components into a wavefunction of order n. It follows that the shape of this high-order structure is thus tuned by n sets of spatiotemporal shifts and eigenvalues.
- If the seeding solution to the Darboux scheme is a plane wave, then the first-order components take the form of modulationally oscillating breathers. Whether

localised in space or time, each solitary component can be transformed into one doubly-localised crest, known as a Peregrine breather, by taking a limit of zero modulation frequency. However, no two breathers in nonlinear superposition can have the same eigenvalue or corresponding frequency, even as the latter approaches zero. Certainly, in this degenerate limit detailed in Chapter 3, an asymmetry must exist regarding the number of modulational peaks per component wavetrain. This means that, in the rogue wave limit, one component will produce one Peregrine breather for a compound structure, another will provide two, a third will donate three, and so on.

- If each component is spatiotemporally aligned at a common origin, the rogue wave limit applied to a breather of order n will generate a corresponding fused NLSE rogue wave solution of order n. However, if each component is spatiotemporally shifted by the same finite amount, then the entire structure is translated to a new origin. Moreover, if each component shift is proportional to κ^2, where κ is a factor common to each component frequency, a linear relation between shift coefficients and squared frequency ratio coefficients is necessary and sufficient to fission the compound wavefunction into a triangular arrangement of $n(n+1)/2$ Peregrine breathers, referred to in this thesis as rogue wave quanta. This concept of an existence condition was introduced in Chapter 4.

- Each quantum imparts a 2π phase shift to any carrier wave that passes though the extreme event, although this effect is localised between its zero-amplitude envelope troughs. This pair of phase singularities is capable of causing wave dislocation, a phenomenon which affects wave steepness and contributes to broadening the dangerous aspects of an oceanic extreme event beyond large amplitudes alone. However, a rogue wave NLSE solution of order n can only maximally impart a phase shift of $2\pi n$, which restricts the possible arrangements of quanta in both fused and fissioned form. This was elaborated in Chapter 5.

- The existence condition for the cascade can be extended for other orders of shift. For example, a quadratic relation between coefficients of both shifts proportional to κ^4 and squared frequency ratios is responsible for the production of a rogue wave pentagram. Existence conditions for heptagrams, enneagrams, and so, continue in logical fashion. Concisely, $\kappa^{2(m-1)}$ proportionality in spatiotemporal shifts requires the relevant relation to be a polynomial with order $m-1$, so as to reproduce fission into an array of rogue wave quanta with a rotational quasi-symmetry of degree $2m-1$. Accordingly, if $m=n$ for a multi-rogue wave of order n, then the fissioning process replicates a circular cluster from Chapter 2. Hence all these can be considered fundamental high-order rogue wave solutions, categorisable into a hierarchy by their spatiotemporal geometries, as established in Chapter 6. These existence conditions can also be enforced independently of each other, allowing numerous arrangements to be hybridised.

- Replacing the plane wave background with a cnoidal seed does not conceptually invalidate the rogue wave hierarchy. As demonstrated in Chapter 7, all the typical compound solutions can still be nonlinearly superimposed onto the cnoidal oscillations. Moreover, there is a deep bijective connection between collisions formed from $n+1$ solitons and NLSE rogue wave solutions of order n. Additionally, cnoidal waves enrich the set of possible multi-rogue wavefunctions by allowing for diffuse spatiotemporally localised perturbations in an otherwise regular pattern of envelope oscillations.

- Finally, as briefly discussed in Chapter 8, there is plenty of evidence to suggest that the rogue wave hierarchy remains valid for numerous other nonlinear systems. In particular, discretisations, couplings and extensions involving higher-order nonlinearities do not inherently contradict the existence of the classification scheme developed within this thesis.

Final Words

The research in this thesis has been conducted at a time in which the topic of rogue waves can be considered part of both the pop-cultural and scientific zeitgeist. Indeed, inspired by the power and devastation they symbolise, the media and public have embraced the phenomenon. It sometimes seems that every seventh wave crashing into a boat is considered 'freak', while every sudden market movement is feared to be 'rogue'. But this is no surprise. The psychology of awe has always driven the imagination to seek the extreme, the so-called "rare wonders of nature" [171]. What is then more extreme and rare than a rogue wave itself?

It is not unexpected then that the publications presented in this thesis have had a substantial impact already, particularly in a topic area as young and dynamic as the study of multi-rogue waves. Certainly, at the time of this writing, the earliest publications involving rogue triplets [1], circular clusters [2] and degenerate breathers [3] have each been cited over 25 times. Some of these ensuing investigations have been complementary to the quest for a rogue wave hierarchy of the NLSE [71, 72, 89, 90, 172–174], while others have taken these concepts to nonlinear systems far beyond [73, 75, 91, 92, 145, 146, 175, 176]. Given that compound rogue waves have been already glimpsed in experiments for the first time [76, 77], it may not be long before humankind is able to controllably engineer its own extreme events.

Finally, as a concluding observation, it is clear that this discipline shares a characteristic with the phenomenon it researches, in that it essentially "appeared from nowhere". However, unlike that same phenomenon, I personally have high hopes and great expectations that it will not "disappear without a trace".

PhD Publications

[1] A. Ankiewicz, D. J. Kedziora, and N. Akhmediev, "Rogue wave triplets", *Phys. Lett. A*, vol. 375, no. 28-29, pp. 2782 – 2785, 2011. (Times cited on ISI by submission date: 39).

[2] D. J. Kedziora, A. Ankiewicz, and N. Akhmediev, "Circular rogue wave clusters", *Phys. Rev. E*, vol. 84, p. 056611, Nov 2011. Copyright 2011 by the American Physical Society. (Times cited on ISI by submission date: 35).

[3] D. J. Kedziora, A. Ankiewicz, and N. Akhmediev, "Second-order nonlinear Schrödinger equation breather solutions in the degenerate and rogue wave limits", *Phys. Rev. E*, vol. 85, p. 066601, Jun 2012. Copyright 2012 by the American Physical Society. (Times cited on ISI by submission date: 26).

[4] D. J. Kedziora, A. Ankiewicz, and N. Akhmediev, "Triangular rogue wave cascades", *Phys. Rev. E*, vol. 86, no. 5, p. 056602, 2012. Copyright 2012 by the American Physical Society. (Times cited on ISI by submission date: 13).

[5] D. J. Kedziora, A. Ankiewicz, and N. Akhmediev, "The phase patterns of higher-order rogue waves", *J. Opt.*, vol. 15, no. 6, p. 064011, 2013. (Times cited on ISI by submission date: 1).

[6] D. J. Kedziora, A. Ankiewicz, and N. Akhmediev, "Classifying the hierarchy of nonlinear-Schrödinger-equation rogue-wave solutions", *Phys. Rev. E*, vol. 88, no. 1, p. 013207, 2013. Copyright 2013 by the American Physical Society. (Times cited on ISI by submission date: 11).

[7] D. J. Kedziora, A. Ankiewicz, and N. Akhmediev, "Rogue waves and solitons on a cnoidal background", *Eur. Phys. J. Spec. Top.*, vol. 223, no. 1, pp. 43–62, 2014. With kind permission of The European Physical Journal (EPJ). (Times cited on ISI by submission date: 1).

Collaborative Publications

[8] K. W. Chow, H. N. Chan, D. J. Kedziora, and R. H. J. Grimshaw, "Rogue Wave Modes for the Long Wave–Short Wave Resonance Model", *J. Phys. Soc. Jpn.*, vol. 82, no. 7, pp. 074001–074001, 2013.

[9] H. N. Chan, K. W. Chow, D. J. Kedziora, R. H. J. Grimshaw, and E. Ding, "Rogue wave modes for a derivative nonlinear Schrödinger model", *Phys. Rev. E*, vol. 89, no. 3, p. 032914, 2014.

Consolidated Bibliography

[10] K. Dysthe, H. E. Krogstad, and P. Müller, "Oceanic Rogue Waves", *Annu. Rev. Fluid Mech.*, vol. 40, no. 1, pp. 287–310, 2008.

[11] A. Chabchoub, N. P. Hoffmann, and N. Akhmediev, "Rogue Wave Observation in a Water Wave Tank", *Phys. Rev. Lett.*, vol. 106, no. 20, p. 204502, 2011.

[12] D. R. Solli, C. Ropers, P. Koonath, and B. Jalali, "Optical rogue waves", *Nature*, vol. 450, p. 1054, 2007.

[13] B. Kibler, J. Fatome, C. Finot, G. Millot, F. Dias, G. Genty, N. Akhmediev, and J. M. Dudley, "The Peregrine soliton in nonlinear fibre optics", *Nat. Phys.*, vol. 6, pp. 790–795, 2010.

[14] N. Akhmediev, J. M. Dudley, D. R. Solli, and S. K. Turitsyn, "Recent progress in investigating optical rogue waves", *J. Opt.*, vol. 15, no. 6, p. 060201, 2013.

[15] Y. V. Bludov, V. V. Konotop, and N. Akhmediev, "Matter rogue waves", *Phys. Rev. A*, vol. 80, p. 033610, 2009.

[16] L. Wen, L. Li, Z.-D. Li, S.-W. Song, X.-F. Zhang, and W. M. Liu, "Matter rogue wave in Bose-Einstein condensates with attractive atomic interaction", *Eur. Phys. J. D*, vol. 64, no. 2, pp. 473–478, 2011.

[17] H. Bailung, S. K. Sharma, and Y. Nakamura, "Observation of Peregrine solitons in a multicomponent plasma with negative ions", *Phys. Rev. Lett.*, vol. 107, no. 25, p. 255005, 2011.

[18] W. M. Moslem, P. K. Shukla, and B. Eliasson, "Surface plasma rogue waves", *Europhys. Lett.*, vol. 96, no. 2, p. 25002, 2011.

[19] Y. Zhen-Ya, "Financial rogue waves", *Commun. Theor. Phys.*, vol. 54, no. 5, p. 947, 2010.

[20] N. Akhmediev and E. Pelinovsky, "Editorial–Introductory remarks on Discussion & Debate: Rogue Waves–Towards a Unifying Concept?", *Eur. Phys. J. Spec. Top.*, vol. 185, no. 1, pp. 1–4, 2010.

[21] J. Cartwright and H. Nakamura, "What kind of a wave is Hokusai's Great wave off Kanagawa?", *Notes Rec. R. Soc.*, vol. 63, no. 2, pp. 119–135, 2009.

[22] J. M. Dudley, V. Sarano, and F. Dias, "On Hokusai's great wave off Kanagawa: localization, linearity and a rogue wave in sub-Antarctic waters", *Notes Rec. R. Soc.*, vol. 67, no. 2, pp. 159–164, 2013.

[23] A. Chabchoub, N. P. Hoffmann, M. Onorato, and N. Akhmediev, "Super Rogue Waves: Observation of a Higher-Order Breather in Water Waves", *Phys. Rev. X*, vol. 2, p. 011015, Mar 2012.

[24] I. Georgescu, "Exhibition: The great rogue wave", *Nat. Phys.*, vol. 9, no. 9, pp. 526–526, 2013.

[25] S. Haver, "Evidences of the existence of freak waves", in *Rogue Waves*, pp. 129–140, 2001.

[26] D. H. Peregrine, "Interaction of water waves and currents", *Adv. Appl. Mech.*, vol. 16, pp. 9–117, 1976.

[27] R. Smith, "Giant waves", *J. Fluid Mech.*, vol. 77, no. 3, pp. 417–431, 1976.

[28] I. Nikolkina and I. Didenkulova, "Rogue waves in 2006-2010", *Nat. Hazards Earth Syst. Sci.*, vol. 11, pp. 2913–2924, 2011.

[29] S. Lehner and H. Gunther, "Extreme wave statistics from radar data sets", in *2004 IEEE International Geoscience and Remote Sensing Symposium Proceedings*, vol. 3, pp. 1880–1883, IEEE, 2004.

[30] C. Kharif and E. Pelinovsky, "Physical mechanisms of the rogue wave phenomenon", *Eur. J. Mech. B/Fluids.*, vol. 22, no. 6, pp. 603 – 634, 2003.

[31] P. C. Liu and K. R. MacHutchon, "Are There Different Kinds of Rogue Waves?", *J. Offshore Mech. Arct. Eng.*, vol. 130, no. 2, p. 021007, 2008.

[32] N. Mori and P. A. E. M. Janssen, "On kurtosis and occurrence probability of freak waves", *J. Phys. Oceanogr.*, vol. 36, no. 7, pp. 1471–1483, 2006.

[33] M. Onorato, T. Waseda, A. Toffoli, L. Cavaleri, O. Gramstad, P. A. E. M. Janssen, T. Kinoshita, J. Monbaliu, N. Mori, A. R. Osborne, M. Serio, C. T. Stansberg, H. Tamura, and K. Trulsen, "Statistical Properties of Directional Ocean Waves: The Role of the Modulational Instability in the Formation of Extreme Events", *Phys. Rev. Lett.*, vol. 102, p. 114502, Mar 2009.

[34] P. Müller, C. Garrett, and A. Osborne, "Rogue waves", *Oceanography*, vol. 18, no. 3, p. 66, 2005.

[35] P. Peterson, T. Soomere, J. Engelbrecht, and E. van Groesen, "Soliton interaction as a possible model for extreme waves in shallow water", *Nonlinear Proc. Geoph.*, vol. 10, pp. 503–510, 2003.

[36] T. Soomere, "Rogue waves in shallow water", *Eur. Phys. J. Spec. Top.*, vol. 185, no. 1, pp. 81–96, 2010.

[37] G. Z. Forristall, "Understanding rogue waves: Are new physics really necessary", in *Proceedings of the 14th Aha Hulikoá Hawaiian Winter Workshop on Rogue Waves*, 2005.

[38] M. Onorato, S. Residori, U. Bortolozzo, A. Montina, and F. T. Arecchi, "Rogue waves and their generating mechanisms in different physical contexts", *Phys. Rep.*, vol. 528, no. 2, pp. 47–89, 2013.

[39] I. V. Lavrenov and A. V. Porubov, "Three reasons for freak wave generation in the non-uniform current", *Eur. J. Mech. B/Fluids.*, vol. 25, no. 5, pp. 574–585, 2006.

[40] C. Guedes Soares, Z. Cherneva, and E. M. Antão, "Characteristics of abnormal waves in North Sea storm sea states", *Appl. Ocean Res.*, vol. 25, no. 6, pp. 337–344, 2003.

[41] J. Touboul, J.-P. Giovanangeli, C. Kharif, and E. Pelinovsky, "Freak waves under the action of wind: experiments and simulations", *Eur. J. Mech. B/Fluids.*, vol. 25, no. 5, pp. 662–676, 2006.

[42] A. R. Osborne, M. Onorato, and M. Serio, "The nonlinear dynamics of rogue waves and holes in deep-water gravity wave trains", *Phys. Lett. A*, vol. 275, no. 5, pp. 386–393, 2000.

[43] N. Akhmediev, J. M. Soto-Crespo, and A. Ankiewicz, "Extreme waves that appear from nowhere: On the nature of rogue waves", *Phys. Lett. A*, vol. 373, no. 25, pp. 2137–2145, 2009.

[44] A. Sergeeva, E. Pelinovsky, and T. Talipova, "Nonlinear random wave field in shallow water: variable Korteweg-de Vries framework", *Nat. Hazards Earth Syst. Sci.*, vol. 11, no. 2, pp. 323–330, 2011.

[45] H. Hasimoto and H. Ono, "Nonlinear modulation of gravity waves", *J. Phys. Soc. Jpn.*, vol. 33, no. 3, pp. 805–811, 1972.

[46] A. R. Osborne, *Nonlinear Ocean Waves And The Inverse Scattering Transform*. Elsevier, 2010.

[47] D. Peregrine, "Water waves, nonlinear Schrödinger equations and their solutions", *J. Austral. Math. Soc. Ser. B*, vol. 25, no. 01, pp. 16–43, 1983.

[48] N. Akhmediev, A. Ankiewicz, and M. Taki, "Waves that appear from nowhere and disappear without a trace", *Phys. Lett. A*, vol. 373, no. 6, pp. 675 – 678, 2009.

[49] V. Shrira and V. Geogjaev, "What makes the Peregrine soliton so special as a prototype of freak waves?", *J. Eng. Math.*, vol. 67, no. 1, pp. 11–22, 2010.

[50] S. Birkholz, E. T. Nibbering, C. Brée, S. Skupin, A. Demircan, G. Genty, and G. Steinmeyer, "Spatiotemporal Rogue Events in Optical Multiple Filamentation", *Phys. Rev. Lett.*, vol. 111, no. 24, p. 243903, 2013. (Image from `http://phys.org/news/2013-12-optical-rogue-storm-tube.html`).

[51] K. Hammani, B. Kibler, C. Finot, P. Morin, J. Fatome, J. M. Dudley, and G. Millot, "Peregrine soliton generation and breakup in standard telecommunications fiber", *Optics Letters*, vol. 36, p. 112, 2011.

[52] J. S. Russell, "III. Experimental Researches into the Laws of Certain Hydrodynamical Phenomena that accompany the Motion of Floating Bodies, and have not previously been reduced into conformity with the known Laws of the Resistance of Fluids", *Trans. R. Soc. Edinb.*, vol. 14, no. 01, pp. 47–109, 1839.

[53] R. K. Bullough and P. J. Caudrey, *The soliton and its history*. Springer, 1980.

[54] A. Hasegawa and F. Tappert, "Transmission of stationary nonlinear optical pulses in dispersive dielectric fibers. I. Anomalous dispersion", *Appl. Phys. Lett.*, vol. 23, no. 3, pp. 142–144, 1973.

[55] J. Kasparian, P. Béjot, J.-P. Wolf, and J. M. Dudley, "Optical rogue wave statistics in laser filamentation", *Opt. Express*, vol. 17, pp. 12070–12075, Jul 2009.

[56] K. Hammani, B. Kibler, C. Finot, and A. Picozzi, "Emergence of rogue waves from optical turbulence", *Phys. Lett. A*, vol. 374, no. 34, pp. 3585–3589, 2010.

[57] A. Toffoli, A. Babanin, M. Onorato, and T. Waseda, "Maximum steepness of oceanic waves: Field and laboratory experiments", *Geophys. Res. Lett.*, vol. 37, no. 5, 2010.

[58] A. V. Smith, B. T. Do, G. R. Hadley, and R. L. Farrow, "Optical damage limits to pulse energy from fibers", *IEEE J. Sel. Top. Quant. Electron.*, vol. 15, no. 1, pp. 153–158, 2009.

[59] N. Akhmediev and V. I. Korneev, "Modulation instability and periodic solutions of the nonlinear Schrödinger equation", *Teor. Mat. Fiz.*, vol. 69, pp. 189–194, 1986. English translation in: [Theor. Math. Phys., **69**, 1089 (1986)].

[60] V. B. Efimov, A. N. Ganshin, G. Kolmakov, P. McClintock, and L. Mezhov-Deglin, "Rogue waves in superfluid helium", *Eur. Phys. J. Spec. Top.*, vol. 185, p. 181193, 2010.

[61] L. Stenflo and M. Marklund, "Rogue waves in the atmosphere", *J. Plasma Phys.*, vol. 76, no. 3-4, pp. 293–295, 2010.

[62] E. Pelinovsky, E. Shurgalina, and N. Chaikovskaya, "The scenario of a single freak wave appearance in deep water - dispersive focusing mechanism framework", *Nat. Hazards Earth Syst. Sci.*, vol. 11, pp. 127–134, 2011.

[63] N. Akhmediev, J. M. Soto-Crespo, and A. Ankiewicz, "How to excite a rogue wave", *Phys. Rev. A*, vol. 80, p. 043818, 2009.

[64] F. T. Arecchi, G. Giacomelli, P. L. Ramazza, and S. Residori, "Vortices and defect statistics in two-dimensional optical chaos", *Phys. Rev. Lett.*, vol. 67, no. 27, pp. 3749–3752, 1991.

[65] A. Calini and C. Schober, "Homoclinic chaos increases the likelihood of rogue wave formation", *Phys. Lett. A*, vol. 298, no. 5, pp. 335–349, 2002.

[66] G. F. Clauss, C. E. Schmittner, J. Hennig, C. G. Soares, N. Fonseca, and R. Pascoal, "Bending moments of an FPSO in rogue waves", in *ASME 2004 23rd International Conference on Offshore Mechanics and Arctic Engineering*, pp. 455–462, American Society of Mechanical Engineers, 2004.

[67] D. R. Solli, C. Ropers, and B. Jalali, "Active control of rogue waves for stimulated supercontinuum generation", *Phys. Rev. Lett.*, vol. 101, no. 23, p. 233902, 2008.

[68] N. Akhmediev, J. M. Soto-Crespo, and A. Ankiewicz, "Could rogue waves be used as efficient weapons against enemy ships?", *Eur. Phys. J. Spec. Top.*, vol. 185, no. 1, pp. 259–266, 2010.

[69] N. Akhmediev, A. Ankiewicz, and J. M. Soto-Crespo, "Rogue waves and rational solutions of the nonlinear Schrödinger equation", *Phys. Rev. E*, vol. 80, no. 2, p. 026601, 2009.

[70] A. Ankiewicz, P. A. Clarkson, and N. Akhmediev, "Rogue waves, rational solutions, the patterns of their zeros and integral relations", *J. Phys. A: Math. Gen.*, vol. 43, p. 122002, 2010.

[71] Y. Ohta and J. Yang, "General high-order rogue waves and their dynamics in the nonlinear Schrödinger equation", *Proc. R. Soc. A.*, vol. 468, no. 2142, pp. 1716–1740, 2012.

[72] J. S. He, H. R. Zhang, L. H. Wang, K. Porsezian, and A. S. Fokas, "Generating mechanism for higher-order rogue waves", *Phys. Rev. E*, vol. 87, no. 5, p. 052914, 2013.

[73] J. He, S. Xu, and K. Porsezian, "N-order bright and dark rogue waves in a resonant erbium-doped fiber system", *Phys. Rev. E*, vol. 86, no. 6, p. 066603, 2012.

[74] C.-Q. Dai and H.-P. Zhu, "Superposed Kuznetsov-Ma solitons in a two-dimensional graded-index grating waveguide", *J. Opt. Soc. Am.B*, vol. 30, no. 12, pp. 3291–3297, 2013.

[75] C.-Q. Dai and H.-P. Zhu, "Superposed Akhmediev breather of the (3+1)-dimensional generalized nonlinear Schrödinger equation with external potentials", *Ann. Phys.*, vol. 341, pp. 142–152, 2014.

[76] M. Erkintalo, K. Hammani, B. Kibler, C. Finot, N. Akhmediev, J. M. Dudley, and G. Genty, "Higher-Order Modulation Instability in Nonlinear Fiber Optics", *Phys. Rev. Lett.*, vol. 107, p. 253901, 2011.

[77] A. Chabchoub and N. Akhmediev, "Observation of rogue wave triplets in water waves", *Phys. Lett. A*, vol. 377, no. 38, pp. 2590–2593, 2013.

[78] V. E. Zakharov and A. B. Shabat, "Exact theory of two-dimensional self-focusing and one-dimensional self-modulation of waves in nonlinear media", *J. Exp. Theor. Phys.*, vol. 34, pp. 62–69, 1972.

[79] T. B. Benjamin and J. E. Feir, "The disintegration of wave trains on deep water Part 1. Theory", *J. Fluid Mech.*, vol. 27, no. 03, pp. 417–430, 1967.

[80] K. Tai, A. Hasegawa, and A. Tomita, "Observation of modulational instability in optical fibers", *Phys. Rev. Lett.*, vol. 56, no. 2, p. 135, 1986.

[81] E. A. Kuznetsov, "Solitons in a parametrically unstable plasma", in *Doklady Akademiia Nauk SSSR*, vol. 236, pp. 575–577, 1977.

[82] Y.-C. Ma, "The perturbed plane-wave solutions of the cubic Schrodinger equation", *Stud. Appl. Maths.*, vol. 60, pp. 43–58, 1979.

[83] R. Hirota, "Direct methods in soliton theory", in *Solitons*, pp. 157–176, Springer, 1980.

[84] V. B. Matveev and M. Salle, *Darboux transformations and solitons*. Springer-Verlag Berlin, Heidelberg, 1991.

[85] P. Dubard, P. Gaillard, C. Klein, and V. B. Matveev, "On multi-rogue wave solutions of the NLS equation and positon solutions of the KdV equation", *Eur. Phys. J. Spec. Top.*, vol. 185, no. 1, pp. 247–258, 2010.

[86] P. Dubard and V. B. Matveev, "Multi-rogue waves solutions to the focusing NLS equation and the KP-I equation", *Nat. Hazards Earth Syst. Sci.*, vol. 11, pp. 667–672, Mar. 2011.

[87] N. Akhmediev and N. V. Mitskevich, "Extremely high degree of N-soliton pulse compression in an optical fiber", *IEEE J. Quantum. Electron.*, vol. 27, no. 3, pp. 849–857, 1991.

[88] P. Gaillard, "Families of quasi-rational solutions of the NLS equation and multi-rogue waves", *J. Phys. A: Math. Gen.*, vol. 44, p. 5204, Oct. 2011.

[89] L. Ling and L.-C. Zhao, "Simple determinant representation for rogue waves of the nonlinear Schrödinger equation", *Phys. Rev. E*, vol. 88, no. 4, p. 043201, 2013.

[90] P. Gaillard, "Six-parameters deformations of fourth order Peregrine breather solutions of the nonlinear Schrödinger equation", *J. Math. Phys.*, vol. 54, no. 7, p. 073519, 2013.

[91] L. Li, Z. Wu, L. Wang, and J. He, "High-order rogue waves for the Hirota equation", *Ann. Phys.*, vol. 334, pp. 198–211, 2013.

[92] Y. Zhang, L. Guo, S. Xu, Z. Wu, and J. He, "The hierarchy of higher order solutions of the derivative nonlinear Schrödinger equation", *Commun. Nonlinear Sci. Comput. Simulat.*, vol. 19, no. 6, pp. 1706–1722, 2014.

[93] N. Akhmediev and A. Ankiewicz, *Solitons: nonlinear pulses and beams*, vol. 5 of *Optical and Quantum Electronics*. Chapman & Hall London, 1997. Chapters 3-4.

[94] H. Frauenkron and P. Grassberger, "Interaction of nonlinear Schrodinger solitons with an external potential", *J. Phys. A: Math. Gen.*, vol. 28, no. 17, p. 4987, 1995.

[95] R. J. Glauber, "Coherent and incoherent states of the radiation field", *Phys. Rev.*, vol. 131, no. 6, p. 2766, 1963.

[96] D. J. Kaup and A. C. Newell, "Solitons as particles, oscillators, and in slowly changing media: a singular perturbation theory", *Proc. R. Soc. London Ser. A*, vol. 361, no. 1707, pp. 413–446, 1978.

[97] R. Rajaraman, *Solitons and instantons*. North-Holland, 1982.

[98] A. Chabchoub, N. Hoffmann, M. Onorato, A. Slunyaev, A. Sergeeva, E. Pelinovsky, and N. Akhmediev, "Observation of a hierarchy of up to fifth-order rogue waves in a water tank", *Phys. Rev. E*, vol. 86, no. 5, p. 056601, 2012.

[99] N. Akhmediev and A. Ankiewicz, "Spatial soliton X-junctions and couplers", *Opt. Commun.*, vol. 100, pp. 186 – 192, 1993.

[100] L. Gagnon and N. Stevenart, "N-soliton interaction in optical fibers: the multiple-pole case", *Opt. Lett.*, vol. 19, pp. 619 – 621, 1994.

[101] J. Satsuma and N. Yajima, "B. Initial Value Problems of One-Dimensional Self-Modulation of Nonlinear Waves in Dispersive Media", *Prog. Theor. Phys. Supp.*, vol. 55, pp. 284–306, 1974.

[102] V. E. Zakharov and A. A. Gelash, "Nonlinear stage of modulation instability", *Phys. Rev. Lett.*, vol. 111, no. 5, p. 054101, 2013.

[103] N. Akhmediev, V. M. Eleonskii, and N. E. Kulagin, "Exact first-order solutions of the nonlinear Schrödinger equation", *Teor. Mat. Fiz.*, vol. 72, pp. 183 – 196, 1987. English translation in: [Theor. Math. Phys., **72**, 809 (1987).

[104] B. F. Sanders, N. D. Katopodes, and J. P. Boyd, "Spectral modeling of nonlinear dispersive waves", *J. Hydraul. Eng.*, vol. 124, no. 1, pp. 2–12, 1998.

[105] G. M. Muslu and H. A. Erbay, "Higher-order split-step Fourier schemes for the generalized nonlinear Schrödinger equation", *Math. Comput. Simulat.*, vol. 67, no. 6, pp. 581–595, 2005.

[106] D. Pathria and J. L. Morris, "Pseudo-spectral solution of nonlinear Schrödinger equations", *J. Comput. Phys.*, vol. 87, no. 1, pp. 108–125, 1990.

[107] C. M. Schober, "Melnikov analysis and inverse spectral analysis of rogue waves in deep water", *Eur. J. Mech. B/Fluids.*, vol. 25, no. 5, pp. 602–620, 2006.

[108] G. F. Clauss, "Dramas of the sea: episodic waves and their impact on offshore structures", *Appl. Ocean Res.*, vol. 24, no. 3, pp. 147–161, 2002.

[109] N. Devine, A. Ankiewicz, G. Genty, J. Dudley, and N. Akhmediev, "Recurrence phase shift in Fermi-Pasta-Ulam nonlinear dynamics", *Phys. Lett. A*, vol. 375, no. 46, pp. 4158 – 4161, 2011.

[110] N. Karjanto and E. Van Groesen, "Note on wavefront dislocation in surface water waves", *Phys. Lett. A*, vol. 371, no. 3, pp. 173–179, 2007.

[111] D. J. Jones, S. A. Diddams, J. K. Ranka, A. Stentz, R. S. Windeler, J. L. Hall, and S. T. Cundiff, "Carrier-Envelope Phase Control of Femtosecond Mode-Locked Lasers and Direct Optical Frequency Synthesis", *Science*, vol. 288, pp. 635 – 639, 2000.

[112] S. T. Cundiff, "Attosecond Physics: Better by half", *Nat. Phys.*, vol. 3, pp. 16 – 18, 2007.

[113] A. Chabchoub, N. P. Hoffmann, and N. Akhmediev, "Observation of rogue wave holes in a water wave tank", *J. Geophys. Res.: Oceans (1978–2012)*, vol. 117, no. C11, 2012.

[114] Andonowati, N. Karjanto, and E. van Groesen, "Extreme wave phenomena in down-stream running modulated waves", *Appl. Math. Model.*, vol. 31, no. 7, pp. 1425 – 1443, 2007.

[115] M. V. Berry and M. R. Dennis, "Phase singularities in isotropic random waves", *Proc. R. Soc. London Ser. A*, vol. 456, no. 2001, pp. 2059–2079, 2000.

[116] G. Gbur, T. D. Visser, and E. Wolf, "Anomalous behavior of spectra near phase singularities of focused waves", *Phys. Rev. Lett.*, vol. 88, no. 1, p. 013901, 2001.

[117] A. Slunyaev, I. Didenkulova, and E. Pelinovsky, "Rogue waters", *Contemp. Phys.*, vol. 52, no. 6, pp. 571–590, 2011.

[118] A. Ankiewicz, J. M. Soto-Crespo, and N. Akhmediev, "Rogue waves and rational solutions of the Hirota equation", *Phys. Rev. E*, vol. 81, p. 046602, 2010.

[119] Y. Tao and J. He, "Multisolitons, breathers, and rogue waves for the Hirota equation generated by the Darboux transformation", *Phys. Rev. E*, vol. 85, no. 2, p. 026601, 2012.

[120] V. Aleshkevich, Y. Kartashov, and V. Vysloukh, "Cnoidal waves compression by means of multisoliton effect", *Opt. Commun.*, vol. 185, no. 4, pp. 305–314, 2000.

[121] M. Wilson, V. Aboites, A. N. Pisarchik, F. Ruiz-Oliveras, and M. Taki, "Stable Cnoidal Wave Formation in an Erbium-Doped Fiber Laser", *Appl. Phys. Express*, vol. 4, no. 11, pp. 112701–112701, 2011.

[122] A. Korpel and P. P. Banerjee, "Exact decomposition of cnoidal waves into associated solitons", *Phys. Lett. A*, vol. 82, no. 3, pp. 113–115, 1981.

[123] H. J. Shin, "Soliton scattering from a finite cnoidal wave train in a fiber", *Phys. Rev. E*, vol. 63, no. 2, p. 026606, 2001.

[124] H. J. Shin, "Soliton on a cnoidal wave background in the coupled nonlinear Schrödinger equation", *J. Phys. A: Math. Gen.*, vol. 37, no. 33, p. 8017, 2004.

[125] N. Akhmediev and A. Ankiewicz, "First-order exact solutions of the nonlinear Schrödinger equation in the normal-dispersion regime", *Phys. Rev. A*, vol. 47, no. 4, p. 3213, 1993.

[126] K. W. Chow, "A class of doubly periodic waves for nonlinear evolution equations", *Wave Motion*, vol. 35, no. 1, pp. 71–90, 2002.

[127] V. P. Ruban, "Two different kinds of rogue waves in weakly crossing sea states", *Phys. Rev. E*, vol. 79, no. 6, p. 065304, 2009.

[128] L. Cavaleri, L. Bertotti, L. Torrisi, E. Bitner-Gregersen, M. Serio, and M. Onorato, "Rogue waves in crossing seas: The Louis Majesty accident", *J. Geophys. Res.: Oceans (1978–2012)*, vol. 117, no. C11, 2012.

[129] V. E. Zakharov and A. M. Rubenchik, "Instability of waveguides and solitons in nonlinear media", *J. Exp. Theor. Phys.*, vol. 38, no. 3, pp. 494–500, 1974.

[130] B. Deconinck, D. E. Pelinovsky, and J. D. Carter, "Transverse instabilities of deep-water solitary waves", *Proc. R. Soc. A*, vol. 462, no. 2071, pp. 2039–2061, 2006.

[131] Z. Yan, V. V. Konotop, and N. Akhmediev, "Three-dimensional rogue waves in nonstationary parabolic potentials", *Phys. Rev. E*, vol. 82, no. 3, p. 036610, 2010.

[132] W. Yue-Yue and D. Chao-Qing, "Spatiotemporal Rogue Waves for the Variable-Coefficient (3+ 1)-Dimensional Nonlinear Schrödinger Equation", *Commun. Theor. Phys.*, vol. 58, no. 2, p. 255, 2012.

[133] H. Goldschmidt *et al.*, "Integrability criteria for systems of nonlinear partial differential equations", *J. Diff. Geom.*, vol. 1, no. 3-4, pp. 269–307, 1967.

[134] M. Lakshmanan and S. Rajaseekar, *Nonlinear dynamics: integrability, chaos and patterns*. Springer, 2003.

[135] C. Gu, H. Hu, and Z. Zhou, *Darboux transformations in integrable systems: theory and their applications to geometry*, vol. 26. Springer, 2006.

[136] J. C. Eilbeck and M. Johansson, "The discrete nonlinear Schrödinger equation-20 years on", in *Conference on Localization and Energy Transfer in Nonlinear Systems*, p. 44, 2003.

[137] M. J. Ablowitz, B. Prinari, and A. D. Trubatch, *Discrete and continuous nonlinear Schrödinger systems*, vol. 302. Cambridge University Press, 2004.

[138] A. Ankiewicz, N. Akhmediev, and J. M. Soto-Crespo, "Discrete rogue waves of the Ablowitz-Ladik and Hirota equations", *Phys. Rev. E*, vol. 82, no. 2, p. 026602, 2010.

[139] Y. V. Kartashov, B. A. Malomed, and L. Torner, "Solitons in nonlinear lattices", *Rev. Mod. Phys.*, vol. 83, no. 1, p. 247, 2011.

[140] M. J. Ablowitz and J. F. Ladik, "Nonlinear differential-difference equations", *J. Math. Phys.*, vol. 16, no. 3, pp. 598–603, 1975.

[141] X. Liu and Y. Zeng, "On the Ablowitz–Ladik equations with self-consistent sources", *J. Phys. A: Math. Theor.*, vol. 40, no. 30, p. 8765, 2007.

[142] Q. Zhenyun, "A generalized Ablowitz–Ladik hierarchy, multi-Hamiltonian structure and Darboux transformation", *J. Math. Phys.*, vol. 49, no. 6, p. 063505, 2008.

[143] N. Akhmediev, J. M. Soto-Crespo, A. Ankiewicz, and N. Devine, "Early detection of rogue waves in a chaotic wave field", *Phys. Lett. A*, vol. 375, no. 33, pp. 2999–3001, 2011.

[144] F. Baronio, A. Degasperis, M. Conforti, and S. Wabnitz, "Solutions of the vector nonlinear Schrödinger equations: evidence for deterministic rogue waves", *Phys. Rev. Lett.*, vol. 109, no. 4, p. 044102, 2012.

[145] N. V. Priya, M. Senthilvelan, and M. Lakshmanan, "Akhmediev breathers, Ma solitons, and general breathers from rogue waves: A case study in the Manakov system", *Phys. Rev. E*, vol. 88, no. 2, p. 022918, 2013.

[146] B.-G. Zhai, W.-G. Zhang, X.-L. Wang, and H.-Q. Zhang, "Multi-rogue waves and rational solutions of the coupled nonlinear Schrödinger equations", *Nonlinear Anal. Real World Appl.*, vol. 14, no. 1, pp. 14–27, 2013.

[147] U. Bandelow and N. Akhmediev, "Persistence of rogue waves in extended nonlinear Schrödinger equations: Integrable Sasa-Satsuma case", *Phys. Lett. A*, vol. 376, pp. 1558 – 1561, 2012.

[148] S. Chen, "Twisted rogue-wave pairs in the Sasa-Satsuma equation", *Phys. Rev. E*, vol. 88, no. 2, p. 023202, 2013.

[149] M. Tsutsumi and S. Hatano, "Well-posedness of the Cauchy problem for the long wave-short wave resonance equations", *Nonlinear Anal. Theory Methods Appl.*, vol. 22, no. 2, pp. 155–171, 1994.

[150] P. Gao and B. Guo, "Homoclinic orbits for the coupled nonlinear Schrödinger system and long–short wave equation", *Phys. Lett. A*, vol. 340, no. 1, pp. 209–211, 2005.

[151] M. Funakoshi and M. Oikawa, "The resonant interaction between a long internal gravity wave and a surface gravity wave packet", *J. Phys. Soc. Jpn.*, vol. 52, no. 6, pp. 1982–1995, 1983.

[152] A. D. Craik, *Wave interactions and fluid flows*. Cambridge University Press, 1988.

[153] O. C. Wright, "Homoclinic Connections of Unstable Plane Waves of the Long-Wave–Short-Wave Equations", *Stud. Appl. Maths.*, vol. 117, no. 1, pp. 71–93, 2006.

[154] E. V. Doktorov and S. B. Leble, *A Dressing Method in Mathematical Physics*. Springer, 2007.

[155] S. Chen, P. Grelu, and J. M. Soto-Crespo, "Dark-and bright-rogue-wave solutions for media with long-wave–short-wave resonance", *Phys. Rev. E*, vol. 89, no. 1, p. 011201, 2014.

[156] O. C. Wright, "Sasa-Satsuma equation, unstable plane waves and heteroclinic connections", *Chaos, Solitons & Fractals*, vol. 33, no. 2, pp. 374–387, 2007.

[157] L. Ling and Q. P. Liu, "A long waves-short waves model: Darboux transformation and soliton solutions", *J. Math. Phys.*, vol. 52, no. 5, p. 053513, 2011.

[158] U. Bandelow and N. Akhmediev, "Solitons on a background, rogue waves, and classical soliton solutions of the Sasa–Satsuma equation", *J. Opt.*, vol. 15, no. 6, p. 064006, 2013.

[159] E. Lo and C. C. Mei, "A numerical study of water-wave modulation based on a higher-order nonlinear Schrödinger equation", *J. Fluid Mech.*, vol. 150, pp. 395–416, 1985.

[160] K. Trulsen and K. B. Dysthe, "A modified nonlinear Schrödinger equation for broader bandwidth gravity waves on deep water", *Wave motion*, vol. 24, no. 3, pp. 281–289, 1996.

[161] A. Ankiewicz, J. M. Soto-Crespo, M. A. Chowdhury, and N. Akhmediev, "Rogue waves in optical fibers in presence of third-order dispersion, self-steepening, and self-frequency shift", *J. Opt. Soc. Am.B*, vol. 30, no. 1, pp. 87–94, 2013.

[162] X. Wang, B. Yang, Y. Chen, and Y. Yang, "Higher-order rogue wave solutions of the Kundu–Eckhaus equation", *Phys. Scr.*, vol. 89, no. 9, p. 095210, 2014.

[163] H. H. Chen, Y. C. Lee, and C. S. Liu, "Integrability of nonlinear Hamiltonian systems by inverse scattering method", *Phys. Scr.*, vol. 20, no. 3-4, p. 490, 1979.

[164] S. Xu, J. He, and L. Wang, "The Darboux transformation of the derivative nonlinear Schrödinger equation", *J. Phys. A: Math. Theor.*, vol. 44, no. 30, p. 305203, 2011.

[165] S. Xu and J. He, "The rogue wave and breather solution of the Gerdjikov-Ivanov equation", *J. Math. Phys.*, vol. 53, no. 6, p. 063507, 2012.

[166] B. Yang, W.-G. Zhang, H.-Q. Zhang, and S.-B. Pei, "Generalized Darboux transformation and rogue wave solutions for the higher-order dispersive nonlinear Schrödinger equation", *Phys. Scr.*, vol. 88, no. 6, p. 065004, 2013.

[167] M. J. Ablowitz, D. J. Kaup, A. C. Newell, and H. Segur, "The inverse scattering transform-Fourier analysis for nonlinear problems", *Stud. Appl. Maths.*, vol. 53, pp. 249–315, 1974.

[168] T. Kano, "Normal form of nonlinear Schrödinger equation", *J. Phys. Soc. Jpn.*, vol. 58, no. 12, pp. 4322–4328, 1989.

[169] M. Lakshmanan, K. Porsezian, and M. Daniel, "Effect of discreteness on the continuum limit of the Heisenberg spin chain", *Phys. Lett. A*, vol. 133, no. 9, pp. 483–488, 1988.

[170] A. Ankiewicz, Y. Wang, S. Wabnitz, and N. Akhmediev, "Extended nonlinear Schrödinger equation with higher-order odd and even terms and its rogue wave solutions", *Phys. Rev. E*, vol. 89, no. 1, p. 012907, 2014.

[171] V. J. Konecni, "The aesthetic trinity: Awe, being moved, thrills", *Bulletin of Psychology and the Arts*, vol. 5, no. 2, pp. 27–44, 2005.

[172] B. Guo, L. Ling, and Q. Liu, "Nonlinear Schrödinger equation: Generalized Darboux transformation and rogue wave solutions", *Phys. Rev. E*, vol. 85, no. 2, p. 026607, 2012.

[173] P. Gaillard, "Degenerate determinant representation of solutions of the nonlinear Schrödinger equation, higher order Peregrine breathers and multi-rogue waves", *J. Math. Phys.*, vol. 54, no. 1, p. 013504, 2013.

[174] P. Dubard and V. B. Matveev, "Multi-rogue waves solutions: from the NLS to the KP-I equation", *Nonlinearity*, vol. 26, no. 12, p. R93, 2013.

[175] B. Guo, L. Ling, and Q. P. Liu, "High-Order Solutions and Generalized Darboux Transformations of Derivative Nonlinear Schrödinger Equations", *Stud. Appl. Maths.*, vol. 130, no. 4, pp. 317–344, 2013.

[176] W.-P. Zhong, M. R. Belić, and T. Huang, "Rogue wave solutions to the generalized nonlinear Schrödinger equation with variable coefficients", *Phys. Rev. E*, vol. 87, no. 6, p. 065201, 2013.

[177] N. Akhmediev and A. Ankiewicz, "Modulation instability, Fermi-Pasta-Ulam recurrence, rogue waves, nonlinear phase shift, and exact solutions of the Ablowitz-Ladik equation", *Phys. Rev. E*, vol. 83, p. 046603, Apr 2011.

[178] N. Akhmediev, V. M. Eleonskii, and N. E. Kulagin, "Generation of a periodic sequence of picosecond pulses in an optical fiber. Exact solutions", *Zh. Eksp. Teor. Fiz.*, vol. 89, pp. 1542–1551, 1985. English translation in: [Sov. Phys. JETP, **62**, 894 (1985)].

[179] N. N. Akhmediev, V. I. Korneev, and N. V. Mitskevich, "N-modulation signals in a single-mode optical fiber with allowance for nonlinearity", *Zh. Eksp. Teor. Fiz.*, vol. 94, pp. 159–170, 1988. English translation in: [Sov. Phys. JETP, **67**, 89 (1988)].

[180] A. V. Babanin, T. Waseda, I. Shugan, and H.-H. Hwung, "Modulational Instability in Directional Wave Fields, and Extreme Wave Events", in *ASME 2011 30th International Conference on Ocean, Offshore and Arctic Engineering*, pp. 409–415, American Society of Mechanical Engineers, 2011.

[181] M. Bertola and A. Tovbis, "Universality for the Focusing Nonlinear Schrödinger Equation at the Gradient Catastrophe Point: Rational Breathers and Poles of the Tritronquée Solution to Painlevé I", *Comm. Pure Appl. Math.*, vol. 66, no. 5, pp. 678–752, 2013.

[182] U. Bortolozzo, L. Pastur, P. L. Ramazza, M. Tlidi, and G. Kozyreff, "Bistability between Different Localized Structures in Nonlinear Optics", *Phys. Rev. Lett.*, vol. 93, p. 253901, Dec 2004.

[183] H. S. Chiu, K. W. Chow, and C. H. Tsang, "Studies of freak or rogue waves by the nonlinear Schrödinger model", in *Proceedings of the 33rd IAHR Congress*, pp. 6264–6270, 2009.

[184] K. W. Chow, R. Conte, and N. Xu, "Analytic doubly periodic wave patterns for the integrable discrete nonlinear Schrödinger (Ablowitz–Ladik) model", *Phys. Lett. A*, vol. 349, no. 6, pp. 422–429, 2006.

[185] D. Clamond, "Cnoidal-type surface waves in deep water", *J. Fluid Mech.*, vol. 489, pp. 101–120, 2003.

[186] S. Cuenda and A. Sánchez, "Length scale competition in nonlinear Klein—Gordon models: A collective coordinate approach", *Chaos: An Interdisciplinary Journal of Nonlinear Science*, vol. 15, no. 2, p. 023502, 2005.

[187] D. Clamond, M. Francius, J. Grue, and C. Kharif, "Long time interaction of envelope solitons and freak wave formations", *Eur. J. Mech. B/Fluids.*, vol. 25, pp. 536 – 553, 2006.

[188] I. Didenkulova, "Shapes of freak waves in the coastal zone of the Baltic Sea (Tallinn Bay)", *Boreal Environ. Res.*, vol. 16, no. suppl A, pp. 138–148, 2011.

[189] J. M. Dudley, G. Genty, F. Dias, B. Kibler, and N. Akhmediev, "Modulation instability, Akhmediev Breathers and continuous wave supercontinuum generation", *Opt. Express*, vol. 17, p. 21497, 2009.

[190] K. B. Dysthe and K. Trulsen, "Note on Breather type Solutions of the NLS as models for freak-waves", *Phys. Scr.*, vol. T82, pp. 48–52, 1999.

[191] E. Pelinovsky and C. Kharif, *Extreme Ocean Waves*. Springer, Berlin, Heidelberg, 2008.

[192] F. T. Arecchi, U. Bortolozzo, A. Montina, and S. Residori, "Granularity and Inhomogeneity Are the Joint Generators of Optical Rogue Waves", *Phys. Rev. Lett.*, vol. 106, p. 153901, 2011.

[193] M. A. García-Ñustes, I. Rondón, J. A. González, and R. Chacón, "Kink propagation in inhomogeneous systems driven by spatiotemporal perturbations", *J. Phys: Conf. Ser.*, vol. 246, no. 1, p. 012008, 2010.

[194] C. Garrett and J. Gemmrich, "Rogue waves", *Phys. Today*, vol. 62, pp. 62–63, 2009.

[195] S. Kamvissis, K. D. T.-R. McLaughlin, and P. D. Miller, *Semiclassical Soliton Ensembles for the Focusing Nonlinear Schrodinger Equation (AM-154)*, vol. 154. Princeton University Press, 2003.

[196] C. Kharif, E. Pelinovsky, and A. Slunyaev, *Rogue waves in the ocean*. Springer, 2009.

[197] P. Leboeuf and N. Pavloff, "Bose-Einstein beams: Coherent propagation through a guide", *Phys. Rev. A*, vol. 64, no. 3, p. 033602, 2001.

[198] S. L. Lu Li, Zhonghao Li and G. Zhou, "Modulation instability and solitons on a cw background in inhomogeneous optical fiber media", *Opt. Commun.*, vol. 234, pp. 169 – 176, 2004.

[199] M. Shats, H. Punzmann, and H. Xia, "Capillary Rogue Waves", *Phys. Rev. Lett.*, vol. 104, p. 104503, 2010.

[200] Q.-H. Park and H. J. Shin, "Parametric Control of Soliton Light Traffic by cw Traffic Light", *Phys. Rev. Lett.*, vol. 82, pp. 4432 – 4435, 1999.

[201] P. L. Ramazza, U. Bortolozzo, and L. Pastur, "Phase singularities in triangular dissipative solitons", *J. Opt. A: Pure Appl. Opt.*, vol. 6, no. 5, p. S266, 2004.

[202] R. Sabry, W. M. Moslem, and P. K. Shukla, "Amplitude modulation of hydromagnetic waves and associated rogue waves in magnetoplasmas", *Phys. Rev. E*, vol. 86, no. 3, p. 036408, 2012.

[203] P. K. Shukla and W. M. Moslem, "Alfvénic rogue waves", *Phys. Lett. A*, vol. 376, no. 12, pp. 1125–1128, 2012.

[204] M. Tajiri and Y. Watanabe, "Breather solutions to the focusing nonlinear Schrödinger equation", *Phys. Rev. E*, vol. 57, pp. 3510 – 3519, 1998.

[205] I. Ten and H. Tomita, "Simulation of the ocean waves and appearance of freak waves", in *Reports of RIAM Symposium*, no. 17SP1-2, pp. 10–11, 2006.

[206] A. Tovbis, S. Venakides, and X. Zhou, "On semiclassical (zero dispersion limit) solutions of the focusing nonlinear Schrödinger equation", *Comm. Pure Appl. Math.*, vol. 57, no. 7, pp. 877–985, 2004.

[207] K. Trulsen, "Crest pairing predicted by modulation theory", *J. Geophys. Res.*, vol. 103, no. C2, pp. 3143–3147, 1998.

[208] V. V. Voronovich, V. I. Shrira, and G. Thomas, "Can bottom friction suppress freak wave formation?", *J. Fluid Mech.*, vol. 604, pp. 263 – 296, 2008.

[209] S. Wabnitz and N. Akhmediev, "Efficient modulation frequency doubling by induced modulation instability", *Opt. Commun.*, vol. 283, p. 1152, 2010.

[210] R. L. Wiegel, "A presentation of cnoidal wave theory for practical application", *J. Fluid Mech.*, vol. 7, no. 02, pp. 273–286, 1960.

[211] H. C. Yuen and B. M. Lake, "Instabilities of waves on deep water", *Annu. Rev. Fluid Mech.*, vol. 12, pp. 303–334, 1980.